

Electromagnetic excitation of the $\Delta(1232)$ -resonance

Vladimir Pascalutsa ^{a,b,c}, Marc Vanderhaeghen ^{a,b}, Shin Nan Yang ^d

^a*Physics Department, The College of William & Mary, Williamsburg, VA 23187, USA*

^b*Theory Center, Jefferson Lab, 12000 Jefferson Ave, Newport News, VA 23606, USA*

^c*ECT*, Villa Tambosi, Str. delle Tabarelle 286, I-38050 Villazzano (Trento), Italy*

^d*Department of Physics and Center for Theoretical Sciences, National Taiwan University, Taipei 10617, Taiwan*

Abstract

We review the description of the lowest-energy nucleon excitation — the $\Delta(1232)$ -resonance. Much of the recent effort has been focused on the precision measurements of the nucleon to Δ transition by means of electromagnetic probes. We review the results of those measurements and confront them with the state-of-the-art calculations based on chiral effective-field theories (EFT), lattice QCD, and QCD-inspired models. Some of the theoretical approaches are reviewed in detail. In particular, we describe the chiral EFT of QCD in the energy domain of the Δ -resonance, and its applications to the electromagnetic nucleon-to- Δ transition ($\gamma N \Delta$). We also describe the recent dynamical and unitary-isobar models of pion electroproduction which are extensively used in the extraction of the $\gamma^* N \Delta$ form factors from experiment. Furthermore, we discuss the link of the $\gamma^* N \Delta$ form factors to generalized parton distributions (GPDs), as well as the predictions of perturbative QCD for these transition form factors. The present status of understanding the Δ -resonance properties and the nature of its excitation is summarized.

Key words: Delta(1232) resonance, Electromagnetic form factors, Meson production

PACS: 14.20.Gk, 13.40.Gp, 13.60.Le

prepared for Physics Reports

Contents

1	Introduction	5
2	The electromagnetic $N \rightarrow \Delta$ transition in QCD	8
2.1	Definitions and conventions	9
2.1.1	The $\gamma^* N \Delta$ vertex and form factors	9
2.1.2	The $\gamma^* \Delta \Delta$ vertex and form factors	14
2.2	Experimental information at the real photon point	14
2.3	Physical interpretation: quark and pion-cloud models	16
2.3.1	Constituent quark models	16
2.3.2	Pion cloud models	18
2.3.3	Intrinsic quadrupole moment and the issue of shape	21
2.4	Large N_c limit	23
2.5	Chiral effective field theory	26
2.6	Lattice QCD and chiral extrapolation	30
2.6.1	Lattice simulations	30
2.6.2	Chiral extrapolations	34
2.7	The $N \rightarrow \Delta$ generalized parton distributions (GPDs)	39
2.7.1	Definition of $N \rightarrow N$ and $N \rightarrow \Delta$ GPDs and sum rules	39
2.7.2	Model for the magnetic dipole $N \rightarrow \Delta$ GPD	44
2.7.3	Model for the electric quadrupole $N \rightarrow \Delta$ GPD	47
2.7.4	GPDs and transverse structure of hadrons	49
2.8	The $\gamma^* N \Delta$ transition in perturbative QCD (pQCD)	50
2.8.1	pQCD predictions for helicity amplitudes and form factors	50
2.8.2	The road to “asymptopia”	54
3	Phenomenology of pion photo- and electroproduction	56

3.1	Introductory remarks	56
3.1.1	Measurement of pion photoproduction amplitudes	57
3.1.2	Measurement of pion electroproduction amplitudes	58
3.2	Dynamical models	61
3.2.1	General framework: unitarity, relativity, gauge invariance	61
3.2.2	Sato-Lee model	64
3.2.3	Dubna-Mainz-Taipei model	67
3.2.4	Dynamical Utrecht-Ohio model	72
3.3	MAID - a phenomenological multipole solution	74
3.4	Dispersion relation approach	76
4	Chiral effective-field theory in the Δ -resonance region	79
4.1	Effective chiral Lagrangians	79
4.2	Inclusion of the spin-3/2 fields	82
4.3	Chiral Lagrangians with Δ 's	86
4.4	Power counting, renormalization and naturalness	89
4.5	In practice: the next-to-leading order calculations	93
4.5.1	Pion-nucleon scattering	93
4.5.2	Pion photo- and electroproduction	96
4.5.3	Compton scattering	101
4.5.4	Radiative pion photoproduction	102
4.5.5	Errors due to neglect of N^2LO effects	105
5	Results for observables and discussion	108
5.1	Introductory remarks	108
5.2	Pion photoproduction	109
5.3	Pion electroproduction	114

6	Beyond the one-photon exchange approximation	123
6.1	General formalism	123
6.2	Partonic calculation of two-photon exchange effects	126
7	Conclusions and outlook	129
A	General analysis of the electromagnetic pion production on the nucleon	133
A.1	Kinematical details	133
A.2	CGLN decomposition	134
A.3	Helicity amplitudes	134
A.4	Multipole decomposition	135
A.5	Isospin decomposition	136
	References	139

1 Introduction

The $\Delta(1232)$ resonance — the first excited state of the nucleon — dominates the pion-production phenomena and plays a prominent role in the physics of the strong interaction. This resonance, first witnessed more than 50 years ago by Fermi and collaborators [1] in pion scattering off protons at the Chicago cyclotron (now Fermilab), is a distinguished member of the large family of excited baryons. It is the lightest baryon resonance, with a mass of 1232 MeV, less than 300 MeV heavier than the nucleon. Despite its relatively broad width of 120 MeV (corresponding with the lifetime of $10^{-23}s$), the Δ is very well isolated from other resonances. It is almost an ideally elastic πN resonance, 99% of the time it decays into the nucleon and pion, $\Delta \rightarrow N\pi$. The only other decay channel – electromagnetic, $\Delta \rightarrow N\gamma$, contributes less than 1% to the total decay width (even though this channel will preoccupy the larger part of this review). The $\Delta(1232)$ has isospin 3/2 and as such comes in four different charge states: Δ^{++} , Δ^+ , Δ^0 , and Δ^- , all with (approximately) the same mass and width. The spin of the $\Delta(1232)$ is also 3/2, and it is the lightest known particle with such a spin.

The Δ -resonance dominates many nuclear phenomena at energies above the pion-production threshold [2] (for recent reviews see [3,4]). In cosmology it is largely responsible for the “GZK cut-off”[5], which occurs due the suppression of the high-energy cosmic ray flux by the cosmic microwave background (CMB). Once the energy of the cosmic rays is sufficient to produce the Δ -resonance in the scattering off the CMB photons, the rate of observed rays drops dramatically (for a recent calculation see [6]). This effect puts a cutoff on the primary cosmic ray energy at around 10^{19} eV for the rays coming from a distance larger than a few tens of Mpc.

In a laboratory, the Δ ’s are produced in scattering the pion, photon, or electron beams off a nucleon target. High-precision measurements of the $N \rightarrow \Delta$ transition by means of electromagnetic probes became possible with the advent of the new generation of electron beam facilities, such as LEGS, BATES, ELSA, MAMI, and Jefferson Lab. Many such experimental programs devoted to the study of electromagnetic properties of the Δ have been completed in the past few years.

The current experimental effort has been accompanied by exciting developments on the theoretical side, most recently in the fields of lattice QCD and chiral effective-field theories. These recent experimental and theoretical advances in understanding the Δ -resonance properties are the main subjects of this review.

The *electromagnetic* $N \rightarrow \Delta$ (or, in short $\gamma N \Delta$) transition is predominantly of the magnetic dipole ($M1$) type. A first understanding of the $\gamma N \Delta$ transition can be obtained based on symmetries of Quantum Chromodynamics (QCD) and its large number-of-color (N_c) limit. The spin-flavor global symmetry of QCD, is utilized by many quark models and is exactly realized in the large- N_c limit. In the quark-model picture, the $N \rightarrow \Delta$ transition is described by a spin flip of a quark in the s -wave state, which in the $\gamma N \Delta$ case leads to the magnetic dipole ($M1$) type of transition. Any d -wave admixture in the nucleon *or* the Δ wave functions allows also for the electric ($E2$) and Coulomb ($C2$) quadrupole transitions. Therefore, by measuring the latter two transitions, one is able to assess the presence of the d -wave components and hence quantify to which extent the nucleon or the Δ wave function deviates from the spherical shape. In this way one can hope to understand to which extent these particles are “deformed”.

The d -wave component of Δ ’s wave function can be separately assessed by measuring the

electric quadrupole moment of the Δ . However, this would be extremely difficult because of the tiny lifetime of the Δ . The small d -state probability of the Δ 's wave function also enters into the Δ magnetic dipole moment, which is being measured, but the extraction of a small number from such a quantity is also very complicated. The $\gamma N \Delta$ transition, on the other hand, was accurately measured in the pion photo- and electro-production reactions in the Δ -resonance energy region. The $E2$ and $C2$ transitions were found to be relatively small but non-zero at moderate momentum-transfers (Q^2), the ratios $R_{EM} = E2/M1$ and $R_{SM} = C2/M1$ are at the level of a few percent.

Because the Δ excitation energy is only around 300 MeV and because it almost entirely decays into πN , pions are expected to play a prominent role in the Δ properties. Early calculations of the $\gamma N \Delta$ transition within chiral bag models revealed the importance of the pion cloud effects. Recall that pions are the Goldstone bosons of the spontaneously broken chiral symmetry of QCD. As the strength of the Goldstone boson interactions is proportional to their energy, at sufficiently low energy a perturbative expansion is possible. With the advent of the chiral effective field theory (χ EFT) of QCD [7–9] and its extensions to the Δ -resonance region, it has become possible to study the nucleon and Δ -resonance properties in a profoundly different way. The advantages of such an approach are apparent: χ EFT is a low-energy effective field theory of QCD and as such it provides a firm theoretical foundation, with all the relevant symmetries and scales of QCD built in consistently. The $\gamma N \Delta$ transition provides new challenges for χ EFT as it involves the interplay of two light mass scales : the pion mass and the $N - \Delta$ mass difference. This topic will preoccupy a large part of this review, and we discuss up to which energy/momentum scales such an approach can be expected to hold.

Considerable progress has recently been achieved as well in the lattice QCD simulations of hadronic properties. They hold the promise to compute non-perturbative properties of QCD from first principles. The present state-of-the-art results for hadronic structure quantities, such as the $\gamma N \Delta$ transition form factors, are obtained for pion masses above 300 MeV. Therefore, they can only be confronted with experiment after an extrapolation down to the physical pion mass of 140 MeV. Such extrapolation can be obtained with the aid of χ EFT, where the pion mass dependence is systematically calculable. The χ EFT framework thus provides a connection between lattice QCD calculations and experiment.

The quark structure of the $N \rightarrow \Delta$ transition is accessible through the phenomenon of asymptotic freedom of QCD at short distances. In a hard scattering process, such as $\gamma^* N \rightarrow \gamma \Delta$ where the virtual photon γ^* transfers a large momentum, the QCD factorization theorems allow one to separate the perturbative and non-perturbative stages of the interaction. In this way, one accesses in experiment the non-perturbative matrix elements parametrized in terms of new parton distributions, which are generalizations of the quark distributions from deep inelastic scattering experiments. One obtains in this way quark distribution information for the $N \rightarrow \Delta$ transition, and the $\gamma N \Delta$ form factors are obtained as first moments of such $N \rightarrow \Delta$ generalized parton distributions.

Traditionally, the resonance parameters are extracted from pion electroproduction experiments by using unitary isobar models, which in essence are unitarized tree-level calculations based on phenomenological Lagrangians. However, as discussed above, at low Q^2 the $\gamma N \Delta$ -transition shows great sensitivity to the “pion cloud”, which until recently could only be comprehensively studied within dynamical models, which will also be reviewed here.

The outline of this review is as follows. In Sect. 2, we introduce the definitions for the $\gamma N \Delta$

and $\gamma\Delta\Delta$ form factors and review the experimental status of the $\gamma N\Delta$ transition at the real photon point. We then discuss our present theoretical understanding of the $\gamma N\Delta$ transition. Some physical insight is obtained from QCD inspired models based on quark degrees of freedom, pion degrees of freedom, as well as from the large N_c limit. The chiral symmetry of QCD is reviewed and the role of pions in the $\gamma N\Delta$ transition highlighted. We review the status of the lattice QCD calculations and their limitations. Subsequently, we discuss the quark structure of the $N \rightarrow \Delta$ transition. We introduce generalized parton distributions for the $N \rightarrow \Delta$ transition and discuss our phenomenological information of such distributions based on their relation to the $\gamma N\Delta$ form factors. Finally, we confront predictions made by perturbative QCD at very large momentum transfers with the available data.

The theoretical formalism of dynamical models will be discussed in detail in Sect. 3, and compared with other approaches such as unitary isobar models and dispersion relations.

In Sect. 4, we will review how χ EFT can be applied to study the $\gamma N\Delta$ -transition at low momentum transfers. It will be discussed that the χ EFT may provide a theoretically consistent and phenomenologically viable framework for the extraction of the resonance parameters. In particular we will review how the Δ can be introduced in a χ EFT and discuss the field-theoretic intricacies due to the spin-3/2 nature of the Δ . We will apply the χ EFT formalism to pion electroproduction in the Δ region and discuss applications to other complementary processes such as Compton scattering and radiative pion photoproduction in the Δ region. The convergence of the perturbative χ EFT expansion will also be addressed.

In Sect. 5, we compare predictions of both dynamical models and χ EFT to the pion photo- and electroproduction observables.

The information on the $\gamma N\Delta$ transition as discussed above is obtained from pion electroproduction assuming that the interaction is mediated by a single photon exchange. In Sect. 6, we give a brief description of our understanding of corrections to this process beyond the one-photon exchange, which may become relevant with increasing Q^2 .

Finally in Sect. 7, we give our conclusions and spell out some open issues in this field.

Several reviews exist in the literature on various aspects of the $\gamma N\Delta$ transition. Among the more recent reviews, we refer the reader to Ref. [10] where the formalism to extract $\gamma N\Delta$ form factors from pion photo- and electroproduction observables is outlined in detail. The experimental status of the $\gamma N\Delta$, and γNN^* transitions as obtained from meson photoproduction experiments is well described in Ref. [11]. The status of pion electroproduction experiments in the Δ region as well as a previous review of dynamical models can be found in Ref. [12].

2 The electromagnetic $N \rightarrow \Delta$ transition in QCD

Both the nucleon and the $\Delta(1232)$ can be considered as quantum states in the rich and complex spectrum of the quark-gluon system. It is well established that the underlying theory which should describe this spectrum is Quantum Chromodynamics (QCD). However, direct calculations in QCD of quantities such as the baryon spectrum, form factors, and parton distributions are extremely difficult, because they require non-perturbative methods. Only the lattice simulations have achieved some limited success to date in computing the hadron properties from first principles. Even then, such calculations are severely limited by the presently available computing power.

Fortunately, some insight into the properties of the spectrum can be obtained based on general principles of QCD, such as the global symmetries and large number-of-colors (N_C) limit of QCD. After introducing the definitions of $\gamma^* N \Delta$ and $\gamma^* \Delta \Delta$ form factors in Sect. 2.1, and reviewing the experimental status on the $\gamma N \Delta$ transition at the real photon point in Sect. 2.2, we shall discuss in Sect. 2.3 the predictions for the $\gamma N \Delta$ transition due to the *spin-flavor symmetry*, utilized by many quark models and exactly realized in the large- N_c limit, as discussed in Sect. 2.4. Furthermore, we shall compare predictions for the $\gamma N \Delta$ transition from QCD inspired models based on quark degrees of freedom as well as pion degrees of freedom to gain some physical insights.

In Sect. 2.5, we shall discuss the *chiral symmetry* of QCD and the role of pions in the electromagnetic $N \rightarrow \Delta$ transition. A chiral effective field theory is able to provide predictions for the low momentum transfer behavior of the $\gamma^* N \Delta$ form factors.

In Sect. 2.6, we shall discuss the present lattice QCD calculations and their limitations. Present lattice QCD calculations are performed for quark masses sizably larger than their values in nature, corresponding with pion mass values of around 0.3 GeV or larger. It will be discussed how the chiral effective field theory is also able to predict the pion mass dependence of the $\gamma^* N \Delta$ form factors and in this way extrapolate present lattice QCD calculations to the physical pion mass value.

In Sect. 2.7, we shall review the quark structure of the $N \rightarrow \Delta$ transition and discuss generalized parton distributions (GPDs) for the electromagnetic $N \rightarrow \Delta$ transition. The GPDs can be accessed in hard exclusive processes such as deeply virtual Compton scattering where the hard probe ensures that the process occurs on a quark which is taken out of the initial nucleon and inserted into the final Δ . We shall see that the $\gamma^* N \Delta$ form factors are obtained as the first moment in the struck quark momentum fraction of such GPDs, which provide much richer information on the $N \rightarrow \Delta$ transition at the quark level.

Finally, in Sect. 2.8, we shall consider the $N \rightarrow \Delta$ transition in the formalism of perturbative QCD (pQCD). These considerations are valid only at very small distances, where quarks nearly do not interact — asymptotic freedom. In this limit, the $\gamma^* N \Delta$ form factors correspond with a hard photon which hits a quark in the nucleon. The struck quark shares the large momentum with the other two (near collinear) valence quarks in such a way that the final three quark state has Δ quantum numbers. We shall discuss the predictions made in this limit and confront them with the experimental status of the $\gamma^* N \Delta$ form factors at large momentum transfers.



Fig. 1. $\gamma^* N \Delta$ vertex (left panel) and $\pi N \Delta$ vertex (right panel). The four-momenta of the nucleon (Δ) and of the photon (pion) are given by p (p') and q (k) respectively. The four-vector index of the spin 3/2 field is given by α , and μ is the four-vector index of the photon field.

2.1 Definitions and conventions

Throughout this review we shall use the following conventions for the metric and γ -matrices: $g^{\mu\nu} = \text{diag}(1, -1, -1, -1)$, $\{\gamma^\mu, \gamma^\nu\} = 2g^{\mu\nu}$, $\gamma_5 = i\gamma^0\gamma^1\gamma^2\gamma^3$, $\varepsilon_{0123} = +1$. The $\gamma N \Delta$ and $\gamma \Delta \Delta$ form factors are introduced as follows.

2.1.1 The $\gamma^* N \Delta$ vertex and form factors

The general spin structure of the pion- and photon-induced $N \rightarrow \Delta$ transitions, see Fig. 1, can be written as:

$$\bar{u}_\alpha(p') \Gamma_{\pi N \Delta}^\alpha u(p) \equiv \frac{h_A}{2f_\pi} \bar{u}_\alpha(p') k^\alpha T_a^\dagger u(p) F_{\pi N \Delta}(k^2), \quad (2.1)$$

$$\begin{aligned} \langle \Delta(p') | e J^\mu(0) | N(p) \rangle &\equiv i \bar{u}_\alpha(p') \Gamma_{\gamma N \Delta}^{\alpha\mu} u(p) \\ &\equiv i \sqrt{\frac{2}{3}} \frac{3e(M_\Delta + M_N)}{2M_N[(M_\Delta + M_N)^2 + Q^2]} \\ &\quad \times \bar{u}_\alpha(p') \left\{ g_M(Q^2) \varepsilon^{\alpha\mu\rho\sigma} p'_\rho q_\sigma \right. \\ &\quad + g_E(Q^2) (q^\alpha p'^\mu - q \cdot p' g^{\alpha\mu}) i\gamma_5 \\ &\quad \left. + g_C(Q^2) (q^\alpha q^\mu - q^2 g^{\alpha\mu}) i\gamma_5 \right\} u(p), \end{aligned} \quad (2.2)$$

where k is the pion and q is the photon 4-momentum, p (p') is the nucleon (the Δ) 4-momentum, M_N (M_Δ) is the nucleon (the Δ) mass, u is the nucleon spinor, and u_α represents the spin-3/2 Δ vector-spinor. In Eqs. (2.1) and (2.2), the spin dependence in the N and Δ spinors is understood. The operator T_a^\dagger in Eq. (2.1), with $a = 1, 2, 3$ corresponding with the Cartesian pion fields π^a , is the isospin $1/2 \rightarrow 3/2$ transition operator. The operator J^μ is the electromagnetic current operator, and the factor $\sqrt{2/3}$ in front of Eq. (2.2) corresponds with the isospin factor for the photon induced $p \rightarrow \Delta^+$ transition. Furthermore, $f_\pi \simeq 92.4$ MeV is the pion decay constant, h_A is a dimensionless constant representing the strength of the $\pi N \rightarrow \Delta$ transition and thus related to the decay width of the Δ to πN , see Sect. 4.5.1.

The strong transition form factor $F_{\pi N \Delta}$ is normalized as $F_{\pi N \Delta}(m_\pi^2) = 1$, and can in principle depend as well on the invariant mass of the nucleon and Δ , *i.e.*, p^2 and p'^2 . However, unless ex-

plicitly specified, we assume that nucleon and Δ are on the mass shell and therefore $p^2 = M_N^2$, $\not{p} u(p) = M_N u(p)$, $p'^2 = M_\Delta^2$, $\not{p}' u_\alpha(p') = M_\Delta u_\alpha(p')$, and $p'_\alpha u^\alpha(p') = 0 = \gamma_\alpha u^\alpha(p')$. We use the covariant normalization convention for the spinors, *i.e.* $\bar{u}(p)u(p) = 2M_N$, and $\bar{u}_\alpha(p')u^\alpha(p') = -2M_\Delta$.

In Eq. (2.2), the electromagnetic form factors g_M , g_E , and g_C represent the strength of the magnetic dipole, electric quadrupole, and Coulomb quadrupole $N \rightarrow \Delta$ transitions, respectively, as a function of the momentum transfer: $Q^2 = -q^2$. Note that for the real photon case, $Q^2 = 0$, only the magnetic and electric transitions are possible, the Coulomb term drops out.

These electromagnetic form factors relate to the more conventional magnetic dipole (G_M^*), electric quadrupole (G_E^*) and Coulomb quadrupole (G_C^*) form factors of Jones and Scadron [13] as follows¹:

$$\begin{aligned} G_M^*(Q^2) &= g_M + \frac{1}{Q_+^2} \left[\frac{1}{2}(-M_\Delta^2 + M_N^2 + Q^2) g_E + Q^2 g_C \right], \\ G_E^*(Q^2) &= \frac{1}{Q_+^2} \left[\frac{1}{2}(-M_\Delta^2 + M_N^2 + Q^2) g_E + Q^2 g_C \right], \\ G_C^*(Q^2) &= \frac{1}{Q_+^2} \left[(-M_\Delta^2 + M_N^2 + Q^2) g_C - 2M_\Delta^2 g_E \right], \end{aligned} \quad (2.3)$$

where Q_\pm is defined as:

$$Q_\pm \equiv \sqrt{(M_\Delta \pm M_N)^2 + Q^2}. \quad (2.4)$$

Equivalently, one can also parametrize the $\gamma^* N \Delta$ transition through three helicity amplitudes $A_{1/2}$, $A_{3/2}$ and $S_{1/2}$, which are defined in the Δ rest frame as illustrated in Fig. 2. These Δ rest frame helicity amplitudes are defined through the following matrix elements of the electromagnetic current operator²:

$$\begin{aligned} A_{3/2} &\equiv -\frac{e}{\sqrt{2}q_\Delta} \frac{1}{(4M_N M_\Delta)^{1/2}} \langle \Delta(\vec{0}, +3/2) | \mathbf{J} \cdot \epsilon_{\lambda=+1} | N(-\vec{q}, +1/2) \rangle, \\ A_{1/2} &\equiv -\frac{e}{\sqrt{2}q_\Delta} \frac{1}{(4M_N M_\Delta)^{1/2}} \langle \Delta(\vec{0}, +1/2) | \mathbf{J} \cdot \epsilon_{\lambda=+1} | N(-\vec{q}, -1/2) \rangle, \\ S_{1/2} &\equiv \frac{e}{\sqrt{2}q_\Delta} \frac{1}{(4M_N M_\Delta)^{1/2}} \langle \Delta(\vec{0}, +1/2) | J^0 | N(-\vec{q}, +1/2) \rangle, \end{aligned} \quad (2.5)$$

where the spin projections are along the z -axis (chosen along the virtual photon direction) and where the transverse photon polarization vector entering in $A_{1/2}$ and $A_{3/2}$ is given by $\epsilon_{\lambda=+1} =$

¹ The form factors G_M^* , G_E^* , and G_C^* used throughout this work correspond with the ones also used in Ref. [14], except for the sign of G_C^* which is chosen to be opposite in Ref. [14]. The sign convention used in this work leads to positive values of all three form factors at $Q^2 = 0$, see Sect. 4.

² Note that the normalization of Eq. (2.5) corresponds with covariant spinor normalization, *i.e.* $\bar{u}(p)u(p) = 2M_N$ and $\bar{u}_\alpha(p')u^\alpha(p') = -2M_\Delta$.

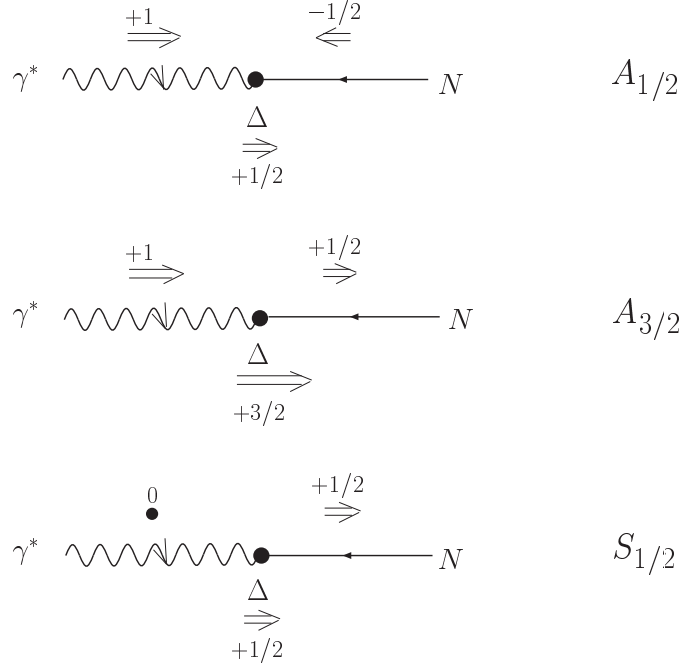


Fig. 2. $\gamma^* N \rightarrow \Delta$ helicity amplitudes in the Δ rest frame. The γ , N , and Δ spin projections onto the z -axis, which is chosen along the virtual photon direction, are indicated on the figure. The corresponding helicity amplitudes are indicated on the right.

$-1/\sqrt{2}(1, i, 0)$. Furthermore in Eq. (2.5), e is the proton electric charge, related to the fine-structure constant as $\alpha_{em} \equiv e^2/(4\pi) \simeq 1/137$, and q_Δ is the magnitude of the virtual photon three-momentum in the Δ rest frame:

$$q_\Delta \equiv |\mathbf{q}| = \frac{Q_+ Q_-}{2M_\Delta}. \quad (2.6)$$

The helicity amplitudes are functions of the photon virtuality Q^2 , and can be expressed in terms of the Jones-Scadron $\gamma^* N \Delta$ form factors, by using Eq. (2.2), as :

$$\begin{aligned} A_{3/2} &= -N \frac{\sqrt{3}}{2} \{G_M^* + G_E^*\} , \\ A_{1/2} &= -N \frac{1}{2} \{G_M^* - 3G_E^*\} , \\ S_{1/2} &= N \frac{q_\Delta}{\sqrt{2}M_\Delta} G_C^*, \end{aligned} \quad (2.7)$$

where N is defined as :

$$N \equiv \frac{e}{2} \left(\frac{Q_+ Q_-}{2M_N^3} \right)^{1/2} \frac{(M_N + M_\Delta)}{Q_+}. \quad (2.8)$$

The above helicity amplitudes are expressed in units $\text{GeV}^{-1/2}$, and reduce at $Q^2 = 0$ to the photo-couplings quoted by the Particle Data Group [15].

Experimentally, the $\gamma^* N \Delta$ helicity amplitudes are extracted from the $M1$, $E2$, and $C2$ multipoles for the $\gamma^* N \rightarrow \pi N$ process at the resonance position, *i.e.* for πN *c.m.* energy $W = M_\Delta$. These pion electroproduction multipoles are denoted by $M_{1+}^{(3/2)}$, $E_{1+}^{(3/2)}$, and $S_{1+}^{(3/2)}$ (following standard notation, see *e.g.* Ref. [16] and Sect. 3 for more details), where the subscript refers to the partial wave $l = 1$ in the πN system and “+” indicates that the total angular momentum is $J = l + 1/2$, being $3/2$. The superscript $(3/2)$ in the multipole notation refers to the total isospin $3/2$. The $\gamma^* N \Delta$ helicity amplitudes $A_{3/2}$, $A_{1/2}$, and $S_{1/2}$ are obtained from the $\gamma^* N \rightarrow \pi N$ resonant multipoles as [17]:

$$\begin{aligned} A_{3/2} &= -\frac{\sqrt{3}}{2} \left\{ \bar{M}_{1+}^{(3/2)} - \bar{E}_{1+}^{(3/2)} \right\}, \\ A_{1/2} &= -\frac{1}{2} \left\{ \bar{M}_{1+}^{(3/2)} + 3 \bar{E}_{1+}^{(3/2)} \right\}, \\ S_{1/2} &= -\sqrt{2} \bar{S}_{1+}^{(3/2)}, \end{aligned} \tag{2.9}$$

where $\bar{M}_{1+}^{(3/2)}$, $\bar{E}_{1+}^{(3/2)}$, and $\bar{S}_{1+}^{(3/2)}$ are obtained from the imaginary parts of the resonant multipoles at the resonance position $W = M_\Delta$ as:

$$\bar{M}_{1+}^{(3/2)}(Q^2) \equiv \sqrt{\frac{2}{3}} a_\Delta \text{Im} M_{1+}^{(3/2)}(Q^2, W = M_\Delta), \tag{2.10}$$

where $\sqrt{2/3}$ is an isospin factor, and similar relations define $\bar{E}_{1+}^{(3/2)}$ and $\bar{S}_{1+}^{(3/2)}$. In these relations, a_Δ is given by:

$$a_\Delta = \left(\frac{4\pi k_\Delta M_\Delta \Gamma_\Delta}{q_\Delta M_N} \right)^{1/2}, \tag{2.11}$$

where Γ_Δ denotes the Δ width, which we take as $\Gamma_\Delta = 0.115 \text{ GeV}$, and k_Δ denotes the magnitude of the pion three-momentum in the πN *c.m.* frame at the resonance position ($W = M_\Delta$):

$$k_\Delta \equiv |\mathbf{k}| = \frac{1}{2M_\Delta} \left[(M_\Delta + M_N)^2 - m_\pi^2 \right]^{1/2} \cdot \left[(M_\Delta - M_N)^2 - m_\pi^2 \right]^{1/2}, \tag{2.12}$$

which yields $k_\Delta = 0.227 \text{ GeV}$. Furthermore, for $Q^2 = 0$, $q_\Delta = 0.259 \text{ GeV}$ and $a_\Delta \simeq 1.29 \text{ GeV}^{1/2}$.

We can extract the Jones-Scadron $\gamma^* N \Delta$ form factors from the multipoles at the resonance position. Combining Eqs. (2.7) and (2.9), we obtain:

$$\begin{aligned}
\bar{M}_{1+}^{(3/2)} &= N G_M^*, \\
\bar{E}_{1+}^{(3/2)} &= -N G_E^*, \\
\bar{S}_{1+}^{(3/2)} &= -N \frac{q_\Delta}{2M_\Delta} G_C^*. \tag{2.13}
\end{aligned}$$

Of special interest are the multipole ratios at the position of the Δ resonance. The ratio of electric quadrupole ($E2$) over magnetic dipole ($M1$) is denoted by : $R_{EM} = E2/M1$ (sometimes also denoted by EMR), whereas the ratio of Coulomb quadrupole ($C2$) over magnetic dipole is denoted by $R_{SM} = C2/M1$ (sometimes also denoted by CMR):

$$\begin{aligned}
R_{EM} \equiv EMR &\equiv \frac{\bar{E}_{1+}^{(3/2)}}{\bar{M}_{1+}^{(3/2)}} = \frac{A_{1/2} - \frac{1}{\sqrt{3}} A_{3/2}}{A_{1/2} + \sqrt{3} A_{3/2}}, \\
R_{SM} \equiv CMR &\equiv \frac{\bar{S}_{1+}^{(3/2)}}{\bar{M}_{1+}^{(3/2)}} = \frac{\sqrt{2} S_{1/2}}{A_{1/2} + \sqrt{3} A_{3/2}}. \tag{2.14}
\end{aligned}$$

Using the relations of Eq. (2.13), these ratios can be expressed in terms of the Jones-Scadron form factors as:

$$R_{EM} = -\frac{G_E^*}{G_M^*}, \quad R_{SM} = -\frac{Q_+ Q_-}{4M_\Delta^2} \frac{G_C^*}{G_M^*}. \tag{2.15}$$

From the values of the $\gamma^* N\Delta$ form factors at $Q^2 = 0$, one can extract some interesting static quantities. For the dominant $M1$ transition, one can extract the static $N \rightarrow \Delta$ transition magnetic moment $\mu_{N \rightarrow \Delta}$ from the value of G_M^* at $Q^2 = 0$ as [18]:

$$\mu_{N \rightarrow \Delta} = \sqrt{\frac{M_\Delta}{M_N}} G_M^*(0), \tag{2.16}$$

which is expressed in nuclear magnetons $\mu_N \equiv e/(2M_N)$.

Furthermore, from the value of G_E^* at $Q^2 = 0$, one can extract a static $N \rightarrow \Delta$ quadrupole transition moment $Q_{N \rightarrow \Delta}$ as [18]:

$$Q_{N \rightarrow \Delta} = -6 \sqrt{\frac{M_\Delta}{M_N}} \frac{1}{M_N q_\Delta(0)} G_E^*(0), \tag{2.17}$$

where $q_\Delta(0)$ is obtained from Eq. (2.6) for $Q^2 = 0$, as $q_\Delta(0) = (M_\Delta^2 - M_N^2)/2M_\Delta$.

Finally, we also like to note that in the literature, one sometimes uses so-called Ash form factors for the $\gamma^* N\Delta$ transition [19]. They are simply related to the Jones-Scadron form factors as:

$$G_{M, Ash}^*(Q^2) = \frac{(M_N + M_\Delta)}{Q_+} G_M^*(Q^2), \tag{2.18}$$

and analogously for the electric and Coulomb quadrupole form factors.

2.1.2 The $\gamma^*\Delta\Delta$ vertex and form factors

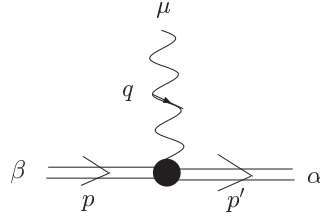


Fig. 3. The $\gamma^*\Delta\Delta$ vertex. The four-momenta of the initial (final) Δ and of the photon are given by p (p') and q respectively. The four-vector indices of the initial (final) spin 3/2 fields are given by β (α), and μ is the four-vector index of the photon field.

Consider the coupling of a photon to a Δ , Fig. 3. The matrix element of the electromagnetic current operator J^μ between spin 3/2 states can be decomposed into four multipole transitions: a Coulomb monopole (C0), a magnetic dipole (M1), an electric quadrupole (E2) and a magnetic octupole (M3). We firstly write a Lorentz-covariant decomposition which exhibits manifest electromagnetic gauge-invariance:

$$\begin{aligned}
\langle \Delta(p') | e J^\mu(0) | \Delta(p) \rangle &\equiv \bar{u}_\alpha(p') \Gamma_{\gamma\Delta\Delta}^{\alpha\beta\mu}(p', p) u_\beta(p) \\
&= -e \bar{u}_\alpha(p') \left\{ e_\Delta F_1^*(Q^2) g^{\alpha\beta} \gamma^\mu \right. \\
&\quad + \frac{i}{2M_\Delta} \left[F_2^*(Q^2) g^{\alpha\beta} + F_4^*(Q^2) \frac{q^\alpha q^\beta}{(2M_\Delta)^2} \right] \sigma^{\mu\nu} q_\nu \\
&\quad \left. + \frac{F_3^*(Q^2)}{(2M_\Delta)^2} \left[q^\alpha q^\beta \gamma^\mu - \frac{1}{2} q \cdot \gamma (g^{\alpha\mu} q^\beta + g^{\beta\mu} q^\alpha) \right] \right\} u_\beta(p) ,
\end{aligned} \tag{2.19}$$

where F_i^* are the $\gamma^*\Delta\Delta$ form factors, e_Δ is the electric charge in units of e (e.g., $e_{\Delta^+} = +1$), such that $F_1^*(0) = 1$. The relation to the multipole decomposition [20,21] can be written in terms of the magnetic dipole (μ_Δ), electric quadrupole (Q_Δ) and magnetic octupole (O_Δ) moments, given by:

$$\mu_\Delta = \frac{e}{2M_\Delta} [e_\Delta + F_2^*(0)] , \tag{2.20a}$$

$$Q_\Delta = \frac{e}{M_\Delta^2} [e_\Delta - \frac{1}{2} F_3^*(0)] , \tag{2.20b}$$

$$O_\Delta = \frac{e}{2M_\Delta^3} [e_\Delta + F_2^*(0) - \frac{1}{2} (F_3^*(0) + F_4^*(0))] . \tag{2.20c}$$

2.2 Experimental information at the real photon point

In this section we briefly summarize the experimental information on the $\gamma N\Delta$ transition at $Q^2 = 0$.

The $\gamma N\Delta$ transition can be studied both in nucleon Compton scattering $\gamma N \rightarrow \gamma N$ and in the pion photoproduction reaction $\gamma N \rightarrow \pi N$. The highest precision data on the $\gamma N\Delta$ $M1$ and $E2$ amplitudes have been obtained in pion photoproduction experiments on a proton target, using linearly polarized photons, both by the MAMI/A2 Collaboration [22,23] and the LEGS Collaboration [24,25]. A detailed discussion of these $\gamma N \rightarrow \pi N$ data will be presented in Sect. 5.1.

We quote here the real photon $\gamma N\Delta$ amplitudes at the resonance position ($W = M_\Delta$) for a proton target resulting from these high precision measurements. The MAMI/A2 Collaboration obtained the values [23]:

$$\begin{aligned} A_{1/2} &= -(131 \pm 1) [10^{-3} \text{GeV}^{-1/2}], \\ A_{3/2} &= -(251 \pm 1) [10^{-3} \text{GeV}^{-1/2}], \\ R_{EM} &= -(2.5 \pm 0.1_{\text{stat.}} \pm 0.2_{\text{syst.}}) \%. \end{aligned} \quad (2.21)$$

The LEGS Collaboration obtained the values [25]:

$$\begin{aligned} A_{1/2} &= -(135.7 \pm 1.3_{\text{stat.}+\text{syst.}} \pm 3.7_{\text{model}}) [10^{-3} \text{GeV}^{-1/2}], \\ A_{3/2} &= -(266.9 \pm 1.6_{\text{stat.}+\text{syst.}} \pm 7.8_{\text{model}}) [10^{-3} \text{GeV}^{-1/2}], \\ R_{EM} &= -(3.07 \pm 0.26_{\text{stat.}+\text{syst.}} \pm 0.24_{\text{model}}) %. \end{aligned} \quad (2.22)$$

As summary of the above experiments, the Particle Data Group quotes as values [15]³:

$$\begin{aligned} A_{1/2} &= -(135 \pm 6) [10^{-3} \text{GeV}^{-1/2}], \\ A_{3/2} &= -(250 \pm 8) [10^{-3} \text{GeV}^{-1/2}], \\ R_{EM} &= -(2.5 \pm 0.5) %. \end{aligned} \quad (2.23)$$

The experimental information on the $M1$ $\gamma N\Delta$ transition can equivalently be expressed in terms of $G_M^*(0)$ using Eq. (2.13) or equivalently in terms of the transition magnetic moment $\mu_{p \rightarrow \Delta^+}$ using Eq. (2.16). Using the experimental values of Eq. (2.21), Ref. [26] extracted the values:

$$\begin{aligned} G_M^*(0) &= 3.02 \pm 0.03, \\ \mu_{p \rightarrow \Delta^+} &= [3.46 \pm 0.03] \mu_N. \end{aligned} \quad (2.24)$$

The value for the $E2$ $\gamma N\Delta$ transition can equivalently be expressed in terms of a quadrupole transition moment using Eq. (2.17). Using the experimental values of Eq. (2.21), Ref. [18] extracted:

³ Note that the central values of $A_{1/2}$ and $A_{3/2}$ quoted by PDG[15] yield $R_{EM} = -1.64\%$ when using Eq. (2.14), and therefore do not exactly correspond with the central value $R_{EM} = -2.5\%$ they quote. The photo-couplings are based on an analysis of a larger number of experiments, and within their error bars are compatible with the quoted value for R_{EM} though.

$$Q_{p \rightarrow \Delta^+} = -(0.0846 \pm 0.0033) \text{ fm}^2. \quad (2.25)$$

2.3 Physical interpretation: quark and pion-cloud models

2.3.1 Constituent quark models

In a quark model, the nucleon appears as the ground state of a quantum-mechanical three-quark system in a confining potential. In such a picture, the ground state baryons (composed of the light up (u), down (d) and strange (s) quark flavors) are described by $SU(6)$ spin-flavor symmetric wave functions, supplemented by an antisymmetric color wave function.

In the Isgur-Karl model [27], the constituent quarks move in a harmonic oscillator type confining potential. For the ground state baryons, the three constituent quarks are in the $1s$ oscillator ground state, corresponding with the [56]-plet of $SU(6)$. The harmonic oscillator states can be represented by $|B\ 2S+1L_J\rangle_t$, where B stands for either N or Δ states, S specifies the spin, L the orbital angular momentum ($L = S, P, D, \dots$ in the common spectroscopic notation), and J the total angular momentum of the three-quark state. Furthermore, $t (= S, M, A)$ refers to the symmetry type : symmetric (S), mixed symmetric (M) or anti-symmetric (A) under exchange of the quarks in both the spin-flavor and space parts of the baryon wave function. In the Isgur-Karl model, the long-range confining potential is supplemented by an interquark force corresponding with one-gluon exchange. The one-gluon exchange leads to a color hyperfine interaction between quarks i and j of the form:

$$H_{hyperfine}^{ij} = \frac{2}{3} \frac{\alpha_s}{m_i m_j} \left\{ \frac{8\pi}{3} \mathbf{S}_i \cdot \mathbf{S}_j \delta^3(\mathbf{r}_{ij}) + \frac{1}{r_{ij}^3} \left[\frac{3(\mathbf{S}_i \cdot \mathbf{r}_{ij})(\mathbf{S}_j \cdot \mathbf{r}_{ij})}{r_{ij}^2} - \mathbf{S}_i \cdot \mathbf{S}_j \right] \right\}, \quad (2.26)$$

with α_s the strong coupling constant, $\mathbf{S}_i(m_i)$ the spin (mass) of quark i , and where $\mathbf{r}_{ij}(r_{ij})$ specify the vector (distance) between quarks i and j . The first term in Eq. (2.26) corresponds with a zero-range spin-spin interaction, whereas the second term corresponds with a tensor force. The color hyperfine interaction of Eq. (2.26) breaks the $SU(6)$ symmetry and leads to a mass splitting between $N(939)$ and $\Delta(1232)$, often referred to as the hyperfine splitting. It was found that it also predicts well the mass splittings between octet and decuplet baryons [28]. Furthermore, the tensor force in Eq. (2.26) will produce a D -state ($L = 2$) admixture in the N and Δ ground states [29,30]. Because of this hyperfine interaction, the $N(939)$ and $\Delta(1232)$ states are described as superpositions of $SU(6)$ configurations. Including configurations up to the $2\hbar\omega$ oscillator shell, they are given by (using the notation introduced above):

$$|N(939)\rangle = a_S |N\ ^2S_{1/2}\rangle_S + a'_S |N\ ^2S'_{1/2}\rangle_S + a_M |N\ ^2S_{1/2}\rangle_M + a_D |N\ ^4D_{1/2}\rangle_M \quad (2.27)$$

$$|\Delta(1232)\rangle = b_S |\Delta\ ^4S_{3/2}\rangle_S + b'_S |\Delta\ ^4S'_{3/2}\rangle_S + b_D |\Delta\ ^4D_{3/2}\rangle_S + b'_D |\Delta\ ^2D_{3/2}\rangle_M. \quad (2.28)$$

By diagonalizing the hyperfine interaction and fitting to the baryon spectrum the wave function coefficients in Eqs. (2.27,2.28) were obtained as [30]:

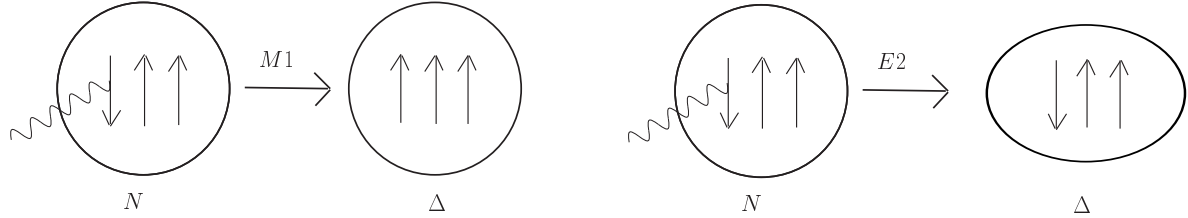


Fig. 4. Schematic picture within a quark model of a $M1$ (left panel) and $E2$ (right panel) $N \rightarrow \Delta$ transition induced by the interaction of a photon with a single quark in the nucleon. The $M1$ transition involves a S -wave spatial wave function, whereas the $E2$ transition in this picture requires N and/or Δ wave functions to have a D -wave component (indicated by a non-spherical shape).

$$a_S \simeq 0.93, \quad a'_S \simeq -0.29, \quad a_M \simeq -0.23, \quad a_D \simeq -0.04, \quad (2.29)$$

$$b_S \simeq 0.97, \quad b'_S \simeq +0.20, \quad b_D \simeq -0.10, \quad b'_D \simeq 0.07. \quad (2.30)$$

It is evident from the value of the coefficients in Eqs. (2.29,2.30) that the S -wave component dominates the N and Δ wave functions in a constituent quark model. The $\Delta(1232)$ resonance is obtained from the nucleon by a spin flip of one of the quarks in the $1s$ state so as to give a state of total spin $3/2$. Therefore the electromagnetic $N \rightarrow \Delta$ transition is dominantly a $M1$ transition [31], see Fig. 4 (left panel). Using $SU(6)$ flavor symmetry, i.e. setting $a_S = b_S = 1$ and $a'_S = a_M = a_D = b'_S = b_D = b'_D = 0$ in Eqs. (2.27,2.28), yields the relation between the magnetic moments of proton and $p \rightarrow \Delta^+$ as:

$$\mu_{p \rightarrow \Delta^+} = \frac{2\sqrt{2}}{3} \mu_p = 2.63 \mu_N \quad (SU(6) \text{ symmetric quark model}). \quad (2.31)$$

This is about 25 % lower than the experimental number Eq. (2.24). $SU(6)$ breaking effects, due to the hyperfine interaction, decrease the quark model prediction even further to a value around $2.3 \mu_N$. A very similar small number is also obtained in the MIT bag model calculation of Ref. [32]. The underestimate of $\mu_{N \rightarrow \Delta}$ in quark models is hinting at the importance of degrees of freedom beyond constituents quarks as will be discussed further on.

The small non-zero values of b_D and b'_D in Eq. (2.30) imply that the D -wave probability in the $\Delta(1232)$ ground state is around 1 %. As a result of such D -wave components, the N and Δ charge densities become non-spherical. For a static charge distribution, a measure of the non-sphericity (or deformation) is given by its quadrupole moment. Since the nucleon has spin $1/2$, any intrinsic quadrupole moment of the nucleon cannot be directly measured though because angular momentum conservation forbids a non-zero matrix element of a ($L = 2$) quadrupole operator between spin $1/2$ states. However this quadrupole deformation may reveal itself in an electromagnetically induced transition from the spin $1/2$ N to the spin $3/2$ Δ state, see Fig. 4 (right panel). In this way, the tensor force between quarks gives rise to non-zero values for the $E2/M1 (R_{EM})$ and $C2/M1 (R_{SM})$ ratios. It is interesting to note that the connection between the D -wave admixture in the N and Δ wave functions and the electromagnetic $N \rightarrow \Delta$ transition was already hinted at in the early paper of Glashow [33]. Using the D -wave admixture of Eqs. (2.29,2.30), Ref. [30] obtained the value $R_{EM} \simeq -0.41\%$. Similar small negative values were also obtained in other non-relativistic quark model calculations, see Refs. [34–36], which predict values in the range: $-0.8\% < R_{EM} < -0.3\%$. Such a small value for R_{EM} already

indicates that any effect of deformation in the nucleon and/or Δ ground state is rather small and is sensitive to details of the wave function. In particular, Drechsel and Giannini [37] demonstrated that a calculation of the $N \rightarrow \Delta$ quadrupole transition within the quark model can be very sensitive to a truncation in the quark model basis. Due to such truncation (e.g. to a $2\hbar\omega$ oscillator basis as in [30]) the charge-current operator for the quadrupole $N \rightarrow \Delta$ transition violates gauge invariance which can lead to R_{EM} ratios which differed by an order of magnitude when calculated either from the charge or current operator. Drechsel and Giannini showed that when performing a $2\hbar\omega$ truncation in the quark model basis, a calculation based on the charge operator is more stable than a calculation based on the current operator. By using N and Δ 3-quark wave functions which have a D -state probability of around 1%, they obtained a value of $R_{EM} \simeq -2\%$ and a Δ quadrupole moment $Q_\Delta \simeq -0.078 \text{ fm}^2$ [37,38].

The error induced due to the truncation in the quark model basis has been further investigated in the relativized quark model calculation of Capstick and Karl [39,40]. Using wave functions which have been expanded in a large harmonic oscillator basis up to $6\hbar\omega$ states, and are solutions of a relativized Hamiltonian, they obtained an even smaller negative value: $R_{EM} \simeq -0.21\%$.

2.3.2 Pion cloud models

Even though the constituent quark model, despite its simplicity, is relatively successful in predicting the structure and spectrum of low-lying baryons, it under-predicts $\mu_{N \rightarrow \Delta}$ by more than 25 % and leads to values for the R_{EM} ratio which are typically smaller than experiment. More generally, constituent quark models don't satisfy the symmetry properties of the QCD Lagrangian. In nature, the up and down (current) quarks are nearly massless. In the exact massless limit, the QCD Lagrangian is invariant under $SU(2)_L \times SU(2)_R$ rotations of left (L) and right (R) handed quarks in flavor space. This so-called chiral symmetry is spontaneously broken in nature leading to the appearance of massless Goldstone modes. For two flavors, there are three Goldstone bosons (pions), which acquire a mass due to the small explicit breaking of the chiral symmetry (proportional to the current quark mass). As the pion is the lightest hadron, one expects it to dominate the long distance behavior of hadron wave functions, and to yield characteristic signatures in the low-momentum transfer behavior of hadronic form factors. Furthermore, as the $\Delta(1232)$ resonance nearly entirely decays into πN (up to a small electromagnetic correction), one may expect pions to be of particular relevance in the electromagnetic $N \rightarrow \Delta$ transition. Therefore, a natural way to qualitatively improve on the above discussed constituent quark models is to include pionic degrees of freedom.

An early investigation of the $\gamma N \Delta$ transition including pion field effects was performed by Kaelbermann and Eisenberg [41] within the *chiral bag model*. The chiral (or, cloudy) bag model improves the MIT bag model by introducing an elementary, perturbative pion which couples to quarks in the bag in such a way that chiral symmetry is restored [42]. Bermuth *et al.* [43] partially corrected and repeated the calculation of Ref. [41] for two formulations of the chiral bag model: one with pseudoscalar (PS) surface coupling and one with pseudovector (PV) volume coupling of the pions. It was found that using the charge operator to calculate the quadrupole amplitude decreases the sensitivity to truncation effects which manifest themselves in a violation of gauge invariance in a model calculation. For a bag radius around $R \simeq 1.0 \text{ fm}$, the

photo-couplings in the chiral bag model are [43]:

$$\begin{aligned} A_{3/2} &= -198 \ [10^{-3} \text{ GeV}^{-1/2}], & R_{EM} &= -1.8\%, & (\text{PS}), \\ A_{3/2} &= -171 \ [10^{-3} \text{ GeV}^{-1/2}], & R_{EM} &= -2.0\%, & (\text{PV}). \end{aligned}$$

A comparison with experimental data and the predictions of quark models, see Table 1, shows that the chiral bag model calculation for PS coupling yields an $A_{3/2}$ amplitude that is larger than quark models, but still smaller than experiment. For PV coupling, there is a seagull term with opposite sign which yields a partial cancellation and deteriorates the agreement with experiment.

Lu *et al.* [44] in a later calculation within the chiral bag model improved upon the previous calculations by applying a correction for the center-of-mass motion of the bag. It was found that with a smaller bag radius, $R \approx 0.8$ fm, one is able to obtain a reasonable size for the magnitude of the helicity amplitudes, see Table 1. For such a small bag radius, the pionic effects are crucial as they account for around 75 % of the total strength of the amplitude $A_{3/2}$.

For the R_{EM} ratio, Bermuth *et al.* [43] obtained $R_{EM} \simeq -2\%$, close to experiment, whereas Lu *et al.* [44] obtained a value $R_{EM} \simeq -0.03\%$, in disagreement with experiment. Lu *et al.* found severe cancellations between the $A_{1/2}$ and $A_{3/2}$ amplitudes in Eq. (2.14), leading to the very small value for R_{EM} . In the chiral bag model the quadrupole amplitude $E2$ has no contribution from the bare bag, which is a pure S -state. Thus, the transition is mediated solely by the pion cloud. To get a more realistic value for R_{EM} within the chiral bag model, one probably must either deform the bag or carry out a diagonalization like in the quark model (configuration mixing) [45].

The pion-cloud contributions also play an important role in the *linear σ -model* and *chiral chromodielectric model* of Ref. [46], even though these models still under-predict the magnitude of the helicity amplitudes, see Table 1.

The R_{EM} ratio has also been calculated in *Skyrme models* [47–49], which have only pionic degrees of freedom. In the Skyrme model, the nucleon appears as a soliton solution of an effective nonlinear meson field theory. Wirzba and Weise [47] performed a modified Skyrme model calculation, at leading order in the number of colors N_c , based on the chiral effective Lagrangian, which corresponds with the standard Skyrme model supplemented by stabilizing fourth and sixth order terms in the pion fields. This calculation obtained R_{EM} values between -2.5% and -6% , depending on the coupling parameters of the stabilizing terms [47]. Certainly, the sign and order of magnitude of these results are consistent with the empirical result. Walliser and Holzwarth [49] included rotational corrections, which are of order $1/N_c$, and lead to a quadrupole distortion of the classical soliton solution. Including such corrections, one finds a very good description of the photo-couplings (see Table 1) and obtained a ratio $R_{EM} = -2.3\%$, consistent with experiment.

A model which has both quark and pion degrees of freedom and interpolates between a constituent quark model and the Skyrme model is the *chiral quark soliton model* (χ QSM). This model is based on the interaction of quarks with Goldstone bosons resulting from the spontaneous breaking of chiral symmetry. As for the Skyrme model, the χ QSM is essentially based on the $1/N_c$ expansion. Its effective chiral action has been derived from the instanton model of the QCD vacuum [50], which provides a natural mechanism of chiral symmetry breaking and

enables one to generate dynamically the constituent quark mass.

Although in reality the number of colors $N_c = 3$, the extreme limit of large N_c is known to yield useful insights. At large N_c the nucleon is heavy and can be viewed as N_c “valence” quarks bound by a self-consistent pion field (the “soliton”) whose energy coincides with the aggregate energy of the quarks of the negative-energy Dirac continuum [51]. A successful description of static properties of baryons, such as mass splittings, axial constants, magnetic moments, form factors, has been achieved (typically at the 30 % level or better, see Ref. [52] for a review of early results). After reproducing masses and decay constants in the mesonic sector, the only free parameter left to be fixed in the baryonic sector is the constituent quark mass. The good agreement of the χ QSM with the empirical situation is achieved for quark mass $M_q \simeq 420$ MeV.

The χ QSM was also applied to the calculation of the $\gamma N \Delta$ transition [53,54]. In this model, the Δ is a bound state which corresponds to a soliton rotating in flavor space. The rotational energy is responsible for the $N - \Delta$ mass splitting. With a constituent quark mass $M_q = 420$ MeV, the empirical $N - \Delta$ mass splitting is well reproduced. The $\gamma N \Delta$ amplitudes are obtained taking rotational ($1/N_c$) corrections into account. In this way, Silva *et al.* [54] obtained as result: $R_{EM} = -2.1\%$ (in the two-flavor case), fairly close to the experimental ratio, considering that in the χ QSM calculation no parametrization adjustment has been made to the $N \rightarrow \Delta$ transition. However, the value of the $M1 \gamma N \Delta$ amplitude is largely underpredicted in the χ QSM, which is also reflected in an underprediction of the magnitude of the photo-couplings, see Table 1.

The above calculations incorporating the chiral symmetry of QCD (to lowest order in the pion fields) highlight the role of the pionic degrees of freedom in the $\gamma N \Delta$ transition. A number of subsequent works have therefore revisited quark models, which break chiral symmetry, by including two-body exchange currents. As an example of such approach we consider the work of Buchmann, Hernandez and Faessler [55].

When the one-gluon exchange potential between quarks is complemented by a one-pion and one-sigma exchange potential between the quarks, the pion exchange gives rise to an additional tensor interaction between the quarks. The one-pion exchange then requires the presence of two-body exchange currents between the quarks due to current conservation. Within the non-relativistic framework, Buchmann *et al.* [55] found that the overall effect of the exchange currents on the dominant $M1 \gamma N \Delta$ transition are relatively small due to cancellation. As a result, the transition magnetic moment comes out to be underpredicted: $\mu_{p \rightarrow \Delta^+} \simeq 2.5 [\mu_N]$, similar to the non-relativistic quark model without exchange currents. This is also reflected in the helicity amplitudes obtained in [55] and quoted in Table 1). They are smaller in the magnitude than the experimental values.

However, the two-body exchange currents lead to non-vanishing $\gamma N \Delta$ quadrupole ($E2$ or $C2$) amplitudes [55], even if the quark wave functions have no D -state admixture. In this picture, the Δ is excited by flipping the spins of two quarks, see Fig. 5. According to Buchmann *et al.*, this mechanism yields $R_{EM} \simeq -3.5\%$.

Also within their quark model, Buchmann *et al.* related the $N \rightarrow \Delta$ and Δ^+ quadrupole moments to the neutron charge radius as⁴:

⁴ See also Refs. [56,57] for an analogous relation between the $N \rightarrow \Delta$ quadrupole form factor G_C^* and the neutron electric form factor. Possible higher order corrections to Eq. (2.32) allowed by QCD were recently investigated in Ref. [58] within a general parametrization method, see also Ref. [25].

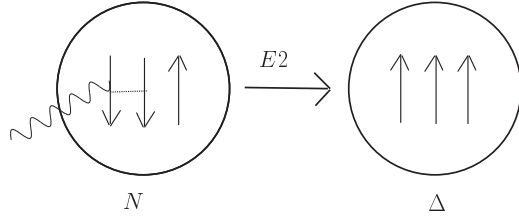


Fig. 5. Schematic picture within a quark model of an $E2 N \rightarrow \Delta$ transition induced by the interaction of a photon with two quarks in the nucleon (correlated through, *e.g.*, one-pion exchange). Both N and Δ wave functions are S -states.

$$Q_{p \rightarrow \Delta^+} = \frac{1}{\sqrt{2}} r_n^2, \quad Q_{\Delta^+} = r_n^2. \quad (2.32)$$

The origin of these relations in the model calculation of Ref. [55] is the dominance of two-body exchange currents in both $Q_{p \rightarrow \Delta^+}$, Q_{Δ^+} and r_n^2 . Using the experimental neutron charge radius, $r_n^2 = -0.113(3) \text{ fm}^2$, the relations of Eq. (2.32) yield:

$$Q_{p \rightarrow \Delta^+} = -0.08 \text{ fm}^2, \quad Q_{\Delta^+} = -0.113 \text{ fm}^2. \quad (2.33)$$

The value of $Q_{p \rightarrow \Delta^+}$ is close to the empirical determination of Eq. (2.25).

Recently, the $\gamma^* N \Delta$ transition form factors were calculated in a Lorentz covariant chiral quark approach [62], where baryons are modeled as bound states of constituent quarks dressed by a cloud of pseudoscalar mesons. To calculate baryon matrix elements, a phenomenological hadron-quark vertex form factor was used, which parametrizes the distribution of quarks inside a given baryon. In Ref. [62], a Gaussian form was adopted for this hadron-quark form factor which involves a size parameter Λ_B , which was used as a free parameter. Using a value $\Lambda_B \simeq 0.8 \text{ GeV}$, it was found that the contribution of the meson cloud to the static properties of light baryons is up to 20 % and, together with the relativistic corrections, helps to explain how the shortfall in the SU(6) prediction for $\mu_{N \rightarrow \Delta}$ is ameliorated.

As a summary, we list in Table 1 the $\gamma N \Delta$ photo-couplings $A_{1/2}$ and $A_{3/2}$ as well as the ratio R_{EM} in the various models discussed above.

2.3.3 Intrinsic quadrupole moment and the issue of shape

The relations of Eq. (2.32) were further interpreted by Buchmann [59] in terms of an intrinsic quadrupole moment of the nucleon and Δ states. The intrinsic quadrupole moment Q^0 of a static charge distribution $\rho(\vec{r})$ is given by:

$$Q^0 = \int d^3 \vec{r} \rho(\vec{r}) (3z^2 - r^2), \quad (2.34)$$

which is defined w.r.t. the body fixed frame. A charge distribution concentrated along the z -axis (symmetry axis of the system) corresponds with $Q^0 > 0$ (prolate deformation), whereas a charge distribution concentrated in the equatorial xy -plane corresponds with $Q^0 < 0$ (oblate

	$A_{1/2} [10^{-3} \text{ GeV}^{-1/2}]$	$A_{3/2} [10^{-3} \text{ GeV}^{-1/2}]$	$R_{EM} [\%]$
experiment			
Ref. [15]	-135 ± 6	-250 ± 8	-2.5 ± 0.5
SU(6) symmetry	-107	-185	0
non-relativistic quark models			
Refs. [29,30,34–37]	-103	-179	-2 to 0
relativized quark model			
Refs. [39,40]	-108	-186	-0.2
MIT bag model, Ref. [32]	-102	-176	0
chiral (cloudy) bag models			
Ref. [43] : (PS, $R = 1 \text{ fm}$)	-106	-198	-1.8
Ref. [43] : (PV, $R = 1 \text{ fm}$)	-91	-171	-2.0
Ref. [44] : (+ recoil, $R = 0.8 \text{ fm}$)	-134	-233	-0.03
linear σ -model, Ref. [46]	-107	-199	-1.8
chromodielectric model, Ref. [46]	-70	-131	-1.9
Skyrme models			
Ref. [47]			-6 to -2.5
Ref. [49] : (+ $1/N_c$ corrections)	-136	-259	-2.3
chiral quark soliton model			
Ref. [54] : SU(2) flavor	-70.5	-133	-2.1
quark model + π, σ exchange			
Ref. [55]	-91	-182	-3.5
chiral quark model ($\Lambda_B = 0.8 \text{ GeV}$)			
Ref. [62]	-124.3	-244.7	-3.1

Table 1

Summary of the values of the $\gamma N \Delta$ helicity amplitudes $A_{1/2}$ and $A_{3/2}$ at $Q^2 = 0$, and the ratio $R_{EM}(Q^2 = 0)$ in different models compared with experiment.

deformation). This intrinsic quadrupole moment has to be distinguished from a measured (or spectroscopic) quadrupole moment Q . As an example, for a rigid rotor (which was considered within the context of the collective nuclear shell model [61]) these quantities are related as:

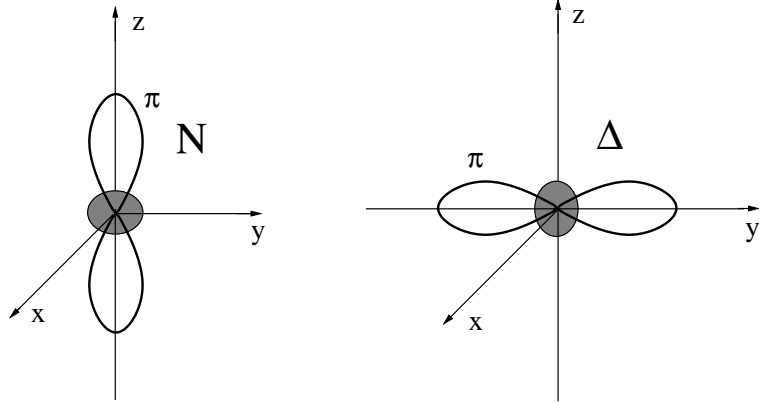


Fig. 6. Model picture of the intrinsic quadrupole deformation of the nucleon (left) and Δ (right) within the pion cloud model of Ref. [59]. In the N , the p -wave pion cloud is concentrated along the polar (symmetry) axis leading to a prolate deformation, whereas in the Δ , the pion cloud is concentrated in the equatorial plane, corresponding to an oblate deformation. Figure from Ref. [59].

$$Q = \frac{3J_z^2 - J(J+1)}{(J+1)(2J+3)} Q^0, \quad (2.35)$$

where J_z is the projection of the nucleon total spin J onto its symmetry axis (z -axis in a body fixed frame). The difference between Q^0 and Q represents the averaging of the nonspherical charge distribution due to its rotational motion as seen in the laboratory frame. One verifies from Eq. (2.35) that the multiplication factor is zero for a spin 1/2 particle, yielding $Q_p = 0$ for the proton. Eq. (2.35) does not preclude however that the proton has an intrinsic quadrupole moment Q_p^0 . Ref. [59] obtained both within the quark model and within a pion cloud model that:

$$Q_{\Delta^+}^0 = r_n^2 = -Q_p^0, \quad (2.36)$$

which they interpreted as a proton (Δ^+) which has a prolate (oblate) intrinsic deformation respectively. Within the pion cloud model calculation of Ref. [59], the nucleon consists of a spherically symmetric quark core surrounded by a pion with orbital angular momentum $l = 1$, as illustrated in Fig. 6. In this model, the pion cloud is responsible for the non-zero values of the quadrupole moments Q_p^0 and $Q_{\Delta^+}^0$.

Estimates such as Eq. (2.36) of intrinsic quadrupole moments are surely useful to reveal details of a given model calculation and gain physical insight. One should keep in mind, however, that, even though a specific model such as the rigid rotor relates the intrinsic and total quadrupole moments, only the latter is directly related to observables.

2.4 Large N_c limit

Though the results from the different QCD inspired models discussed above may provide us with physical insight on the $\gamma N \Delta$ transition, they are not a rigorous consequence of QCD. In the

following subsections, we will discuss what is known on the $\gamma N \Delta$ transition from approaches which are a direct consequence of QCD in some limit, such as chiral effective field theory (chiral limit of small pion masses or momentum transfers) or lattice QCD simulations (continuum limit).

Another first-principle technique is the $1/N_c$ expansion of QCD proposed by 't Hooft [63] and developed furthermore by Witten [64]. The large- N_c limit is unique in that it provides a perturbative parameter at all energy scales. This expansion has proved quite useful in describing the properties of baryons, such as, ground-state and excited baryon masses, magnetic moments, electromagnetic decays, see *e.g.*, Refs. [65,66] for reviews.

In the large N_c limit, the baryons are infinitely heavy and can be treated as static. In this limit the baryon sector of QCD has an exact contracted $SU(2N_f)$ spin-flavor symmetry, where N_f is the number of light quark flavors. The large N_c limit thus validates many of the quark model $SU(6)$ spin-flavor symmetry results without making any model assumption (such as assuming non-relativistic quark dynamics for the baryon wave functions). For example, the ratio of proton to neutron magnetic moments in the large- N_c limit is predicted to be given by $\mu_p/\mu_n = -3/2$ in agreement with the naive quark model. Likewise at leading order in $1/N_c$, the $N \rightarrow \Delta$ transition magnetic moment $\mu_{N\Delta}$ is related to the isovector combination of proton and neutron magnetic moments as [67]:

$$\mu_{p \rightarrow \Delta^+} = \frac{1}{\sqrt{2}} (\mu_p - \mu_n), \quad (2.37)$$

up to a correction of order $1/N_c^2$. Using the empirical values for μ_p and μ_n , one obtains in the large N_c limit $\mu_{N \rightarrow \Delta} = 3.23 \mu_N$, within 10 % of the experimental value of Eq. (2.24).

The R_{EM} ratio for the $\gamma N \Delta$ transition is shown to be of order $1/N_c^2$ [68]. Thus, the smallness of the $\gamma N \Delta$ R_{EM} ratio is naturally explained in the large N_c limit. Using Eq. (2.14), this can equivalently be expressed as a large N_c prediction for the $\gamma N \Delta$ helicity amplitudes:

$$\frac{A_{3/2}}{A_{1/2}} = \sqrt{3} + \mathcal{O}\left(\frac{1}{N_c^2}\right). \quad (2.38)$$

The large N_c limit also allows to obtain relations between the Δ and $N \rightarrow \Delta$ quadrupole moments [69]:

$$\frac{Q_{\Delta^+}}{Q_{p \rightarrow \Delta^+}} = \frac{2\sqrt{2}}{5} + \mathcal{O}\left(\frac{1}{N_c^2}\right). \quad (2.39)$$

This result for Q_{Δ^+} is different from the quark model ratio of Eq. (2.32) as explained in [69]. Using the phenomenological value of Eq. (2.25) for $Q_{p \rightarrow \Delta^+}$, the large N_c relation of Eq. (2.39) yields for the Δ^+ quadrupole moment:

$$Q_{\Delta^+} = -(0.048 \pm 0.002) \text{ fm}^2, \quad (2.40)$$

accurate up to corrections of order $1/N_c^2$.

Buchmann, Hester and Lebed [69] derived recently another relation by making the additional assumption that the baryon charge radii and quadrupole moments arise from the same contributions. This assumption holds true when, *e.g.*, the interaction between quarks arises from one-gluon or one-pion exchange, for which the ratio of spin-spin and tensor terms in the Hamiltonian is fixed. Under this assumption, one finds a large- N_c relation between the $N \rightarrow \Delta$ quadrupole moment and the neutron charge radius r_n^2 [69]:

$$Q_{p \rightarrow \Delta^+} = \frac{1}{\sqrt{2}} r_n^2 \frac{N_c}{N_c + 3} \sqrt{\frac{N_c + 5}{N_c - 1}}, \quad (2.41)$$

where both $Q_{p \rightarrow \Delta^+}$ and r_n^2 are of order $1/N_c^2$.

The factor on the *rhs* of Eq. (2.41) after r_n^2 is unity both for the cases $N_c = 3$ and $N_c \rightarrow \infty$, and deviates from unity by only about 1 % for all values in between. Therefore the large N_c limit predicts to good approximation the same relation of Eq. (2.32), $Q_{p \rightarrow \Delta^+} = 1/\sqrt{2} r_n^2$, which was also derived in the quark model and pion cloud model, and which was found to be consistent with the empirical value of Eq. (2.25) for $Q_{p \rightarrow \Delta^+}$.

More recently, Cohen has argued [70,71] that the relations, such as in Eqs. (2.39) and (2.41), may be significantly altered in the real world where the pions are light. When taking $N_c \rightarrow \infty$ at a fixed value of m_π , the N - Δ mass difference, which goes as $1/N_c$, vanishes. Therefore, the “usual” large- N_c limit implies that one is in the region $M_\Delta - M_N \ll m_\pi$, where, for instance, the Δ is stable. Cohen points out that the large- N_c limit and the chiral limit ($m_\pi \rightarrow 0$) do not commute and for quantities which diverge in the chiral limit, such as the charge radii, one expects chiral corrections to dominate over the large- N_c predictions. Although the region $M_\Delta - M_N \ll m_\pi$ is not accessible in nature, lattice QCD results, which are currently obtained in this regime (see Sect. 2.6), may provide an interesting testing ground for the above large N_c predictions.

Let us conclude the discussion of the large- N_c relations by observing a new relation, *i.e.*:

$$R_{SM} = R_{EM}, \quad \text{for } Q^2 = 0 \quad \text{and } N_c \rightarrow \infty. \quad (2.42)$$

To derive this relation we follow the arguments given in the Appendix of Ref. [72]. Namely, we first make use of the expression of the ratios in terms of little g ’s of Eq. (2.2), at $Q^2 = 0$:

$$R_{EM} = \frac{1}{g_M - \frac{\Delta}{2(M_N + M_\Delta)} g_E} \frac{\Delta}{2(M_N + M_\Delta)} g_E, \quad (2.43a)$$

$$R_{SM} = \frac{1}{g_M - \frac{\Delta}{2(M_N + M_\Delta)} g_E} \left[\frac{\Delta}{2(M_N + M_\Delta)} g_E + \frac{\Delta^2}{4M_\Delta^2} g_C \right], \quad (2.43b)$$

where $\Delta = M_\Delta - M_N$ is the N - Δ mass difference. These are general expressions, which can, *e.g.*, be obtained by substituting Eq. (2.3) into Eq. (2.15). Now, the little g ’s are the coupling constants from an effective Lagrangian (see Sect. 4.3) and, as can be seen from the similar operator structure of the corresponding terms, these constants have the same large- N_c scaling.

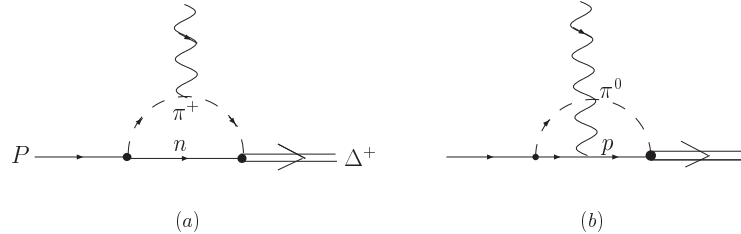


Fig. 7. The πN loop corrections to the $\gamma p \Delta^+$ vertex as calculated in χ EFT. Diagram (a) : $\pi^+ n$ loop where the photon couples to the π^+ ; diagram (b) : $\pi^0 p$ loop where the photon couples to the charge of the proton.

Finally, we only need to recall that the baryon masses go as N_c , while the N - Δ mass difference as $1/N_c$:

$$M_N, M_\Delta \sim N_c, \quad \Delta \sim 1/N_c \quad \text{for } N_c \rightarrow \infty, \quad (2.44)$$

to see that the g_C term in R_{SM} is of higher $1/N_c$ order, and hence the relation Eq. (2.42) holds. From Eq. (2.43), one immediately verifies that both of these quantities are of order $1/N_c^2$.

2.5 Chiral effective field theory

The $\gamma N \rightarrow \Delta$ transition has also been studied within the chiral effective field theory (χ EFT) expansions based on chiral Lagrangians with nucleon and Δ -isobar fields. In this framework the expansion for each of the $\gamma^* N \Delta$ -transition form factors begins with a low-energy constant (LEC), which then receives the chiral loop corrections of the type depicted in Fig. 7.

A first such study was performed by Butler, Savage and Springer [83] in the framework of heavy-baryon χ PT [84]. At leading order they obtained a “chiral log” (*i.e.*, $\ln m_\pi$) enhancement of the $E2$ transition, which lead to relatively large and positive values of R_{EM} . Their result thus showed that the chiral correction to the $E2$ transition diverges in the chiral limit.

A more comprehensive study was subsequently carried out by Gellas *et al.* [85] using the so-called “small scale expansion” (SSE) [86], also called “ ϵ -expansion”. In the SSE scheme the two light scales in the problem: the pion mass (m_π) and the Δ -resonance excitation energy ($\Delta \equiv M_\Delta - M_N$) are counted as having the same size. In addition, the heavy-baryon (semi-relativistic) expansion is performed. The calculation of Ref. [85] was performed to order p^3 , which is the next-to-leading order for $M1$ and leading order for the $E2$ and $C2$ transitions. More recently, Gail and Hemmert [87] have updated this work and analyzed some of the higher-order contributions. In overall, they show a good agreement with the low Q^2 data for the $\gamma N \rightarrow \Delta$ transition, as will be illustrated below. However, as a note of caution, one should point out that the R_{EM} and R_{SM} ratios are reasonably well described only upon adding a nominally higher-order (p^5) counter term with an unnaturally large LEC ($C_s \simeq -17 \text{ GeV}^{-2}$ in the notation of Ref. [87]).

Two of us [88,89] have recently computed the $\gamma^* N \Delta$ form factors in a manifestly covariant (no heavy-baryon expansions) χ EFT expansion. In the chiral limit, it was found that the $C2$

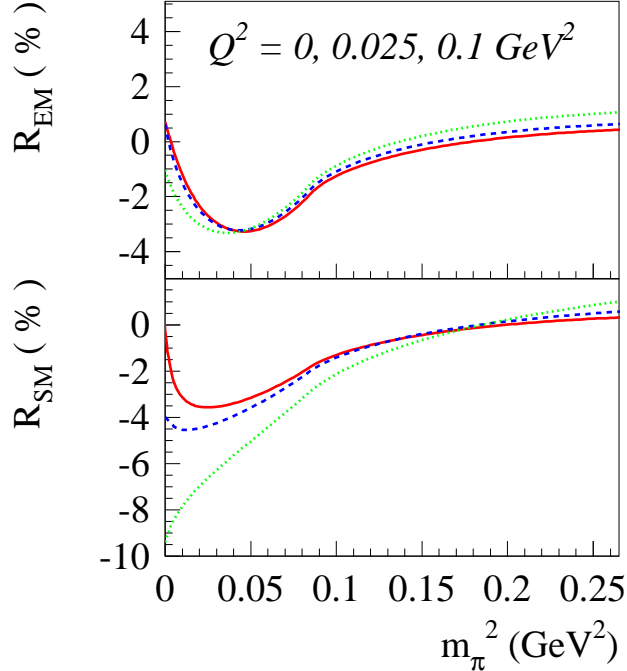


Fig. 8. The pion mass dependence of R_{EM} and R_{SM} for three fixed values of Q^2 : 0 (solid curves), 0.025 GeV^2 (dashed curves), and 0.1 GeV^2 (dotted curves), resulting from the χ EFT calculation of Refs. [88,89]. The figure shows the absence (presence) of the $\ln m_\pi$ divergence for R_{EM} (R_{SM}) at $Q^2 = 0$.

transition diverges for $Q^2 = 0$, which is also in agreement with the result of Ref. [87]⁵. The coefficient of the chiral log turns out to be small. Only for tiny pion masses one starts to see the dominance of the chiral log in the $C2$ transition, see Fig. 8.

Our χ EFT study of the $\gamma N \Delta$ transition [88,89] utilizes the “ δ -expansion” scheme of Ref. [90]. In this scheme the two light scales $\delta \equiv \Delta/\Lambda_{\chi\text{SB}}$ and $\epsilon \equiv m_\pi/\Lambda_{\chi\text{SB}}$, with $\Lambda_{\chi\text{SB}} \sim 1 \text{ GeV}$ the chiral symmetry breaking scale, are treated differently. In contrast, the SSE assumes $\epsilon \sim \delta$, which leads to an unsatisfactory feature that the Δ -resonance contributions are always estimated to be of the same size as the nucleon contributions (hence, overestimating the Δ contribution at lower energies and underestimating some of them at the resonance energies). In the δ -expansion, one counts $\epsilon = \delta^2$, which is the closest integer-power relation between these parameters in the real world.

At the physical pion mass, the δ -expansion provides an energy-dependent power-counting scheme designed to take into account the large variation of the Δ -resonance contributions with energy. As such it allows for an efficient calculation of observables in the resonance region. The relevant LECs can in this fashion be directly extracted from observables. In Refs. [88,89] the

⁵ This result of both Refs. [87] and [88,89] is in disagreement with Butler *et al.* [83] where a chiral log enhancement was reported for $E2$ at $Q^2 = 0$ instead of $C2$.

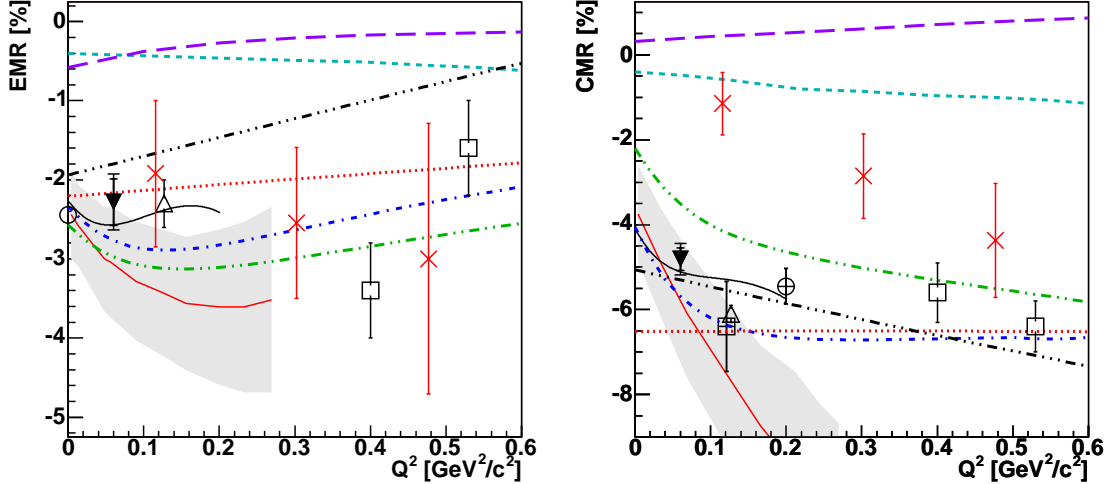


Fig. 9. The low Q^2 dependence of the quadrupole ratios EMR (left panel) and CMR (right panel) for the $\gamma^* p \rightarrow \Delta$ transition. The data are from MAMI : Refs. \circ [23], \oplus [77], \boxplus [78], \blacktriangledown [79]; from Bates \triangle [80]; and from CLAS \square [81]. The lattice QCD calculations with linear pion mass extrapolations are shown as \times [82]. Two chiral EFT calculations are shown: the δ -expansion result from Ref. [88,89] (red solid curves with error estimates), and the ε -expansion result of Ref. [87] (black solid curves). The dynamical model predictions from SL [14] (green dashed-double-dotted curves) and DMT [91] (blue dashed-dotted curves) are shown alongside the phenomenological MAID2003 [92] (red dotted curves) and SAID [93] (black dashed-triple-dotted curves) models. The hypercentral (long dashed curves) [94] and relativistic (short dashed curves) [39] constituent quark models have been included. Figure from Ref. [79].

three LECs corresponding to the three $\gamma N \Delta$ transitions are all extracted from a next-to-leading (NLO) calculation of pion photo- and electro-production observables (see Sect. 4.5.2). The resulting prediction of the Q^2 dependence is then shown to be in a qualitative agreement with phenomenological extractions.

Namely, in Fig. 9, we show the present experimental situation for the R_{EM} and R_{SM} ratios at low Q^2 and compare the data with χ EFT calculations, dynamical and phenomenological model predictions, as well as quark model predictions. One sees from Fig. 9, that the R_{EM} ratio stays small and negative, around -2 to -3 % up to momentum-transfer of around 0.5 GeV^2 .

The R_{SM} ratio displays a steep slope at low Q^2 (Siegert limit), and seems to level off to a negative value around -6 to -7 % above $Q^2 \simeq 0.1$ GeV^2 . Both the χ EFT calculations are consistent with the low Q^2 dependence of the R_{EM} and R_{SM} ratios. The δ -expansion results are quoted with a theoretical uncertainty band as will be explained in Sect. 4. Furthermore, one sees from Fig. 9 that the constituent quark models largely under-predict the R_{EM} and R_{SM} ratios, as discussed above. The dynamical models of Refs. [14,91], which include pionic degrees of freedom, are in qualitative agreement with the empirical Q^2 dependence.

In Fig. 10, we compare Q^2 -dependence of the the pion cloud contributions to the $\gamma^* N \Delta$ form factors in dynamical models versus χ EFT. In χ EFT the values of the form factors G_M^* , G_E^* , and G_C^* at the real photon point are related to three LECs g_M , g_E , and g_C appearing in the chiral Lagrangian (see Sect. 4), and determined from a fit to the data. Similarly, in the dynamical models the values at $Q^2 = 0$ are determined from a fit to the same data. However, the renormalization of the pion loop contributions is done in a dramatically different fashion. In χ EFT one uses

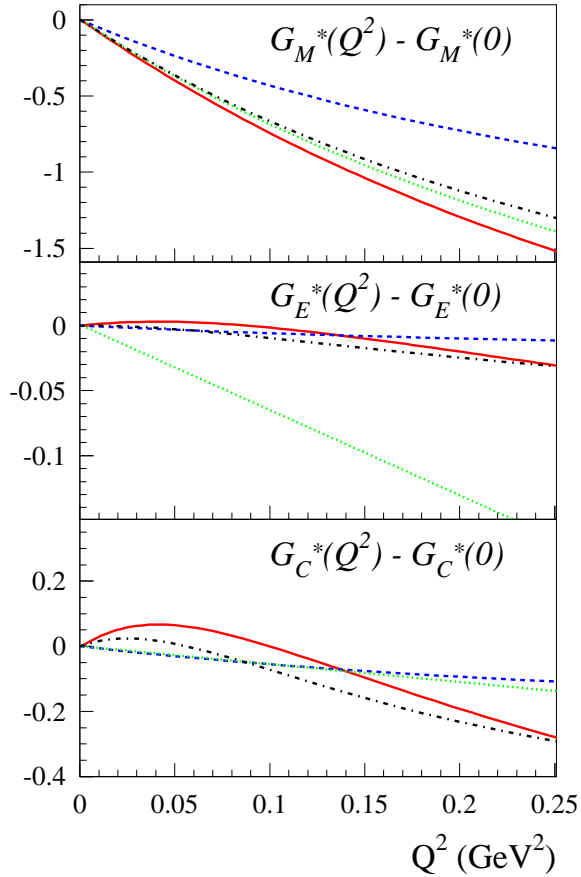


Fig. 10. Comparison of the pion cloud in the dynamical model and chiral EFT calculations for the low Q^2 behavior of the Jones Scadron form factors G_M^* , G_E^* , and G_C^* (with value at $Q^2 = 0$ subtracted). The dynamical model predictions from SL [14] are shown for both the 'bare' version of the model (blue dashed curves) where the pion loop diagrams are not accounted for, and 'dressed' version of the model (black dashed dotted curves) which include the pion loop diagrams. The chiral EFT calculation of Ref. [88,89] are shown without (green dotted curves) and with (red solid curves) the pion loop diagrams.

the dimensional regularization and absorbs infinities and other power-counting violating pieces into the LECs. In dynamical models, the loops are regularized by a cutoff, which is then fitted to the data. As the result the pion cloud contributions do not satisfy the chiral power-counting, and are usually larger than the ones obtained from χ EFT.

Therefore, to compare the dynamical model and χ EFT results directly we consider the difference $G_M^*(Q^2) - G_M^*(0)$, and analogously for G_E^* and G_C^* , such that the above renormalization-scheme dependence drops out. In Fig. 10, we compare the results of the dynamical model of Ref. [14] with the χ EFT results of Ref. [88,89]. For both the dynamical model and χ EFT we show the results with and without the pion-loop effects, which for these difference-quantities appear to be similarly renormalized.

From this comparison, we conclude that the full result, including the pion-loop contributions, is very similar in both the dynamical model and the χ EFT approach, for all the three form fac-

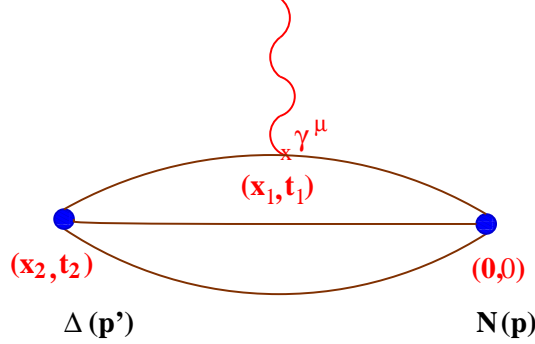


Fig. 11. The $\gamma^* N \Delta$ matrix element as evaluated in lattice QCD. The photon couples to one of the quarks in the nucleon at a fixed time t_1 to produce a Δ .

tors. The pion cloud contribution to G_M^* appears to be larger in the dynamical model than in the χ EFT calculation. This difference in size is mainly due to the photon coupling to the anomalous magnetic moments of the nucleons in the loops, which are included in the dynamical model, but not in χ EFT since they are of higher than NLO considered in Refs. [88,89]. For the Coulomb quadrupole form factor G_C^* , one sees a very similar role of the pion cloud in both approaches, giving rise to a structure around $Q^2 \simeq 0.03 - 0.05 \text{ GeV}^2$. For the electric quadrupole form factor G_E^* , on the other hand, one notices a qualitatively different behavior. Whereas the effect of the pion cloud is very small in the dynamical model calculation, a strong, nearly linear Q^2 dependence of the pion loops arises in χ EFT.

The role of the pion cloud will further be elucidated within the dynamical models in Sect. 3, and χ EFT in Sect. 4.

2.6 Lattice QCD and chiral extrapolation

2.6.1 Lattice simulations

Lattice QCD calculations of nucleon structure quantities have matured considerably in the recent past. They provide an *ab initio* calculation of quantities such as the $\gamma^* N \Delta$ transition form factors from the underlying theory of QCD. The first such calculation was performed by Leinweber, Draper and Woloshyn [73].

The calculation of the $\gamma^* N \Delta$ form factors requires the evaluation of three-point functions, which involve the computation of a sequential propagator, see Fig. 11. Leinweber *et al.* [73] evaluated these in the so-called fixed current approach, which requires the current to have a fixed direction and to carry a fixed momentum. The initial and final states, on the other hand, can vary without requiring further inversions, which are the time-consuming part of the evaluation of three-point functions. For rather large quark masses, corresponding with pion masses in the range $m_\pi \simeq 0.65 - 0.95 \text{ GeV}$, they obtained [73]: $R_{EM} = (-3 \pm 8)\%$. This initial result clearly indicates the need for high statistics to establish a non-zero value for a quantity such as R_{EM} .

Alexandrou, de Forcrand and Tsapalis [74] studied the deformation of baryons with spin higher than 1/2 in lattice QCD via three-density correlators. Such three-density correlators, when considered at a fixed time t , are function of the two relative distances \mathbf{r}_1 and \mathbf{r}_2 between

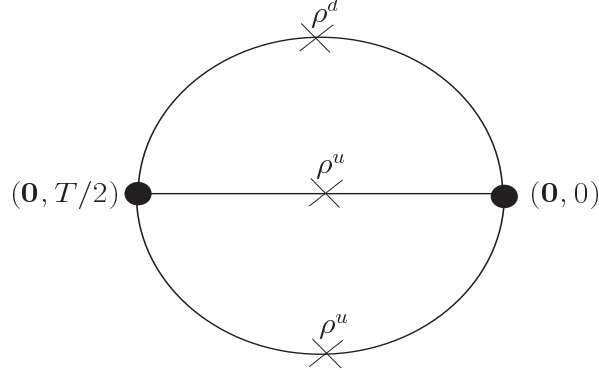


Fig. 12. Three-density correlator of a baryon as defined in Eq. (2.45) and used in the lattice gauge calculations of Ref. [74]. The source (right) and sink (left) are taken at the same spatial location, and are separated by a Euclidean time distance $T/2$. The crosses indicate the density insertions ρ^u (ρ^d) into the up (down) quark lines respectively.

the three quarks in a baryon B and are defined as:

$$C(\mathbf{r}_1, \mathbf{r}_2, t) = \int d^3\mathbf{r}' \langle B | \rho^d(\mathbf{r}', t) \rho^u(\mathbf{r}' + \mathbf{r}_1, t) \rho^u(\mathbf{r}' + \mathbf{r}_2, t) | B \rangle, \quad (2.45)$$

where the density insertion ρ^q ($q = u, d$) into an up (u) or down (d) quark line is given by the normal order product:

$$\rho^q(\mathbf{r}, t) = : \bar{q}(\mathbf{r}, t) \gamma^0 q(\mathbf{r}, t) : \quad (2.46)$$

so that disconnected graphs are excluded. These correlation functions of quark densities, which, being expectation values of local operators, are gauge invariant, reduce in the non-relativistic limit to the wave function squared. The three-density correlator for a baryon is shown schematically in Fig. 12⁶. For simplicity, the baryon source and sink are taken at the same spatial location. Denoting the lattice extent in Euclidean time by T and taking periodic boundary conditions, yields a maximum time separation between source and sink of $T/2$. To isolate the ground state baryon, both the time distances between the source and the insertions (t) and between the sink and the insertions ($T/2 - t$) are taken to be as large as possible in such calculations.

In Ref. [74], the correlator has been calculated in both quenched and unquenched lattice QCD for a Δ^+ in a spin $+3/2$ state. The quenched calculation was performed for pion masses in the range $m_\pi \simeq 0.35 - 0.65$ GeV, and no signal of deformation has been observed. This may not come as a surprise, because in a quenched calculation, where graphs with disconnected quark loops are neglected, pion cloud effects are only partially accounted for. It was discussed above in the context of phenomenological models that pion cloud effects are partly responsible for hadron deformation. This was checked by performing an unquenched lattice QCD calculation with two heavy dynamical quarks, using the Wilson Dirac operator in the same quark mass range as the quenched calculations [74]. The resulting correlator for the Δ^+ is displayed in a

⁶ In addition to one-density insertions into each u -quark line, one can also have two-density insertions into the same u -quark line. The latter contribution was however checked to be small [74].

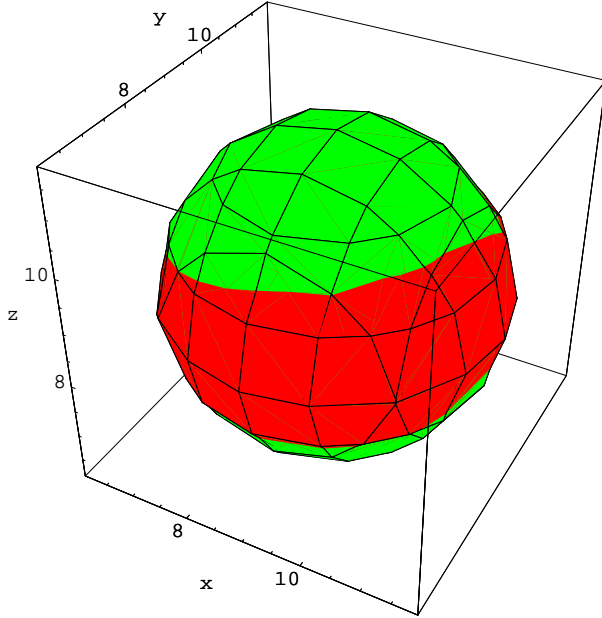


Fig. 13. Three-dimensional contour plot of the correlator (red) for the Δ^+ state with spin projection $+3/2$ (the z -axis denotes the spin direction) as it follows from lattice QCD calculations [74] for two heavy dynamical quarks, corresponding with a pion mass $m_\pi > 0.6$ GeV. The contour (red), corresponding with a value (0.8) for the correlator which has been chosen to show large distances, indicates a slightly oblate deformation of the Δ^+ in the $+3/2$ spin state. For comparison, the contour of a sphere is also shown (green). Figure from Ref. [74].

three-dimensional contour plot in Fig. 13. The unquenched lattice QCD calculation indicates a slightly oblate deformation for the Δ^+ in a spin $+3/2$ state, in agreement with the negative value of the Δ^+ quadrupole moment obtained from the large N_c estimate of Eq. (2.40). It will be very interesting to check if this signal can be consolidated by higher statistics results using lighter quark masses and a larger lattice.

A direct calculation of the $\gamma^* N \Delta$ transition form factors on the lattice has also been performed recently. Based on the method of Ref. [73], the Nicosia-MIT group [75] has performed a high-statistics calculations of the $\gamma^* N \Delta$ form factors. The Nicosia-MIT group has also implemented several improvements of the algorithm, such as smearing techniques to effectively filter the ground state, check on the volume dependence of the results, use of a larger lattice such as to simulate smaller quark masses. Both quenched and unquenched results have been obtained. The quenched calculation was performed for pion masses in the range $m_\pi \simeq 0.4 - 0.9$ GeV. The unquenched calculation, using dynamical Wilson fermions, was performed in the range of $m_\pi \simeq 0.5 - 0.8$ GeV. At such pion mass values, both the quenched and unquenched calculations give R_{EM} values in the range from -1 to -5 %. For pion masses in the range 0.5 - 0.8 GeV unquenching effects were found to be within statistical errors, which means that pion cloud contributions, expected to drive the R_{EM} value more negative are suppressed for these large quark (pion) masses.

In order to compare the calculated R_{EM} values with experiment, the Nicosia-MIT group uses a linear fit in m_π^2 (corresponding with a linear fit in the quark mass) was used to extrapolate down to the physical pion mass. Such a naive extrapolation can not be justified, as will be discussed below. Nonetheless, using such a linear extrapolation, the R_{EM} value at $Q^2 = 0.4$ GeV 2

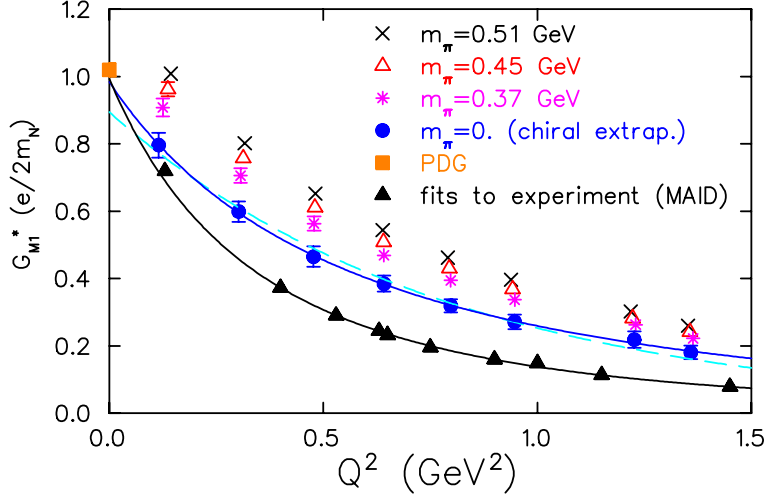


Fig. 14. Quenched lattice QCD results for the Q^2 dependence of the (Ash) form factor $G_{M1}^* = G_{M,Ash}^*/3$, as defined in Eq. (2.18) for three values of m_π as indicated on the figure. The (blue) solid circles are the result of a linear extrapolation in m_π^2 . The experimental value at $Q^2 = 0$ (red square, PDG) corresponds with the value given in Eq. (2.24). The lower solid curve corresponds with a fit to the data, according to the MAID analysis [26]. Figure from Ref. [82].

was found to be [75] :

$$R_{EM}(Q^2 = 0.4 \text{ GeV}^2) = (-4.4 \pm 1.7) \% \quad (\text{quenched}), \\ R_{EM}(Q^2 = 0.4 \text{ GeV}^2) = (-3.7 \pm 1.2) \% \quad (\text{unquenched}),$$

which is to be compared with the experimental number of Ref. [81]: $R_{EM} = (-3.4 \pm 0.4 \pm 0.4) \%$. One sees that the lattice QCD calculation clearly supports a negative value of R_{EM} , in basic agreement with experiment.

In the subsequent work of the Nicosia-MIT group [82], the $\gamma^* N\Delta$ form factors were studied within a fixed sink method in which the initial state, created at time zero, has the nucleon quantum numbers, and the final state, annihilated at a later time t_2 has the Δ quantum numbers. The current can couple to a quark line at any time slice t_1 , see Fig. 11, carrying any possible value of the lattice momentum. Implementing further improvements, the method of Ref. [82] is superior to the fixed current approach discussed above, yielding a more accurate evaluation of all three $\gamma^* N\Delta$ form factors. The calculations in Ref. [82] were performed in the quenched approximation for pion masses: $m_\pi = 0.51, 0.45$, and 0.37 GeV , which are also smaller than in the previous calculations.

The quenched lattice QCD results of Ref. [82] for the magnetic $\gamma^* N\Delta$ form factor are shown in Fig. 15 together with a linear extrapolation in m_π^2 of the lattice results. The lattice results show a decrease of G_M^* with decreasing pion mass. However the linear extrapolated values in m_π^2 are still lying significantly above the experimental results. The most likely explanation of this discrepancy is the inadequacy in the linear extrapolation. At low momentum transfer, where chiral effective field theory can be applied, one expects chiral logs to appear in the form factors, as will be discussed further on.

In Fig. 15, the quenched lattice QCD results of Ref. [82] are shown for the $\gamma^* N\Delta$ ratios R_{EM}

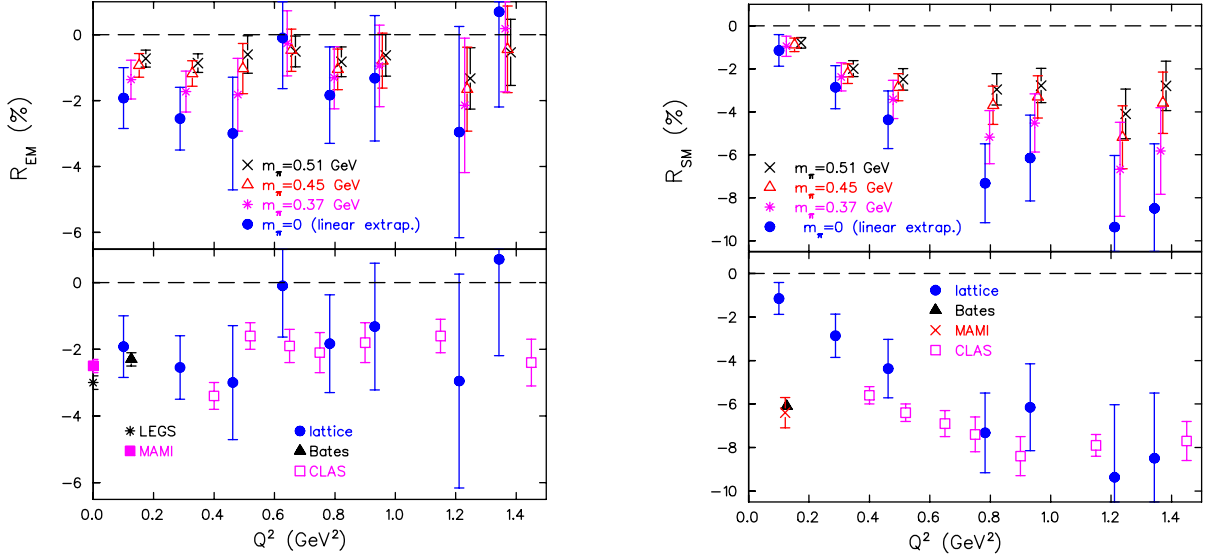


Fig. 15. Quenched lattice QCD results for the Q^2 dependence of the $\gamma^* N \Delta$ ratios R_{EM} (left panels) and R_{SM} (right panels), for three values of m_π as indicated on the figure. The (blue) solid circles are the result of a linear extrapolation in m_π^2 . In the lower panels a comparison with experimental data is shown: real photon points from MAMI [23] and LEGS [25]; finite Q^2 values are from BATES [95,80] (solid triangles), MAMI [78] (cross), and JLab/CLAS [81] (open boxes). Figure from Ref. [82].

and R_{SM} , together with a linear extrapolation in m_π^2 . For the R_{EM} ratio, the lattice results are accurate enough to show a negative value, which becomes more negative as one approaches the chiral limit. The linearly extrapolated lattice results seem to be in good agreement with the experiment, although the lattice results at larger Q^2 values show some scatter. The R_{SM} ratio is clearly negative over the whole Q^2 range. For $Q^2 \gtrsim 0.5 \text{ GeV}^2$, the linearly extrapolated lattice results are in agreement with experiment. At lower Q^2 on the other hand, the linearly extrapolated lattice results fall increasingly short of the data, and cannot explain the large negative value of R_{SM} established in experiment. The present empirical results for R_{SM} at low Q^2 have reached a high level of accuracy and have been cross-checked by several experiments at both BATES [95,312,80] and MAMI [78,77], all obtain a rather large negative R_{SM} ratio of around -6% at low Q^2 . This puzzle was studied in Refs. [87–89] within the framework of χ EFT, yeiding some interesting results as is discussed in the following.

2.6.2 Chiral extrapolations

The extrapolation in the quark mass m_q is not straightforward, because the non-analytic dependencies, such as $\sqrt{m_q}$ and $\ln m_q$, become important as one approaches the small physical value of m_q . Therefore naive extrapolations often fail, while spectacular non-analytic effects are found in a number of different quantities, see *e.g.*, Refs. [96,97]. The χ EFT, discussed in the previous section, provides a framework to compute these non-analytic terms. We will first address the quark mass dependence of the nucleon and Δ masses within χ EFT, which have been discussed extensively in the literature, see *e.g.* Refs. [98–105]. Subsequently, we will review the predictions for the pion mass dependence of the $\gamma^* N \Delta$ form factors.

In the χ EFT including Δ degrees of freedom, the pion mass dependence of N and Δ masses

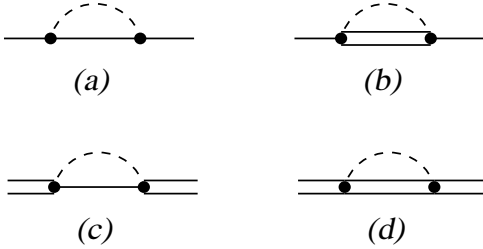


Fig. 16. The nucleon and Δ self-energy contributions in χ EFT. Dashed lines represent pion propagators, solid lines represent nucleon propagators, whereas double lines represent Δ propagators.

is calculated from the self-energy diagrams of Fig. 16. Near the chiral limit, i.e. for $m_\pi < \Delta \equiv M_\Delta - M_N$, the pion mass dependence for the N and Δ masses goes as [98]:

$$M_N = M_N^{(0)} - 4c_{1N}m_\pi^2 - \frac{3}{32\pi f_\pi^2}g_A^2m_\pi^3 + \frac{2}{(8\pi f_\pi)^2}h_A^2 \frac{m_\pi^4}{\Delta} \ln m_\pi + O(m_\pi^4), \quad (2.47)$$

$$M_\Delta = M_\Delta^{(0)} - 4c_{1\Delta}m_\pi^2 - \frac{3}{32\pi f_\pi^2} \frac{25}{81}H_A^2m_\pi^3 - \frac{1}{2(8\pi f_\pi)^2}h_A^2 \frac{m_\pi^4}{\Delta} \ln m_\pi + O(m_\pi^4). \quad (2.48)$$

The non-analytic terms (proportional to m_π^3 , $m_\pi^4/\Delta \ln m_\pi$,...) on the *rhs* of Eqs. (2.47,2.48) are predictions of χ EFT obtained from the loop diagrams of Fig. 16. These loop expressions depend on the coupling constants appearing in the lowest order chiral Lagrangian (see Sect. 4 for details): $g_A = 1.267$ is the axial coupling of the nucleon, $h_A \simeq 2.85$ is the $\pi N \Delta$ coupling constant (in the notation of Ref. [105]), and H_A is the axial $\pi \Delta \Delta$ coupling constant, which is related with g_A through the $SU(6)$ relation, which coincides with the large N_c relation: $H_A = (9/5)g_A \simeq 2.28$. The analytic terms on the *rhs* of Eqs. (2.47,2.48) are low-energy constants which have to be determined from experiment or from a fit to lattice QCD results. In particular M_N^0 (M_Δ^0) is the N (Δ) mass in the chiral limit, and the term proportional to c_{1N} ($c_{1\Delta}$) is the quark mass contribution to the N (Δ) mass. For the nucleon, it is obtained from the experimental information on the pion-nucleon σ -term.

The above formulas of Eqs. (2.47,2.48) can be fitted to full lattice QCD results for the N and Δ masses. Care has to be taken however when fitting to quenched lattice QCD results, where sea quark loop effects are neglected. The quenched approximation also modifies the leading chiral expansion of baryon masses in the corresponding effective field theory, see Ref. [106]. For instance, in the quenched approximation, the pion mass dependence of N and Δ masses contain a term linear in m_π , whereas such a term is absent in the full QCD expansions of Eqs. (2.47,2.48).

In Ref. [100], the m_π dependence of N and Δ masses have been fitted to lattice results using both the quenched theory and full QCD. The non-analytic terms have been calculated from the one-loop diagrams of Fig. 16, including a phenomenological form factor at the πNN , $\pi N\Delta$ and $\pi \Delta \Delta$ vertices to account for the finite size of the pion source. The parameters in the analytic terms were treated as free parameters and fit to the lattice results. Such a fit, is shown in Fig. 17. One clearly sees that this procedure is able to successfully account for the different behavior of the m_π dependence of N and Δ masses in quenched as compared to full QCD. One notices that the effect of unquenching is larger for the Δ as compared to the N . It will be interesting to test

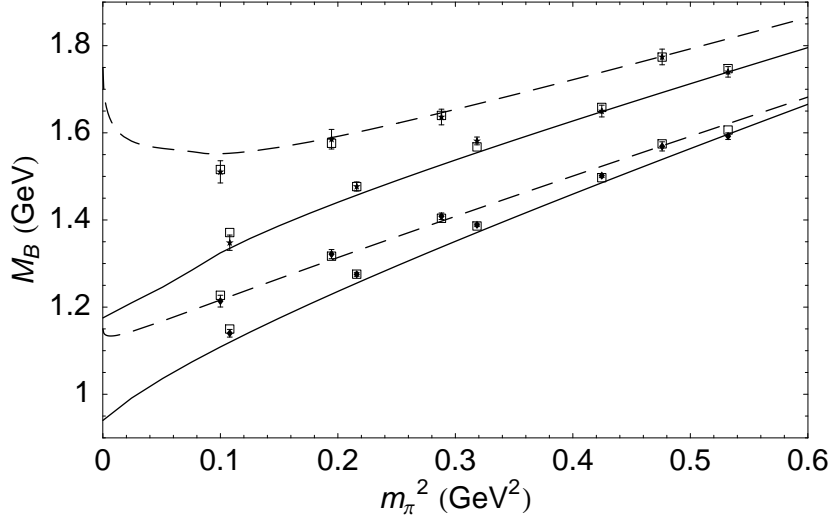


Fig. 17. Pion-mass dependence of the N and Δ masses according to Ref. [100] compared with lattice QCD results. The solid symbols are lattice results from the MILC Collaboration [107]. Solid symbols from bottom to top correspond with the nucleon unquenched, nucleon quenched, Δ unquenched, and Δ quenched lattice results. The open boxes are the fit of Ref. [100] to N and Δ masses accounting for finite volume and lattice spacing artifacts, as described in the text. The curves describe the infinite-volume limit for dynamical (solid curves) and quenched (dashed curves) N and Δ masses.

the more singular behavior of the quenched result for the Δ as lattice results become available for smaller pion masses.

A comparison of both quenched and full QCD also allows to draw interesting conclusions on the physical nature of the $N - \Delta$ mass splitting, because the effect of the pion cloud is only partly accounted for in the quenched theory. Ref. [100] found that only about 50 MeV of the observed 300 MeV $N - \Delta$ mass splitting arises from the pion cloud, while the rest arises from short distance processes, such as gluon exchange. This short distance contribution is responsible for the finite $N - \Delta$ mass splitting in the chiral limit (i.e. when $m_\pi \rightarrow 0$).

To account for higher order terms in the chiral expansion, the m_π dependence of M_N and M_Δ has been studied by two of us [105] in a manifestly covariant χ EFT framework consistent with analyticity. The resulting relativistic loop corrections obey the chiral power-counting, after renormalizations of the available counter-terms are done. The relativistic expressions also contain the nominally higher-order terms, which are necessary to satisfy the analyticity constraint. In such approach, the analytic terms in the quark mass arising from the one-loop pion diagrams of Fig. 16 are partially resummed. We found [105] that the convergence of the chiral expansion for M_N and M_Δ can be improved without introducing additional parameters. In Fig. 18, the results for the m_π dependence of N and Δ -resonance masses in this approach are compared with full lattice QCD results. For both N and Δ , the chiral limit mass values $M_N^{(0)}$ ($M_\Delta^{(0)}$) and the parameters c_{1N} ($c_{1\Delta}$) are fitted. As is seen from the figure, with this two-parameter form for M_N and M_Δ , a good description of lattice results is obtained up to $m_\pi^2 \simeq 0.5$ GeV 2 .

Having discussed the m_π dependence of M_N and M_Δ , we turn to the m_π dependence of the $\gamma^* N \Delta$ transition form factors. The study of the m_π -dependence is crucial to connect to lattice QCD results, which at present can only be obtained for larger pion masses (typically $m_\pi \gtrsim 0.3$ GeV) as discussed above in Fig. 14 for G_M^* , and in Fig. 15 for R_{EM} and R_{SM} .

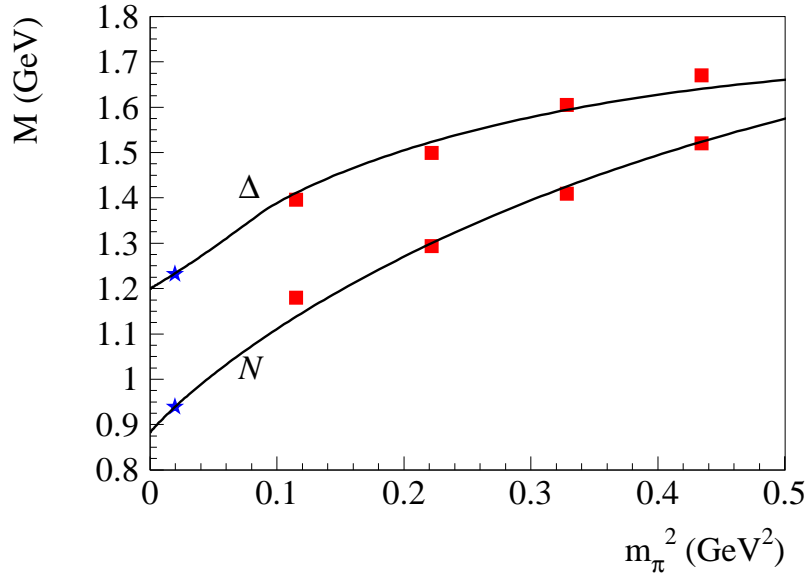


Fig. 18. Pion-mass dependence of the N and Δ masses. The curves are two-parameter expressions for M_N and M_Δ according to the manifestly covariant χ EFT framework of Ref. [105]. For both N and Δ , the chiral limit mass values $M_N^{(0)}$ ($M_\Delta^{(0)}$) and the parameters c_{1N} ($c_{1\Delta}$) are fitted. The red squares are lattice results from the MILC Collaboration [107] in full QCD. The stars represent the physical mass values.

In Fig. 19, the m_π -dependence of the *magnetic* $\gamma^* N \Delta$ -transition (Jones-Scadron) form factor G_M^* is shown in the relativistic χ EFT framework of Refs. [88,89]. It is calculated from the one-loop diagrams of Fig. 7. Recall that the value of G_M^* at $Q^2 = 0$ is determined by the low-energy constant g_M . The Q^2 -dependence then follows as a prediction of the NLO result, and Fig. 19 shows that this prediction is consistent with the experimental value at $Q^2 = 0.127 \text{ GeV}^2$ and physical pion mass. The m_π -dependence of G_M^* is also completely fixed at NLO, no new parameters appear.

In Fig. 19, the result for G_M^* at $Q^2 = 0.127 \text{ GeV}^2$ is shown both when the m_π -dependence of the nucleon and Δ masses is included and when it is not. Accounting for the m_π -dependence in M_N and M_Δ , as shown in Fig. 18, changes the result for G_M^* quite significantly. The χ EFT calculation, with the m_π dependence of M_N and M_Δ included, is in a qualitatively good agreement with the lattice data shown in the figure. The χ EFT result also follows an approximately linear behavior in m_π^2 , although it falls about 10 - 15 % below the lattice data. This is just within the uncertainty of the NLO results. One should also keep in mind that the lattice simulations of Ref. [82] are not done in full QCD, but are “quenched”, so discrepancies are not unexpected.

In Fig. 20, the m_π -dependence of the ratios R_{EM} and R_{SM} is shown within the same relativistic χ EFT framework and compared to the lattice QCD calculations. As discussed above, the recent state-of-the-art lattice calculations of R_{EM} and R_{SM} [82] use a *linear*, in the quark mass ($m_q \propto m_\pi^2$), *extrapolation* to the physical point, thus assuming that the non-analytic m_q -dependencies are negligible. The thus obtained value for R_{SM} at the physical m_π value displays a large discrepancy with the experimental result, as seen in Fig. 15. The relativistic χ EFT calcu-

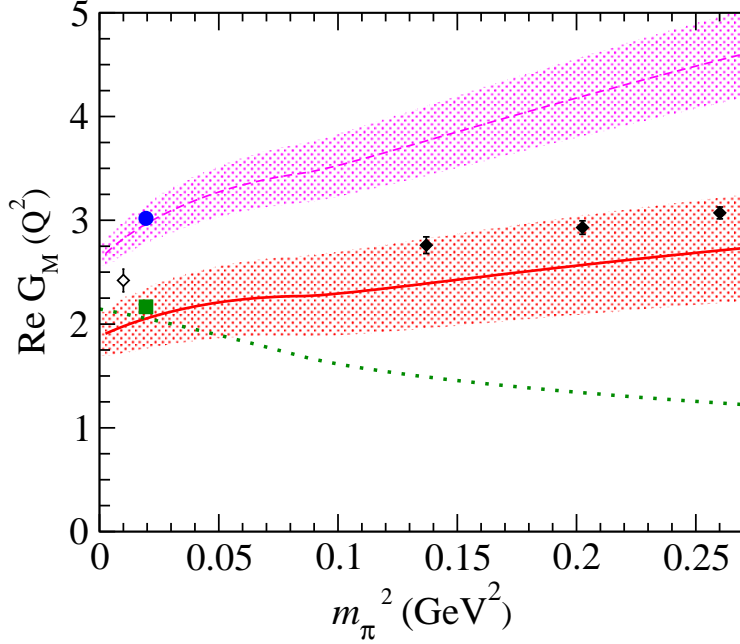


Fig. 19. The pion mass dependence of the real part of the Jones-Scadron $\gamma^* N\Delta$ form factor G_M^* for $Q^2 = 0$ and $Q^2 = 0.127$ GeV 2 in the relativistic χ EFT framework of Refs. [88,89]. The solid (dashed) curves are the NLO results for $Q^2 = 0.127$ GeV 2 ($Q^2 = 0$) respectively, including the m_π dependence of M_N and M_Δ . The green dotted curve is the corresponding result for $Q^2 = 0.127$ GeV 2 where the m_π dependence of M_N and M_Δ is not included. The blue circle for $Q^2 = 0$ is a data point from MAMI [23], and the green square for $Q^2 = 0.127$ GeV 2 is a data point from BATES [95,80]. The three filled black diamonds at larger m_π are lattice calculations [82] for Q^2 values of 0.125, 0.137, and 0.144 GeV 2 respectively, whereas the open diamond near $m_\pi \simeq 0$ represents their extrapolation assuming linear dependence in m_π^2 . Figure from Ref. [89].

lation [88,89], on the other hand, shows that the non-analytic dependencies are *not* negligible. While at larger values of m_π , where the Δ is stable, the ratios display a smooth m_π dependence, at $m_\pi = \Delta$ there is an inflection point, and for $m_\pi \leq \Delta$ the non-analytic effects are crucial, as was also observed for the Δ -resonance magnetic moment [108,109].

One also sees from Fig. 20 that, unlike the result for G_M^* , there is only little difference in the ratios between the χ EFT calculations with the m_π -dependence of M_N and M_Δ accounted for, and where this m_π dependence of the masses is neglected. The χ EFT framework of Refs. [88,89] thus shows that the assumption of a linear extrapolation in m_π^2 is not valid for R_{EM} and R_{SM} . Once the non-analytic dependencies on the quark mass as they follow from χ EFT are accounted for, there is no apparent discrepancy between the lattice results of Ref. [82] and the experimental results for R_{SM} .

To test the difference between quenched and full lattice QCD results for the $\gamma^* N\Delta$ form factors, new lattice calculations, within full QCD, are underway [110]. The full QCD results obtained so far [110] using dynamical Wilson fermions are more noisy but in agreement with those obtained in the quenched theory. It will be interesting to test the predicted strong non-analytic effects in the R_{EM} and R_{SM} ratios as shown in Fig. 20 once high statistics full lattice QCD results for pion masses smaller than 0.3 GeV become available.

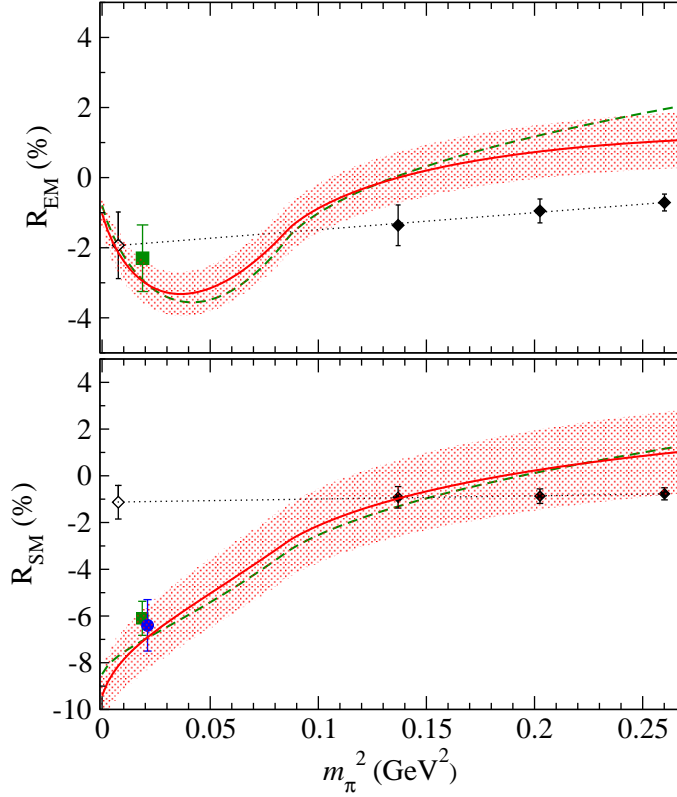


Fig. 20. The pion mass dependence of R_{EM} (upper panel) and R_{SM} (lower panel), at $Q^2 = 0.1 \text{ GeV}^2$. The blue circle is a data point from MAMI [78], the green squares are data points from BATES [95,80]. The three filled black diamonds at larger m_π are lattice calculations [82], whereas the open diamond near $m_\pi \simeq 0$ represents their extrapolation assuming linear dependence in m_π^2 . Red solid curves: NLO result when accounting for the m_π dependence in M_N and M_Δ ; green dashed curves: NLO result of Refs. [88,89], where the m_π -dependence of M_N and M_Δ was not accounted for. The error bands represent the estimate of theoretical uncertainty for the NLO calculation. Figure from Ref. [89].

2.7 The $N \rightarrow \Delta$ generalized parton distributions (GPDs)

2.7.1 Definition of $N \rightarrow N$ and $N \rightarrow \Delta$ GPDs and sum rules

So far we have discussed the $N \rightarrow \Delta$ transition as revealed with the help of the electromagnetic probe. By measuring the response of the hadron to a virtual photon, one measures the matrix element of a well-defined quark-gluon operator (in this case the vector operator $\bar{q}\gamma^\mu q$) over the hadronic state. This matrix element can be parametrized in terms of the $\gamma^* N \Delta$ transition form factors, revealing the quark-gluon structure of the hadron. We are however not limited in nature to probes such as photons (or W, Z bosons for the axial transition). The phenomenon of asymptotic freedom of QCD, meaning that at short distances the interactions between quarks and gluons become weak, provides us with more sophisticated QCD operators to explore the structure of hadrons. Such operators can be accessed by selecting a small size configuration of quarks and gluons, provided by a hard reaction, such as deep inelastic scattering (DIS), or hard exclusive reactions such as deeply virtual Compton scattering (DVCS). We will be mostly

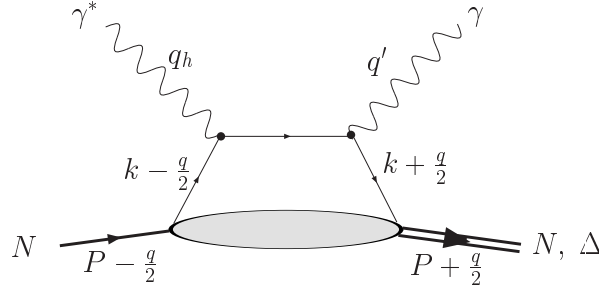


Fig. 21. The “handbag” diagram for the $N \rightarrow N$ and $N \rightarrow \Delta$ DVCS processes. Provided the virtuality of the initial photon (with momentum q_h) is sufficiently large, the QCD factorization theorem allows to express the total amplitude as the convolution of a Compton process at the quark level and a non-perturbative amplitude parametrized in terms of generalized parton distributions (lower blob). The diagram with the photon lines crossed is also understood.

interested here in DVCS reactions which are of the type $\gamma^*(q_h) + N(p) \rightarrow \gamma(q') + B(p')$, where the virtual photon momentum q_h is the hard scale, and where the final state B stands for either the nucleon N or the Δ state. The common important feature of such hard reactions is the possibility to separate clearly the perturbative and nonperturbative stages of the interactions, this is the so-called factorization property. The all order factorization theorem for the DVCS process on the nucleon has been proven in Refs. [111–113]. Qualitatively one can say that the hard reactions allow one to perform a “microsurgery” of a nucleon by removing in a controlled way a quark of one flavor and spin and implanting instead another quark (in general with a different flavor and spin) in the final baryon. It is illustrated in Fig. 21 for the case of the DVCS process with a Δ in the final state. The non-perturbative stage of such hard exclusive electroproduction processes is described by universal objects, so-called generalized parton distributions (GPDs) [114–116], see Refs. [117–120] for reviews and references.

Before discussing the $N \rightarrow \Delta$ GPDs, we start by briefly reviewing the $N \rightarrow N$ GPDs. The nucleon structure information entering the nucleon DVCS process, can be parametrized at leading twist-2 level, in terms of four (quark chirality conserving) GPDs⁷. The GPDs depend on three variables : the quark longitudinal momentum fractions x and ξ , and the momentum transfer $Q^2 = -q^2$ to the hadron. The light-cone momentum⁸ fraction x is defined by $k^+ = xP^+$, where k is the quark loop momentum and P is the average nucleon momentum $P = (p + p')/2$, where $p(p')$ are the initial (final) nucleon four-momenta respectively, see Fig. 21. The skewedness variable ξ is defined by $q^+ = -2\xi P^+$, where $q = p' - p$ is the overall momentum transfer in the process, and where $2\xi \rightarrow x_B/(1 - x_B/2)$ in the Bjorken limit: $x_B = Q_h^2/(2p \cdot q_h)$ is the usual Bjorken scaling variable, with $Q_h^2 = -q_h^2 > 0$ the virtuality of the hard photon. Furthermore, the third variable entering the GPDs is given by the invariant $Q^2 = -q^2$, being the total squared momentum transfer to the nucleon. The DVCS process corresponds with the kinematics $Q_h^2 \gg Q^2, M_N^2$, so that at twist-2 level, terms proportional to Q^2/Q_h^2 or M_N^2/Q_h^2 are neglected in the amplitude. In a frame where the virtual photon momentum q_h^μ and the average nucleon momentum P^μ are collinear along the z -axis and in opposite

⁷ we do not consider chirally odd GPDs, which are also discussed in the literature, see e.g. the review of Ref. [119]

⁸ using the definition $a^\pm \equiv 1/\sqrt{2}(a^0 \pm a^3)$ for the light-cone components

directions, one can parametrize the non-perturbative object entering the nucleon DVCS process as (we follow Ref. [115]) ⁹:

$$\begin{aligned} & \frac{1}{2\pi} \int dy^- e^{ixP^+y^-} \langle N(p') | \bar{\psi}(-y/2) \gamma \cdot n \psi(y/2) | N(p) \rangle \Big|_{y^+ = \vec{y}_\perp = 0} \\ &= H^q(x, \xi, Q^2) \bar{u}(p') \gamma \cdot n u(p) + E^q(x, \xi, Q^2) \bar{u}(p') i\sigma^{\mu\nu} \frac{n_\mu q_\nu}{2M_N} u(p), \end{aligned} \quad (2.49)$$

where ψ is the quark field of flavor q , u the nucleon spinor, and n^μ is a light-cone vector along the negative z -direction which can be expressed at twist-2 level ¹⁰ in terms of the external momenta as:

$$q_h = -2\xi P + \frac{Q_h^2}{4\xi} n, \quad q = -2\xi P + q_\perp, \quad q' = \frac{Q_h^2}{4\xi} n - q_\perp, \quad (2.50)$$

where $q_\perp = (0, \mathbf{q}_\perp, 0)$ is the transverse component of the momentum transfer q , satisfying $q_\perp \cdot n = q_\perp \cdot P = 0$. Furthermore the light-cone vector n , satisfying $n^2 = 0$ is normalized in such a way that $n \cdot P = 1$. The *lhs* of Eq. (2.49) can be interpreted as a Fourier integral along the light-cone distance y^- of a quark-quark correlation function, representing the process where a quark is taken out of the initial nucleon (having momentum p) at the space-time point $y/2$, and is put back in the final nucleon (having momentum p') at the space-time point $-y/2$. This process takes place at equal light-cone time ($y^+ = 0$) and at zero transverse separation ($\vec{y}_\perp = 0$) between the quarks. The resulting one-dimensional Fourier integral along the light-cone distance y^- is with respect to the quark light-cone momentum xP^+ . The *rhs* of Eq. (2.49) parametrizes this non-perturbative object in terms of the GPDs H^q and E^q for a quark of flavor q . The quark vector operator ($\gamma \cdot n$) corresponds at the nucleon side to a vector transition (parametrized by the function H^q) and a tensor transition (parametrized by the function E^q). Analogously, there are two GPDs corresponding with a quark axial vector operator ($\gamma \cdot n \gamma_5$), which are commonly denoted by the polarized GPDs \tilde{H}^q and \tilde{E}^q .

The variable x in the GPDs runs from -1 to 1. Therefore, the momentum fractions of the active quarks ($x + \xi$) for the initial quark and ($x - \xi$) for the final quark can either be positive or negative. Since positive (negative) momentum fractions correspond to quarks (antiquarks), it has been noted in [116] that in this way, one can identify two regions for the GPDs: when $x > \xi$ both partons represent quarks, whereas for $x < -\xi$ both partons represent antiquarks. In these regions, the GPDs are the generalizations of the usual parton distributions from DIS. Actually, in the forward direction, the GPD H reduces to the quark (anti-quark) density distribution $q(x)$ ($\bar{q}(x)$) obtained from DIS:

⁹ In all non-local expressions we always assume the gauge link $P \exp(ig \int dx^\mu A_\mu)$ ensuring the color gauge invariance of expressions.

¹⁰ For kinematical expressions including correction terms proportional to Q^2/Q_h^2 and M_N^2/Q_h^2 , which are formally of higher twist, see e.g. Ref. [118]

$$H^q(x, 0, 0) = \begin{cases} q(x), & x > 0, \\ -\bar{q}(-x), & x < 0. \end{cases} \quad (2.51)$$

The function E (and likewise the function \tilde{E} for the axial operator) are not measurable through DIS because the associated tensor in Eq. (2.49) vanishes in the forward limit ($q \rightarrow 0$). Therefore, E is a new leading twist function, which is accessible by measuring hard exclusive electroproduction reactions, such as DVCS.

As the momentum fractions of initial and final quarks are different, one accesses quark momentum correlations in the nucleon. Furthermore, in the region $-\xi < x < \xi$, one parton connected to the lower blob in Fig. 21 represents a quark and the other one an antiquark. In this region, the GPDs behave like a meson distribution amplitude and contain completely new information about nucleon structure, because the region $-\xi < x < \xi$ is absent in DIS, which corresponds to the limit $\xi \rightarrow 0$.

Besides coinciding with the quark distributions at vanishing momentum transfer, the generalized parton distributions have interesting links with other nucleon structure quantities. The first moments of the GPDs are related to the elastic form factors of the nucleon through model independent sum rules. By integrating Eq. (2.49) over x , one obtains for any ξ the following relations for a particular quark flavor [115] :

$$\int_{-1}^{+1} dx H^q(x, \xi, Q^2) = F_1^q(Q^2), \quad \int_{-1}^{+1} dx E^q(x, \xi, Q^2) = F_2^q(Q^2), \quad (2.52)$$

where $F_1^q(Q^2)$ represents the elastic Dirac form factor for the quark flavor q in the nucleon. These quark form factors are expressed, using $SU(2)$ isospin, as flavor combinations of the proton and neutron elastic form factors as:

$$F_1^u = 2F_1^p + F_1^n + F_1^s, \quad F_1^d = 2F_1^n + F_1^p + F_1^s, \quad (2.53)$$

where F_1^p and F_1^n are the proton and neutron electromagnetic form factors respectively, with $F_1^p(0) = 1$ and $F_1^n(0) = 0$. In Eq. (2.53) F_1^s is the strangeness form factor of the nucleon (which is neglected in the practical calculations below). Relations similar to Eq. (2.53) hold for the Pauli form factors F_2^q . At $Q^2 = 0$, the normalizations of the Dirac form factors are given by: $F_1^u(0) = 2$ ($F_1^d(0) = 1$) so as to yield the normalization of 2 (1) for the u (d)-quark distributions in the proton. The normalizations of the Pauli form factor at $Q^2 = 0$ are given by $F_2^q(0) = \kappa_q$ (for $q = u, d$), where κ_u, κ_d can be expressed in terms of the proton (κ_p) and neutron (κ_n) anomalous magnetic moments as:

$$\kappa_u \equiv 2\kappa_p + \kappa_n = +1.673, \quad \kappa_d \equiv \kappa_p + 2\kappa_n = -2.033. \quad (2.54)$$

The sum rules of Eq. (2.52) also satisfy the condition that they are independent of ξ , which is a consequence of Lorentz invariance ¹¹.

¹¹ This is the simplest example of a so-called polynomiality condition when calculating moments of GPDs.

We next discuss the $N \rightarrow \Delta$ matrix element for the vector twist-2 operator, which was worked out in Refs. [121,118]. There are four $N \rightarrow \Delta$ helicity amplitudes for the vector operator ¹². However, gauge invariance for the electromagnetic current operator leads to only three electromagnetic form factors. Hence there are strictly speaking four GPDs for the vector $N \rightarrow \Delta$ transition, of which one has a vanishing first moment. We will neglect this GPD which has a vanishing first moment in the following, guided by large N_c arguments (see below) where this GPD is subdominant. The non-perturbative object entering the $N \rightarrow \Delta$ DVCS process (lower blob in Fig. 21) can then be expressed as [121,118]:

$$\begin{aligned} & \frac{1}{2\pi} \int dy^- e^{ixP^+y^-} \langle \Delta(p_\Delta) | \bar{\psi}(-y/2) \gamma \cdot n \tau_3 \psi(y/2) | N(p) \rangle \Big|_{y^+ = \vec{y}_\perp = 0} \\ &= \sqrt{\frac{2}{3}} u^\alpha(p_\Delta) \left\{ H_M(x, \xi, Q^2) \left(-\mathcal{K}_{\alpha\mu}^M \right) n^\mu + H_E(x, \xi, Q^2) \left(-\mathcal{K}_{\alpha\mu}^E \right) n^\mu \right. \\ & \quad \left. + H_C(x, \xi, Q^2) \left(-\mathcal{K}_{\alpha\mu}^C \right) n^\mu \right\} u(p), \end{aligned} \quad (2.55)$$

where $u^\alpha(p_\Delta)$ is the Rarita-Schwinger spinor for the Δ -field, $\tau_3/2$ is the third isospin generator for quarks, and $\sqrt{2/3}$ is the isospin factor for the $p \rightarrow \Delta^+$ transition. Furthermore, in Eq. (2.55), the covariants $\mathcal{K}_{\alpha\mu}^{M,E,C}$ are the magnetic dipole, electric quadrupole, and Coulomb quadrupole Jones-Scadron covariants [13]:

$$\begin{aligned} \mathcal{K}_{\alpha\mu}^M &= -i \frac{3(M_\Delta + M_N)}{2M_N Q_+^2} \varepsilon_{\alpha\mu\lambda\sigma} P^\lambda q^\sigma, \\ \mathcal{K}_{\alpha\mu}^E &= -\mathcal{K}_{\alpha\mu}^M - \frac{6(M_\Delta + M_N)}{M_N Q_+^2 Q_-^2} \varepsilon_{\alpha\sigma\lambda\rho} P^\lambda q^\rho \varepsilon_{\mu\kappa\delta}^\sigma P^\kappa q^\delta \gamma_5, \\ \mathcal{K}_{\alpha\mu}^C &= -i \frac{3(M_\Delta + M_N)}{M_N Q_+^2 Q_-^2} q_\alpha (q^2 P_\mu - q \cdot P q_\mu) \gamma_5. \end{aligned} \quad (2.56)$$

Here $P = (p_\Delta + p)/2$, $q = p_\Delta - p$, and $p_\Delta^2 = M_\Delta^2$. In Eq. (2.55), the GPDs H_M , H_E , and H_C for the $N \rightarrow \Delta$ vector transition are linked with the three $N \rightarrow \Delta$ vector current (Jones-Scadron) transition form factors G_M^* , G_E^* , and G_C^* introduced in Eq. (2.3) through the sum rules:

$$\int_{-1}^1 dx H_{M,E,C}(x, \xi, Q^2) = 2 G_{M,E,C}^*(Q^2), \quad (2.57)$$

where the factor 2 arises because the electromagnetic form factors are conventionally defined with isospin generator $\tau_3/2$ in the current operator in contrast to the operator τ_3 in Eq. (2.55) adopted in Refs. [121,118] to define GPDs. The above sum rules allow us to make a prediction for the $N \rightarrow \Delta$ form factors provided we have a model for the $N \rightarrow \Delta$ GPDs. Such a model will be discussed in the following sections. Conversely, the existing precise experimental

¹² Analogously, there are four GPDs at twist-2 level for the $N \rightarrow \Delta$ axial transition, see Refs. [121,118] for details

information on the $N \rightarrow \Delta$ vector form factors provides a strong constraint on the $N \rightarrow \Delta$ GPDs. As discussed above, the GPDs are however much richer observables and provide us with quark distribution information in the Δ resonance. They can be accessed by the $N \rightarrow \Delta$ DVCS process as discussed in Ref. [122]. First experiments which are sensitive to the $N \rightarrow \Delta$ GPDs have recently been reported [123].

2.7.2 Model for the magnetic dipole $N \rightarrow \Delta$ GPD

Here we will be guided by the large N_c limit, which allows to connect the $N \rightarrow \Delta$ GPD H_M , to the $N \rightarrow N$ isovector GPDs. For the magnetic $N \rightarrow \Delta$ transition, it was shown in Ref. [121] that, in the large N_c limit, the relevant $N \rightarrow \Delta$ GPD H_M can be expressed in terms of the nucleon isovector GPD $E^u - E^d$:

$$H_M(x, \xi, Q^2) = 2 \frac{G_M^*(0)}{\kappa_V} \left\{ E^u(x, \xi, Q^2) - E^d(x, \xi, Q^2) \right\}, \quad (2.58)$$

where $\kappa_V = \kappa_p - \kappa_n = 3.70$. Within the large N_c approach used in Ref. [121], the value $G_M^*(0)$ is given by $G_M^*(0) = \kappa_V / \sqrt{2}$ ¹³, which is about 20% smaller than the experimental number¹⁴. In order to give more realistic estimates, we will therefore use in the following calculations the phenomenological value $G_M^*(0) \approx 3.02$ of Eq. (2.24). All other (sub-dominant) GPDs for the vector $N \rightarrow \Delta$ transition vanish at leading order in the $1/N_c$ expansion, consistent with the large N_c limit for the $\gamma N \Delta$ form factors discussed in Subsect. 2.4.

Using the large N_c estimate of Eq. (2.58), the sum rule Eq. (2.57) for G_M^* can be written as:

$$\begin{aligned} G_M^*(Q^2) &= \frac{G_M^*(0)}{\kappa_V} \int_{-1}^{+1} dx \left\{ E^u(x, \xi, Q^2) - E^d(x, \xi, Q^2) \right\}, \\ &= \frac{G_M^*(0)}{\kappa_V} \left\{ F_2^p(Q^2) - F_2^n(Q^2) \right\}, \end{aligned} \quad (2.59)$$

where $F_2^p - F_2^n$ is the isovector combination of the proton (p) - neutron (n) Pauli form factors. Because the sum rule of Eq. (2.59) is independent of ξ , we only need to constrain the GPD E^q for $\xi = 0$ in order to evaluate G_M^* . The sum rule (2.59) was used in Ref. [124], using a model [126] in which the Gaussian ansatz for GPDs is modified at large Q^2 by terms having a power-law behavior. Refs. [127,128] used parametrizations which are motivated from the expected

¹³ Note the typo in the formula for H_M in Ref. [121]. Due to a different choice of isospin factors for the vector and axial vector transitions chosen there, one should correct Eq. (7) in Ref. [121] to be $H_M = \sqrt{2}(E^u - E^d)$ instead of $H_M = \sqrt{\frac{2}{3}}\sqrt{2}(E^u - E^d)$.

¹⁴ Note that in the large N_c limit, the isovector combination $H^u - H^d$ is suppressed, therefore one could as well give an estimate $\mu_{p \rightarrow \Delta^+} \simeq G_M^*(0) \simeq \frac{1}{\sqrt{2}}(\mu_p - \mu_n) \simeq 3.32$ (where the magnetic moments are expressed in nuclear magnetons whereas G_M^* is dimensionless), corresponding with Eq. (2.37) where $M_\Delta \simeq M_N$ in the large N_c limit. This estimate is accurate at the 10 % level.

Regge behavior of the GPDs at small x and Q^2 . In Ref. [128], the function $E^q(x, 0, Q^2)$ at low Q^2 was parametrized through a Regge-type form (denoted by model $R1$) as:

$$E_{R1}^q(x, 0, Q^2) = e^q(x) x^{\alpha' Q^2}. \quad (2.60)$$

The forward magnetic densities $e^q(x)$ - unlike the usual forward parton densities $q(x)$ - are unfortunately not known from experiment at present. The simplest idea is to take them proportional to the valence up-quark ($u_v(x)$) and down-quark ($d_v(x)$) densities as:

$$e^u(x) = \frac{\kappa_u}{2} u_v(x) \quad \text{and} \quad e^d(x) = \kappa_d d_v(x), \quad (2.61)$$

which satisfy the normalization constraint of Eq. (2.52) at $Q^2 = 0$:

$$\kappa_q = \int dx e^q(x). \quad (2.62)$$

where κ_u and κ_d are defined in Eq. (2.54). One thus sees that the functions $e^q(x)$ encode the quark distribution information giving rise to the nucleon anomalous magnetic moments.

As shown in Ref. [128], the Regge model $R1$ fits the nucleon Dirac (F_1) and Pauli (F_2) form factor data for small momentum transfers $Q^2 \lesssim 0.5 \text{ GeV}^2$. However, at larger Q^2 the $R1$ model gives too strong suppression, and it consequently falls considerably short of the data for $Q^2 > 1 \text{ GeV}^2$.

Experimentally, the proton helicity flip form factor $F_2(Q^2)$ has a faster power fall-off at large Q^2 than $F_1(Q^2)$. This means that the $x \sim 1$ behavior of the functions $e(x)$ and $q(x)$ should be different. To produce a faster decrease with Q^2 , the $x \sim 1$ limit of the density $e^q(x)$ should have extra powers of $1 - x$ compared to that of $q(x)$. Aiming to avoid introducing too many free parameters, Ref. [128] tried the next simplest ansatz for $e^q(x)$ by just multiplying the valence quark distributions by an additional factor $(1 - x)^{\eta_q}$, i.e. by taking:

$$e^u(x) = \frac{\kappa_u}{N_u} (1 - x)^{\eta_u} u_v(x) \quad \text{and} \quad e^d(x) = \frac{\kappa_d}{N_d} (1 - x)^{\eta_d} d_v(x), \quad (2.63)$$

where the normalization factors N_u and N_d

$$N_u = \int_0^1 dx (1 - x)^{\eta_u} u_v(x), \quad N_d = \int_0^1 dx (1 - x)^{\eta_d} d_v(x), \quad (2.64)$$

guarantee the condition of Eq. (2.62). In such modified Regge parametrization (denoted by $R2$), the GPD E^q entering the sum rule Eq. (2.59) for G_M^* was parametrized in Ref. [128] as:

$$E_{R2}^q(x, 0, Q^2) = \frac{\kappa_q}{N_q} (1 - x)^{\eta_q} q_v(x) x^{\alpha' (1-x) Q^2}, \quad (2.65)$$

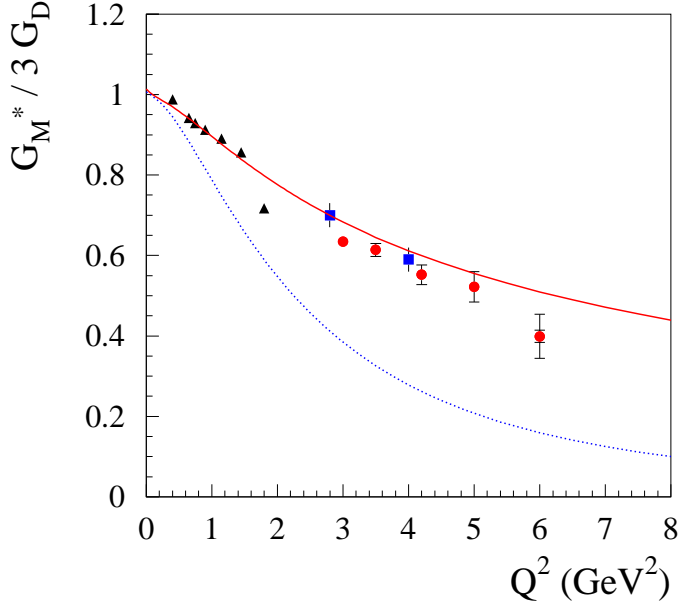


Fig. 22. The $N \rightarrow \Delta$ magnetic transition (Jones-Scadron) form factor G_M^* , relative to the dipole form (multiplied by a factor 3). The curves are calculated from a parametrization of the $N \rightarrow \Delta$ magnetic GPD H_M of Ref. [128]. Blue dotted curve : Regge GPD parametrization according to Eq. (2.60). Red solid curve : modified Regge GPD parametrization according to Eq. (2.65). The data points are from JLab Hall C [130] (blue squares), and JLab CLAS : Refs. [81] (black triangles) and [131] (red circles). The data of Refs. [81,131] have been analyzed using the unitary isobar model of Ref. [132].

with q_v the valence quark distribution ($q = u, d$), and where the powers η_u and η_d have been determined from a fit to the nucleon form factor data as $\alpha' = 1.105 \text{ GeV}^{-2}$, $\eta_u = 1.713$ and $\eta_d = 0.566$. Note that a value $\eta_q = 2$ corresponds to a $1/Q^2$ asymptotic behavior of the ratio $F_2^q(Q^2)/F_1^q(Q^2)$ at large Q^2 .

In the following estimates, the unpolarized valence quark distributions are taken at input scale $\mu^2 = 1 \text{ GeV}^2$ from the MRST2002 global NNLO fit [129] as:

$$u_v = 0.262 x^{-0.69} (1 - x)^{3.50} (1 + 3.83 x^{0.5} + 37.65 x), \quad (2.66)$$

$$d_v = 0.061 x^{-0.65} (1 - x)^{4.03} (1 + 49.05 x^{0.5} + 8.65 x). \quad (2.67)$$

For the one-parameter Regge form $R1$ of Eq. (2.60) the same parameter value $\alpha' = 1.105 \text{ GeV}^{-2}$ was chosen as in the model $R2$, which gives a good description of the proton charge radius. In Fig. 22, we show the results for the sum rule predictions for G_M^* using the GPD parametrizations of Eqs. (2.60) and (2.65). It is seen that both the Regge and modified Regge parametrizations yield a magnetic $N \rightarrow \Delta$ form factor which decreases faster than a dipole, in qualitative agreement with the data. The $R1$ Regge parametrization though gives too large suppression at larger Q^2 , as was also observed for the nucleon elastic form factors in Ref. [128].

For the modified Regge parametrization $R2$, it is seen that the sum rule prediction based on the large N_c estimate of Eq. (2.59) gives a good quantitative description of the data over the whole Q^2 range without adjusting any parameters beyond the three parameters α' , η_u , and η_d which were determined from a fit to the nucleon elastic form factor data.

2.7.3 Model for the electric quadrupole $N \rightarrow \Delta$ GPD

In this section, we make a very first attempt to model the electric quadrupole GPD, H_E . As in our modeling of H_M , we will also be guided by the large N_c limit. In the large N_c limit, Eq. (2.41) provides a relation between the $N \rightarrow \Delta$ quadrupole moment and the neutron charge radius r_n^2 , which for $N_c = 3$ reduces to:

$$Q_{p \rightarrow \Delta^+} = \frac{1}{\sqrt{2}} r_n^2. \quad (2.68)$$

Using Eq. (2.17), we can express Eq. (2.68) in a relation for $G_E^*(0)$, which reads to leading accuracy in the $1/N_c$ -expansion as:

$$G_E^*(0) = -\frac{1}{6} r_n^2 \frac{1}{\sqrt{2}} \frac{(M_\Delta^2 - M_N^2)}{2}. \quad (2.69)$$

For small values of Q^2 , we can express the neutron electric form factor as $G_E^n(Q^2) \approx -r_n^2 Q^2/6$. Therefore, a natural extension of the large N_c relation of Eq. (2.69) to finite Q^2 is given by:

$$G_E^*(Q^2) = \frac{1}{\sqrt{2}} \frac{(M_\Delta^2 - M_N^2)}{2} \frac{G_E^n(Q^2)}{Q^2}. \quad (2.70)$$

The prediction which follows from the large N_c motived expression of Eq. (2.70) is tested in Fig. 23 by comparing the Q^2 dependence of the neutron electric form factor G_E^n and the $N \rightarrow \Delta$ R_{EM} ratio. For G_E^n we use the modified Regge parametrization $R2$ of [128], which is seen to give a fairly good description of the available double polarization data. The R_{EM} ratio is calculated using the large N_c relations Eq. (2.70) for G_E^* , and Eq. (2.59) for G_M^* , as discussed in Sect. 2.7.2. These relations express the $N \rightarrow \Delta$ form factors in terms of nucleon elastic form factors. By using the three parameter $R2$ Regge form for the nucleon elastic form factors, we obtain in this way a prediction for R_{EM} without adjusting any additional parameter. One sees that this yields a R_{EM} ratio which has both the right size and displays a relatively flat Q^2 behavior, up to a Q^2 value of about 1.5 GeV 2 , in surprisingly good agreement with the data.

The form factor G_E^* is obtained from the first moment of the electric quadrupole $N \rightarrow \Delta$ GPD H_E through the sum rule of Eq. (2.57). We can therefore use Eq. (2.70) to propose a relation between the $N \rightarrow \Delta$ GPD H_E and the neutron electric GPD combination, which is consistent with this form factor sum rule, as:

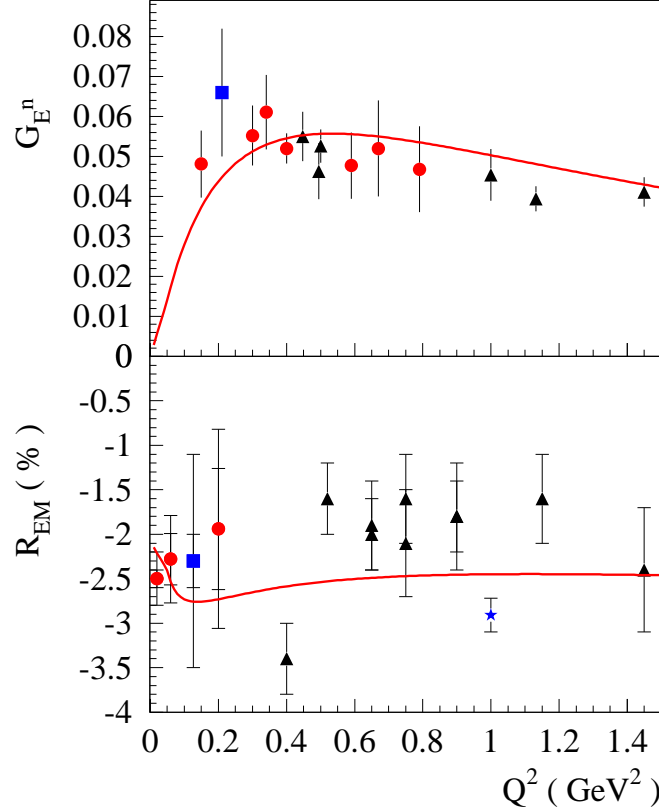


Fig. 23. GPD calculations for the Q^2 dependence of the neutron electric form factor G_E^n (upper panel) in comparison with the $N \rightarrow \Delta R_{EM}$ ratio (lower panel). For the neutron electric form factor, the modified Regge GPD parametrization $R2$ of Ref. [128] is used. For the R_{EM} ratio, the large N_c relations Eq. (2.70) for G_E^* , and Eq. (2.59) for G_M^* are used, which express the $N \rightarrow \Delta$ form factors in terms of nucleon elastic form factors, which in turn are calculated using the modified Regge GPD parametrization $R2$. The data points for G_E^n are from MAMI [133–136] (red circles), NIKHEF [137] (blue square), and JLab [138–140] (black triangles). The data points for R_{EM} are from BATES at $Q^2 = 0.127$ [80] (blue square); MAMI (red circles): $Q^2 = 0$ [23], $Q^2 = 0.06$ [79], $Q^2 = 0.2$ [141]; JLab CLAS [81] (black triangles); and JLab HallA [142] (blue star).

$$H_E(x, 0, Q^2) = \frac{1}{\sqrt{2}} \frac{(M_\Delta^2 - M_N^2)}{Q^2} \left\{ H^{(n)}(x, 0, Q^2) - \frac{Q^2}{4M_N^2} E^{(n)}(x, 0, Q^2) \right\}, \quad (2.71)$$

where the neutron GPDs are obtained in terms of the u - and d -quark flavor GPDs as: $H^{(n)} = -1/3H^u + 2/3H^d$, and $E^{(n)} = -1/3E^u + 2/3E^d$.

An interesting topic for future work is to perform different model calculations for H_M , H_E , and H_C , as well as provide lattice QCD predictions for its moments, in order to cross-check the above estimates for H_M and H_E .

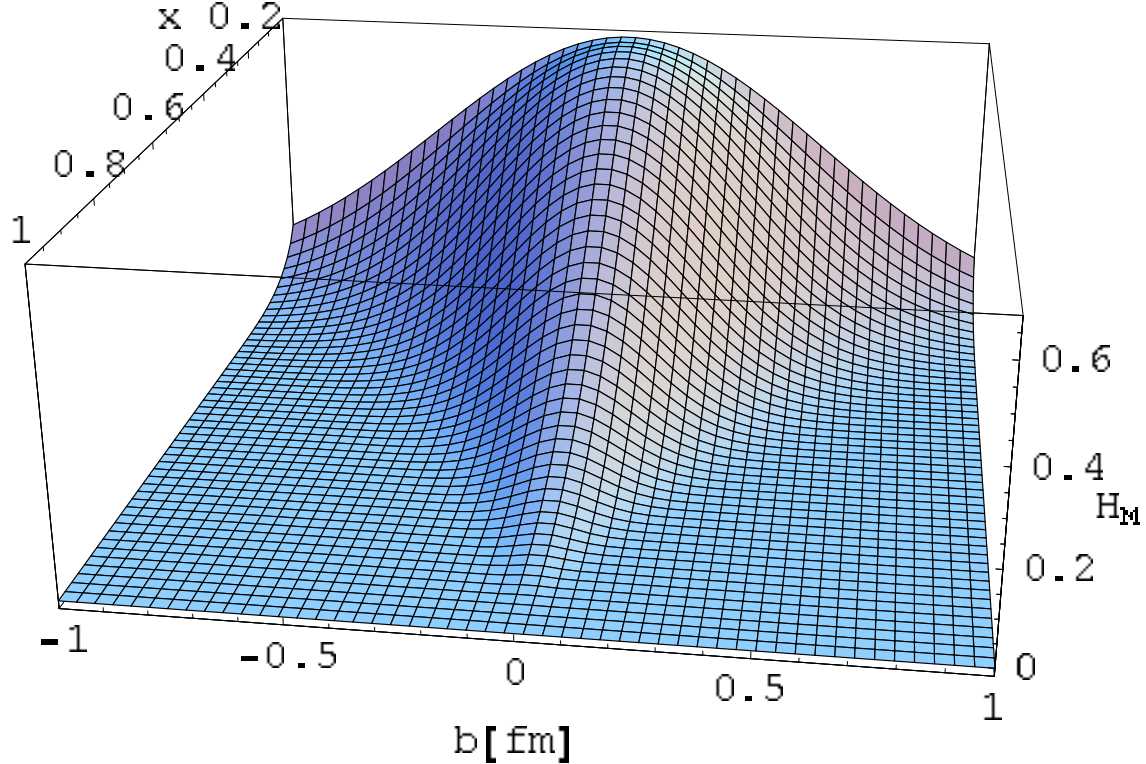


Fig. 24. The magnetic dipole $N \rightarrow \Delta$ GPD H_M as function of the quark momentum fraction x and the quark position b in the transverse plane (perpendicular to the average direction of the fast moving baryons), where b stands for either $(\mathbf{b}_\perp)_x$ or $(\mathbf{b}_\perp)_y$. The calculation is based on the modified Regge parametrization $R2$ of Eq. (2.65).

2.7.4 GPDs and transverse structure of hadrons

The interplay between the x and Q^2 -dependence of the GPDs contains new nucleon structure information beyond the information encoded in forward parton distributions depending only on x , or form factors depending only on Q^2 . It has been shown that by a Fourier transform of the Q^2 -dependence of GPDs, it is conceivable to access the distributions of parton in the transverse plane, see Ref. [143], and to provide a 3-dimensional picture of the nucleon [144].

For $\xi = 0$, one can define the impact parameter versions of GPDs are obtained through a Fourier integral in transverse momentum q_\perp . For the GPD E^q , this reads as:

$$E^q(x, \mathbf{b}_\perp) \equiv \int \frac{d^2 \mathbf{q}_\perp}{(2\pi)^2} e^{i \mathbf{b}_\perp \cdot \mathbf{q}_\perp} E^q(x, 0, -\mathbf{q}_\perp^2), \quad (2.72)$$

and analogous definitions for the other GPDs. These impact parameter GPDs have the physical meaning of measuring the probability to find a quark which carries longitudinal momentum fraction x at a transverse position \mathbf{b}_\perp (relative to the transverse center-of-momentum) in a nucleon, see Refs. [143,145].

When translating the GPD parametrization $R2$ of Eq. (2.65), into the impact parameter space, we obtain for the GPD E :

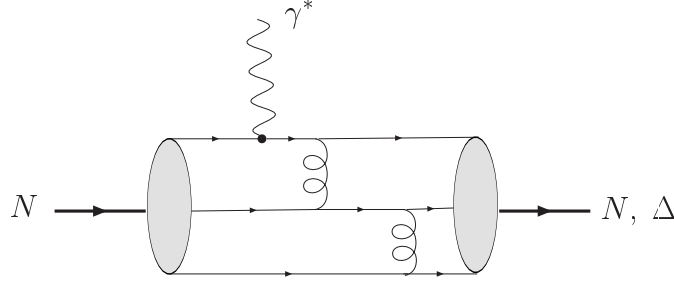


Fig. 25. Perturbative QCD picture for the nucleon elastic and $N \rightarrow \Delta$ transition electromagnetic form factors. The highly virtual photon resolves the leading three-quark Fock states of N and Δ , described by a distribution amplitude. The large momentum is transferred between the quarks through two successive gluon exchanges (only one of several possible lowest-order diagrams is shown).

$$E^q(x, \mathbf{b}_\perp) = \frac{\kappa_q}{N_q} (1-x)^{\eta_q} q_v(x) \frac{e^{-\mathbf{b}_\perp^2 / [-4\alpha'(1-x) \ln x]}}{4\pi [-\alpha'(1-x) \ln x]}. \quad (2.73)$$

Using the large N_c relation Eq. (2.58) we can then express the impact parameter version of the magnetic GPD H_M as:

$$H_M(x, \mathbf{b}_\perp) = 2 \frac{G_M^*(0)}{\kappa_V} \{ E^u(x, \mathbf{b}_\perp) - E^d(x, \mathbf{b}_\perp) \}. \quad (2.74)$$

In Fig. 24, we display the impact parameter magnetic GPD $H_M(x, \mathbf{b}_\perp)$ using the Regge parametrization R2 of Eq. (2.73) for $E^q(x, \mathbf{b}_\perp)$. It is clearly seen from this image that for large values of x , the quark distributions are concentrated at small values of \mathbf{b}_\perp , reflecting the distribution of valence quarks in the core of the N and Δ . On the other hand, at small values of x , the distribution in transverse position extends much further out.

2.8 The $\gamma^* N \Delta$ transition in perturbative QCD (p QCD)

2.8.1 p QCD predictions for helicity amplitudes and form factors

The electro-excitation of the Δ provides a famous test for perturbative QCD, where scaling and selection rules for dominant helicity amplitudes were derived and are expected to be valid at sufficiently high momentum transfers Q^2 [146]. A photon of sufficient high virtuality will see a nucleon (or Δ) consisting of three massless quarks moving collinear with the nucleon. When measuring an elastic nucleon form factor or a $N \rightarrow \Delta$ transition form factor, the final state consists again of three massless collinear quarks. In order for this (unlikely process) to happen, the large momentum of the virtual photon has to be transferred among the three quarks through two hard gluon exchanges as illustrated in Fig. 25. This hard scattering mechanism is generated by valence quark configurations with small transverse size and finite light cone momentum fractions of the total hadron momentum carried by each valence quark. The hard amplitude can be written in a factorized form [147–149,146], as a product of a perturbatively calculable hard

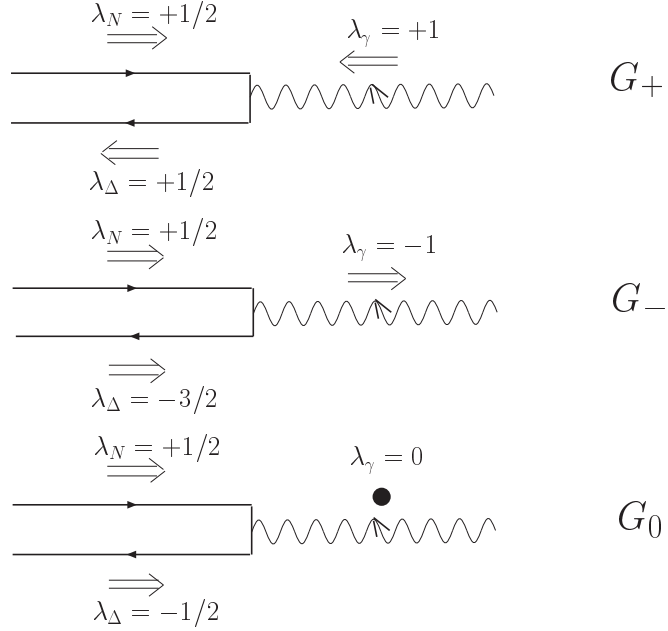


Fig. 26. $\gamma^* N \rightarrow \Delta$ helicity amplitudes in the Breit frame, where N , Δ , and γ^* momenta are collinear with the N momentum, and where the N and Δ three-momenta have the same magnitude but opposite sign. The γ , N , and Δ helicities (λ_γ , λ_N , and λ_Δ respectively) are indicated on the figure. The corresponding helicity form factors in the notation of Ref. [150] are indicated on the right.

scattering amplitude and two distribution amplitudes describing how the large longitudinal momentum of the initial and final hadrons is shared between their constituents. Because each gluon in such hard scattering process carries a virtuality proportional to Q^2 , this leads to the pQCD prediction that the helicity conserving nucleon Dirac form factor F_1 should fall as $1/Q^4$ (modulo $\ln Q^2$ factors) at sufficiently high Q^2 . Processes such as in Fig. 25, where the interactions among the quarks proceed via gluon or photon exchange, both of which are vector interactions, conserve the quark helicity in the limit when the quark masses or off-shell effects can be neglected. In contrast to the helicity conserving form factor F_1 , the nucleon Pauli form factor F_2 involves a helicity flip between the initial and final nucleons. Hence it requires one helicity flip at the quark level, which is suppressed at large Q^2 . Therefore, for collinear quarks, i.e. moving in a light-cone wave function state with orbital angular momentum projection $l_z = 0$ (along the direction of the fast moving hadron), the asymptotic prediction for F_2 leads to a $1/Q^6$ fall-off at high Q^2 .

To derive the analogous relations for the $\gamma^* N \Delta$ transition form factors, it is most convenient to work in a Breit frame, in which the photon, N , and Δ momenta are collinear with the incoming N . The outgoing Δ momentum has opposite direction but the same magnitude three-momentum. In this way, three independent $N \rightarrow \Delta$ helicity form factors were introduced in Ref. [150] as illustrated in Fig. 26. They are defined as (for $m = +, -, 0$):

$$G_m \equiv \frac{1}{2M_N} \langle \Delta, \lambda_\Delta = \lambda_\gamma - \frac{1}{2} | \epsilon_\mu^{(m)} \cdot J^\mu | N, \lambda_N = +\frac{1}{2} \rangle, \quad (2.75)$$

where J^μ is the electromagnetic current operator, and the factor $1/(2M_N)$ is chosen to make G_m dimensionless. The γ , N , and Δ helicities are denoted by λ_γ , λ_N , and λ_Δ respectively. The transverse polarization vectors (for a photon moving in the z -direction) are $\epsilon^\pm = (0, \mp 1, -i, 0)/\sqrt{2}$, and the longitudinal polarization vector satisfies $\epsilon_\mu^{(0)} \cdot \epsilon^{(0)\mu} = 1$, $\epsilon_\mu^{(0)} \cdot \epsilon^{(\pm)\mu} = 0$, and $\epsilon_\mu^{(0)} \cdot q^\mu = 0$. One can express the $N \rightarrow \Delta$ helicity form factors G_+ , G_- , and G_0 in terms of the Jones-Scadron form factors G_M^* , G_E^* , and G_C^* as:

$$\begin{aligned} G_- &\equiv -\frac{\sqrt{3}}{2\sqrt{2}} \frac{Q_- (M_\Delta + M_N)}{2M_N^2} \{G_M^* + G_E^*\}, \\ G_+ &\equiv \frac{1}{2\sqrt{2}} \frac{Q_- (M_\Delta + M_N)}{2M_N^2} \{G_M^* - 3G_E^*\}, \\ G_0 &\equiv \frac{1}{2} \frac{Q_- (M_\Delta + M_N)}{2M_N^2} \frac{Q}{M_\Delta} \{-G_C^*\}. \end{aligned} \quad (2.76)$$

Using the hadron helicity-conserving property of QCD at high Q^2 , it is then easy to derive the asymptotic behavior of the $\gamma^* N \Delta$ transition form factors. Since G_+ is the only helicity amplitude with the same helicity between initial N and final Δ , it will be the leading amplitude. At large Q^2 , two-gluon exchange between collinear quarks yields a $1/Q^3$ behavior for G_+ [150]. The amplitudes G_0 and G_- , requiring helicity flips, are asymptotically zero relative to G_+ . For each helicity flip, one expects one additional (m/Q) power suppression in pQCD, where m is some quark mass scale. In this way, G_0 (G_-), requiring one (two) helicity flips, yield a large Q^2 behavior as $1/Q^4$ ($1/Q^5$) respectively [150].

Using the relations of Eq. (2.76), one can also derive the large Q^2 behavior of the Jones Scadron form factors as well as the R_{EM} and R_{SM} ratios. For the magnetic $\gamma^* N \Delta$ form factor G_M^* , one obtains a $1/Q^4$ behavior for $Q^2 \rightarrow \infty$. Furthermore, because G_- is asymptotically zero relative to G_+ , Eq. (2.76) yields $G_E^* \rightarrow -G_M^*$ in the limit $Q^2 \rightarrow \infty$. This yields equivalently $R_{EM} \rightarrow +1$ for $Q^2 \rightarrow \infty$. Likewise, the $1/Q^4$ behavior for G_0 yields $R_{SM} \rightarrow \text{constant}$ for $Q^2 \rightarrow \infty$ [150].

We can test how well the above baryon form factor pQCD scaling predictions are satisfied at the available momentum transfers, see Fig. 27. One firstly sees from Fig. 27 that the proton Dirac form factor, which has been measured up to about 30 GeV 2 , displays an approximate $1/Q^4$ scaling above 10 GeV 2 . For the proton ratio F_2^p/F_1^p , the data up to 5.6 GeV 2 show no sign of a $1/Q^2$ behavior as predicted by pQCD. Instead, the data show that the ratio F_2^p/F_1^p falls less fast than $1/Q^2$ with increasing Q^2 . In Ref. [155], the assumption of quarks moving collinearly, underlying the pQCD prediction, has been investigated. It has been shown in Ref. [155] that by including components in the nucleon light-cone wave functions with quark orbital angular momentum projection $l_z = 1$, one obtains the behavior $F_2/F_1 \rightarrow \ln^2(Q^2/\Lambda^2)/Q^2$ at large Q^2 , with Λ a non-perturbative mass scale. Choosing Λ in the range 0.2 – 0.4 GeV, Ref. [155] found that the data for F_2^p/F_1^p support such double-logarithmic enhancement. A same analysis, including states of orbital angular momentum projection $l_z = 1$ in the N or Δ light-cone wave functions, which find their physical origin in the transverse momentum of the quarks in the N and Δ , was also performed for the $\gamma^* N \Delta$ Coulomb transition form factor G_C^* [156]. It was shown in Ref. [156] that due to the orbital motion of the partons, R_{SM} acquires a double-

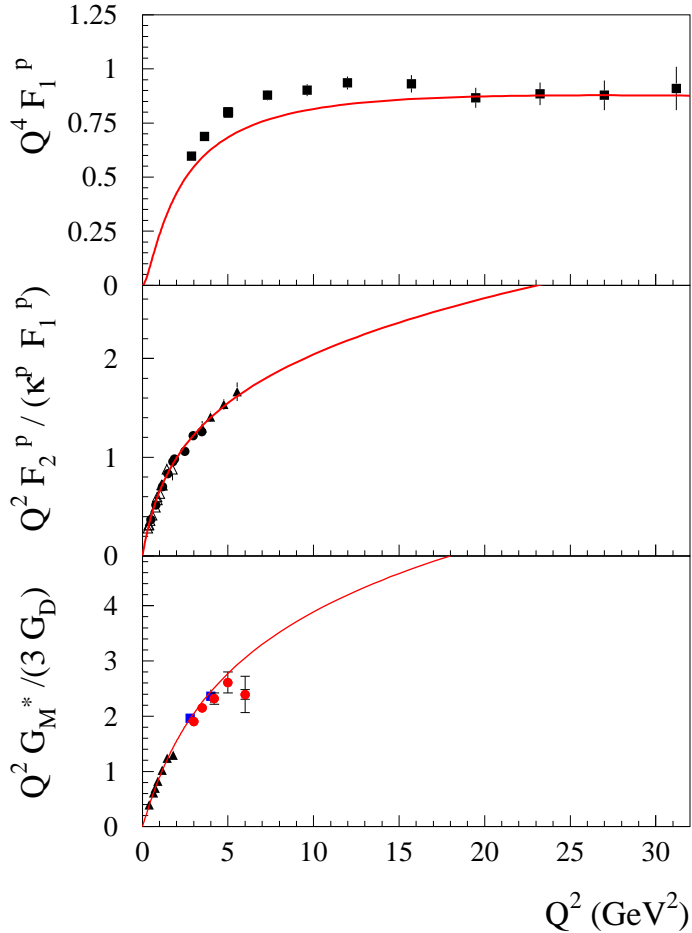


Fig. 27. Test of baryon form factor scaling predictions. Top panel : proton Dirac form factor multiplied by Q^4 ; middle panel : ratio of Pauli to Dirac proton form factors multiplied by Q^2 ; lower panel : ratio of the $N \rightarrow \Delta$ magnetic transition (Jones-Scadron) form factor G_M^* multiplied by Q^2 to the dipole form factor G_D . The data for F_1^p are from [151] (solid squares). Data for the ratio F_2^p/F_1^p are from [152] (solid circles), [153] (open triangles), and [154] (solid triangles). Data for G_M^* as in Fig. 22. The red curve is the calculation based on the three parameter modified Regge GPD parametrization $R2$ of Ref. [128].

logarithmic correction $\ln^2(Q^2/\Lambda^2)$ at large Q^2 compared with the standard scaling analysis, according to which $R_{SM} \rightarrow \text{constant}$ for $Q^2 \rightarrow \infty$. The arguments of Refs. [155,156] still rely on pQCD and it remains to be seen by forthcoming data at higher Q^2 if this prediction already sets in in the few GeV^2 region.

The test of the scaling behavior of the magnetic $\gamma^* N \Delta$ form factor G_M^* is also shown on Fig. 27. As pQCD predicts a $1/Q^4$ asymptotic scaling behavior, the ratio G_M^*/G_D (with G_D the dipole form factor) should approach a constant. The data for G_M^* up to about 6 GeV^2 again do not support this scaling behavior. One sees instead from Fig. 27 that the data for G_M^* seem to support a similar Q^2 behavior as for F_2 . The pQCD prediction for the R_{EM} ratio which should approach $+100\%$ at high Q^2 also fails dramatically. The R_{EM} ratio is measured to be minus a few percent out to $Q^2 \simeq 6 \text{ GeV}^2$ [131], with no clear indication of a zero crossing. Also the

R_{SM} ratio which has also been measured up to $Q^2 \simeq 6 \text{ GeV}^2$ [131], does not seem to settle to a constant at large Q^2 .

2.8.2 The road to “asymptopia”

Although at high enough Q^2 , the pQCD scaling predictions should set in, the available data for the nucleon and $N \rightarrow \Delta$ electromagnetic form factors show that one is still far away from this regime. This has been further investigated in several theoretical approaches.

In Refs.[157,158], it has been argued that the above described hard scattering mechanism is suppressed at accessible momentum transfers relative to the Feynman mechanism [159], also called soft mechanism. The soft mechanism involves only one active quark, and the form factor is obtained as an overlap of initial and final hadron wave functions. The hard scattering mechanism on the other hand, involving three active quarks, requires the exchange of two gluons each of which brings in a suppression factor $\alpha_s/\pi \sim 0.1$. One therefore expects the hard scattering mechanism for F_1^p or G_M^* to be numerically suppressed by a factor 1/100 compared to the soft term. Even though the soft mechanism is suppressed asymptotically by a power of $1/Q^2$ relative to the hard scattering mechanism, it may well dominate at accessible values of Q^2 . In Refs.[157,158], the soft contribution to the $\gamma^* N \Delta$ form factors has been estimated using a model based on local quark-hadron duality. In this approach it was found that the $\gamma N \Delta$ transition is dominated by the magnetic form factor G_M^* , while the electric quadrupole G_E^* and Coulomb quadrupole G_C^* form factors are small at accessible momentum transfers, in qualitative agreement with the data.

In a more recent work [160], the soft contribution to the $\gamma^* N \Delta$ form factors was evaluated within the light-cone sum rule approach. In this approach, one analyzes a matrix element, in which the Δ is represented by an interpolating field η_μ of Ref. [161]. More specifically, one computes the correlation function of this interpolating field and the electromagnetic current operator J_ν given by the matrix element:

$$T_{\mu\nu}(P, q) = i \int d^4y e^{iq \cdot y} \langle 0 | T\{\eta_\mu(0) J_\nu(y)\} | N(P) \rangle, \quad (2.77)$$

between the vacuum and a single-nucleon state $|N(P)\rangle$. It was found in Ref. [160] that the sum rule for G_M^* is dominated by contributions of subleading twist-4. They involve quark configurations with a minus light-cone projection of one of the quark field operators, which can be interpreted as the importance of orbital angular momentum. The calculations of Ref. [160] are in agreement with the experimental observations that the R_{EM} and R_{SM} ratios are small, although in the region of low $Q^2 < 2 \text{ GeV}^2$, the result for G_M^* is a factor of two below the data.

In Sect. 2.7, we have shown that the nucleon elastic and $N \rightarrow \Delta$ transition form factors can be obtained from model independent GPD sum rules. These GPDs, represented by the lower blob in Fig. 21, are non-perturbative objects which include higher Fock components in the N and Δ wave functions. One can use a GPD parametrization to provide an estimate of the soft contributions, and expects this non-perturbative approach to be relevant in the low and intermediate Q^2 region for the form factors. This is shown in Fig. 27 (solid curves) from which one sees that the GPD Regge parametrization R2, discussed in Sect. 2.7.2 is able to explain at the same

time an approximate $1/Q^4$ behavior for F_1^p and a behavior for F_2^p/F_1^p which falls less steep than $1/Q^2$. For G_M^* , one sees from Fig. 27 that the GPD sum rule evaluation based on the large N_c relation of Eq. (2.59) is supported by the available data up to about 6 GeV^2 . Forthcoming experiments at the Jefferson Lab 12 GeV facility will extend the data for F_2^p/F_1^p and G_M^* to Q^2 values around 15 GeV^2 . Such measurements will allow to quantify in detail the higher Fock components in the N and Δ wave functions versus the simple three-quark Fock component, and pave the road to “asymptopia”.

3 Phenomenology of pion photo- and electroproduction

We will first review the dynamical model calculations which have been carried out by various groups and then turn to MAID, which is a variation of the effective Lagrangian method and has been very successful in describing the data. Lastly, we give a brief description on the current status of the dispersion-relation approach.

3.1 Introductory remarks

The electromagnetic production of pions is the main source of information about the electromagnetic properties of nucleon resonances, such as the $\Delta(1232)$. Certainly the experimental measurements alone are not enough to obtain a quantitative insight, a theoretical interpretation of the resonance-excitation mechanism is necessary to extract, *e.g.*, the strength of the $\gamma N \Delta$ transition. One can distinguish three major theoretical tools which were developed in the last millennium for this purpose:

- (i) *dispersion theory*, first proposed by Chew *et al.* [162] for photoproduction, and by Fubini *et al.* [163] for electroproduction, has been successfully applied in the first multipole analyses [164,165] as well as in the modern ones [166–168]. The dispersion approach is based on general principles, such unitarity, analyticity, crossing symmetry, as well as relies on a phenomenological input from the πN scattering. A more detailed description of this approach is given in Subsect. 3.4.
- (ii) *effective Lagrangian approach*, where both πN scattering and pion production are calculated based on the same effective Lagrangian in terms of hadron fields. First attempts to develop this picture were made by Peccei [169], Olsson and Osypowsky [170]. More recently, this approach was extensively developed at RPI [171], Madrid [172], Gent [173], KVI [174], and Giessen [175]. It is important to emphasize that in this approach the effective Lagrangian is used only at tree level (nowadays usually by a unitarization procedure). This can be considered as a weakness of this approach since, as is now known from χ EFT calculations, the chiral loop corrections give rise to interesting and appreciable effects.
- (iii) *dynamical models*, where the tree-level effective Lagrangian is treated as a hadron-exchange potential of a quantum-mechanical scattering problem. First such models were developed by Tanabe and Ohta [176] and Yang [177]. Many more were developed over the past two decades, see it *e.g.*, [178,179,14,180,91,181,182]. Three of these will be detailed below, where also the pros and cons of this approach in general will be addressed.

In addition, the phenomenological multipole solutions SAID [183] and MAID [184] have proven to be useful in interpreting the experiment, as well as in obtaining the empirical information about individual amplitudes. Without these tools, it is extremely difficult to extract the various amplitudes from experiment. In the rest of this subsection we discuss how it can be done in principle.

3.1.1 Measurement of pion photoproduction amplitudes

Naively, without considering the discrete ambiguities, one would conclude that seven measurements are needed to determine the four pion photoproduction helicity amplitudes of H'_i 's, ($i = 1, 4$) (four magnitudes plus three phases) up to an arbitrary overall phase. The discrete ambiguities arise because the observables are all bilinear product of helicity amplitudes. To determine the amplitudes, mathematically speaking, amounts to solve a set of nonlinear equations. The solutions are not necessarily unique and the ambiguities could arise if the number of observables measured are not enough. According to Ref. [185], nine measurements are required if all amplitudes would be determined without discrete ambiguities. Careful analysis by Chiang and Tabakin [186], however, reveals that only eight measurements would be sufficient to resolve all ambiguities, namely, four appropriately chosen double-spin observables, along with three single-spin observables and the unpolarized differential cross section.

In pion photoproduction, there are 15 polarization observables (for detail see [10]). Among them three are three single polarization observables, namely, the polarized photon asymmetry $\Sigma(\theta)$, polarized target asymmetry $T(\theta)$ and the recoil nucleon polarization $P(\theta)$. The rest are the 12 double polarization observables which describe reactions with polarized beam-polarized target, polarized beam-recoil nucleon polarization, and polarized target-recoil nucleon polarization. They are commonly denoted as $E, F, G, H, Cx', Cz', Ox', Oz', Tx', Tz', Lx'$, and Lz' . For definition see, e.g., Refs. [185,187].

We illustrate here only the differential cross section and one of the single polarization observables, the polarized photon asymmetry, which has been extensively investigated experimentally in the study of $E2/M1$ mixing ratio for the $N \rightarrow \Delta$ transition.

The unpolarized differential cross section for the pion photoproduction can be expressed in terms of the helicity amplitudes H_i 's (see Appendix) as follows:

$$\frac{d\sigma}{d\Omega} = \frac{|\mathbf{k}|}{2|\mathbf{q}|} \sum_{i=1}^4 |H_i|^2. \quad (3.1)$$

The *polarized photon asymmetry* is defined as,

$$\Sigma = \frac{d\sigma_{\perp} - d\sigma_{\parallel}}{d\sigma_{\perp} + d\sigma_{\parallel}}, \quad (3.2)$$

where $d\sigma_{\perp}$ ($d\sigma_{\parallel}$) is the differential cross section for a linearly polarized photon with polarization vector perpendicular (parallel) to the reaction plane. In terms of the helicity amplitudes, $d\sigma_{\perp}$ ($d\sigma_{\parallel}$) are given as

$$\begin{aligned} \frac{d\sigma_{\perp}}{d\Omega} &= \frac{|\mathbf{k}|}{2|\mathbf{q}|} (|H_1 + H_4|^2 + |H_2 - H_3|^2), \\ \frac{d\sigma_{\parallel}}{d\Omega} &= \frac{|\mathbf{k}|}{2|\mathbf{q}|} (|H_1 - H_4|^2 + |H_2 + H_3|^2). \end{aligned} \quad (3.3)$$

The expressions given above contain contributions from all partial waves. However, in the case of π^0 photoproduction in the $\Delta(1232)$ resonance region where most of the current experimental information are derived from, the dominant contributions come from s - and p -wave multipoles. Therefore, a truncated multipole approximation is often used in the analysis of the data for this reaction and only E_{0+} , E_{1+} , M_{1+} and M_{1-} multipoles are kept. Such an approximation greatly simplifies the analysis and allows one to express the differential cross section in the following simple form :

$$\frac{d\sigma_j}{d\Omega} = \frac{k}{q} [A_j + B_j \cos \theta + C_j \cos^2 \theta] \quad (3.4)$$

where the coefficients A_j , B_j and C_j are bilinear functions of the s - and p - wave multipoles and j indicates the parallel (\parallel), perpendicular (\perp), and unpolarized (0) components. These coefficients are quadratic functions of the s - and p -wave amplitudes. The parametrization Eq. (3.4) can be used separately for $d\sigma_{\perp}$ and $d\sigma_{\parallel}$ in the analysis of the photon asymmetry. In Refs. [22,24], it was found that $d\sigma_{\parallel}$ is very sensitive to the small E_{1+} multipole due to the interference with large M_{1+} . We can see this from the following expressions :

$$\begin{aligned} A_{\parallel} &= |E_{0+}|^2 + |3E_{1+} + M_{1+} - M_{1-}|^2, \\ B_{\parallel} &= 2\text{Re}[E_{0+}(3E_{1+} + M_{1+} - M_{1-})^*], \\ C_{\parallel} &= 12\text{Re}[E_{1+}(M_{1+} - M_{1-})^*]. \end{aligned} \quad (3.5)$$

In Ref. [22,24] this sensitivity was used for the experimental determination of the R_{EM} ratio of Eq. (2.14), because at the Δ resonance position one has,

$$R_{EM} \simeq \frac{1}{12} \frac{C_{\parallel}}{A_{\parallel}}. \quad (3.6)$$

3.1.2 Measurement of pion electroproduction amplitudes

Consider now the pion electroproduction¹⁵ which kinematically is illustrated in Fig. 28. In this diagram the four-momenta of the initial and final electron are defined as, $l_i = (e_i, \mathbf{q}_{iL})$, $l_f = (e_f, \mathbf{q}_{fL})$, while the momenta of the other particles are given as,

- in the *lab* frame: $q = (\omega_{\mathbf{q}_L}, \mathbf{q}_L)$, $p = (M_N, \mathbf{0})$, $p' = (p'_{0L}, \mathbf{p}'_L)$, and $k = (\omega_{\mathbf{k}_L}, \mathbf{k}_L)$;
- in the center-of-mass (*c.m.*) of the πN system: $q = (\omega_{\mathbf{q}}, \mathbf{q})$, $k = (\omega_{\mathbf{k}}, \mathbf{k})$, $p = (E, -\mathbf{q})$, and $p' = (E', -\mathbf{k})$.

More kinematical details can be found in the Appendix.

¹⁵ Until Sect. 6 we assume that the electroproduction process proceeds via the one-photon exchange. In this case, electroproduction differs from photoproduction only in that the incoming photon is now virtual,

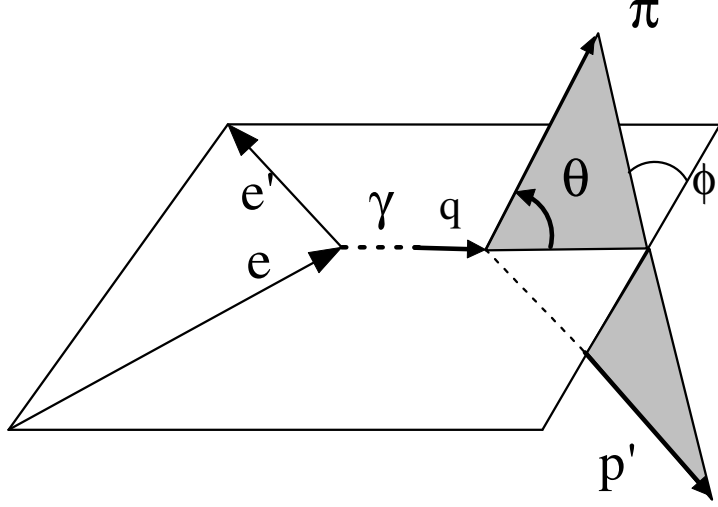


Fig. 28. Kinematics for pion the electroproduction on the nucleon.

The 5-fold differential cross section, in the case of the unpolarized target and beam, can be written as:

$$\frac{d\sigma}{d\Omega_f d\epsilon_f d\Omega_\pi} = \Gamma \frac{d\sigma_v}{d\Omega_\pi}, \quad (3.7)$$

which defines the virtual photon cross section,

$$\begin{aligned} \frac{d\sigma_v}{d\Omega_\pi} = & \frac{d\sigma_T}{d\Omega_\pi} + \varepsilon \frac{d\sigma_L}{d\Omega_\pi} + \varepsilon \frac{d\sigma_{TT}}{d\Omega_\pi} \cos 2\phi_\pi + \sqrt{2\varepsilon(1+\varepsilon)} \frac{d\sigma_{TL}}{d\Omega_\pi} \cos \phi_\pi \\ & + h \sqrt{2\varepsilon(1-\varepsilon)} \frac{d\sigma_{TL'}}{d\Omega_\pi} \sin \phi_\pi, \end{aligned} \quad (3.8)$$

where

$$\varepsilon = \left[1 + 2 \frac{\mathbf{q}_L^2}{Q^2} \tan^2 \frac{\theta_e}{2} \right]^{-1}, \quad \Gamma = \frac{\alpha_{em}}{2\pi^2} \frac{e_f}{e_i} \frac{K}{Q^2} \frac{1}{1-\varepsilon}. \quad (3.9)$$

$\varepsilon, h, \theta_e, \mathbf{q}_L, e_i$, and e_f denote the degree of transverse polarization of the virtual photon, the helicity of the incoming electron, the angle between the incident and final electrons, the three-momentum of the virtual photon, energy of the initial and final electron in the *lab* frame, respectively. Γ is the flux of the virtual photon and $K = (s - M_N^2)/2M_N$, often called the ‘equivalent photon energy’.

In Eq. (3.7), e_f, Ω_f denote the energy and solid-angle of the scattered electron in the laboratory, respectively, and ϕ is the tilt angle between the electron scattering plane and the reaction plane, as shown in Fig. 28. $d\Omega_\pi$ is the pion solid-angle differential measured in the *c.m.* frame of the final pion and nucleon. Since Γ can be interpreted as the number of virtual photons per electron scattered into $d\epsilon_f$ and $d\Omega_f$, the quantity on the r.h.s. of Eq. (3.7), $d\sigma_v/d\Omega_\pi$ then represents the *c.m.* differential cross section for pion photoproduction by virtual photons.

Also let us note that Eq. (3.8) differs slightly from Eq. (20) of Ref. [10] often used in the

and hence in additional to transverse polarizations can have the longitudinal or scalar ones.

literature, where the degree of longitudinal polarization of the virtual photon $\varepsilon_L = (Q^2/\omega_{\mathbf{q}_L}^2)\varepsilon$ appears in some of the coefficients in Eq. (3.8). The difference can be viewed as a different definition for the longitudinal cross sections which simply modifies their relations with the nuclear response functions [188] by a kinematical constant, as will be specified below.

The first two terms in Eq. (3.8) are the transverse (T) and longitudinal (L) cross sections. They do not depend on the pion azimuthal angle ϕ . The fourth and fifth terms describe the transverse-longitudinal interferences (TL and TL'). They contain an explicit factor $\sin \theta$ [189] and therefore vanish along the axis of the momentum transfer. The same is true for the third term, a transverse-transverse interference (TT), proportional to $\sin^2 \Theta$.

In the pion-nucleon *c.m.* frame, it is useful to express these cross sections in terms of five response functions which depend only on three independent variables, i.e. $R = R(Q^2, W, \Theta)$. The corresponding expressions are the following

$$\begin{aligned} \frac{d\sigma_T}{d\Omega_\pi} &= \frac{|\mathbf{k}|}{q_W} R_T, & \frac{d\sigma_{TT}}{d\Omega_\pi} &= \frac{|\mathbf{k}|}{q_W} R_{TT}, \\ \frac{d\sigma_L}{d\Omega_\pi} &= \frac{|\mathbf{k}|}{q_W} \frac{Q^2}{\omega_{\mathbf{q}}^2} R_L, & \frac{d\sigma_{TL}}{d\Omega_\pi} &= \frac{|\mathbf{k}|}{q_W} \frac{Q}{\omega_{\mathbf{q}}} R_{TL}, & \frac{d\sigma_{TL'}}{d\Omega_\pi} &= \frac{|\mathbf{k}|}{q_W} \frac{Q}{\omega_{\mathbf{q}}} R_{TL'}. \end{aligned} \quad (3.10)$$

with $q_W = (W^2 - M_N^2)/2W$ the "photon equivalent *c.m.* energy", and $\omega_{\mathbf{q}} = (W^2 - Q^2 - M_N^2)/2W$ the virtual photon energy in the *c.m.* frame. The five response functions may be expressed in terms of the six independent CGLN amplitudes F_1, \dots, F_6 . Explicit expressions can be found in Ref. [10]. In terms of the helicity amplitudes we can get simple expressions for the response functions:

$$\begin{aligned} R_T &= \frac{1}{2}(|H_1|^2 + |H_2|^2 + |H_3|^2 + |H_4|^2), \\ R_L &= (|H_5|^2 + |H_6|^2), \\ R_{TT} &= \text{Re}(H_3 H_2^* - H_4 H_1^*), \\ R_{TL} &= \frac{1}{\sqrt{2}} \text{Re}[H_5^*(H_1 - H_4) + H_6^*(H_2 + H_3)], \\ R_{TL'} &= -\frac{1}{\sqrt{2}} \text{Im}[(H_1 - H_4)H_5^* + (H_2 + H_3)H_6^*]. \end{aligned} \quad (3.11)$$

Many pion electroproduction experiments in the Δ resonance region have been performed to study the electromagnetic $N \rightarrow \Delta$ transition. Most of them are on π^0 production reaction, with either unpolarized electron beam ($h = 0$) or longitudinal electron beam ($h \pm 1$). By measuring coincident cross sections at different azimuthal angles ϕ ($\phi = 0$, in plane and $\phi \neq 0$ out of plane) and different polar angles θ , it has been possible to obtain data on $\sigma_{TT}, \sigma_{LT}, \sigma_{LT'}$ and unpolarized cross section $\sigma_0 = \sigma_T + \varepsilon \sigma_L$. Values for the M_{1+} , R_{EM} , and R_{SM} have been inferred from the models which provide an overall agreement with the data. This will be discussed in more detail in Sect. 5.

We mention in passing that, again naively, without considering the discrete ambiguities, one would expect that eleven measurements would be required to determine the six pion electroproduction helicity amplitudes of H'_i s, ($i = 1, \dots, 6$) (six magnitudes plus five phases) up to

an arbitrary overall phase. However, in contrast to the case of photoproduction, the question of how many measurements are needed to determine all amplitudes without discrete ambiguities has not been properly addressed yet.

3.2 Dynamical models

Here we turn to the discussion of the dynamical models and as an example consider three of the more recent ones: the model of Sato and Lee (SL) [14], DMT (Dubna-Mainz-Taipei) model [91], and the DUO (dynamical Utrecht-Ohio) model [182].

3.2.1 General framework: unitarity, relativity, gauge invariance

The dynamical model formulation for the pion electromagnetic production reaction starts from the following scattering equation

$$\begin{pmatrix} t_{\pi\pi} & t_{\pi\gamma} \\ t_{\gamma\pi} & t_{\gamma\gamma} \end{pmatrix} = \begin{pmatrix} v_{\pi\pi} & v_{\pi\gamma} \\ v_{\gamma\pi} & v_{\gamma\gamma} \end{pmatrix} + \begin{pmatrix} v_{\pi\pi} & v_{\pi\gamma} \\ v_{\gamma\pi} & v_{\gamma\gamma} \end{pmatrix} \begin{pmatrix} G_\pi & 0 \\ 0 & G_\gamma \end{pmatrix} \begin{pmatrix} t_{\pi\pi} & t_{\pi\gamma} \\ t_{\gamma\pi} & t_{\gamma\gamma} \end{pmatrix}, \quad (3.12)$$

for the following four processes

$$\begin{aligned} \pi N \rightarrow \pi N, & \quad \pi N \rightarrow \gamma^* N, \\ \gamma^* N \rightarrow \pi N, & \quad \gamma^* N \rightarrow \gamma^* N, \end{aligned} \quad (3.13)$$

where the transition matrices t 's are related to the elements of the T -matrix by a kinematical factor and v 's are the driving potentials of the πN scattering ($\pi\pi$), pion electromagnetic absorption ($\pi\gamma$), production ($\gamma\pi$), and the nucleon Compton scattering ($\gamma\gamma$). G_π and G_γ are, respectively, the pion-nucleon and photon-nucleon two-particle propagators.

To first order in e , the transition matrix element for $\gamma^* N \rightarrow \pi N$, in a dynamical model is then given as

$$t_{\gamma\pi} = v_{\gamma\pi} + v_{\gamma\pi} G_0 t_{\pi N}, \quad (3.14)$$

with

$$t_{\pi N} = v_{\pi N} + v_{\pi N} G_0 t_{\pi N}, \quad (3.15)$$

where we have replaced the subscript $\pi\pi$ used in (3.12) by πN and introduced $G_0 \equiv G_\pi$ which will be used hereafter. In this approximation, only the integral equation Eq. (3.15) for πN scattering has to be solved and the rest is determined in a one-loop calculation.

In a Bethe-Salpeter (BS) formulation, Eqs. (3.14) and (3.15) are four-dimensional equations and the driving terms v 's represent the sums of all two-particle irreducible amplitudes. Two

approximations are commonly made to simplify the solution of the BS equation [190]. The first is to approximate the driving potentials by the tree diagrams of an effective chiral Lagrangian and the other is to replace G_0 by a propagator g_0 which would reduce the dimensionality of the integral equations from four to three. g_0 is chosen to have an invariant form so that the covariance of the original equation is preserved. The reduction in the dimensionality is achieved with a δ -function in g_0 which imposes a constraint on the time component of the relative momentum variable, i.e., the relative energy. In addition, this new propagator must be chosen such that the resulting scattering amplitude has a correct elastic cut from the elastic threshold $(m_\pi + M_N)^2$ to ∞ in the complex s plane, as required by the unitarity condition.

It is well known for example, see Ref. [191], that the choice of g_0 is rather arbitrary and can be done in infinitely many different ways. In Ref. [190], a class of three dimensional equations of the following form,

$$\begin{aligned} \hat{G}_0(k; P) = & \frac{1}{(2\pi)^3} \int \frac{ds'}{s - s' + i\varepsilon} f(s, s') [\alpha(s, s') \not{P} + \not{k} + M_N] \\ & \times \delta^{(+)}([\eta_N(s') P' + k]^2 - m_N^2) \delta^{(+)}([\eta_\pi(s') P' - k]^2 - m_\pi^2). \end{aligned} \quad (3.16)$$

were employed to investigate the πN scattering. In Eq. (3.16), $P' = \sqrt{\frac{s'}{s}} P$ defines the "off-shellness" of the intermediate states. The superscript (+) associated with δ -functions means that only the positive energy part is kept in defining the nucleon propagator. $k = \eta_\pi(s)p - \eta_N(s)q$ is the relative momentum k with η 's any function of s constrained by the condition $\eta_\pi(s) + \eta_N(s) = 1$. To have a correct πN elastic cut, the arbitrary functions $f(s, s')$ and $\alpha(s, s')$ must satisfy the conditions

$$f(s, s) = 1, \quad \alpha(s, s) = \eta_N(s). \quad (3.17)$$

It is easy to verify that for $(m_\pi + M_N)^2 \leq s \leq \infty$, Eqs. (3.16) and (3.17) give the correct discontinuity of the propagator \hat{G}_0

$$\begin{aligned} Disc[\hat{G}_0(k; P)] = & \frac{-i}{(2\pi)^2} (\eta_N(s) \not{P} + \not{k} + M_N) \delta^{(+)}([\eta_N(s) P + k]^2 - M_N^2) \\ & \times \delta^{(+)}([\eta_\pi(s) P - k]^2 - m_\pi^2). \end{aligned} \quad (3.18)$$

The class of propagators given in Eq. (3.16) has the feature that both particles in the intermediate states are put equally off-mass-shell such that the relative energy dependence in the interaction is removed. Several three dimensional formulations developed in the literature, including those developed by Blankenbecler and Sugar [192], Kadyshevsky [193], Thompson [194], and Cooper and Jennings [195], can be derived from using Eqs. (3.16) and (3.17) and were studied in detail in [196] for πN scattering. All of these schemes set $\eta_N(s) = \varepsilon_N(s)/(\varepsilon_N(s) + \varepsilon_\pi(s))$ and $\eta_\pi(s) = \varepsilon_\pi(s)/(\varepsilon_N(s) + \varepsilon_\pi(s))$, where $\varepsilon_N(s) = (s + M_N^2 - m_\pi^2)/2\sqrt{s}$ and $\varepsilon_\pi(s) = (s - M_N^2 + m_\pi^2)/2\sqrt{s}$ are the center of mass (*c.m.*) energies of nucleon and pion, respectively. The resultant πN interaction obtained with Cooper-Jennings reduction scheme has been extensively used in the DMT model calculation for the pion electromagnetic production reactions.

The functions $\alpha(s, s')$ and $f(s, s')$ specific to the Cooper-Jennings reduction are

$$\alpha(s, s') = \eta_N(s), \quad (3.19)$$

$$f(s, s') = \frac{4\sqrt{ss'}\varepsilon_N(s')\varepsilon_\pi(s')}{ss' - (m_N^2 - m_\pi^2)^2}. \quad (3.20)$$

The resulting three-dimensional scattering equations then take the Lipmann-Schwinger form

$$t_{\gamma\pi} = v_{\gamma\pi} + v_{\gamma\pi}g_0t_{\pi N}, \quad t_{\pi N} = v_{\pi N} + v_{\pi N}g_0t_{\pi N}. \quad (3.21)$$

One of the most important features of the dynamical model approach is that it provides a unified theoretical framework to describe πN scattering and pion production in a consistent way. In most cases, $v_{\pi N}$ is derived from a tree approximation to an effective chiral Lagrangian which involves field operators of the nucleon, Δ , pion, rho meson, and a fictitious scalar meson σ [190]. Pseudovector πNN coupling is used as it is consistent with the leading order of chiral perturbation theory. It leads to a driving term which includes the direct and crossed N and Δ terms, and the t -channel σ - and ρ -exchange terms.

Furthermore in the dynamical models, one needs to specify the $\gamma N \Delta$ vertex, shown in Fig. 1. It is described by Eq. (2.2) with g_M , g_E , and g_C , the magnetic dipole $M1$, electric quadrupole $E2$, and Coulomb quadrupole $C2$ excitation strength of the Δ , respectively. They are then only three new parameters in the dynamical model, besides those determined by the πN scattering and $V \rightarrow \pi\gamma$ reactions, to be determined from the electromagnetic pion production data.

Since multiple pion rescattering in the final state is treated explicitly, unitarity is inherent in Eq. (3.21). In fact, if we take

$$g_0 = \frac{1}{E - H_0 + i\varepsilon}, \quad (3.22)$$

with H_0 the free Hamiltonian of the pion-nucleon system, then a multipole decomposition of Eq. (3.21) gives [177]

$$t_{\gamma\pi}^\alpha(k_E, q; E + i\varepsilon) = e^{i\delta_\alpha} \cos \delta_\alpha \times \left[v_{\gamma\pi}^\alpha(k_E, q) + P \int_0^\infty dk' \frac{k'^2 R_{\pi N}^\alpha(k_E, k') v_{\gamma\pi}^\alpha(k', q)}{E - E_{\pi N}(k')} \right], \quad (3.23)$$

where δ_α and $R_{\pi N}^\alpha$ are the πN scattering phase shift and reaction matrix, in channel α , respectively; k_E is the pion on-shell momentum and $q = |\mathbf{q}|$ is the photon momentum. In the energy region where only two channels are open: πN elastic scattering and single pion photo- or electroproduction, $v_{\gamma\pi}$, $v_{\pi N}$ and the reaction matrix $R_{\pi N}$ are real numbers. In this case we see explicitly from Eq. (3.23) that the phase of the $t_{\gamma\pi}^\alpha$ is equal to the πN scattering phase in the corresponding channel, e.g.,

$$t_{\gamma\pi}^\alpha(k_E, q; E) = |t_{\gamma\pi}^\alpha(k_E, q; E)| e^{i\delta_\alpha(E)}. \quad (3.24)$$

This is the well known Fermi-Watson theorem [197]. This theorem, which is a consequence the unitarity of the S-matrix, and time-reversal invariance, imposes a phase condition on the individual multipole amplitudes below the two-pion production threshold. It simplifies the analysis of the pion photo- and electroproduction processes in the Δ resonance region connecting the real and imaginary parts of the reaction amplitudes.

Gauge invariance of the electromagnetic interaction requires the following current conservation condition,

$$t_{\gamma\pi}(\varepsilon \rightarrow q_\mu) = 0, \quad (3.25)$$

as $t_{\gamma\pi}$ is proportional to $T_{fi} = \varepsilon_\mu J^\mu$ of Eq. (A.3). The first term $v_{\gamma\pi}$ in $t_{\gamma\pi}$ of Eq. (3.21) clearly satisfies the current conservation condition of Eq. (3.25) for on-mass-shell incoming and outgoing particles since it is obtained from the tree diagrams of a Lagrangian resulting from gauging a chiral effective Lagrangian for πN scattering. However, there is a fundamental difficulty to impose the current conservation condition on the second term $t_{\gamma\pi}$ of Eq. (3.21), which represents the sum of the following ladder series,

$$v_{\gamma\pi} g_0 t_{\pi N} = v_{\gamma\pi} g_0 v_{\pi N} + v_{\gamma\pi} g_0 v_{\pi N} g_0 v_{\pi N} + \dots \quad (3.26)$$

It is well-known that the sum of a set of diagrams is gauge invariant if photon is hooked to every line which carries charge. Consequently, $v_{\gamma\pi} g_0 t_{\pi N}$ is not a gauge invariant quantity. It is inherent in the approximation scheme which leads to Eq. (3.21). There are many recipes proposed [198, 178, 91, 182] to make it to satisfy the current conservation condition of Eq. (3.25). However, they are all *ad hoc* in nature and hence not unique.

The dynamical model approach as summarized in Eq. (3.21) hence contains four theoretical ingredients. The first one is the choice of $v_{\gamma\pi}$. It is commonly chosen to consist of tree diagrams of a chiral effective Lagrangian [170], which include the Born terms in pseudoscalar coupling, contribution from t -channel (ρ, ω) vector meson exchanges, and s - and u -channel Δ -exchanges. Different dynamical calculations differ mostly in the ρNN and ωNN coupling constants used. The second ingredient concerns the choice of the three-dimensional propagator g_0 . Another input is the model chosen for $t_{\pi N}$ since experimental πN phase shifts constrain only the on-shell behavior while the physical pion production multipole amplitude $t_{\gamma\pi}$ depends on the half-off-shell matrix elements of $t_{\pi N}$. The off-shell πN rescattering effects have been shown [199] to play an important role to explain the threshold π^0 data. The last theoretical ingredient is the recipe employed to satisfy the current conservation condition of Eq. (3.25).

3.2.2 Sato-Lee model

The Sato-Lee (SL) model [14] made a strong effort to derive the driving terms of $v_{\gamma\pi}$ and $v_{\pi N}$ of Eq. (3.21) in a consistent manner.

SL started from a model Lagrangian with N, Δ, π , and ρ fields which would generate the tree

diagrams of ChPT. The strong interaction Lagrangian is then extended to include the γ field with "minimal substitution". The Lagrangians which describe the $\gamma\pi V$ interaction of Eq. (3.42) with $V = (\rho, \omega)$ and the $\gamma N \Delta$ vertex of Fig. 1 are then added. The unique feature of SL's calculation is that they then use a unitary transformation method, called the SKO method [200], to derive from the above-mentioned Lagrangian an energy-independent effective Hamiltonian. The essence of the SKO method is to systematically eliminate the virtual processes from the considered Hamiltonian by using unitary transformation. The so-called "virtual processes" are the processes like $N \leftrightarrow N\pi$, $N \leftrightarrow N\rho$, $N \leftrightarrow \pi\Delta$, and $\pi \leftrightarrow \pi\rho$, which can not take place in the free space because of the energy-momentum conservation. The effects of the virtual processes are included as effective operators in the resultant Hamiltonian. Another advantage of such a scheme is that it does not have to perform the renormalization for the nucleon as the $N \leftrightarrow N\pi$ vertex has been transformed away since it is a "virtual" process.

The final effective energy-independent Hamiltonian of SL model then takes the form

$$H_{eff} = H_0 + v_{\pi N}^B + v_{\gamma\pi}^B + (h_{\pi N \Delta}^{(0)} + h_{\gamma N \Delta}^{(0)} + h.c.), \quad (3.27)$$

where $v_{\pi N}^B$ is the background πN potential, and $v_{\gamma\pi}^B$ describes the background $\gamma N \rightarrow \pi N$ transition. $v_{\pi N}^B$ contains Born terms and t -channel ρ exchange, while $v_{\gamma\pi}^B$ is consisted of Born terms in PV coupling and t -channel (ρ, ω) vector-meson exchange. $h_{\pi N \Delta}^{(0)}$ and $h_{\gamma N \Delta}^{(0)}$ denote the $\pi N \rightarrow \Delta^{(0)}$ and $\gamma^* N \rightarrow \Delta^{(0)}$ excitations of a bare $\Delta^{(0)}$, respectively. The matrix elements of $h_{\pi N \Delta}^{(0)}$ and $h_{\gamma N \Delta}^{(0)}$ take the familiar forms, cfr. Sect. 2.

$$\langle \Delta^0 | h_{\pi N \Delta}^{(0)} | \mathbf{k}a \rangle = -\frac{f_{\pi N \Delta}^0}{m_\pi} \frac{i}{\sqrt{(2\pi)^3}} \frac{1}{\sqrt{2\omega(\mathbf{k})}} \sqrt{\frac{E_N(\mathbf{k}) + M_N}{2E_N(\mathbf{k})}} (\mathbf{S} \cdot \mathbf{k}) T_a, \quad (3.28)$$

$$\begin{aligned} \langle \Delta^0 | h_{\gamma N \Delta}^{(0)} | \mathbf{q} \rangle &= -\frac{1}{\sqrt{(2\pi)^3}} \frac{1}{\sqrt{2\omega(\mathbf{q})}} \sqrt{\frac{E_N(\mathbf{q}) + M_N}{2E_N(\mathbf{q})}} \frac{3(M_\Delta + M_N)}{4M_N(E_N(\mathbf{q}) + M_N)} T_3 \\ &\quad \times \{iG_M^*(Q^2)\mathbf{S} \times \mathbf{q} \cdot \boldsymbol{\varepsilon} + G_E^*(Q^2)(\mathbf{S} \cdot \boldsymbol{\varepsilon} \boldsymbol{\sigma} \cdot \mathbf{q} + \mathbf{S} \cdot \mathbf{q} \boldsymbol{\sigma} \cdot \boldsymbol{\varepsilon}) \\ &\quad - \frac{G_C^*(Q^2)}{M_\Delta} \mathbf{S} \cdot \mathbf{q} \boldsymbol{\sigma} \cdot \mathbf{q} \boldsymbol{\varepsilon}_0\}, \end{aligned} \quad (3.29)$$

where T and \mathbf{S} are the isospin and spin $\frac{1}{2} \rightarrow \frac{3}{2}$ transition operators, respectively.

The driving terms v 's in Eq. (3.21) in the SL model are then given by

$$v_{\pi N} = v_{\pi N}^B + v_{\pi N}^\Delta, \quad v_{\gamma\pi} = v_{\gamma\pi}^B + v_{\gamma\pi}^\Delta, \quad (3.30)$$

where

$$v_{\pi N}^\Delta = \frac{h_{\pi N \Delta}^{(0)\dagger} h_{\pi N \Delta}^{(0)}}{E - M_\Delta^{(0)}}, \quad v_{\gamma\pi}^\Delta = \frac{h_{\pi N \Delta}^{(0)\dagger} h_{\gamma N \Delta}^{(0)}}{E - M_\Delta^{(0)}}. \quad (3.31)$$

The energy denominators ($E - M_{\Delta}^{(0)}$) in Eq. (3.31) arise because SL have chosen g_0 in Eq. (3.21) to be the Schrödinger propagator, i.e., $g_0 = 1/(E - H_0)$.

Following Ref. [176], SL decomposed, with the use of two-potential formula, the resulting t -matrix as follows [201],

$$t_{\gamma\pi}(E) = \tilde{t}_{\gamma\pi}^B(E) + \tilde{t}_{\gamma\pi}^{\Delta}(E), \quad t_{\pi N}(E) = \tilde{t}_{\pi N}^B(E) + \tilde{t}_{\pi N}^{\Delta}(E), \quad (3.32)$$

where the background contributions $\tilde{t}_{\gamma\pi}^B(E)$ and $\tilde{t}_{\pi N}^B(E)$ are given by,

$$\tilde{t}_{\gamma\pi}^B(E) = v_{\gamma\pi}^B + v_{\gamma\pi}^B g_0(E) \tilde{t}_{\pi N}^B(E), \quad \tilde{t}_{\pi N}^B(E) = v_{\pi N}^B + v_{\pi N}^B g_0(E) \tilde{t}_{\pi N}^B(E). \quad (3.33)$$

This kind of background terms are further denoted as ‘‘non-resonant’’ background because they do not contain any resonance contributions from $v_{\gamma\pi}^{\Delta}$ or $v_{\pi N}^{\Delta}$ of Eq. (3.31). Note that in partial channel α , the on-shell matrix elements of both $\tilde{t}_{\gamma\pi}^B(k_E, q; E + i\varepsilon)$ and $\tilde{t}_{\pi N}^B(E)(k_E, k_E; E + i\varepsilon)$ have the same phase δ_{α}^B as can be proven in the same way as Eq. (3.23).

The Δ contribution to πN scattering $\tilde{t}_{\pi N}^{\Delta}(E)$ in Eq. (3.32) takes the form

$$\tilde{t}_{\pi N}^{\Delta}(E) = \bar{h}_{\pi N \Delta}^{\dagger}(E) g_{\Delta} h_{\pi N \Delta}(E), \quad (3.34)$$

where $h_{\pi N \Delta}(E)$ describes the dressed πNN vertex

$$h_{\pi N \Delta}(E) = h_{\pi N \Delta}^{(0)} + h_{\pi N \Delta}^{(0)} g_0(E) \tilde{t}_{\pi N}^B(E), \\ \bar{h}_{\pi N \Delta}^{\dagger}(E) = h_{\pi N \Delta}^{(0)\dagger} + \tilde{t}_{\pi N}^B(E) g_0(E) h_{\pi N \Delta}^{(0)\dagger}. \quad (3.35)$$

It can be easily seen that the physical matrix elements of both $h_{\pi N \Delta}(E)$ and $\bar{h}_{\pi N \Delta}^{\dagger}(E)$, i.e., $h_{\pi N \Delta}(E + i\varepsilon, \mathbf{k}_E)$ and $\bar{h}_{\pi N \Delta}^{\dagger}(E + \varepsilon, \mathbf{k}_E)$, have the phase δ_{α} . Note that $\bar{h}_{\pi N \Delta}^{\dagger}(E) \neq h_{\pi N \Delta}^{\dagger}(E)$. $g_{\Delta}(E)$ is the dressed Δ propagator,

$$g_{\Delta}^{-1} = g_0^{-1} - \Sigma_{\Delta}(E), \quad (3.36)$$

where the Δ self-energy $\Sigma_{\Delta}(E)$ is given by

$$\Sigma_{\Delta}(E) = h_{\pi N \Delta}^{(0)} g_0 \bar{h}_{\pi N \Delta}^{\dagger}(E). \quad (3.37)$$

The matrix element of $\Sigma_{\Delta}(E)$ is related to the dressed mass $M_{\Delta}(E)$ and the width $\Gamma_{\Delta}(E)$ of the physical Δ by

$$\langle \Delta^{(0)} | \Sigma_{\Delta}(E + i\varepsilon) | \Delta^{(0)} \rangle = M_{\Delta}(E) - i \frac{\Gamma_{\Delta}(E)}{2}. \quad (3.38)$$

Similarly, the Δ contribution to $\gamma^* N$ reaction $\tilde{t}_{\gamma\pi}^\Delta(E)$ can be expressed as

$$\tilde{t}_{\gamma\pi}^\Delta(E) = \bar{h}_{\pi N \Delta}^\dagger(E) g_\Delta h_{\gamma N \Delta}(E), \quad (3.39)$$

where

$$\begin{aligned} h_{\gamma N \Delta}(E) &= h_{\gamma N \Delta}^{(0)} + h_{\pi N \Delta}^{(0)} g_0(E) \tilde{t}_{\gamma\pi}^B(E) \\ &= h_{\gamma N \Delta}^{(0)} + h_{\pi N \Delta}(E) g_0(E) v_{\gamma\pi}^B. \end{aligned} \quad (3.40)$$

To solve the integral equation for $\tilde{t}_{\pi N}^B$ in Eq. (3.33), SL introduced dipole form factors for $v_{\pi N}^B$ and the $\pi N \Delta$ vertex. Because the form factors they introduced for the different pieces in $v_{\pi N}^B$ are different and it is difficult to keep track of the gauge invariance in the unitary transformation, Sato and Lee did not attempt to address the question of maintaining current conservation in their calculation.

In short, Sato and Lee derived an effective Hamiltonian consisting of bare $\Delta \leftrightarrow \pi N, \gamma N$ vertex interactions and energy-independent meson-exchange $\pi N, \gamma N \rightarrow \pi N$ transition potential operators, by applying a unitary transformation to a model Lagrangian of $N, \Delta, \pi, \rho, \omega$, and γ fields in order to achieve consistency in describing $\gamma^* \pi$ reactions and πN scatterings. Form factors are added to the resultant effective Hamiltonian and with the use of a Schroedinger propagator, the parameters are adjusted to give a good description of the existing data. The issue of gauge invariance was not addressed in their formulation.

3.2.3 Dubna-Mainz-Taipei model

Dubna-Mainz-Taipei (DMT) model was developed in two stages. When the dynamical approach was first proposed in Ref. [177], a phenomenological separable form for $v_{\pi N}$ and the Schroedinger propagator $(E - H_0)^{-1}$, together with a $v_{\gamma\pi}$ derived from a chiral effective Lagrangian, were employed in Eq. (3.21). Efforts were then made to construct a meson-exchange model for the πN scattering [179,190] (called Taipei-Argonne πN model hereafter), in order to achieve consistency in the treatment of πN scattering and $\gamma\pi$ reactions. However, the resultant πN interaction was used in Eq. (3.21) only to describe the pion threshold photoproduction in [179]. Putting together the meson-exchange models of $v_{\gamma\pi}$ and $v_{\pi N}$ and apply them to the photo- and electroproduction of pion in the resonance region was performed only recently in Ref. [91].

In the TA πN model, several three-dimensional reduction schemes of the Bethe-Salpeter equation for a model Lagrangian involving N, Δ, π, σ , and ρ fields were investigated. It was found that all of the resultant meson-exchange πN models can give similar good description of the πN phase shifts up to 400 MeV. However, they have significant differences in describing the πNN and $\pi N \Delta$ form factors and πN off-shell t -matrix elements.

The TA model contains almost identical physics input as the SL πN model. Namely, the Lagrangian they considered both consist of π, ρ, N, Δ fields except that the TA model also includes the t -channel σ exchange. The relevant interaction Lagrangian used in the TA model is given as follows:

$$\begin{aligned}
\mathcal{L}_I = & \frac{f_{\pi NN}^{(0)}}{m_\pi} \bar{N} \gamma_5 \gamma_\mu \vec{\tau} \cdot \partial^\mu \vec{\pi} N - g_{\sigma\pi\pi}^{(s)} m_\pi \sigma(\vec{\pi} \cdot \vec{\pi}) - \frac{g_{\sigma\pi\pi}^{(v)}}{2m_\pi} \sigma \partial^\mu \vec{\pi} \cdot \partial_\mu \vec{\pi} \\
& - g_{\sigma NN} \bar{N} \sigma N - g_{\rho NN} \bar{N} \{ \gamma_\mu \vec{\rho}^\mu + \frac{\kappa_V^\rho}{4M_N} \sigma_{\mu\nu} (\partial^\mu \vec{\rho}^\nu - \partial^\nu \vec{\rho}^\mu) \} \cdot \frac{1}{2} \vec{\tau} N \\
& - g_{\rho\pi\pi} \vec{\rho}^\mu \cdot (\vec{\pi} \times \partial_\mu \vec{\pi}) - \frac{g_{\rho\pi\pi}}{4m_\rho^2} (\delta - 1) (\partial^\mu \vec{\rho}^\nu - \partial^\nu \vec{\rho}^\mu) \cdot (\partial_\mu \vec{\pi} \times \partial_\nu \vec{\pi}) \\
& + \{ \frac{g_{\pi N \Delta}^{(0)}}{m_\pi} \bar{\Delta}_\mu [g^{\mu\nu} - (Z + \frac{1}{2}) \gamma^\mu \gamma^\nu] \vec{T}^\dagger N \cdot \partial_\nu \vec{\pi} + h.c. \}, \tag{3.41}
\end{aligned}$$

where Δ_μ is the Rarita-Schwinger field operator. The parameters, namely, all the coupling constants, the bare nucleon and Δ masses $m_N^{(0)}$ and $m_\Delta^{(0)}$, and the "off-mass-shell coupling parameters" Z for the $\pi N \Delta$ vertex [170], are adjusted such that the predictions of $t_{\pi N}$ agree well with the experimental data, including nucleon mass, renormalized πNN couplings constant $f_{\pi NN}^2/4\pi = 0.079$ and the s - and p -wave πN phase shifts.

The effective chiral Lagrangian for the strong interaction is then extended to include the electromagnetic interaction in a gauge invariant way, i.e., with the minimal substitution of $\partial_\mu \rightarrow \partial_\mu - ieA_\mu$. In addition, the t -channel vector-meson (ρ, ω) exchange is known to make non-negligible contribution. The relevant effective Lagrangian is given by

$$\mathcal{L}_{V\pi\gamma} = \frac{e\lambda_V}{m_\pi} \varepsilon_{\mu\nu\rho\sigma} (\partial^\mu A^\nu) \pi_i \partial^\rho (\omega^\sigma \delta_{i3} + \rho_i^\sigma), \tag{3.42}$$

$$\mathcal{L}_{VNN} = g_{VNN} \bar{N} \left(\gamma_\mu V^\mu - \frac{\kappa_V}{2M_N} \sigma_{\mu\nu} \partial^\nu V^\mu \right) N, \tag{3.43}$$

where N and $V (= \rho, \omega)$ denote the nucleon and vector meson field, respectively. λ_V is the radiative coupling determined by $V \rightarrow \pi\gamma$ decay. The interaction described above would give rise to a contribution to $v_{\gamma\pi}$ of Eq. (3.21) which contains the Born terms in pseudoscalar coupling and the t -channel (ρ, ω) vector-meson exchanges and is normally called the background transition potential and denoted by $v_{\gamma\pi}^B$.

However, different theoretical treatments lead to difference in $v_{\pi N}$ even for the same set of diagrams considered. For example, for the u -channel nucleon exchange diagram, TA model has (omitting the isospin indeces)

$$v_{\pi N}^{u-ex}(p', k'; p, k) = \left(\frac{f_{\pi NN}}{m_\pi} \right)^2 \gamma_5 k S_N(p' - k) \gamma_5 k', \tag{3.44}$$

where $S_N(p) = (\not{p} - M_N + i\varepsilon)^{-1}$ is the nucleon propagator. In SL model, however, with the use of the unitary transformation, Eq. (3.44) becomes,

$$v_{\pi N}^{u-ex}(p', k'; p, k) = \left(\frac{f_{\pi NN}}{m_\pi} \right)^2 \gamma_5 k \frac{1}{2} [S_N(p' - k) + S_N(p - k') \gamma_5 k'] \gamma_5 k', \tag{3.45}$$

instead. In addition, SL used $g_0 = 1/(E - H_0)$ in solving the equation $t_{\pi N} = v_{\pi N} + v_{\pi N} g_0 t_{\pi N}$, while the TA model considered many different three-dimensional propagators.

In the DMT model calculations of [91] for electromagnetic pion production, only the meson-exchange πN model for $v_{\pi N}$, obtained with the Cooper-Jennings [195] three-dimensional reduction scheme, has been employed. It was chosen because Cooper and Jennings [195] argued that the reduction scheme they developed has the advantage of preserving the chiral symmetry contained in the original Lagrangian. However, two remarks are in order here. First, even though the $t_{\pi N}$ matrix elements used in the DMT calculations are obtained within the Cooper-Jennings' reduction scheme, namely, the time component of the relative momentum in $v_{\pi N}$ is fixed according to the Cooper-Jennings prescription, all the particles are put on mass-shell in the derivation of $v_{\gamma\pi}$ of DMT. In addition, the Cooper-Jennings propagator was used in solving $t_{\pi N} = v_{\pi N} + v_{\pi N} g_0 t_{\pi N}$ but the Schroedinger propagator is used for g_0 instead in the evaluation of $t_{\gamma\pi} = v_{\gamma\pi} + v_{\gamma\pi} g_0 t_{\pi N}$. With the differences in $v_{\pi N}$ and g_0 as expounded above, it will not be a surprise if the off-shell behaviors of the $t_{\pi N}$ obtained in SL and TA would differ substantially in some kinematical regions.

The prescription used to preserve gauge invariance in the DMT model goes as follows. The aim is to continue k in $v_{\gamma\pi}^\alpha(k, q)$, which is originally derived only for the on-energy-shell values k_E , to the off-energy-shell region as called for in Eq. (3.23). It starts from the expressions for the CGLN amplitudes F'_i 's derived from the tree approximation to the effective chiral Lagrangian used for the model. The F'_i 's can be expressed as linear combination of the invariant amplitudes A'_i 's of Eq. (A.6) as given in Eqs. (Ia-b) in the Appendix of Ref. [202], where the coefficients are functions of Q^2 , the energies of photon, pion, initial and final nucleon, q_0 , k_0 , E , and E' , respectively, and the total energy W . These energy variables are then replaced with expressions in three-momentum $|\mathbf{q}|$ and $|\mathbf{k}|$, e.g., $q_0 = \sqrt{|\mathbf{q}|^2 - Q^2}$, $k_0 = \sqrt{m_\pi^2 + \mathbf{k}^2}$ and $E = \sqrt{M_N^2 + \mathbf{q}^2}$ etc, while W is always kept as the initial energy, namely, $W = |\mathbf{q}| + \sqrt{M_N^2 + \mathbf{q}^2}$. Such substitutions have the property that the threshold behaviors of the F'_i 's are retained, i.e.,

$$\begin{aligned} F_1 &\propto \text{const.}, & F_2 &\propto |\mathbf{q}||\mathbf{k}|, & F_3 &\propto |\mathbf{q}||\mathbf{k}|, \\ F_4 &\propto |\mathbf{k}|^2, & F_7 &\propto \text{const.}, & F_8 &\propto |\mathbf{k}|. \end{aligned} \quad (3.46)$$

In the invariant amplitudes, the Mandelstam invariants t and u appearing in the t - and u -channel exchange diagrams, are expressed in terms of the three-momentum $|\mathbf{q}|$ and $|\mathbf{k}|$ by :

$$t = (p - p')^2 = 2M_N^2 - 2\sqrt{M_N^2 + \mathbf{q}^2}\sqrt{M_N^2 + \mathbf{k}^2} + 2\mathbf{q} \cdot \mathbf{k}, \quad (3.47)$$

$$u = (p - k)^2 = M_N^2 + m_\pi^2 - 2\sqrt{M_N^2 + \mathbf{q}^2}\sqrt{m_\pi^2 + \mathbf{k}^2} - 2\mathbf{q} \cdot \mathbf{k}. \quad (3.48)$$

The resulting expressions of F'_i 's, which are functions of $|\mathbf{q}|$, $|\mathbf{k}|$ and $x = \cos\theta$ are then used to obtain, according to Eq. (If) in Ref. [202], the multipole amplitudes $v_{\gamma\pi}^\alpha(k, q)$ where k can now be off-energy-shell. A dipole form factor $[(\alpha^2 + \mathbf{k}_E^2)/(\alpha^2 + \mathbf{k}^2)]^2$ with $\alpha = 440$ MeV is then multiplied to all the resultant multipoles to ensure the convergence in the integral in Eq. (3.23).

There is another difference between SL and DMT dynamical model calculations. It lies in the scheme in the separation of background and resonance contributions. In the SL model, the full $t_{\gamma\pi}$ is decomposed as in Eqs. (3.32-3.40). In the DMT model, $t_{\gamma\pi}$ is instead decomposed as follows,

$$t_{\gamma\pi}(E) = t_{\gamma\pi}^B(E) + t_{\gamma\pi}^\Delta(E), \quad (3.49)$$

where

$$t_{\gamma\pi}^B(E) = v_{\gamma\pi}^B + v_{\gamma\pi}^B g_0(E) t_{\pi N}(E), \quad (3.50)$$

$$t_{\gamma\pi}^\Delta(E) = v_{\gamma\pi}^\Delta + v_{\gamma\pi}^\Delta g_0(E) t_{\pi N}(E). \quad (3.51)$$

Here $t_{\gamma\pi}^B$, in contrast to $\tilde{t}_{\gamma\pi}^B$ of Eq. (3.33), includes the contributions not only from the nonresonant mechanisms but also some of the contributions from the Δ excitation as contained in the full $t_{\pi N}$ which lead to the renormalization of the vertex $\gamma^* N \Delta$. However, all processes which start with the electromagnetic excitation of a bare resonance are summed up in $t_{\gamma\pi}^\Delta$. One feature of such a decomposition is that each term in Eq. (3.49) would fulfill the condition imposed by Fermi-Watson theorem, i.e., their respective multipole amplitude in channel α would have the same πN phase shift δ_α as in Eq. (3.24).

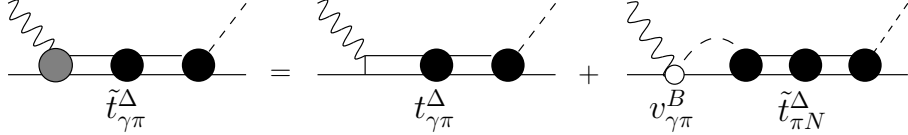


Fig. 29. Relation between dressed and bare $\gamma N \Delta$ vertices of Eq. (3.53). The shaded and solid circles represent the dressed $\gamma N \Delta$ and $\pi N \Delta$ vertices, respectively.

Multipole amplitude of $t_{\gamma\pi}^B$ can be evaluated in a straightforward manner as in Eq. (3.23) once $t_{\pi N}$ is given. For the resonance contribution $t_{\gamma\pi}^\Delta$, it is easy to see that it takes the form of,

$$t_{\gamma\pi}^\Delta(E) = \bar{h}_{\pi N \Delta}^\dagger(E) g_\Delta(E) h_{\gamma N \Delta}^{(0)}. \quad (3.52)$$

The relation between $t_{\gamma\pi}^\Delta$ and $\tilde{t}_{\gamma\pi}^\Delta$ of Eq. (3.34), the Δ resonance contribution with dressed and bare e.m. vertices as depicted in Fig. 29, is given by

$$\tilde{t}_{\gamma\pi}^\Delta(E) = t_{\gamma\pi}^\Delta(E) + v_{\gamma\pi}^B g_0(E) \tilde{t}_{\pi N}^\Delta(E). \quad (3.53)$$

Note that $g_\Delta(E)$, which depends on the physical mass M_Δ and total width Γ_Δ , appears in $\tilde{t}_{\gamma\pi}^\Delta(E)$, $t_{\gamma\pi}^\Delta$ and $\tilde{t}_{\pi N}^\Delta(E)$, so the resonance position and the total width can be extracted from πN scattering. The DMT model calculation takes advantage of this fact and writes the resonance multipole amplitude of Eq. (3.52) in the following form :

$$t_{\gamma\pi}^{\Delta,\alpha}(W, Q^2) = A_\alpha^\Delta(Q^2) \frac{f_{\gamma\Delta}(W) \Gamma_\Delta(W) M_\Delta f_{\pi\Delta}(W)}{M_\Delta^2 - W^2 - i M_\Delta \Gamma_\Delta(W)} e^{i\phi_\alpha(W)}, \quad (3.54)$$

where $f_{\pi\Delta}$ is the usual Breit-Wigner factor describing the decay of a resonance with total width $\Gamma_\Delta(W)$ and physical mass M_Δ . Namely, the well known Breit-Wigner form for the resonance contribution is assumed, in close analogy to the standard way of analysis of the experimental data as done in [92]. The expressions for the form factors $f_{\gamma\Delta}$, $f_{\pi\Delta}$ and total width Γ_Δ will be

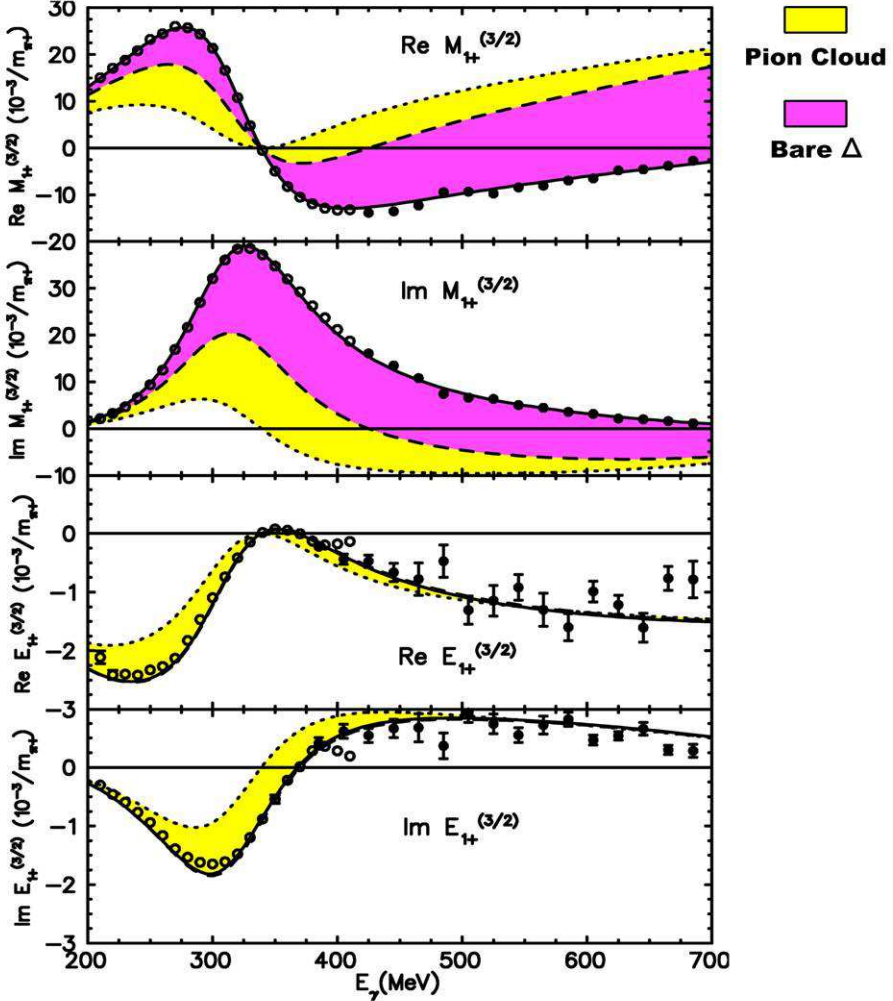


Fig. 30. Real and imaginary parts of the $M_{1+}^{(3/2)}$ and $E_{1+}^{(3/2)}$ multipoles. The dashed (dotted) curves are the results obtained within the DMT model for $t_{\gamma\pi}^B$ including (excluding) the principal value integral contribution in Eq. (3.23). The solid curves are the full DMT results including also the bare Δ excitation. For the E_{1+} multipole, the dashed and solid curves practically coincide due to the small value of the bare \mathcal{E}^Δ . The open circles are the results from the Mainz dispersion relation analysis [166], whereas the solid circles are obtained from the VPI analysis [203].

considered in the next subsection. The energy dependence in $f_{\gamma\Delta}(W)$ is introduced to account for the effect of possible excitation of the Δ via inelastic channels like $\pi\Delta$. The phase $\phi(W)$ in Eq. (3.54) is used to adjust the phase of the resonance contribution to be equal to the corresponding πN phase shift $\delta_{\pi N}$ in the (3,3) channel as required by the Fermi-Watson theorem. At $W = M_\Delta = 1232$ MeV $\phi = 0$ for any Q^2 . Therefore, this phase does not affect the Q^2 dependence of the $\gamma N\Delta$ vertex.

In the SL and DMT models, the Q^2 dependence for the $\gamma N\Delta$ vertex is parametrized in the same way as in Ref. [92], i.e.

$$A_\alpha^\Delta(Q^2) = A_\alpha^\Delta(0) \frac{q_\Delta}{q_W} (1 + \beta_\alpha Q^2) e^{-\gamma_\alpha Q^2} G_D(Q^2), \quad (3.55)$$

with $\alpha = M, E, S$ referring to magnetic dipole, electric quadrupole, or Coulomb quadrupole transitions, where q_Δ is defined in Eq. (2.6), and where q_W is defined below Eq. (3.10). The form factor $G_D(Q^2) = 1/(1 + Q^2/0.71)^2$ is the usual nucleon dipole form factor. In the case of the magnetic transition the parameters β and γ can be determined by fitting $A_M^\Delta(Q^2)$ to the data for the well known G_M^* form factor, which is obtained from the M_{1+} pion electroproduction multipole in the (3,3) channel at $W = M_\Delta = 1232$ MeV, as given by Eq. (2.13).

We want to remind the reader that the definition of the Δ e.m amplitudes in different models can be different. As we have seen above in the SL model they can contain contributions from the excitation of the Δ resonance via the nonresonant mechanism and describe the dressed $\gamma N \Delta$ vertex. In the DMT model such mechanism is included in the unitarized background $t_{\gamma\pi}^B$ and the electromagnetic vertices $A_\alpha^\Delta(Q^2)$ describe the bare e.m. vertices.

In general, in accordance with the considered above dynamical models, the G_M^* form factor can be decomposed in three terms

$$G_M^*(Q^2) = G_M^{bare}(Q^2) + G_M^{pion\,cloud}(Q^2) + G_M^{n.r.\,bcgr.}(Q^2), \quad (3.56)$$

where G_M^{bare} , $G_M^{pion\,cloud}$ and $G_M^{n.r.\,bcgr.}$ are the contributions from $t_{\gamma\pi}^\Delta$, from the second term in rhs of Eq. (3.53) and from the $\tilde{t}_{\gamma\pi}^B$ of Eq. (3.33), respectively. Therefore, different models, which have a different way for the separation of background and resonance contributions, the values for the parameters $\bar{A}_\alpha^\Delta(0)$, β_α and γ_α in Eq. (3.55) can be different. The same arguments are also true for the form factors of the electric and Coulomb transitions.

In Fig. 30, we show the resonant multipoles $M_{1+}^{(3/2)}$ and $E_{1+}^{(3/2)}$ as obtained in the DMT model. For $M_{1+}^{(3/2)}$, one sees a large effect of the pion off-shell rescattering (difference between dotted and dashed curves), which results from the principal value integral part of Eq. (3.23). The total pion rescattering (dashed curves) contributes for half of the $M_{1+}^{(3/2)}$ as seen in Fig. 30 for the DMT model, the remaining half originates from the bare $\gamma N \Delta$ excitation. Furthermore, one sees that almost all of the $E2$ strength is generated by the πN rescattering.

3.2.4 Dynamical Utrecht-Ohio model

The dynamical Utrecht-Ohio (DUO) model has been developed in Refs. [204,182]. The model is based on a πN - γN coupled-channel equation which when solved to the first order in the electromagnetic coupling e leads to the electroproduction amplitude, $T_{\pi\gamma^*} = V_{\pi\gamma^*} + T_{\pi\pi} G_\pi V_{\pi\gamma^*}$, where $V_{\pi\gamma^*}$ is an basic electroproduction potential, G_π is the pion-nucleon propagator and $T_{\pi\pi}$ is the full πN amplitude. Thus, the pion rescattering effects are included as the final state interaction.

The πN amplitude satisfies an integral equation on its own. The details on constructing πN amplitude are presented in [204]. The corresponding fit of this model into the πN elastic scattering phase shifts is shown in Fig. 31.

In Fig. 32 one can see the diagrammatic representation of the DUO model for the pion electroproduction. The model potential $V_{\pi\gamma}$ includes the Born term (using the pseudo-vector πNN

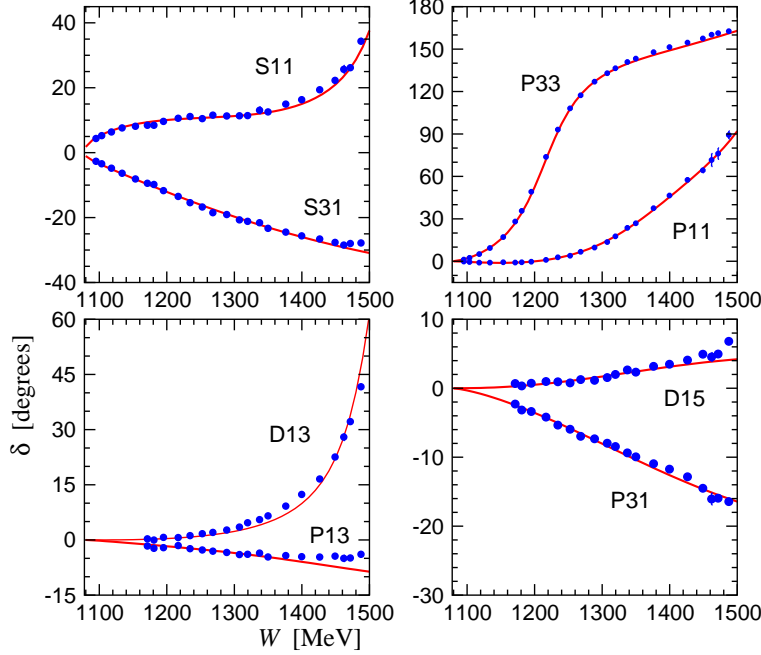


Fig. 31. (Color online) The s -, p -, and some of the d -wave πN scattering phase-shifts in the DUO model (red solid curves). The data points are the results of the SAID single-energy solution SP06 [183].

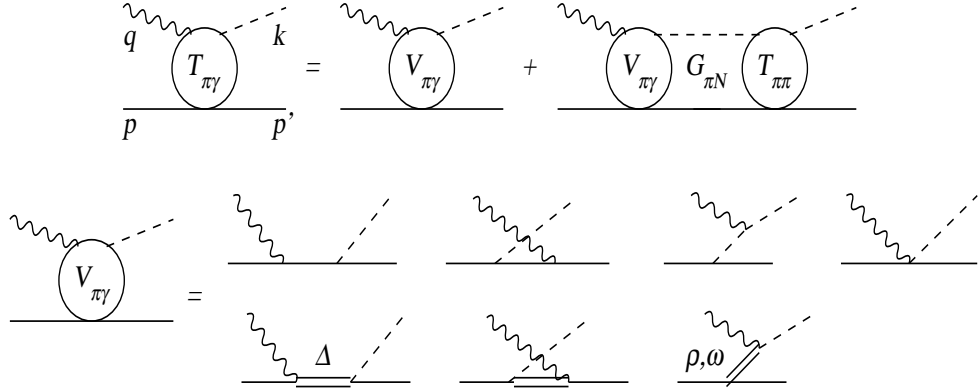


Fig. 32. The electromagnetic pion production amplitude in the DUO model.

coupling), the t -channel exchange of $\rho-$ and $\omega-$ mesons, and the Δ -isobar exchange.

The πN final state interaction dresses the s -channel nucleon and resonance contributions, leading in particular to the mass, field and coupling constant renormalizations. Therefore, both N - and Δ -pole contributions in $V_{\pi\gamma}$ are included using the *bare* mass and coupling parameters obtained from the equation for the πN amplitude. The renormalization conditions together with unitarity demand that the same propagators and πN vertices, including the cutoff functions, appear in both the πN and γN potentials. Thus, all these ingredients are fixed by the analysis of πN scattering.

On the other hand, the electromagnetic interaction is constrained by the electromagnetic *gauge invariance*. At this point one is often concerned with the problem of how to introduce the electromagnetic form factors for nucleon and pion in a way consistent with gauge invariance.

A common solution to this problem is to choose all of the electromagnetic form factors that go into the Born term (i.e., nucleon, pion and axial form factors) to be the same. This prescription does enforce the current conservation, however the Ward-Takahashi (WT) identities cannot be satisfied in this way. Furthermore, it is clear that the requirement of gauge invariance should not be able to restrict the Q^2 dependence of the electromagnetic interaction. Finally, it is known that these form factors need not to be and *are not* the same.

The DUO model introduces the procedure where an arbitrary form factor $F(Q^2)$ can be accommodated by the following replacement of the current:

$$J^\mu \rightarrow J'^\mu(Q^2) = J^\mu + [F(Q^2) - 1] O^{\mu\nu} J_\nu, \quad (3.57)$$

where $O^{\mu\nu} = g^{\mu\nu} - q^\mu q^\nu/q^2$, and q is the photon 4-momentum, $Q^2 = -q^2$. It is easy to see that the resulting current J'^μ obeys exactly the same WT identities as J^μ . Thus, as long as gauge-invariance is implemented at the real-photon point, the inclusion of the form factors via Eq. (3.57) will give the gauge-invariant current for $Q^2 \neq 0$. For example, the bare $NN\gamma$ and $\pi\pi\gamma$ vertex functions and the Kroll-Rudermann term are:

$$\Gamma_{NN\gamma}^\mu = e \gamma^\mu + e [F_1(Q^2) - 1] O^{\mu\nu} \gamma_\nu + \frac{e \kappa_N}{2m_N} F_2(Q^2) i \sigma^{\mu\nu} q_\nu, \quad (3.58a)$$

$$\Gamma_{\pi\pi\gamma}^\mu = e (k + k')^\mu + e [F_\pi(Q^2) - 1] O^{\mu\nu} (k + k')_\nu, \quad (3.58b)$$

$$J_{KR}^\mu = \frac{e g_{\pi N}}{2m_N} \left\{ \gamma^\mu + [F_A(Q^2) - 1] O^{\mu\nu} \gamma_\nu \right\} \gamma_5. \quad (3.58c)$$

This procedure allows one to use the experimentally determined form factors in the Born terms.

3.3 MAID - a phenomenological multipole solution

MAID, developed by the Mainz group, is currently the most comprehensive unitary isobar model which includes contributions from all other known resonances up to second and third resonance regions, in addition to the $\Delta(1232)$. Its first version was published in 1999 [92] as commonly referred to as MAID98. Since then it is updated once every two years to accommodate for the new data by readjusting the parameters and can be accessed to, together with DMT, at the website of Ref. [184].

The basic equations used for the MAID are similar to those of the DMT model [91]. It also starts from the equation $t_{\gamma\pi}(E) = v_{\gamma\pi} + v_{\gamma\pi} g_0(E) t_{\pi N}(E)$ with $g_0 = (E - H_0)^{-1}$. For any resonant channel, the transition potential $v_{\gamma\pi}$ consists of two terms

$$v_{\gamma\pi}(E) = v_{\gamma\pi}^B + v_{\gamma\pi}^R(E), \quad (3.59)$$

where $v_{\gamma\pi}^B$ is the background transition potential and $v_{\gamma\pi}^R(E)$ corresponds to the contribution of the bare resonance excitation. The resulting t -matrix can be decomposed into two terms as in Eqs. (3.49-3.51),

$$t_{\gamma\pi}(E) = t_{\gamma\pi}^B(E) + t_{\gamma\pi}^R(E), \quad (3.60)$$

where

$$t_{\gamma\pi}^B(E) = v_{\gamma\pi}^B + v_{\gamma\pi}^B g_0(E) t_{\pi N}(E), \quad (3.61)$$

$$t_{\gamma\pi}^R(E) = v_{\gamma\pi}^R + v_{\gamma\pi}^R g_0(E) t_{\pi N}(E). \quad (3.62)$$

In MAID, the background potential $v_{\gamma\pi}^{B,\alpha}$ is constructed in the same way as in the DMT model except now the Born terms are calculated with a hybrid model (HM), i.e., an energy dependent mixing of pseudovector-pseudoscalar (PV-PS) πNN coupling ,

$$L_{\pi NN}^{HM} = \frac{\Lambda_m^2}{\Lambda_m^2 + \mathbf{k}_0^2} L_{\pi NN}^{PV} + \frac{\mathbf{k}_0^2}{\Lambda_m^2 + \mathbf{k}_0^2} L_{\pi NN}^{PS}, \quad (3.63)$$

where \mathbf{k}_0 is the asymptotic pion momentum in the πN *c.m.* frame which depends only on W and is not an operator acting on the pion field. From the analysis of the $M_{1-}^{(3/2)}$ and $E_{0+}^{(3/2)}$ multipoles it was found that the most appropriate value for the mixing parameter is $\Lambda_m = 450$ MeV [92]. Note that for the pion pole term, the pion couples with on-shell nucleons only, and HM, PV, and PS couplings are all equivalent. As a matter of fact, only the multipoles E_{0+} , M_{1-} , L_{0+} , and L_{1-} are affected by the use of such a mixed coupling scheme. In all, $v_{\gamma\pi}^{B,\alpha}$ depends on 7 parameters: the PV-PS mixing parameter Λ_m , 4 coupling constants and 2 cut-off parameters for the vector-meson exchange contributions.

In MAID98, the background contribution was given as $t_{\gamma\pi}^{B,\alpha}(\text{MAID98}) = v_{\gamma\pi}^{B,\alpha}(W, Q^2)$, a real and smooth function. The unitarization of the total amplitude was done by introducing an additional phase ϕ in the resonance contribution which ensures the phase of the total amplitude (background plus resonance) be equal to the corresponding pion-nucleon scattering phase δ_α . In the new extended version (MAID2005), all the the background contributions of *s*-, *p*-, *d*- and *f*-waves are complex numbers as prescribed in K-matrix approximation, namely,

$$t_{\gamma\pi}^{B,\alpha}(W, Q^2) = v_{\gamma\pi}^{B,\alpha}(W, Q^2) [1 + it_{\pi N}^\alpha(W)], \quad (3.64)$$

where $t_{\pi N}^\alpha = [\eta_\alpha \exp(2i\delta_\alpha) - 1]/2i$ is the pion-nucleon elastic scattering amplitude with the phase shift δ_α and the inelasticity parameter η_α taken from the analysis of the VPI group (SAID program). Below the two-pion threshold where $\eta_\alpha = 1$, Eq. (3.64) becomes $t_{\gamma\pi}^{B,\alpha}(W, Q^2) = e^{i\delta_\alpha} \cos \delta_\alpha v_{\gamma\pi}^{B,\alpha}(Q^2)$. Such a structure of the background appears naturally from Eq. (3.23) if the principal value integral contribution in the pion rescattering term is neglected. Part of such a “pion cloud” contribution (principal value integral) will be effectively included in the resonance sector with the use of dressed γNR vertex as will be explained below.

As in the DMT model, the resonance contributions $t_{\gamma\pi}^{R,\alpha}(W, Q^2)$ in MAID is parametrized as in Eq. (3.54),

$$t_{\gamma\pi}^{R,\alpha}(W, Q^2) = \bar{A}_\alpha^R(Q^2) \frac{f_{\gamma R}(W) \Gamma_R M_R f_{\pi R}(W)}{M_R^2 - W^2 - i M_R \Gamma_R} e^{i\phi_R}. \quad (3.65)$$

where $\bar{A}_\alpha^R(Q^2)$ should now be interpreted, in contrast to $\bar{A}_\alpha^\Delta(Q^2)$ of Eq. (3.54), as corresponding to the excitation of a dressed resonance in order to partly account for the neglected principle

value integral term of Eq. (3.23) in $t_{\gamma\pi}^{B,\alpha}(W, Q^2)$ of Eq. (3.64). $f_{\pi N}(W)$ is the usual Breit-Wigner factor describing the decay of the N^* resonance with total width Γ_{tot} , partial πN -width $\Gamma_{\pi N}$ and spin j ,

$$f_{\pi N}(W) = \left[\frac{1}{(2j+1)\pi} \frac{k_W}{|\mathbf{k}|} \frac{M_N}{W_R} \frac{\Gamma_{\pi N}}{\Gamma_{tot}^2} \right]^{1/2}, \quad k_W = \frac{W^2 - M_N^2}{2W}. \quad (3.66)$$

The factor $C_{\pi N}$ is $\sqrt{3/2}$ and $-1/\sqrt{3}$ for the isospin 3/2 and isospin 1/2 multipoles respectively. The energy dependence of the partial width $\Gamma_{\pi N}$ is given by

$$\Gamma_{\pi N} = \beta_\pi \Gamma_R \left(\frac{|\mathbf{k}|}{k_R} \right)^{2l+1} \left(\frac{X^2 + k_R^2}{X^2 + \mathbf{k}^2} \right)^l \frac{W_R}{W}, \quad (3.67)$$

where X is a damping parameter, $\Gamma_{tot}(W)$ is the total width, k_R is the pion *c.m.* momentum at the resonance peak ($W = W_R$) and β_π is the single-pion branching ratio. Expressions for the total width can be found in [92]. The W dependence of the γNN^* vertex is given by the form factor

$$f_{\gamma N}(W) = \left(\frac{q_W}{q_R} \right)^n \left(\frac{X^2 + q_R^2}{X^2 + q_W^2} \right), \quad (3.68)$$

where the damping parameter X is the same as in Eq. (3.67) and $q_R = q_W$ at $W = W_R$. The parameter n is defined by the best fit of the experimental multipoles at the photon point ($Q^2=0$). At the resonance position $f_{\gamma N}(W_R) = 1$. The phase $\phi(W)$ in Eq. (3.65) is introduced to adjust the phase of the total multipole to equal to the corresponding πN phase shift δ_α below the two pion threshold. For the *s*- and *p*- waves such unitarization procedure is applied up to $W = 1400$ MeV. At higher energies for these waves the phase $\phi(W)$ is taken as constants. Note that in the case of the $\Delta(1232)$ excitation, the phase $\phi = 0$ at $W=1232$ MeV. In this case, the Fermi-Watson theorem is applied up to $W < 1600$ MeV, where the inelasticity parameter η_α of pion scattering amplitude is still close to 1. For the resonances in the *d*- and *f*-waves resonance phase ϕ assumed to be constant and determined from the best fit.

While in the original version of MAID [92] only the 7 most important nucleon resonances were included with mostly only transverse e.m. couplings, in the new extended version MAID05 all four star resonances below $W = 2$ GeV are included (with transverse electric, $\bar{A}_\alpha^R = \bar{E}_{l\pm}$, magnetic, $\bar{A}_\alpha^R = \bar{M}_{l\pm}$, and coulomb, $\bar{A}_\alpha^R = \bar{S}_{l\pm}$) couplings. They are $P_{33}(1232)$, $P_{11}(1440)$, $D_{13}(1520)$, $S_{11}(1535)$, $S_{31}(1620)$, $S_{11}(1650)$, $D_{15}(1675)$, $F_{15}(1680)$, $D_{33}(1700)$, $P_{13}(1720)$, $F_{35}(1905)$, $P_{31}(1910)$ and $F_{37}(1950)$. For all these 13 resonances the total numbers of the e.m. couplings is 52 (34 for proton and 18 for neutron channels) They are independent of the total energy and depend only on Q^2 . They can be taken as constants in a single- Q^2 analysis, e.g. in photoproduction, where $Q^2 = 0$ but also at any fixed Q^2 , where enough data with W and θ variation is available. Alternatively they can also be parametrized as functions of Q^2

3.4 Dispersion relation approach

The dispersion relations approach, or "S-matrix theory" was developed mostly in the 50's and 60's of the last century. It was suggested as an alternative to the field theoretical approach to the strong interaction to avoid an expansion in the strong coupling constant. The underlying

postulate of this theory is that the S-matrix is a Lorentz-invariant *analytic* function of all momentum variables with only those singularities required by unitarity. It is generally believed that the analyticity arises from the causality property as in the case of Kramers-Kronig relations for the dielectric constant.

The starting point of the dispersion relation approach is the fixed- t dispersion relations which follow from the assumed analytic properties, and from crossing symmetry Eq. (A.17). They can be conveniently written in the following matrix notation as [205]:

$$Re \tilde{A}(s, t, Q^2) = \tilde{A}^{pole}(s, t, Q^2) + \frac{P}{\pi} \int_{s_{thr}}^{\infty} ds' \left[\frac{1}{s' - s} + [\bar{\xi}] \frac{1}{s' - u} \right] Im \tilde{A}(s', t, Q^2), \quad (3.69)$$

where $s_{thr} = (m_\pi + M_N)^2$ and $\tilde{A}^{pole}(s, t, Q^2)$ is the Born term evaluated in pseudoscalar coupling as can be found in [166,205]. It consists of s - and u -channel nucleon poles, and t -channel pion pole with residues proportional to the electromagnetic form factors of the nucleon and pion.

The next step is to apply the multipole projection to the dispersion relations Eq. (3.69) which leads to the following set of coupled integral equations for the CGLN multipoles $\mathcal{M}_\alpha = (E_{l\pm}, M_{l\pm}, L_{l\pm}/\omega)$,

$$Re \mathcal{M}_\alpha(W) = \mathcal{M}_\alpha^{Pole}(W) + \mathcal{M}_\alpha^{Diag}(W) + \frac{1}{\pi} \int_{W_{thr.}}^{\infty} dW' \sum_{\alpha \neq \beta} K_{\alpha\beta}(W, W') Im \mathcal{M}_\beta(W'), \quad (3.70)$$

where α and β are the set of quantum numbers and

$$\mathcal{M}_\alpha^{Diag}(W) = \frac{P}{\pi} \int_{W_{thr.}}^{\infty} dW' \frac{Im \mathcal{M}_\alpha(W') r_\alpha(W')}{(W' - W) r_\alpha(W)} + \frac{1}{\pi} \int_{W_{thr.}}^{\infty} dW' K_{\alpha\alpha}(W, W') Im \mathcal{M}_\alpha(W'). \quad (3.71)$$

The detailed expressions for the kernels K 's and the kinematical factor $r_\alpha(W)$ are given in Refs. [166,206].

One of the methods widely used to calculate the dispersion integrals in Eqs. (3.70)-(3.71) is based on the Fermi-Watson theorem [197] such that below the two-pion threshold, we can use the following relation between the real and imaginary parts of the amplitude:

$$Im \mathcal{M}_\alpha(W, Q^2) = Re \mathcal{M}_\alpha(W, Q^2) \tan \delta_\alpha(W). \quad (3.72)$$

If one further makes an assumption about the high-energy behavior of the multipole phases, we obtain a system of coupled integral equations for $Re \mathcal{M}_\alpha(W)$. This is the standard method to apply fixed- t dispersion relations to pion photoproduction at threshold and in the $\Delta(1232)$ resonance region, which was successfully used by many authors [164–167]. The reliability of this method at low energies ($W < 1400$ MeV) is mainly based on the finding that Eq. (3.72) can

be applied to the important P_{33} multipole, dominated by the $\Delta(1232)$ resonance contribution, with good accuracy up to $W = 1600$ MeV.

Another method to calculate the dispersion integrals is based on isobaric models [207–210] which allow extending the use of fixed- t DR to higher energies. With this approach, the imaginary parts of the pion photo- and electroproduction multipoles are expressed in terms of background (\mathcal{M}^B) and resonance (\mathcal{M}^R) contributions,

$$\text{Im } \mathcal{M}_\alpha(W, Q^2) = \text{Im } \mathcal{M}_\alpha^B(W, Q^2) + \text{Im } \mathcal{M}_\alpha^R(W, Q^2). \quad (3.73)$$

In a recent work [168], both parts were modeled similar to MAID and good agreement with the data is found for the neutral pion photoproduction at threshold.

4 Chiral effective-field theory in the Δ -resonance region

In this section we review the recent extension of chiral perturbation theory into the Δ -resonance region. Such an extension yields the opportunity to study the pion-production processes in the Δ -resonance region within the systematic framework of effective field theory (EFT). Some of the applications that are relevant to the $\gamma N \Delta$ transition will be discussed here.

4.1 Effective chiral Lagrangians

The relevant effective Lagrangian of low-energy QCD will in our case include the pion, the nucleon, and the Δ -isobar fields. The color degrees of freedom, as well as heavier mesons and baryons are assumed to be “integrated out”, thus setting some upper limit on the energy range where this theory is valid. To begin with we need to write down the most general Lagrangian involving these fields and consistent with the underlying symmetries of QCD. In particular, *chiral symmetry* is known to govern the interaction of hadrons at low energies.

Let us briefly recall here that chiral symmetry is a symmetry of massless quark Lagrangian,

$$\mathcal{L}_{\text{quark}} = i \bar{q}_f \not{D} q_f, \quad (4.1)$$

where q_f is the quark field, D is the covariant QCD derivative, and the summation over the flavor index f is understood. This Lagrangian is invariant under the following rotations of quark fields in the flavor space

$$q_f \rightarrow q'_f = \left[\frac{1}{2}(1 - \gamma_5) \exp(i\theta_L^a \tau_{ff'}^a) + \frac{1}{2}(1 + \gamma_5) \exp(i\theta_R^a \tau_{ff'}^a) \right] q_{f'}, \quad (4.2)$$

where index $a = \overline{1, n_f^2 - 1}$, with n_f being the number of flavors, therefore θ 's are $2 \times (n_f^2 - 1)$ independent parameters and τ 's are the $\text{SU}(n_f)$ Pauli matrices. Since the rotations are done independently for the left-handed and right-handed quarks ($\theta_L \neq \theta_R$), we have a global $\text{SU}_L(n_f) \times \text{SU}_R(n_f)$ symmetry, known as chiral symmetry.

In QCD chiral symmetry is broken both spontaneously, by non-perturbative effects of the QCD vacuum, and explicitly, by the quark masses. Both mechanisms break chiral symmetry down to the $\text{SU}(n_f)$ symmetry under rotation Eq. (4.2) with $\theta_L = \theta_R$, the isospin symmetry. The spontaneous chiral-symmetry breaking (χ SB) leads to the generation of the chiral quark condensate, $\langle \bar{q}q \rangle \simeq -(230 \text{ MeV})^3$, and to the appearance of $n_f^2 - 1$ massless modes — Goldstone bosons (GBs). The explicit χ SB mechanism is responsible for giving the mass to the GBs. Accordingly, the effective low-energy Lagrangian of QCD should contain GB fields, and preserve explicit chiral symmetry up to the terms vanishing in the limit of massless GBs masses — the “chiral limit”.

In what follows we restrict our consideration to QCD with two flavors ($n_f = 2$), up and down quarks only. In this case the three Goldstone bosons are the pions, described by a (pseudo)scalar-isovector field π^a . The chiral Lagrangian can conveniently be written in terms of the unimodular

non-linear representation of the pion field:

$$U(x) = e^{2i\hat{\pi}(x)/f_\pi}, \quad \text{with } \hat{\pi} \equiv \frac{1}{2}\pi^a\tau^a = \frac{1}{2} \begin{pmatrix} \pi^0 & \sqrt{2}\pi^+ \\ \sqrt{2}\pi^- & -\pi^0 \end{pmatrix}, \quad (4.3)$$

where $\pi^{\pm,0}$ represent the charge eigenstates of the pion. Under the chiral transformation, $U \rightarrow RUL^\dagger$, with L and R elements of $SU_L(2)$ and $SU_R(2)$, respectively. Therefore, the Lagrangian containing an even number of U 's is chirally symmetric. It is also obvious that only derivatives of U can enter such chirally-symmetric terms. (Terms where U enters without derivatives reduce trivially to terms with derivatives, e.g., $\text{Tr}[U^\dagger \partial_\mu U \partial^\mu U^\dagger U] = \text{Tr}[\partial_\mu U \partial^\mu U^\dagger]$.) This shows that the chirally-symmetric interactions are proportional to the momentum of Goldstone bosons, and therefore is weak at low energies — the fact that plays a crucial role in the construction of the perturbative expansion in powers of momenta, which is utilized in χ PT.

In applications that furthermore will be considered, the isospin-breaking effects are negligible. We therefore shall assume exact isospin symmetry, and in particular take the masses of u and d quarks to be equal ($m_u = m_d \equiv m_q$). The lowest-order chiral Lagrangian of pion fields is then given by¹⁶

$$\mathcal{L}_\pi^{(2)} = \frac{1}{4}f_\pi^2 \text{Tr}[\partial_\mu U \partial^\mu U^\dagger + 2B m_q (U + U^\dagger)], \quad (4.4)$$

where, at this lowest order, $f_\pi \simeq 92.4$ MeV is the pion decay constant and B is related to the scalar quark condensate as $B = -\langle \bar{q}q \rangle / f_\pi^2$. The explicit χ SB, linear in U , term gives rise to the pion mass. Expanding in the pion field,

$$\mathcal{L}_\pi^{(2)} = \frac{1}{2}\partial_\mu \pi^a \partial^\mu \pi^a - \frac{1}{2}m_\pi^2 \pi^2 + O(\pi^4), \quad (4.5)$$

one can identify $m_\pi^2 = 2Bm_q$, which is the celebrated Gell-Mann–Oaks–Renner relation.

Next we include the nucleon, described by an isodoublet spinor field, $N = (p, n)^T$. Its left- and right-handed components, $N_{L,R} = \frac{1}{2}(1 \mp \gamma_5)N$, transform under $SU_L(2) \times SU_R(2)$ as $N_L \rightarrow LN_L$ and $N_R \rightarrow RN_R$. In this representation it is not easy to write down a chirally symmetric Lagrangian. In particular, the nucleon mass term, $M_N \bar{N}N = M_N(\bar{N}_L N_R + \bar{N}_R N_L)$, breaks the symmetry, while should preserve it exactly (because M_N does not vanish in the chiral limit). The trick is to redefine the nucleon field such that the its left- and right-handed components transform in the same way, which is achieved by redefining $N'_L = u N_L$ and $N'_R = u^\dagger N_R$, with $u = \sqrt{U}$. Then, $N'_{L,R} \rightarrow K N'_{L,R}$, where

$$K = \sqrt{R}u \sqrt{L}u^\dagger = \sqrt{L}u^\dagger \sqrt{R}u \quad (4.6)$$

is an $SU_V(2)$ matrix which depends on the pion field. The latter fact demands a little more work for the derivative of the nucleon field, which now transforms as (omitting from now on the prime on the redefined nucleon field): $\partial_\mu N \rightarrow K \partial_\mu N + (\partial_\mu K)N$. Obviously for the Lagrangian construction it is desirable to have a derivative which transforms in the same way as the field, i.e., $D_\mu N \rightarrow K D_\mu N$. Thus, one is led to consider

¹⁶ In the notation $\mathcal{L}^{(i)}$, the superscript indicates the order of the chiral Lagrangian, given here by the number of derivatives of Goldstone-boson fields and insertions of their mass.

$$\begin{aligned}
(\partial_\mu K)K^\dagger &= \sqrt{L}(\partial_\mu u^\dagger)u\sqrt{L^\dagger} + K u^\dagger(\partial_\mu u)K^\dagger \\
&= \sqrt{R}(\partial_\mu u)u^\dagger\sqrt{R^\dagger} + K u(\partial_\mu u^\dagger)K^\dagger.
\end{aligned} \tag{4.7}$$

Noting that $(\partial_\mu u)u^\dagger + u(\partial_\mu u^\dagger) = 0$, it is useful to introduce the SU(2) vector and axial-vector currents,

$$v_\mu \equiv \frac{1}{2} \tau^a v_\mu^a(x) = \frac{1}{2i} (u \partial_\mu u^\dagger + u^\dagger \partial_\mu u), \tag{4.8a}$$

$$a_\mu \equiv \frac{1}{2} \tau^a a_\mu^a(x) = \frac{1}{2i} (u^\dagger \partial_\mu u - u \partial_\mu u^\dagger), \tag{4.8b}$$

and observe that, under $SU_L \times SU_R$, they transform as

$$v_\mu \rightarrow K v_\mu K^\dagger + i(\partial_\mu K)K^\dagger, \tag{4.9a}$$

$$a_\mu \rightarrow K a_\mu K^\dagger. \tag{4.9b}$$

Therefore, the “chiral covariant derivative” of the nucleon field can be defined as follows:

$$D_\mu N = \partial_\mu N + i v_\mu N \rightarrow K D_\mu N. \tag{4.10}$$

The derivative of the axial-vector field can also be defined in a covariant fashion:

$$\mathcal{D}_\mu a_\nu = \partial_\mu a_\nu + i[v_\mu, a_\nu] \rightarrow K \mathcal{D}_\mu a_\nu K^\dagger. \tag{4.11}$$

We are now in position to write down a chiral Lagrangian with nucleon fields. Any hermitian Lagrangian built from a combination of the nucleon and axial-vector fields, as well as their covariant derivatives, will be chirally symmetric. The lowest-order such Lagrangian is given by:

$$\mathcal{L}_N^{(1)} = \overline{N} (i \not{D} - M_N + g_A \not{a} \gamma_5) N, \tag{4.12}$$

where $g_A \simeq 1.267$ is the nucleon axial-coupling constant.

In practice these Lagrangians need to be expanded in the pion field. To do that conveniently we write

$$u = u_1 + i(\hat{\pi}/f_\pi) u_2, \tag{4.13}$$

where $u_{1,2}$ are real functions of $\pi^2 \equiv 4\hat{\pi}^2$:

$$u_1 = \cos \frac{\sqrt{\pi^2}}{2f_\pi} = \sum_{n=0}^{\infty} \frac{1}{(2n)!} \left(-\frac{\pi^2}{4f_\pi^2} \right)^n, \tag{4.14}$$

$$u_2 = \frac{2f_\pi}{\sqrt{\pi^2}} \sin \frac{\sqrt{\pi^2}}{2f_\pi} = \sum_{n=0}^{\infty} \frac{1}{(2n+1)!} \left(-\frac{\pi^2}{4f_\pi^2} \right)^n. \tag{4.15}$$

In terms of these functions, the vector and axial currents are given by

$$v_\mu = -i \left[u_1 \partial_\mu u_1 + (1/f_\pi^2) \hat{\pi} u_2 \partial_\mu (\hat{\pi} u_2) \right] = \frac{1}{4f_\pi^2} \tau^a \varepsilon^{abc} \pi^b (\partial_\mu \pi^c) u_2^2 \\ = \frac{1}{4f_\pi^2} \tau^a \varepsilon^{abc} \pi^b (\partial_\mu \pi^c) \left(1 - \frac{\pi^2}{3! 2f_\pi^2} + \frac{\pi^4}{5! 3f_\pi^4} - \frac{\pi^6}{7! 4f_\pi^6} + \dots \right), \quad (4.16)$$

$$a_\mu = u_1 \partial_\mu (\hat{\pi} u_2) - (\partial_\mu u_1) \hat{\pi} u_2 = \frac{1}{2f_\pi} \tau^a \partial_\mu \pi^b \left[\delta^{ab} u_1 u_2 + (\pi^a \pi^b / \pi^2) (1 - u_1 u_2) \right] \\ = \frac{1}{2f_\pi} \tau^a \partial_\mu \pi^b \left[\delta^{ab} - (\pi^2 \delta^{ab} - \pi^a \pi^b) \left(\frac{1}{3! f_\pi^2} - \frac{\pi^2}{5! f_\pi^4} + \frac{\pi^4}{7! f_\pi^6} + \dots \right) \right]. \quad (4.17)$$

The currents, obviously, are of the first order in the derivatives of the pion field.

Finally let us note that in the presence of the electromagnetic field (A_μ), the electric charge of the pions is accounted for by making the “minimal substitution”: $\partial_\mu \pi^a \rightarrow \partial_\mu \pi^a + e \varepsilon^{ab3} A_\mu \pi^b$, in the above expressions. Similarly, the proton charge is included by the minimal substitution in the chiral derivative as: $D_\mu N \rightarrow D_\mu N - ie \frac{1}{2} (1 + \tau^3) A_\mu N$.

4.2 Inclusion of the spin-3/2 fields

The $\Delta(1232)$ is a spin-3/2 resonance. Therefore its spin content can conveniently be described in terms of a Rarita-Schwinger (RS) field [214]: $\psi_\mu^{(\sigma)}$, where μ is the vector and σ the spinor index; the latter index is omitted in the following. The free Lagrangian of the massive RS field is given by

$$\mathcal{L}_{\text{RS}} = \bar{\psi}_\mu (i \gamma^{\mu\nu\alpha} \partial_\alpha - M \gamma^{\mu\nu}) \psi_\nu, \quad (4.18)$$

where M is the mass, and the totally-antisymmetric products of γ -matrices are defined as: $\gamma^{\mu\nu} = \frac{1}{2} [\gamma^\mu, \gamma^\nu]$, $\gamma^{\mu\nu\alpha} = \frac{1}{2} \{ \gamma^{\mu\nu}, \gamma^\alpha \} = -i \varepsilon^{\mu\nu\alpha\beta} \gamma_\beta \gamma_5$ (using the convention $\varepsilon_{0123} = +1$). The corresponding Euler-Lagrange field equations are:

$$i \gamma^{\mu\nu\alpha} \partial_\alpha \psi_\nu - M \gamma^{\mu\nu} \psi_\nu = 0, \quad (4.19a)$$

$$\partial_\mu (i \gamma^{\mu\nu\alpha} \partial_\alpha - M \gamma^{\mu\nu}) \psi_\nu = 0 = \gamma^{\mu\nu} \partial_\mu \psi_\nu, \quad (4.19b)$$

$$\gamma_\mu (i \gamma^{\mu\nu\alpha} \partial_\alpha - M \gamma^{\mu\nu}) \psi_\nu = 0 = -(2i \gamma^{\mu\nu} \partial_\mu + 3M \gamma^\nu) \psi_\nu, \quad (4.19c)$$

which can equivalently be written as:

$$(i \not{\partial} - M) \psi_\mu = 0, \\ \partial \cdot \psi = 0, \\ \gamma \cdot \psi = 0. \quad (4.20)$$

Thus, the RS field obeys the Dirac equation, supplemented with the auxiliary conditions, or *constraints*.¹⁷ The constraints ensure that the number of independent components of the vector-

¹⁷ A canonical method for determination of constraints is due to Dirac [215]. See Refs. [216–219] for applications of Dirac’s method to the spin-3/2 case.

spinor field is reduced to the physical number of spin degrees of freedom¹⁸ (sDOF).

Note that the constraints are built into the Lagrangian. This is achieved by making the Lagrangian to be symmetric under a certain local transformation of the RS field. To exhibit this local symmetry, observe that the massless RS Lagrangian is, up to a total derivative, symmetric under

$$\psi_\mu(x) \rightarrow \psi_\mu(x) + \partial_\mu \epsilon(x), \quad (4.21)$$

where ϵ is a spinor field. This gauge symmetry is a fermionic analog of the gauge symmetry of the electromagnetic field, and just as in that case, it leads to a reduction of the number of sDOF to 2, as is required for a massless field with a spin. The mass term breaks (partially) this gauge symmetry to raise the number of sDOF to 4, as is required for a massive field with spin 3/2.

Clearly, the coupling of the RS field must be compatible with the free theory construct, in order to preserve the physical sDOF content of the theory. However this fact has largely been ignored in the literature on the field-theoretic description of the Δ . There are plenty of examples of the so-called “inconsistent” couplings, i.e., couplings that violate the free-theory constraints. Besides involving the unphysical sDOF, such couplings lead to fascinating pathologies, such as negative-norm states [220,221] and superluminal (acausal) modes [222,223].

The quest for “consistent” spin-3/2 couplings was raised from time to time, see, e.g., [224–229]. One of the most viable proposals up to date is the one of gauge-invariant couplings [219,230], suggesting that the couplings invariant under the gauge transformation (4.21) are consistent. Indeed, in the case of gauge-invariant couplings, only the mass term breaks the gauge symmetry, hence changing the sDOF content, and it is known to do that in a correct way.

A notable feature of the gauge-invariant couplings is that the corresponding vertices satisfy a transversality condition:

$$p_\mu \Gamma^\mu(p, \dots) = 0, \quad (4.22)$$

where p is the four-momentum and μ is the vector index of a spin-3/2 leg. The RS propagator, obtained by inverting the operator in Eq. (4.18), can be written as the following anticommutator:

$$S_{\mu\nu}(p) = -\frac{1}{3} \left\{ (\not{p} - M)^{-1}, (g_{\mu\nu} - \frac{1}{M^2} p_\mu p_\nu - \frac{1}{2} \gamma_{\mu\nu}) \right\}. \quad (4.23)$$

It apparently contains a spin-1/2 sector, that can be made explicit by writing the propagator in terms of the covariant spin projection operators:

$$S_{\mu\nu}(p) = -\frac{1}{\not{p} - M} P_{\mu\nu}^{(3/2)} + \frac{2}{3M^2} (\not{p} + M) P_{22,\mu\nu}^{(1/2)} - \frac{1}{\sqrt{3}M} \left(P_{12,\mu\nu}^{(1/2)} - P_{21,\mu\nu}^{(1/2)} \right), \quad (4.24)$$

where

$$P_{\mu\nu}^{(3/2)} = g_{\mu\nu} - \frac{1}{3} \gamma_\mu \gamma_\nu - \frac{1}{3p^2} (\not{p} \gamma_\mu p_\nu + p_\mu \gamma_\nu \not{p}) \quad (4.25)$$

projects onto the pure spin-3/2 states, while

¹⁸ In this case the degrees-of-freedom counting goes as follows. The vector-spinor has 16 components, the field equations show that there are 8 conditions on them, and the Dirac equation. The latter halves the number of independent components, and thus in total we have: (16-8)/2=4, the number equal to the number of different spin polarizations of massive spin-3/2 particle.

$$\begin{aligned}
P_{22,\mu\nu}^{(1/2)} &= p_\mu p_\nu / p^2, \\
P_{12,\mu\nu}^{(1/2)} &= p^\varrho p_\nu \gamma_{\mu\varrho} / (\sqrt{3} p^2), \\
P_{21,\mu\nu}^{(1/2)} &= p_\mu p^\varrho \gamma_{\varrho\nu} / (\sqrt{3} p^2)
\end{aligned} \tag{4.26}$$

are projection operators onto the spin 1/2 states. It is easy to see that, in combination with gauge-invariant couplings satisfying Eq. (4.22), the spin-1/2 contributions decouple from observables, e.g.,

$$\Gamma^\mu(p, \dots) S_{\mu\nu}(p) \Gamma^\mu(p, \dots) = \Gamma^\mu(p, \dots) \frac{1}{M - \not{p}} P_{\mu\nu}^{(3/2)}(p) \Gamma^\mu(p, \dots) \tag{4.27}$$

Such a decoupling of the lower-spin contribution is of course a desirable effect and often had been implemented in the literature ‘‘by hand’’. Namely, one would either drop the spin-1/2 terms in the non-local decomposition of the propagator, Eq. (4.23), see, e.g. [231,232,101]), or use a local decomposition, *e.g.*,

$$S_{\mu\nu}(p) = -\frac{1}{\not{p} - M} \frac{p^2}{M^2} P_{\mu\nu}^{(3/2)} + \frac{\not{p} + M}{3M^2} (g_{\mu\nu} - \frac{1}{3} \gamma_\mu \gamma_\nu) + \frac{1}{3M^2} (\gamma_\mu p_\nu - \gamma_\mu p_\nu) , \tag{4.28}$$

and retain only the $P^{(3/2)}$ term therein [233,234,103]. Both methods share a common problem: the *ad hoc* deletion of momentum-dependent terms may destroy the symmetries, such as chiral and electromagnetic-gauge invariances. For example, while the full RS propagator is guaranteed to obey a Ward-Takahashi identity with an electromagnetic coupling obtained by ‘minimal substitution’ into Eq. (4.18), the truncated propagator does not even have an inverse. In other words, since the above-mentioned procedures are not based on a Lagrangian it is not clear how to implement the symmetries. In contrast, the spin-3/2 gauge-invariant couplings ensure the spin-1/2 decoupling automatically. The only question is then how to implement the spin-3/2 gauge and other symmetries in the same Lagrangian. Prior to attempting to answer this, we would like to make one more remark.

While the spin-3/2 gauge-invariant couplings make sense, perhaps equally consistent seems the idea of having couplings which break the gauge symmetry in the same way as the mass term. However, such couplings should then be proportional to the mass, in order to provide consistency in the massless limit. And the couplings proportional to the mass can be rewritten in a gauge-invariant way by using the free-field equation, Eq. (4.19a), or equivalently by a field redefinition. To give an example, consider a coupling of the RS field to a spinor Ψ and a scalar ϕ :

$$\mathcal{L}_{\text{int}} = g M \bar{\Psi} \gamma^{\mu\nu} \psi_\mu \partial_\nu \phi + \text{H.c.}, \tag{4.29}$$

where g is a dimension [mass]⁻² coupling constant. This coupling is known to affect the constraints in the same way as the mass term [235,219]. Upon the field redefinition,

$$\psi_\mu \rightarrow \psi_\mu + g \Psi \partial_\mu \phi, \tag{4.30}$$

we have $\mathcal{L}_{\text{RS}} + \mathcal{L}_{\text{int}} \rightarrow \mathcal{L}_{\text{RS}} + \mathcal{L}'_{\text{int}}$, with the new coupling being

$$\mathcal{L}'_{\text{int}} = ig \bar{\Psi} \gamma^{\mu\nu\alpha} (\partial_\alpha \psi_\mu) \partial_\nu \phi + \text{H.c.}, \tag{4.31}$$

which evidently is a gauge-invariant coupling.

One should emphasize here that the above example is quite exceptional, because in general field redefinitions lead to the appearance of higher-order couplings, the so-called “contact terms”. Their appearance, however, is not troublesome as long as we deal with effective theories, where all possible higher-order term are present anyway, unless forbidden by other symmetries. The latter condition brings us again to the question of how the spin-3/2 gauge symmetry will co-exist with other local or global symmetries of the effective theory, and in particular the chiral symmetry.

Certainly it is not easy, in many cases impossible, to incorporate several different symmetries in a given interaction. For example, in the description of electrically charged RS field, the only possible way to have both the spin-3/2 and the electromagnetic gauge symmetries, in a closed form, is to allow for general covariance in a de-Sitter geometry, resulting in an extended supergravity [237]. In many other cases, e.g., spin-5/2, even such formidable possibilities are unavailable. Nevertheless, within the EFT framework one can envision a following method for inclusion of the spin-3/2 (and other higher-spin) gauge symmetries.

To start with, one may construct the effective Lagrangian disregarding the higher-spin gauge symmetry. Then, in case of a massive spin-3/2 field, the gauge-invariant couplings can be obtained by the following substitution [236]:

$$\psi_\mu \rightarrow \psi'_\mu = (M\gamma^{\mu\sigma})^{-1}\gamma^{\sigma\nu\alpha}i\partial_\alpha\psi_\nu \quad (4.32)$$

everywhere in the interaction Lagrangian. This step ensures the spin-3/2 gauge symmetry while providing an on-shell equivalence of the new and old couplings. Unfortunately in doing so, the other symmetries are likely to be violated since, while the field transforms covariantly under other symmetries, its derivative does not. To restore the other symmetries one needs to replace the derivatives by covariant derivatives (‘minimal substitution’):

$$\partial_\mu\psi_\nu \rightarrow D_\mu\psi_\nu, \quad (4.33)$$

hence violating again the spin-3/2 gauge symmetry.

To break out of this loop, we need to note that generically $D_\mu = \partial_\mu + \Gamma_\mu$, where the “connection” Γ_μ is at least one order higher (in the EFT expansion) than ∂_μ . Then, if the first substitution restores the spin-3/2 symmetry to, say, order n , the other symmetries will be violated only at order $n+1$ or higher. So to order n all the symmetries are satisfied. When going to the next order, we would need to make the minimal substitution to restore the other symmetries to that order and the first substitution to restore the spin-3/2 symmetry. One can continue this procedure to establish all the symmetries to any given order in the effective expansion.

We emphasize that substitution (4.32) is certainly not unique, other free equations of the RS field can be used, e.g.,

$$\psi_\mu = (i/M)\gamma^\nu(\partial_\mu\psi_\nu - \partial_\nu\psi_\mu), \quad (4.34)$$

$$\psi^\mu = (1/M)\varepsilon^{\mu\nu\alpha\beta}\gamma_\beta\gamma_5\partial_\alpha\psi_\nu, \quad (4.35)$$

all leading to gauge-invariant couplings, equivalent at the order where the field equations are used. Further on we will apply this method to write down chiral Lagrangians involving the

Δ -isobar field.

4.3 Chiral Lagrangians with Δ 's

The spin-3/2 isospin-3/2 $\Delta(1232)$ can be represented by a vector-spinor *isoquartet* field, $\Delta_\mu = (\Delta_\mu^{++}, \Delta_\mu^+, \Delta_\mu^0, \Delta_\mu^-)^T$, where the four components correspond to the charge states of the Δ -isobar. Inclusion of an isoquartet into the chiral Lagrangian can be done by generalizing slightly the formalism of Subsect. 4.1 for the isodoublet field to the case of isospin 3/2. It basically amounts to replacing the $SU(2)$ generators in the fundamental representation $(\tau^a/2)$ by the generators in the isospin-3/2 representation. The latter have the following form:

$$\mathcal{T}^1 = \frac{2}{3} \begin{pmatrix} 0 & \sqrt{3}/2 & 0 & 0 \\ \sqrt{3}/2 & 0 & 1 & 0 \\ 0 & 1 & 0 & \sqrt{3}/2 \\ 0 & 0 & \sqrt{3}/2 & 0 \end{pmatrix}, \quad (4.36a)$$

$$\mathcal{T}^2 = \frac{2i}{3} \begin{pmatrix} 0 & -\sqrt{3}/2 & 0 & 0 \\ \sqrt{3}/2 & 0 & -1 & 0 \\ 0 & 1 & 0 & -\sqrt{3}/2 \\ 0 & 0 & \sqrt{3}/2 & 0 \end{pmatrix}, \quad (4.36b)$$

$$\mathcal{T}^3 = \text{diag}(1, \frac{1}{3}, -\frac{1}{3}, -1), \quad (4.36c)$$

and satisfy $\mathcal{T}^a \mathcal{T}^a = 5/3$.

The chiral transformation of the isoquartet field is then given as

$$\Delta_\mu \rightarrow K_4 \Delta_\mu \quad (4.37)$$

where K_4 is a four-dimensional $SU_V(2)$ matrix. Similarly, we introduce the isospin-3/2 vector and axial-vector currents:

$$v_\mu^{(3/2)} \equiv \mathcal{T}^a v_\mu^a(x) = \mathcal{T}^a \text{Tr}(\tau^a v_\mu), \quad (4.38a)$$

$$a_\mu^{(3/2)} \equiv \mathcal{T}^a a_\mu^a(x) = \mathcal{T}^a \text{Tr}(\tau^a a_\mu), \quad (4.38b)$$

and the chiral covariant derivative of the Δ -field:

$$D_\mu \Delta_\nu = (\partial_\mu + i v_\mu^{(3/2)}) \Delta_\nu. \quad (4.39)$$

Before writing down the effective Lagrangians using these ingredients, let us remark on the

other frequently used representation. The so-called *isospurion* representation is based on an isovector-isodoublet field [84,238]: $\Delta_\mu^a = T^a \Delta_\mu$, with T the isospin-1/2-to-3/2 transition matrices defined as

$$T^1 = \frac{1}{\sqrt{6}} \begin{pmatrix} -\sqrt{3} & 0 & 1 & 0 \\ 0 & -1 & 0 & \sqrt{3} \end{pmatrix}, \quad (4.40a)$$

$$T^2 = \frac{-i}{\sqrt{6}} \begin{pmatrix} \sqrt{3} & 0 & 1 & 0 \\ 0 & 1 & 0 & \sqrt{3} \end{pmatrix}, \quad (4.40b)$$

$$T^3 = \sqrt{\frac{2}{3}} \begin{pmatrix} 0 & 1 & 0 & 0 \\ 0 & 0 & 1 & 0 \end{pmatrix}, \quad (4.40c)$$

and satisfying $T^a T^{b\dagger} = \delta^{ab} - \frac{1}{3} \tau^a \tau^b$, $T^{a\dagger} T^a = 1_4$, $\tau^a T^a = 0$. Under a chiral rotation the isospurion transforms as

$$\Delta_\mu^a \rightarrow K^{ab} K \Delta_\mu^b, \quad (4.41)$$

where K , an $SU_V(2)$ matrix given by Eq. (4.6), acts on the doublet components, while $K^{ab} = \frac{1}{2} \text{Tr}(\tau^a K \tau^b K^\dagger)$ transforms the isovector components. Note that the latter object has the following important properties: $K^{ab} \tau^b = K \tau^a K^\dagger$, $K^{ab} K^{bc} = \delta^{ac}$, where δ is the Kronecker symbol. The transformation properties of the isospin-3/2 field in the two different representations are related via:

$$K_4 = T^{a\dagger} K T^b K^{ab}. \quad (4.42)$$

Knowing these relations, one can easily go from one representation to another. They both, of course, are equivalent at the level of observables.

In writing down the chiral Lagrangian we adopt the isoquartet representation. The first-order Lagrangian of the Δ is given by:

$$\mathcal{L}_\Delta^{(1)} = \overline{\Delta}_\mu (i \gamma^{\mu\nu\rho} D_\rho - M_\Delta \gamma^{\mu\nu}) \Delta_\nu - \frac{1}{2} H_A \overline{\Delta}_\mu \not{d}^{(3/2)} \gamma_5 \Delta^\mu, \quad (4.43)$$

where $M_\Delta \simeq 1.232$ GeV is the mass of the Δ -isobar, H_A is the axial coupling constant of the Δ given, in the large- N_C limit, by $H_A = (9/5)g_A$. Note that the electric charge of the Δ can be accounted for by the following minimal substitution: $D_\mu \rightarrow D_\mu - ie\frac{1}{2}(1 + 3\mathcal{T}^3)A_\mu$.

The chiral interactions in Eq. (4.43) obviously do not have the spin-3/2 gauge symmetry, see Eq. (4.21). We follow the program outlined in the previous section to incorporate this constraint. First, we write out the spin-3/2 gauge-invariant couplings which are on-shell equivalent to the ones in Eq. (4.43), e.g.,

$$\begin{aligned} \mathcal{L}_\Delta^{(1)} = & \overline{\Delta}_\mu (i \gamma^{\mu\nu\rho} \partial_\rho - M_\Delta \gamma^{\mu\nu}) \Delta_\nu \\ & - \frac{1}{M_\Delta^2} \varepsilon^{\mu\nu\alpha\beta} (\partial_\alpha \overline{\Delta}_\mu) [\not{d}^{(3/2)} + \frac{1}{2} H_A \not{d}^{(3/2)}] \gamma_5 (\partial_\beta \Delta_\nu). \end{aligned} \quad (4.44)$$

The ‘minimal substitution’ into the second term, which is required to restore the chiral symmetry, generates following higher-order contributions, such as:

$$\mathcal{L}_{\Delta}^{(2)} = -\frac{1}{M_{\Delta}^2} \varepsilon^{\mu\nu\alpha\beta} (\partial_{\alpha} \overline{\Delta}_{\mu}) [\psi^{(3/2)} \gamma_5 + \frac{1}{2} H_A \not{d}^{(3/2)}] v_{\beta}^{(3/2)} \Delta_{\nu} + \text{H.c.} \quad (4.45)$$

The spin-3/2 gauge-symmetry is manifest in the following on-shell equivalent Lagrangian:

$$\mathcal{L}_{\Delta}^{(2)} = -\frac{i}{M_{\Delta}^3} \varepsilon^{\mu\nu\alpha\beta} (\partial_{\alpha} \overline{\Delta}_{\mu}) [\psi^{(3/2)} \gamma_5 + \frac{1}{2} H_A \not{d}^{(3/2)}] v_{\beta}^{(3/2)} \gamma^{\rho} (\partial_{\rho} \Delta_{\nu} - \partial_{\nu} \Delta_{\rho}) + \text{H.c.} \quad (4.46)$$

This is of course not the complete second-order Lagrangian, only the term required by chiral symmetry when the first-order Lagrangian (4.44) is used.

The terms required by chiral symmetry are not only of higher order in the derivatives of the pion field, they are of higher order in pion field itself, and hence in many cases may appear only in multi-loop corrections. Here we shall focus on a single-pion production with no more than one-loop contributions, thus it suffices to consider the couplings with no more than three pion fields. The relevant terms of the chirally and gauge symmetric Lagrangian of the Δ , expanded to third order in the pion field, read

$$\mathcal{L}_{\Delta\Delta\pi}^{(1)} = \frac{H_A}{2M_{\Delta}f_{\pi}} \varepsilon^{\mu\nu\rho\sigma} \overline{\Delta}_{\mu} \mathcal{T}^a (\partial_{\rho} \Delta_{\nu}) \partial_{\sigma} \pi^a + O(\pi^3). \quad (4.47)$$

Similarly, we write a few relevant couplings of the $N\Delta$ -transition Lagrangian in the form which manifests the spin-3/2 gauge symmetry and is expanded to leading order in the pion field:

$$\mathcal{L}_{N\Delta}^{(1)} = \frac{ih_A}{2f_{\pi}M_{\Delta}} \overline{N} T^a \gamma^{\mu\nu\lambda} (\partial_{\mu} \Delta_{\nu}) \partial_{\lambda} \pi^a + \text{H.c.}, \quad (4.48a)$$

$$\mathcal{L}_{N\Delta}^{(2)} = \frac{h_1}{2f_{\pi}M_{\Delta}^2} \overline{N} T^a \gamma^{\mu\nu\lambda} (\partial_{\lambda} \not{d} \pi^a) (\partial_{\mu} \Delta_{\nu}) + \text{H.c.}, \quad (4.48b)$$

$$\mathcal{L}_{N\Delta}^{(2)} = \frac{3ieg_M}{2M_N(M_N + M_{\Delta})} \overline{N} T^3 \partial_{\mu} \Delta_{\nu} \tilde{F}^{\mu\nu} + \text{H.c.}, \quad (4.48c)$$

$$\mathcal{L}_{N\Delta}^{(3)} = \frac{-3e}{2M_N(M_N + M_{\Delta})} \overline{N} T^3 \gamma_5 \left[g_E (\partial_{\mu} \Delta_{\nu}) + \frac{ig_C}{M_{\Delta}} \gamma^{\alpha} (\partial_{\alpha} \Delta_{\nu} - \partial_{\nu} \Delta_{\alpha}) \partial_{\mu} \right] F^{\mu\nu} + \text{H.c.} \quad (4.48d)$$

where $F^{\mu\nu}$ and $\tilde{F}^{\mu\nu}$ are the electromagnetic field strength and its dual. Note that the electric and the Coulomb $\gamma N\Delta$ couplings are of one order higher than the magnetic one, because of the γ_5 which involves the ‘small components’ of the fermion fields and thus introduces an extra power of the 3-momentum.

Finally, for the applications below it will also be useful to write out the magnetic moment coupling for the nucleon and Δ fields:

$$\mathcal{L}_N^{(2)} = \frac{ie}{4M_N} \overline{N} \frac{1}{2} (\kappa_N^{(S)} + \kappa_N^{(V)} \tau_3) \sigma_{\mu\nu} N F^{\mu\nu}, \quad (4.49a)$$

$$\mathcal{L}_\Delta^{(2)} = \frac{ie}{2M_\Delta} \overline{\Delta} \frac{1}{2} [1 + \kappa_\Delta^{(S)} + 3(1 + \kappa_\Delta^{(V)}) \mathcal{T}_3] \Delta_\nu F^{\mu\nu}, \quad (4.49b)$$

where $\kappa^{(S)}, \kappa^{(V)}$ correspond in both the N and Δ case with the isoscalar and isovector anomalous magnetic moments. Also in both cases the anomalous magnetic moments are defined as the deviation from the gyromagnetic ratio ($g = \mu/s$) from 2, the natural value for an elementary particle of any spin s [240–242]. In this notation the magnetic moment of the Δ corresponds with

$$\mu_\Delta = \frac{e}{2M_\Delta} \left(3e_\Delta + \frac{1}{2}\kappa_\Delta^{(S)} + \frac{3}{2}\kappa_\Delta^{(V)} \mathcal{T}_3 \right) \quad (4.50)$$

where $e_\Delta = (1 + 3\mathcal{T}_3)/2$ is the charge of the Δ in units of e .

We should point out that such a choice of the anomalous magnetic moment of the Δ is not (yet) widely used. One usually defines it as a deviation of the magnetic moment from the magneton value: $e e_\Delta / (2M_\Delta)$. Namely, in Eq. (2.20a), $F_2^*(0)$ corresponds precisely with the conventional definition of the anomalous magnetic moment. The relation between the two conventions is obvious: $\kappa_\Delta^{(S,V)} = F_2^{*(S,V)}(0) - 2$.

4.4 Power counting, renormalization and naturalness

The fact that the strength of the chiral interactions goes with derivatives of pion fields allows one to organize a perturbative expansion in powers of pion momentum and mass — the chiral perturbation theory [7,8]. The small expansion parameter is $p/\Lambda_{\chi SB}$, where p is the momentum and $\Lambda_{\chi SB} \sim 4\pi f_\pi \approx 1$ GeV stands for the scale of spontaneous chiral symmetry breaking. Based on this expansion, one should be able to systematically compute the pion-mass dependence of static quantities, such as nucleon mass, magnetic moments, as well as the momentum dependence of scattering processes, such as pion-pion and pion-nucleon scattering. It generically is an effective-field theory (EFT) expansion, in this case a low-energy expansion of QCD. One expects to obtain exactly the same answers as from QCD directly, provided the low-energy constants (LECs) — the parameters of the effective Lagrangian — are known, either from experiment or from QCD itself.

One of the principal ingredients of an EFT expansion is *power counting*. The power counting scheme assigns an order to Feynman graphs arising in loopwise expansion of the amplitudes, and thus defines which graphs need to be computed to a given order in the expansion. In a way, it simply is a tool to estimate the size of different contributions without doing explicit calculations. Of course, the main requirement on a power-counting scheme is that it should estimate the relative size of various contributions correctly. So, if a given graph is power counted to be of subleading order, but in explicit calculations gives a dominant effect, the power-counting scheme fails.

In χPT with pions and nucleons alone, the power counting for a graph with L loops, N_π

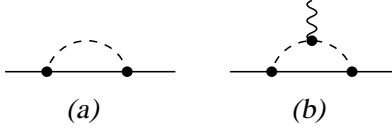


Fig. 33. Nucleon self-energy and electromagnetic-moment corrections to one loop.

(N_N) internal pion (nucleon) lines, and V_k vertices from k th-order Lagrangian, estimates its contribution to go as $p^{n_{\chi\text{PT}}}$, with the power given by [243]:

$$n_{\chi\text{PT}} = 4L - 2N_\pi - N_N + \sum_k kV_k. \quad (4.51)$$

For example, the one-loop correction to the nucleon mass given in Fig. 33(a) is characterized by $L = 1$, $N_\pi = 1$, $N_N = 1$, $V_1 = 2$, while the correction to the nucleon electromagnetic vertex Fig. 33(b) has $L = 1$, $N_\pi = 2$, $N_N = 1$, $V_1 = 2$, and $V_2 = 1$ (two πNN vertices from $\mathcal{L}^{(1)}$ and the $\gamma\pi\pi$ vertex from $\mathcal{L}^{(2)}$). Therefore, both of these graphs count as order p^3 .

Another important ingredient is the *renormalization* program. First of all, although the interactions are non-renormalizable in the usual sense, one always should be able to absorb the infinities into the available LECs. This is ensured simply by the fact that the effective Lagrangian contains all the possible terms allowed by symmetries and entering with arbitrary coefficients. Second, the renormalization program should be compatible with power counting. This issue is related to the arbitrariness of renormalization, namely the arbitrariness of the finite part that remains after the renormalization. In the EFT framework, it is clear that only the parts which satisfy power counting should remain. That is, if power counting estimates the graph to be, say, of order p^3 , but its unrenormalized contribution contains a piece which goes as p^2 , that piece must be completely absorbed into the p^2 counter term. Again symmetries and the generality of the effective Lagrangian ensure that this can always be done.

In the above example of the one-loop correction to the nucleon mass, an explicit calculation shows [243] that the loop produces $\mathcal{O}(m_\pi^0)$ and $\mathcal{O}(m_\pi^2)$ terms, both of which are large. In fact, they are ultravioletly divergent, hence are infinitely large. However, the appears of such terms is not in violation of the power counting, because there are two LECs: the nucleon mass in the chiral limit, $M^{(0)}$, and c_{1N} , which enter at $\mathcal{O}(m_\pi^0)$ and $\mathcal{O}(m_\pi^2)$, respectively, and renormalize away the large contributions coming from the loop. The renormalized result (up to p^4 terms) is given in Eq. (2.47), such that the loop contribution begins at $\mathcal{O}(m_\pi^3)$ in agreement with power counting.

Similarly, in the case of the chiral correction to the electromagnetic interaction, an explicit calculation will reveal (see, e.g., [244,273,249]) that the magnetic contribution goes as

$$\text{Fig. 33(b)} = \frac{e}{2M_N} \varepsilon_\mu \sigma^{\mu\nu} q_\nu \left(\frac{g_A M_N}{4\pi f_\pi} \right)^2 \left[c_0 + c_1 \frac{m_\pi}{M_N} + \mathcal{O}(m_\pi^2) \right], \quad (4.52)$$

where ε and q are the four-vectors of photon polarization and momentum, respectively, and where $c_{0,1}$ are real coefficients which depend only on isospin. Recalling that both the charge e and the photon momentum count as one power of p , we find that the c_0 term is of order p^2 , hence superficially the power counting is violated. However, there is a LEC coming at this order from $\mathcal{L}_N^{(2)}$ in Eq. (4.49). The c_0 term, would it be finite or infinite, can be absorbed by this LEC, thus

providing correct power-counting for the renormalized loop graph.

A cornerstone principle of effective field theories in general is *naturalness*, meaning that the (dimensionless) LECs must be of “natural size”, *i.e.*, of order of unity. Any significant fine-tuning of even a single LEC leads, obviously, to a break-down of the EFT expansion. Therefore, if an EFT describes well the experimental data, but at the expense of fine-tuned LECs, the result is negative: EFT fails in the description of those data. Such an EFT can still be useful for getting insights into the physics beyond the EFT itself. Namely, by looking at the form of the fine-tuned operators, one might be able to deduce which contributions are missing.

For instance, it is well known that the NLO χ PT description of the pion-nucleon elastic scattering, near threshold, requires relatively large values for some of the LECs, see *e.g.*, Ref. [9]. It is not difficult to see that the operators corresponding with those unnatural LECs can be matched to the “integrated out” Δ -resonance contributions. The problem is that the Δ is relatively light, its excitation energy, $\Delta \equiv M_\Delta - M_N \sim 0.3$ GeV, is still quite small compared to $\Lambda_{\chi SB} \sim 1$ GeV. Integrating out the Δ -isobar degrees of freedom corresponds to an expansion in powers of p/Δ , with $p \sim m_\pi$, which certainly is not as good of an expansion as the one in the meson sector, in powers of $p/\Lambda_{\chi SB}$.

The fine-tuning of the “Deltaless” χ PT seems to be lifted by the inclusion of an explicit Δ -isobar. Also, the limit of applicability of the EFT expansion is then extended to momenta of order of the resonance excitation energy, $p \sim \Delta$. Such momenta can still be considered as soft, as long as $\Delta/\Lambda_{\chi SB}$ can be treated as small. The resulting χ PT with pion, nucleon, and Δ -isobar degrees of freedom has two distinct light scales: m_π and Δ . Perhaps the most straightforward way to proceed is to organize a simultaneous expansion in two different small parameters: $\epsilon = m_\pi/\Lambda_{\chi SB}$ and $\delta = \Delta/\Lambda_{\chi SB}$. However, for power counting purposes, it is certainly more convenient to have a single small parameter, and thus a relation between ϵ and δ is usually imposed. We emphasize that the relation is established only at the level of power counting and not in the actual calculations of graphs. In the literature up to date two such relations between ϵ and δ are used: (i) $\epsilon \sim \delta$, which we will commonly refer to as the “ ϵ -expansion” [84,238,86,239,104], (ii) $\epsilon \sim \delta^2$, the “ δ -expansion” [90,247]. The table below (Table 2) summarizes the counting of momenta in the three expansions: Deltaless ($\Delta\chi$ PT), ϵ -expansion, and δ -expansion.

EFT	$p \sim m_\pi$	$p \sim \Delta$
$\Delta\chi$ PT	$\mathcal{O}(p)$	$\mathcal{O}(1)$
ϵ -expansion	$\mathcal{O}(\epsilon)$	$\mathcal{O}(\epsilon)$
δ -expansion	$\mathcal{O}(\delta^2)$	$\mathcal{O}(\delta)$

Table 2

The counting of momenta in the three different χ EFT expansions discussed in the text.

An unsatisfactory feature of the ϵ -expansion is that the Δ -resonance contributions are always estimated to be of the same size as the nucleon contributions. In reality (revealed by actually computing these contributions), they are *suppressed* at low energies and *dominate* in the the Δ -resonance region. Thus, apparently the power-counting in the ϵ -expansion *overestimates* the Δ -contributions at lower energies and *underestimates* them at the resonance energies. The δ -expansion improves on this aspect, as is briefly described in what follows.

In the δ -expansion, the power counting depends on the energy domain, since in the *low-energy*

region ($p \sim m_\pi$) and the *resonance region* ($p \sim \Delta$), the momentum counts differently, see Table 2. This dependence most significantly affects the power counting of the direct resonance exchanges, the so-called one-Delta-reducible (ODR) graphs. Figure 34 illustrates examples of the ODR graphs for the case of Compton scattering on the nucleon. These graphs are all characterized by having a number of ODR propagators, each going as

$$S_{ODR} \sim \frac{1}{s - M_\Delta^2} \sim \frac{1}{2M_\Delta} \frac{1}{p - \Delta}, \quad (4.53)$$

where p is the soft momentum, in this case given by the photon energy. In contrast the nucleon propagator in analogous graphs would go simply as $S_N \sim 1/p$.

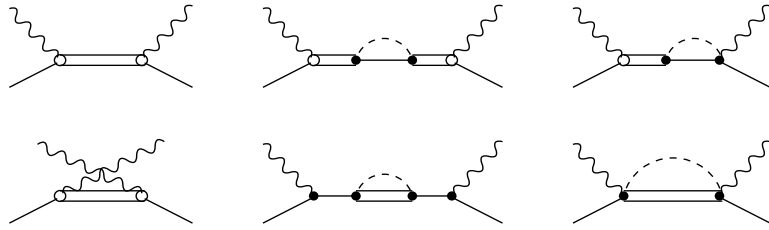


Fig. 34. Examples of the one-Delta-reducible (1st row) and the one-Delta-irreducible (2nd row) graphs in Compton scattering on the nucleon.

Therefore, in the low-energy region, the Δ and nucleon propagators would count as $\mathcal{O}(1/\delta)$ and $\mathcal{O}(1/\delta)$, the Δ being suppressed by one power of the small parameter as compared to the nucleon. In the resonance region, the ODR graphs obviously all become large. Fortunately they all can be subsumed, leading to “dressed” ODR graphs with a definite power-counting index. Namely, it is not difficult to see that the resummation of the classes of ODR graphs results in ODR graphs with only a single ODR propagator of the form

$$S_{ODR}^* = \frac{1}{S_{ODR}^{-1} - \Sigma} \sim \frac{1}{p - \Delta - \Sigma}, \quad (4.54)$$

where Σ is the Δ self-energy. The expansion of the self-energy begins with p^3 , and hence in the low-energy region does not affect the counting of the Δ contributions. However, in the resonance region the self-energy not only ameliorates the divergence of the ODR propagator at $s = M_\Delta^2$ but also determines power-counting index of the propagator. Defining the Δ -resonance region formally as the region of p where

$$|p - \Delta| \leq \delta^3 \Lambda_{\chi SB}, \quad (4.55)$$

we deduce that an ODR propagator, in this region, counts as $\mathcal{O}(1/\delta^3)$. Note that the nucleon propagator in this region counts as $\mathcal{O}(1/\delta)$, hence is suppressed by two powers as compared to ODR propagators. Thus, within the power-counting scheme we have the mechanism for estimating correctly the relative size of the nucleon and Δ contributions in the two energy domains. In Table 3 we summarize the counting of the nucleon, ODR, and one-Delta-irreducible (ODI) propagators in both the ϵ - and δ -expansion.

	ϵ -expansion	δ -expansion	
	$p/\Lambda_{\chi SB} \sim \epsilon$	$p \sim m_\pi$	$p \sim \Delta$
S_N	$1/\epsilon$	$1/\delta^2$	$1/\delta$
S_{ODR}	$1/\epsilon$	$1/\delta$	$1/\delta^3$
S_{ODI}	$1/\epsilon$	$1/\delta$	$1/\delta$

Table 3

The counting for the nucleon, one-Delta-reducible (ODR), and one-Delta-irreducible (ODI) propagators in the two different expansion schemes. The counting in the δ -expansion depends on the energy domain.

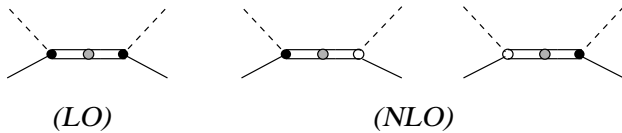


Fig. 35. The leading and next-to-leading order graphs of the πN -scattering amplitude.

We conclude this discussion by giving the general formula for the power-counting index in the δ -expansion. The power-counting index, n , of a given graph simply tells us that the graph is of the size of $\mathcal{O}(\delta^n)$. For a graph with L loops, V_k vertices of dimension k , N_π pion propagators, N_N nucleon propagators, N_Δ Delta propagators, N_{ODR} ODR propagators and N_{ODI} ODI propagators (such that $N_\Delta = N_{ODR} + N_{ODI}$) the index is

$$n = \begin{cases} 2n_{\chi\text{PT}} - N_\Delta, & p \sim m_\pi; \\ n_{\chi\text{PT}} - 3N_{ODR} - N_{ODI}, & p \sim \Delta, \end{cases}$$

where $n_{\chi\text{PT}}$, given by Eq. (4.51), is the index of the graph in χPT with no Δ 's. For further details on the δ counting we refer to Ref. [90]. The rest of this section is devoted to applications of χEFT to several processes that are relevant for the $N \rightarrow \Delta$ transition.

4.5 In practice: the next-to-leading order calculations

4.5.1 Pion-nucleon scattering

The pion-nucleon (πN) scattering amplitude at leading order in the δ -expansion in the resonance region, is given by the graph (LO) in Fig. 35. This is an example of an ODR graph and thus the Δ -propagator counts as δ^{-3} . The leading-order vertices are from $\mathcal{L}^{(1)}$ and since $p \sim \delta$, the whole graph is $\mathcal{O}(\delta^{-1})$.

At the NLO, the graphs labeled (NLO) Fig. 35 begin to contribute. The $\pi N \Delta$ vertices denoted by dots stand for the h_A coupling from $\mathcal{L}_{N\Delta}^{(2)}$ and the circles for the h_1 coupling from $\mathcal{L}_{N\Delta}^{(2)}$, see Eq. (4.48). The NLO graphs are thus $\mathcal{O}(\delta^0)$. It is not difficult to see that graphs containing the loop correction to the vertex, as well as the nucleon-exchange graphs, begin to contribute at $N^2\text{LO}$ [$\mathcal{O}(\delta)$].

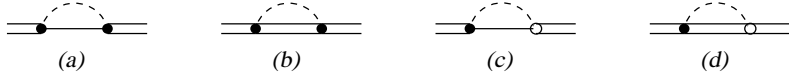


Fig. 36. The leading and next-to-leading order graphs of the Δ self-energy.

The ODR graphs contribute only to the P_{33} and D_{33} partial waves. The D_{33} contribution is due to the “negative-energy states” contribution and is suppressed by δ^3 , as compared to the “positive-energy states” contributions to P_{33} . The D_{33} will therefore be omitted from our considerations.

The P_{33} contribution can conveniently be written in terms of the following partial-wave ‘ K -matrix’:

$$K_{P_{33}} = -\frac{1}{2} \frac{\Gamma(W)}{W - M_\Delta}, \quad (4.56)$$

where $W = \sqrt{s}$ is the total energy and Γ is an energy-dependent width, which arises from the Δ self-energy. At this stage it is already taken into account that the real part of the self-energy will lead to the mass and field renormalization and otherwise are of N^2LO . Thus, only the imaginary part of the self-energy affects the NLO calculation.

In the ODR graphs of Fig. 35, the Δ -propagator is dressed by the self-energy given to NLO by the graphs in Fig. 36. The Lorentz-covariant self-energy of the spin-3/2 Δ is a rank-2 tensor, has the γ -matrix structure and is dependent on one four-momentum. As such, this object can in general be decomposed onto a basis of 10 independent scalar functions. The procedure for computing these functions is cumbersome. The procedure of “dressing” the Rarita-Schwinger propagator with such a self-energy is impossible, because the propagator is derived from the Lagrangian with only two independent structures: the kinetic and the mass term. As discussed above, the form of the Rarita-Schwinger Lagrangian is constrained by the requirement of physical spin degrees-of-freedom count, and hence the expression for the self-energy must be constrained as well. The spin-3/2 gauge-invariant couplings, introduced in the previous two subsections, automatically ensure these constraints. In that case, the most general form of the self-energy can be written as

$$\Sigma_{\alpha\beta}(p) = \Sigma_\Delta(\not{p}) P_{\alpha\beta}^{(3/2)}(p), \quad (4.57)$$

where $\mathcal{P}^{(3/2)}$ is the covariant spin-3/2 projection operator, and $\Sigma_\Delta(\not{p})$ has the spin-1/2 Lorentz form, thus 2 independent Lorentz structures as needed.

The “dressed” propagator of the Δ to NLO is then given as follows:

$$S_{\alpha\beta}(p) = \frac{-Z_2}{(\not{p} - M_\Delta)[1 - Z_2 \Sigma'_\Delta(M_\Delta)] - (M_\Delta^{(B)} - M_\Delta + Z_2 \Sigma_\Delta(M_\Delta))} P_{\alpha\beta}^{(3/2)}(p), \quad (4.58)$$

where $M_\Delta^{(B)}$ is the “bare” mass, Z_2 is the field renormalization constant, and

$$\Sigma'_\Delta(M_\Delta) = \partial/\partial \not{p} \Sigma_\Delta(\not{p})|_{\not{p}=M_\Delta}. \quad (4.59)$$

Our ‘on-shell renormalization’ conditions read:

$$1 - Z_2 \operatorname{Re} \Sigma'_\Delta(M_\Delta) = Z_2, \quad (4.60)$$

$$M_\Delta^{(B)} - M_\Delta + Z_2 \operatorname{Re} \Sigma_\Delta(M_\Delta) = 0, \quad (4.61)$$

and thus the renormalized NLO propagator is given by

$$S_{\alpha\beta}(p) = \frac{-1}{(\not{p} - M_\Delta)[1 - i \operatorname{Im} \Sigma'_\Delta(M_\Delta)] - i \operatorname{Im} \Sigma_\Delta(M_\Delta))} P_{\alpha\beta}^{(3/2)}(p). \quad (4.62)$$

The energy-dependent width in Eq. (4.56) is then given by

$$\Gamma(W) = -2 \operatorname{Im} [\Sigma_\Delta(M_\Delta) + (W - M_\Delta) \Sigma'_\Delta(M_\Delta)]. \quad (4.63)$$

and therefore the expression for the K-matrix becomes

$$K_{P33} = \frac{\operatorname{Im} \Sigma_\Delta(M_\Delta)}{W - M_\Delta} + \operatorname{Im} \Sigma'_\Delta(M_\Delta). \quad (4.64)$$

An elementary calculation (see, *e.g.*, [109]) of the graphs in Fig. 36 yields, in the region $W \in [M_N + m_\pi, M_\Delta + m_\pi]$, the following result:

$$\operatorname{Im} \Sigma(M_\Delta) = -\pi \frac{h_A^2 + 2h_A h_1 \frac{\Delta}{M_\Delta}}{24 M_\Delta^5 (8\pi f_\pi)^2} [(M_N + M_\Delta)^2 - m_\pi^2]^{5/2} (\Delta^2 - m_\pi^2)^{3/2}, \quad (4.65a)$$

$$\begin{aligned} \operatorname{Im} \Sigma'(M_\Delta) = & -\frac{\pi h_A^2}{8 M_\Delta^6 (8\pi f_\pi)^2} [(M_N + M_\Delta)^2 - m_\pi^2]^{3/2} \sqrt{\Delta^2 - m_\pi^2} \\ & \times \left[M_\Delta^4 - (M_N^2 - m_\pi^2)^2 - \frac{1}{3} (\Delta^2 - m_\pi^2) (M_N^2 + M_\Delta M_N - m_\pi^2) \right]. \end{aligned} \quad (4.65b)$$

The πN scattering phase-shift is related to the partial-wave K-matrix simply as

$$\delta_l = \arctan K_l, \quad (4.66)$$

where l stands for the conserved quantum numbers: spin (J), isospin (I) and parity (P). We emphasize that the P_{33} phase (corresponding to $J = 3/2 = I, P = +$) is the only nonvanishing one at NLO in the resonance region, and is computed by substituting the NLO expressions for the self-energy [Eq. (4.65)] into Eq. (4.64). We can then fix the LECs h_A and h_1 by fitting the result to the well-established empirical information about this phase-shift.

Thus, in Fig. 37 the red solid curve shows the NLO description of the empirical P_{33} phase-shift represented by the data points. The curve is obtained by taking $h_A = 2.85$ and $h_1 = 0$, and is characterized by $\chi^2/\text{point} \simeq 1$, where we assume 0.5 degree uncertainty in the empirical values. (The best fit is obtained by slightly decreasing h_A and increasing h_1 to about 0.6, however the improvement is very small and we prefer to neglect h_1 for simplicity). The blue dashed line in Fig. 37 shows the LO result, obtained by neglecting $\operatorname{Im} \Sigma'_\Delta$ and h_1 , and taking $h_A = 2.85$. This corresponds with the so-called “constant width approximation”. At both LO and NLO, the resonance width takes the value $\Gamma(M_\Delta) \simeq 115$ MeV.

Of interest is the position of the resonance in the complex plane, $\sqrt{s_R} = M_\Delta^{(pole)} - (i/2)\Gamma_\Delta^{(pole)}$. In this NLO calculation, the “complex pole” parameters come out to be

$$M_\Delta^{(pole)} = M_\Delta - \frac{\text{Im}\Sigma \text{Im}\Sigma'}{1 + (\text{Im}\Sigma')^2} \simeq 1.211 \text{ GeV}, \quad (4.67a)$$

$$\Gamma_\Delta^{(pole)} = -\frac{2 \text{Im}\Sigma}{1 + (\text{Im}\Sigma')^2} \simeq 0.097 \text{ GeV}. \quad (4.67b)$$

All these numbers are within the range quoted by the Particle Data Group [15].

Fig. 37. (Color online) The energy-dependence of the P33 phase-shift of elastic pion-nucleon scattering in the Δ -resonance region. The red solid (blue dashed) curve represents the NLO (LO) result. The data points are from the SP06 SAID analysis [93].

Note that the calculations presented here satisfy (the two-body πN) unitarity exactly. Indeed, the partial-wave S-matrix obtained from the graphs in Fig. 35 is given by

$$S_l = \frac{1 + iK_l}{1 - iK_l} = e^{2i\delta_l}, \quad (4.68)$$

where K_l and δ_l , given respectively by Eqs. (4.56) and (4.66), are real numbers, hence $|S_l| = 1$.

4.5.2 Pion photo- and electroproduction

We now turn to the analysis of the pion electroproduction process. Since we are using the one-photon-exchange approximation (until Sect. 6), the pion photoproduction can be viewed as the particular case of electroproduction at $Q^2 = 0$.

The pion electroproduction amplitude to NLO in the δ -expansion, in the resonance region, is given by the graphs in Fig. 38, where the shaded blob in the 3rd graph denotes the NLO $\gamma N \Delta$ vertex, given by the graphs in Fig. 39. The 1st graph in Fig. 38 enters at the LO, which here is $\mathcal{O}(\delta^{-1})$. The Δ self-energy in this graph is included to NLO, see Fig. 36. All the other graphs in Fig. 38 are of NLO = $\mathcal{O}(\delta^0)$. Note that the Δ -resonance contribution at NLO is obtained by

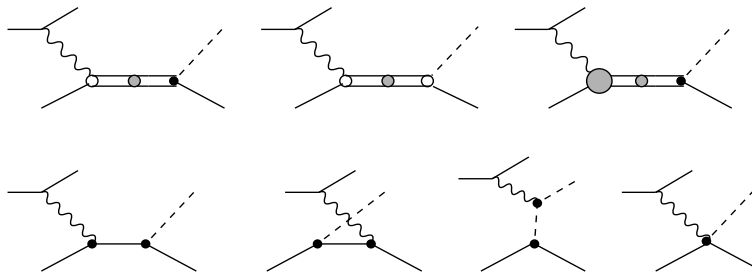


Fig. 38. Diagrams for the $eN \rightarrow e\pi N$ reaction to LO and NLO in the δ -expansion. The dots denote the vertices from the 1st-order Lagrangian, while the circles are the vertices from the 2nd order Lagrangian (e.g., the $\gamma N \Delta$ -vertex in the first two graphs is the g_M coupling from $\mathcal{L}^{(2)}$).

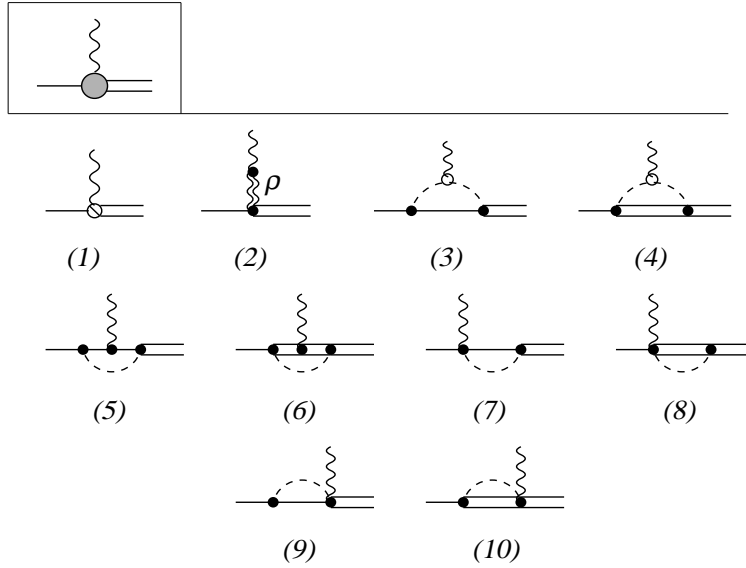


Fig. 39. The $\gamma N \Delta$ vertex at $\mathcal{O}(\delta^3)$. The sliced vertex (1) stands for the g_E and g_C couplings from the 3rd order Lagrangian. The wiggly double line in (2) stands for the vector-meson propagator.

going to NLO in either the $\pi N \Delta$ vertex (2nd graph) or the $\gamma N \Delta$ vertex (3rd graph). Accordingly, the Δ self-energy in these graphs is included, respectively, to NLO (Fig. 36) and to LO [Fig. 36(a)] in the $\pi N \Delta$ coupling.

The vector-meson diagram, Fig. 39(2), contributes to NLO for $Q^2 \sim \Lambda \Delta$. One includes it effectively by giving the g_M -term a dipole Q^2 -dependence (in analogy to how it is usually done for the nucleon isovector form factor):

$$g_M \rightarrow \frac{g_M}{(1 + Q^2/0.71 \text{ GeV}^2)^2}. \quad (4.69)$$

The analogous effect for the g_E and g_C couplings begins at $N^2\text{LO}$.

An important observation is that at $Q^2 = 0$ only the imaginary part (unitarity cut) of the loop graphs in Fig. 39 contributes to the NLO amplitude. Their real-part contributions, after the renormalization of the LECs, begin to contribute at $N^2\text{LO}$, for $Q^2 \ll \Delta \Lambda_{\chi SB}$. At present we will consider only the NLO calculation where the $\pi \Delta$ -loop contributions to the $\gamma N \Delta$ -vertex are omitted since they do not give the imaginary contributions in the Δ -resonance region. We emphasize that such loops might become important at this order for $Q^2 \sim \Delta \Lambda_{\chi SB} \sim 0.3 \text{ GeV}^2$ and should be included for the complete NLO result. The present calculation is thus restricted to values $Q^2 < 0.3 \text{ GeV}^2$.

In Figs. 40–42 we show the results for the pion electroproduction resonant multipoles $M_{1+}^{(3/2)}$, $E_{1+}^{(3/2)}$, and $S_{1+}^{(3/2)}$ as function of the invariant energy $W = \sqrt{s}$ around the resonance position, at $Q^2 = 0$. The $M_{1+}^{(3/2)}$ and $E_{1+}^{(3/2)}$ multipoles are well established by the MAID [92] and SAID [93] partial-wave solutions, thus allowing one to fit two of the three $\gamma N \Delta$ LECs at this order as: $g_M = 2.97$, $g_E = -1.0$. The third LEC is adjusted to for a best description of the pion electroproduction data at low Q^2 (see Sect. 5), yielding $g_C = -2.6$. The latter values translate into $G_M^* = 3.04$, $G_E^* = 0.07$, and $G_C^* = 1.00$ for the Jones-Scadron form-factors at $Q^2 = 0$.

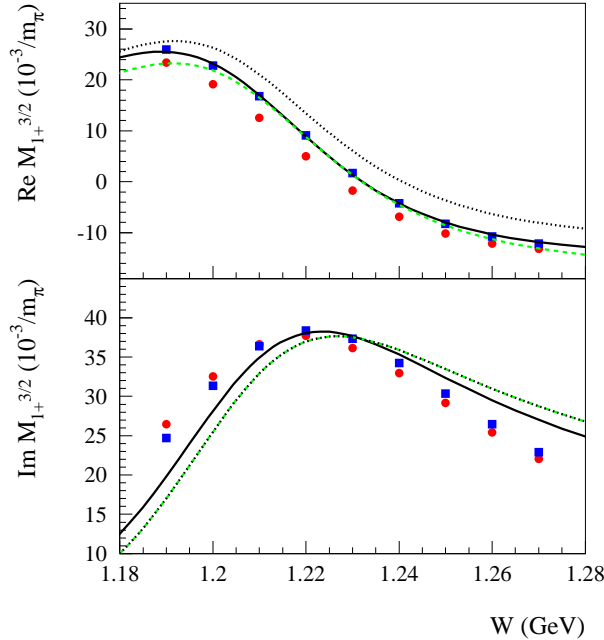


Fig. 40. (Color online) The $M_{1+}^{(3/2)}$ multipole for pion photoproduction as function of the invariant energy. Green dashed curves: Δ contribution without the $\gamma N \Delta$ -vertex loop corrections, [i.e., only the first three graphs in Fig. 38 with Fig. 39(1) contribution are taken into account]. Blue dotted curves: adding the Born contributions, 2nd line in Fig. 38, to the dashed curves. Black solid curves: the NLO calculation, includes all graphs in Fig. 38 as well as the loop corrections. The data point are from the SAID analysis (FA04K) [93] (red circles), and from the MAID 2003 analysis [92] (blue squares).

As is seen from the figure, the NLO results (solid curves) give a good description of the energy dependence of the resonant multipoles in a window of 100 MeV around the Δ -resonance position. Also, these values yield $R_{EM} = -2.2\%$ and $R_{SM} = -3.4\%$.

The dashed curves in these figures show the contribution of the Δ -resonant diagram of Fig. 38 *without* the NLO loop corrections in Fig. 39. For the M_{1+} multipole this is the LO and part of the NLO contributions. For the E_{1+} and S_{1+} multipole the LO contribution is absent (recall that g_E and g_C coupling are of one order higher than the g_M coupling). Hence, the dashed curve represents a partial NLO contribution to E_{1+} and S_{1+} .

Note that such a purely resonant contribution without the loop corrections satisfies unitarity in the sense of the Fermi-Watson theorem [197], which states that the phase of a pion electro-production amplitude \mathcal{M}_l is given by the corresponding pion-nucleon phase-shift:

$$\mathcal{M}_l = |\mathcal{M}_l| e^{i\delta_l} . \quad (4.70)$$

As a direct consequence of this theorem, the real-part of the resonant multipoles must vanish at the resonance position, where the phase-shift crosses 90 degrees.

Upon adding the non-resonant Born graphs (2nd line in Fig. 38) to the dashed curves, one obtains the dotted curves. The non-resonant contributions are purely real at this order and hence the imaginary part of the multipoles do not change. While this is consistent with unitarity for the non-resonant multipoles (recall that the non-resonant phase-shifts are zero at NLO), the Fermi-

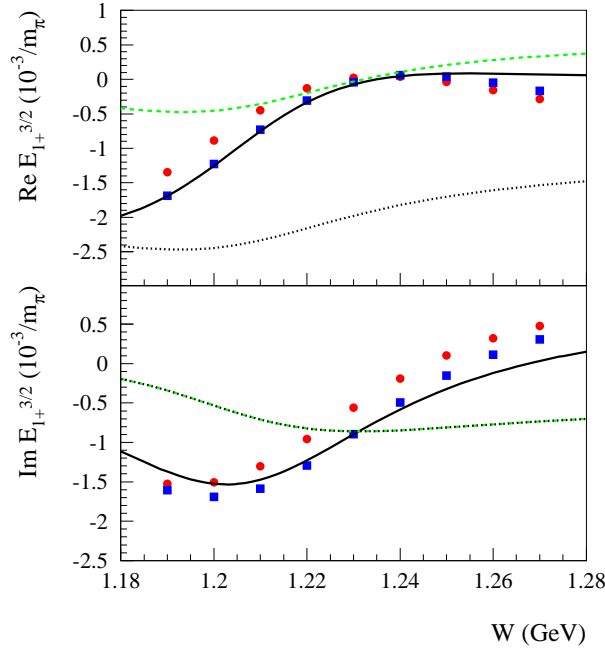


Fig. 41. (Color online) The $E_{1+}^{(3/2)}$ multipole for pion photoproduction. Curve conventions and data points are the same as in Fig. 40.

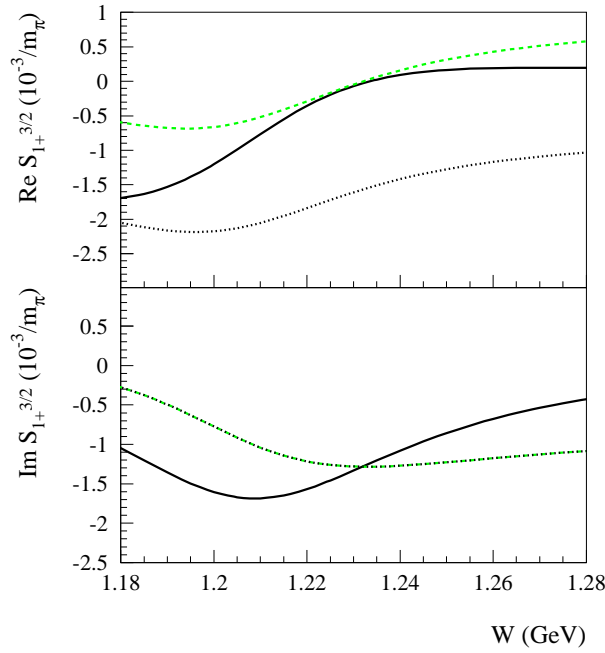


Fig. 42. (Color online) The $S_{1+}^{(3/2)}$ multipole at $Q^2 = 0$ as function of the invariant mass W of the πN system. Curve conventions are the same as in Fig. 40.

Watson theorem in the resonant channels is violated. In particular, one sees that the real parts of the resonant multipoles now fail to cross zero at the resonance position. The complete NLO calculation, shown by the solid curves in the figure includes in addition the πN -loop corrections

in Fig. 39, which obviously restore unitarity. The Fermi-Watson theorem is satisfied exactly in this calculation.

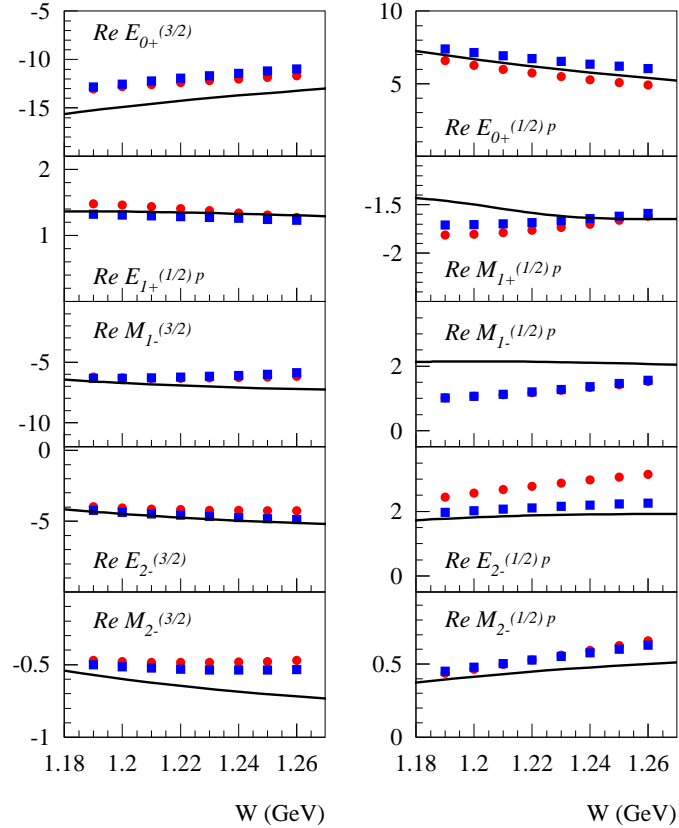


Fig. 43. (Color online) Non-resonant multipole amplitudes (in units $10^{-3}/m_{\pi}$) of pion photoproduction as function of the invariant mass W of the πN system. The solid curves result from our NLO calculation. The data points are from the SAID analysis (FA04K) [93] (red circles), and from the MAID 2003 analysis [92] (blue squares).

Next we examine the results for the non-resonant multipoles, which all receive contributions of the Born graphs only. In Fig. 43, we show the NLO calculations for the non-resonant s -, p - and d -wave pion photoproduction multipoles in the $\Delta(1232)$ region in comparison with the two state-of-the-art phenomenological multipole solutions MAID and SAID. At this order the non-resonant multipoles are purely real. The multipole solutions show indeed that the imaginary parts of non-resonant multipoles, around the Δ resonance, are negligible in comparison to their real parts.

From the figure we conclude that for most of the non-resonant multipoles, the parameter-free NLO results, agree fairly well with the phenomenological solutions. The largest differences are observed for $M_{1-}^{(1/2)p}$ multipole. This multipole corresponds with nucleon quantum numbers. The cause of the appreciable difference in this channel is largely due to the nucleon anomalous magnetic moment contributions, which are not included in this calculation (since they appear at N^2LO), but which are included in the phenomenological solutions.

Finally, in Fig. 44 we show the NLO χ EFT results for the Q^2 dependence of the resonant

multipoles, at the resonance position. The red solid curve is *with* and the green dotted curve *without* the chiral-loop corrections of Fig. 39. The blue dashed curves and the black dashed-dotted curves represent the results of MAID and SAID, respectively. The data point are from the recent MIT-Bates and MAMI experiments. From the figure we observe, in particular, that the chiral loops play a crucial role in the low momentum-transfer dependence of the R_{EM} ratio. The effect of the “pion cloud” is most pronounced in the $E2 \gamma N \Delta$ transition.

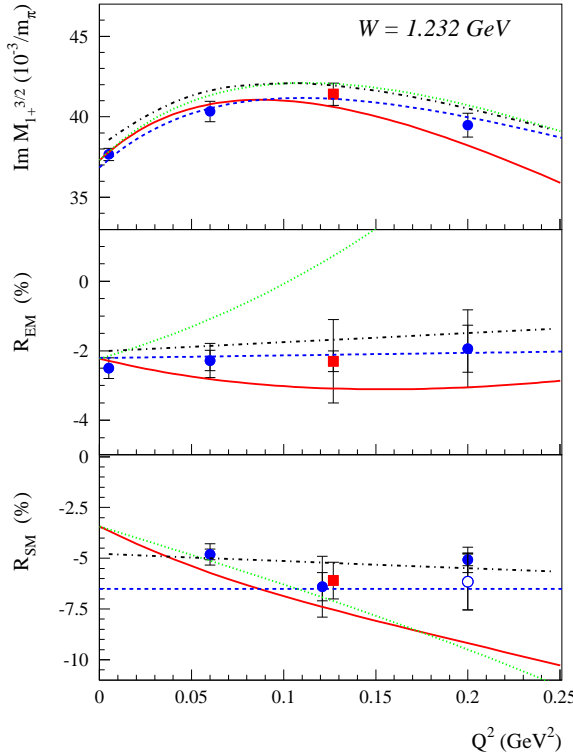


Fig. 44. (Color online) The resonant multipoles of pion electroproduction as function Q^2 at the Δ -resonance position. The green dotted curve is the Δ -contribution alone. The solid curves are results of the NLO calculation of Ref. [89]. Also shown are results of the SAID analysis (FA04K) [93] (black dashed-dotted curves), and the MAID 2003 analysis [92] (blue dashed curves). The data points are from BATES at $Q^2 = 0.127$ [80] and MAMI: $Q^2 = 0$ [23], $Q^2 = 0.06$ [79], $Q^2 = 0.121$ [78], $Q^2 = 0.2$ [77].

4.5.3 Compton scattering

The $\gamma N \Delta$ transition plays an important role in the $\gamma N \rightarrow \gamma N$ process in the Δ -resonance region. Already well below the resonance the effects of the Δ excitation are appreciable, and mostly due to its significant contributions to the magnetic and the backward spin polarizabilities of the nucleon (cf. [72] and references therein):

$$\beta^{(\Delta)} = \frac{2 \alpha_{em} g_M^2}{(M_N + M_\Delta) \Delta} \simeq 6 [\times 10^{-4} \text{ fm}^3], \quad (4.71)$$

$$\gamma_\pi^{(\Delta)} = \frac{\alpha_{em} g_M^2}{(M_N + M_\Delta)^3 \Delta^2} \left(1 + \frac{8\Delta}{M_N} \right) \simeq 9 [\times 10^{-4} \text{ fm}^4]. \quad (4.72)$$

These numbers can for instance be compared with the known empirical values for the proton case [250,251]: $\beta^{(p-exp)} = 3.2 \pm 1.2 [\times 10^{-4} \text{ fm}^3]$, $\gamma_\pi^{(p-exp)} = -38.7 \pm 1.8 [\times 10^{-4} \text{ fm}^4]$, to convince oneself that the effects are significant.

Note also that the leading chiral-loop contribution to magnetic polarizability is $\beta^{(p-LO)} \simeq 1.2$ in the heavy-baryon χ PT [252] and $\beta_p^{(p-RLO)} \simeq -2$ in the manifestly covariant χ PT [253,254]. The latter number is certainly preferred, if we are to reconcile the large Δ contribution to the magnetic polarizability with experiment. More discussion of this issue can be found in Ref. [255].

The calculations of Compton scattering in χ PT without Δ 's are shown to be applicable only to energies not far above the pion-production threshold, $W = M_N + m_\pi$, see Refs. [256,257]. Traditionally calculations of this reaction in the resonance region are done using isobar-type of models [174,175,258] or dispersion-relation approaches [259,260]. Only relatively recently, first attempts to compute the Δ -resonance region in a χ EFT framework have been completed to some degree of success [90,261,262].

In Fig. 45 we show the results of Ref. [90] for the Compton-scattering observables, namely, differential cross-section and the linear beam asymmetry. The results are shown as a function of the photon lab energy, $\omega = (s - M_N^2)/(2M_N)$, and the scattering angle in the center-of-mass system $\theta_{c.m.}$. The complete calculation (red solid curves) represents the NLO result in the δ -expansion over both the low-energy and the resonance energy region. It is instructive to compare it to the NLO calculation in the Deltaless HB χ PT (blue dashed lines). The latter clearly breaks down at energies above the pion-production threshold, $\omega_{\text{thr}} = m_\pi$. These results also demonstrate that the such computed Δ contributions (inferred by the difference between the red solid and blue dashed curves), while being small at low energies, are dominating the resonance region (ω around 340 MeV), in qualitative agreement with the power-counting of the δ -expansion scheme.

In all fairness one should note that the NLO results shown in Fig. 45 are obtained using $g_M = 2.6$ and $g_E = -6.0$, the values of LECs which are inconsistent with the photoproduction analysis in the same expansion scheme [89] (see also the previous subsection). The source of the discrepancy is most likely to be the use of the heavy-baryon expansion in the Compton-scattering work [90]. Relativistic effects are expected to be important in the resonance region. As mentioned above, they already make a significant impact on such low-energy quantities as polarizabilities. A future study of Compton scattering in a manifestly covariant χ EFT framework is called for to clarify this issue.

4.5.4 Radiative pion photoproduction

The radiative pion photoproduction ($\gamma N \rightarrow \pi N \gamma'$) in the Δ -resonance region is used to access experimentally the magnetic dipole moment (MDM) of the Δ -resonance [266]. On the theory side this reaction had extensively been studied within the isobar type of models (*e.g.*, [267–

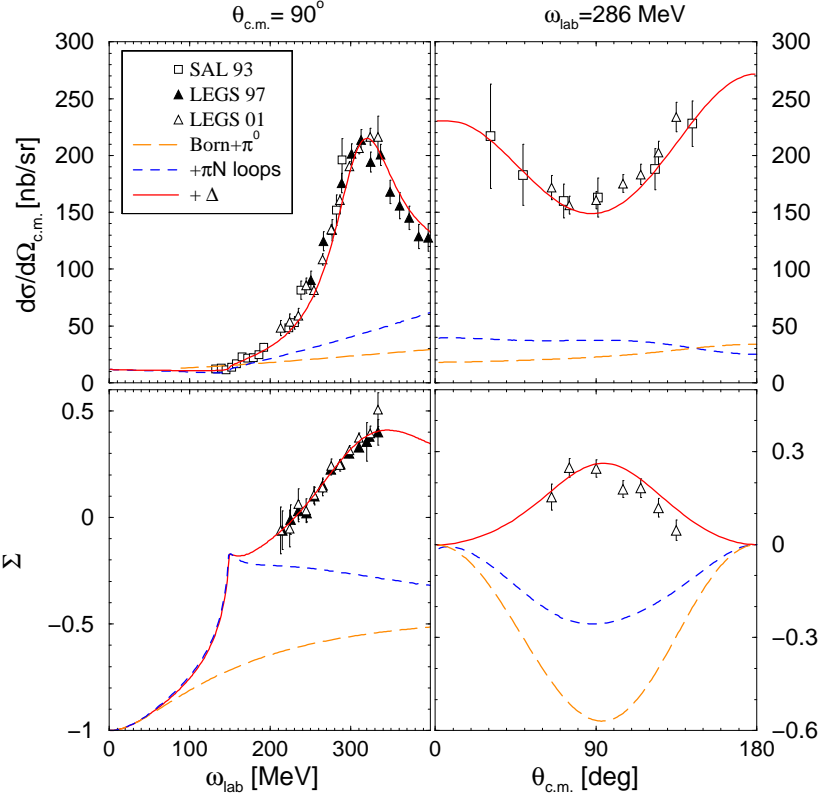


Fig. 45. The χ EFT calculations of the $\gamma p \rightarrow \gamma p$ differential cross section ($d\sigma/d\Omega_{c.m.}$) and the photon beam asymmetry (Σ) compared with recent experimental data: SAL93 [264], LEGS97 [265], LEGS01 [25]. Left panel: energy dependence at a fixed scattering angle. Right panel: angular dependence at a fixed energy. The long-dashed orange line represents the sum of nucleon and pion Born graphs, the blue dashed line gives the NLO Δ -HB χ PT prediction, and the red solid line is the full result at NLO in the δ -expansion [90].

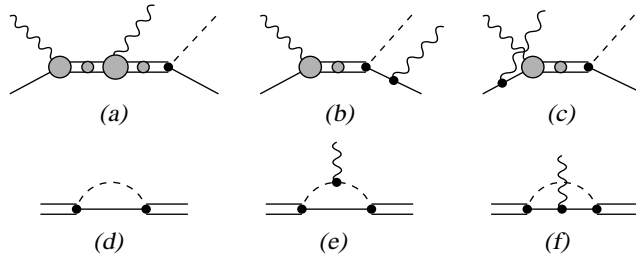


Fig. 46. Diagrams for the $\gamma p \rightarrow \pi^0 p \gamma'$ reaction at NLO in the δ -expansion.

270]). Here, however, we only discuss the more recent study [109] performed within the χ EFT framework.

Consider the amplitude for the $\gamma p \rightarrow \pi^0 p \gamma'$ reaction. The optimal sensitivity to the MDM term is achieved when the incident photon energy is in the vicinity of Δ , while the outgoing photon energy is of order of m_π . In this case the $\gamma p \rightarrow \pi^0 p \gamma'$ amplitude to NLO in the δ -expansion is given by the diagrams Fig. 46(a), (b), and (c), where the shaded blobs, in addition to the couplings from the chiral Lagrangian, contain the one-loop corrections shown in Fig. 46(e), (f).

The general form of the $\gamma\Delta\Delta$ vertex is given in Eq. (2.20). To NLO it suffice to keep only the F_1^* and F_2^* terms, which both receive corrections from chiral loops Fig. 46(e), (f). It is important to emphasize that the Ward-Takahashi identity,

$$q_\mu \Gamma^{\mu\alpha\beta}(p', p) = e \left[(S^{-1})^{\alpha\beta}(p') - (S^{-1})^{\alpha\beta}(p) \right], \quad (4.73)$$

to NLO leads to the relation $F_1^*(0) = 1 - \Sigma'(M_\Delta)$, where Σ' is given in Eq. (4.65). This condition is verified exactly in the NLO calculation [109].

Figure 47 shows the pion mass dependence of real and imaginary parts of the Δ^+ and Δ^{++} MDMs, according to the calculation of Ref. [109]. Each of the two solid curves has a free parameter, the counterterm μ_Δ from $\mathcal{L}_\Delta^{(2)}$, adjusted to agree with the lattice data at larger values of m_π . As can be seen from Fig. 47, the Δ MDM develops an imaginary part when $m_\pi < \Delta$, whereas the real part has a pronounced cusp at $m_\pi = \Delta$. For μ_Δ^+ our curve is in disagreement with the downward trend of the recent lattice data [272]. This trend, however, is known to be an artifact of the “quenched approximation” in the lattice calculations [108]. The dotted line in Fig. 47 shows the result [273] for the magnetic moment of the proton. One can see that μ_{Δ^+} and μ_p , while having very distinct behavior for small m_π , are approximately equal for larger values of m_π .

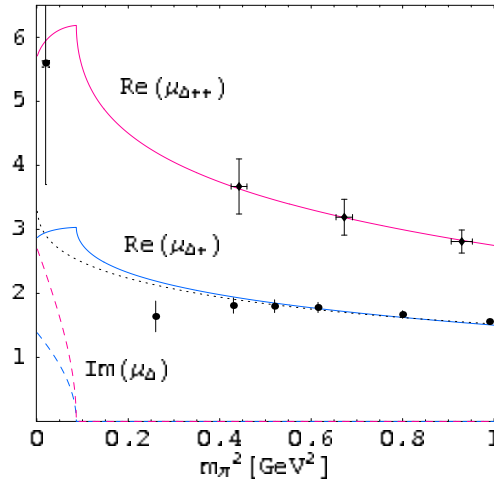


Fig. 47. Pion mass dependence of the real (solid curves) and imaginary (dashed curves) parts of Δ^{++} and Δ^+ MDMs [in nuclear magnetons]. Dotted curve is the result for the proton magnetic moment from Ref. [273]. The experimental data point for Δ^{++} is from PDG analysis [15]. Lattice data are from [271] for Δ^{++} and from [272] for Δ^+ .

We next consider the NLO results for the $\gamma p \rightarrow \pi^0 p \gamma'$ observables. The NLO calculation outlined above, completely fixes the imaginary part of the $\gamma\Delta\Delta$ vertex¹⁹. The expansion for the real part of the $\gamma\Delta\Delta$ begins with LECs from $\mathcal{L}^{(2)}$ which represent the isoscalar and isovector MDM couplings: $\kappa_\Delta^{(S)}$ and $\kappa_\Delta^{(V)}$ in Eq. (4.49). A linear combination of these parameters, $\mu_{\Delta^+} = [3 + (\kappa_\Delta^{(S)} + \kappa_\Delta^{(V)})/2](e/2M_\Delta)$, is to be extracted from the $\gamma p \rightarrow \pi^0 p \gamma'$ observables. Several such observables are shown in Fig. 48 for an incoming photon energy $E_\gamma^{lab} = 400$ MeV as function of the emitted photon energy $E_\gamma'^{c.m.}$.

¹⁹ For an alternative recent calculation of the imaginary part of the Δ MDM see Ref. [263]

In the soft-photon limit ($E'_\gamma^{c.m.} \rightarrow 0$), the $\gamma p \rightarrow \pi^0 p \gamma'$ reaction is completely determined from the bremsstrahlung off the initial and final protons. The deviations of the $\gamma p \rightarrow \pi^0 p \gamma'$ observables, away from the soft-photon limit, will then allow to study the sensitivity to μ_{Δ^+} . It is therefore very useful to introduce the ratio [270]:

$$R \equiv \frac{1}{\sigma_\pi} \cdot E'_\gamma \frac{d\sigma}{dE'_\gamma}, \quad (4.74)$$

where $d\sigma/dE'_\gamma$ is the $\gamma p \rightarrow \pi^0 p \gamma'$ cross section integrated over the pion and photon angles, and σ_π is the angular integrated cross section for the $\gamma p \rightarrow \pi^0 p$ process weighted with the bremsstrahlung factor, as detailed in [270].

This ratio R has the property that in the soft-photon limit, the low energy theorem predicts that $R \rightarrow 1$. One firstly sees from Fig. 48 that the EFT calculation exactly satisfies this low-energy theorem. Furthermore, the EFT result for R shows clear deviations from unity at higher outgoing photon energies, which are in good agreement with the first data for this process [266]. The sensitivity of the EFT calculation to the μ_Δ is a very promising setting for the dedicated second-generation experiment by the Crystal Ball Coll. at MAMI, which is currently under analysis (for first results, see Ref. [274]). It improves upon the statistics of the first experiment (Fig. 48) by at least two orders of magnitude and will allow for a reliable extraction of μ_{Δ^+} using the EFT calculation presented here.

Besides the cross section, the asymmetries for linearly and circularly polarized incident photons are also displayed in Fig. 48. The photon asymmetry for linearly polarized photons, Σ , at $E'_\gamma = 0$ exactly reduces to the $\gamma p \rightarrow \pi^0 p$ asymmetry. From Fig. 48 one sees that in the soft-photon limit, the NLO calculation is in good agreement with the experimental data point, and predicts a nearly constant energy-dependence. It also predicts a weak sensitivity on the MDM value. The linear beam asymmetry is therefore an excellent observable for a consistency check of the EFT calculation.

The asymmetry for circularly polarized photons, Σ_{circ} , (which is exactly zero for a two body process due to reflection symmetry w.r.t. the reaction plane) has been proposed [270] as a unique observable to enhance the sensitivity to μ_Δ . Indeed, in the soft-photon limit, where the $\gamma p \rightarrow \pi^0 p \gamma'$ process reduces to a two-body process, Σ_{circ} is exactly zero. Therefore, its value at higher outgoing photon energies is directly proportional to μ_Δ . One sees from Fig. 48 (lower panel) that the EFT calculation supports this observation, and shows sizably different asymmetries for different values of μ_Δ . A combined fit of all three observables shown in Fig. 48 will therefore allow for a very stringent test of the EFT calculation, which can then be used to extract the Δ^+ MDM.

4.5.5 Errors due to neglect of N^2LO effects

Prior to presenting the results of our NLO calculation, we would like to make an estimate of the theoretical uncertainty due to the neglect of higher-order effects. Some of the next-next-to-leading order (N^2LO) contributions are shown in Fig. 49. Of course, there is no substitute for an actual calculation of those effects, but at present we only know that they must be suppressed by at least one power of δ ($= \Delta/\Lambda_{\chi SB}$) as compared to the NLO and two powers of δ as

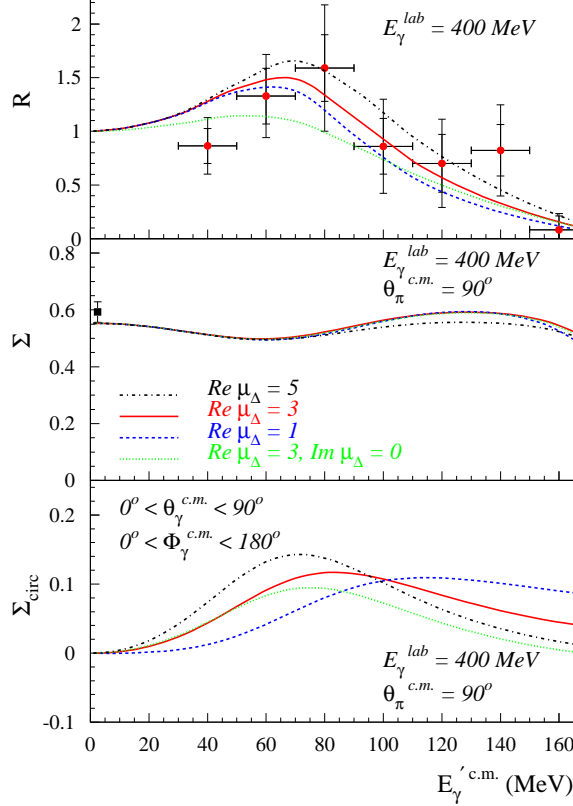


Fig. 48. The outgoing photon energy dependence of the $\gamma p \rightarrow \pi^0 p \gamma'$ observables for different values of $\mu_{\Delta+}$ (in units $e/2M_{\Delta}$). Top panel: the ratio of $\gamma p \rightarrow \pi^0 p \gamma'$ to $\gamma p \rightarrow \pi^0 p$ cross-sections Eq. (4.74). Data points are from [266]. Middle panel: the linear-polarization photon asymmetry of the $\gamma p \rightarrow \pi^0 p \gamma'$ cross-sections differential w.r.t. the outgoing photon energy and pion c.m. angle. The data point at $E'_\gamma = 0$ corresponds with the $\gamma p \rightarrow \pi^0 p$ photon asymmetry from [23]. Lower panel: the circular-polarization photon asymmetry (as defined in [270]), where the outgoing photon angles have been integrated over the indicated range.

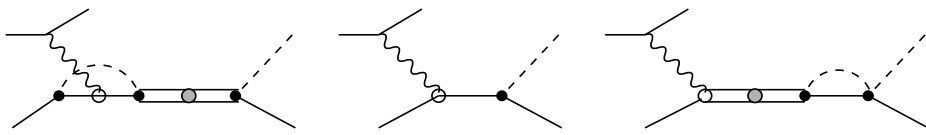


Fig. 49. Examples of N^2LO contributions to the $eN \rightarrow e\pi N$ reaction. Open circles denote the e.m. coupling to the anomalous magnetic moment of the nucleon.

compared to the LO contributions. Therefore, we can *estimate* the size of the N^2LO contribution to an amplitude A as: $A_{NLO} \delta$, or $A_{LO} \delta^2$. The theoretical uncertainty of a calculation up to and including NLO can thus be estimated as:

$$A_{err} = |A_{LO} + A_{NLO}| \delta^2. \quad (4.75a)$$

In cases where the amplitude does not receive any LO contributions, we have no other option than,

$$A_{err} = |A_{\text{NLO}}| \delta. \quad (4.75\text{b})$$

This looks nice and simple, however, there are a few caveats in the implementation of such an estimate. First of all, as we increase the light scales, the expansion parameter must increase too. And this does not concern Δ alone but, in our case, also m_π and Q^2 . Therefore, it is more realistic to estimate the error using an expansion parameter such as:

$$\tilde{\delta} = \frac{1}{3} \left[\frac{\Delta}{M_N} + \left(\frac{m_\pi}{M_N} \right)^{1/2} + \left(\frac{Q^2}{M_N^2} \right)^{1/2} \right], \quad (4.76)$$

where all the light scales are treated on equal footing and hence are averaged over.

Secondly, what if the amplitude happens to vanish at some kinematical point. According to Eq. (4.75) the theoretical calculation at that point would be perfect, which is of course unlikely to be true in reality. So, when considering dependencies on kinematical variable(s), we shall take an *average of the error* over some appropriate region of that variable.

Given these two points, we are led to the following formula for the theoretical uncertainty of the NLO calculation for an amplitude A ,

$$A_{err} = \begin{cases} |A|_{av} \tilde{\delta}^2, & \text{LO} \neq 0 \\ |A|_{av} \tilde{\delta}, & \text{LO} = 0, \end{cases} \quad (4.77)$$

and the subscript “*av*” indicates that the appropriate averaging is performed.

The theoretical uncertainty of the NLO calculation of an observable O is:

$$O_{err} = \begin{cases} 2|O|_{av} \tilde{\delta}^2, & \text{LO} \neq 0 \\ 2|O|_{av} \tilde{\delta}, & \text{LO} = 0, \end{cases} \quad (4.78)$$

where the factor of 2 takes into account that an observable is a product of two amplitudes.

5 Results for observables and discussion

In this Section, we review the current status of pion photo- and electroproduction data in the Δ -resonance region, and discuss the results of the theoretical approaches described above, namely dynamical models and χ EFT. An extensive review of meson productions from the nucleons, including single pion, two pions and η up to second resonance region, has been published recently [12]. Another recent review [11] on meson productions also goes up to the second resonance region, but is restricted only to photoproduction.

After some introductory remarks in Sect. 5.1, we shall consider pion photoproduction in Sect. 5.2. In Sect. 5.3, the focus will be on the electroproduction case for both the low and larger Q^2 regions.

5.1 Introductory remarks

The first experimental work on meson photoproduction dates as early as 1949. However, most of the present precision data became available thanks to the progress made in accelerator and detector technology during the last two decades. At the present time, the new generation of electron accelerators at JLab, ELSA, and MAMI are dedicated to the study of nuclear and hadronic structure and are equipped with state-of-the-art detector systems. The high intensity electron beams, besides being used for electron induced reactions, also provide good photon sources for photonuclear reactions via bremsstrahlung. Another way to produce high energy photon beams is through Compton backscattering. Laser backscattering systems have been installed at BNL (LEGS), ESRF (GRAAL), and at SPring8 (LEPS) to produce photon beams to investigate nucleon resonances and meson photoproduction.

Turning to the theory, let us recall the key ingredients which enter into the dynamical models and the χ EFT calculations. Chiral perturbation theory (χ PT) is now widely accepted as the "basic" theory to describe the low energy interactions of Goldstone bosons among themselves and with other hadrons. There is generally good agreement between the χ PT predictions and experiments [275]. For example, state-of-the-art χ PT calculation on $\gamma p \rightarrow \pi^0 p$ at threshold [276,277], which has gone up to order p^4 and found large contributions from one-loop charge-exchange rescattering, agree beautifully with the new precise measurements [279–284].

The χ EFT δ -expansion presented in Sect. 4 provides an extension of χ PT into the Δ -resonance region. In such scheme, for reactions such as πN scattering and electromagnetic pion production, diagrams with a dressed Δ in the intermediate states (the ODR graphs) as depicted in Fig. 35a and Fig. 38 (upper left diagram) are the leading diagrams²⁰. In the NLO, πN scattering is still dominated by the Δ -excitation diagrams as depicted in Fig. 35. For pion electromagnetic production, only the Born terms with electric γNN coupling, in addition to the loop correction to the $\gamma N\Delta$ vertex as given by graphs in Fig. 39, enter in the NLO. The only question left then is whether the expansion converges. Namely, whether NNLO terms are smaller

²⁰ It is interesting to note that the LO χ EFT calculation provides the field theoretic justification for the previously employed Δ -saturation model (see *e.g.* [285,177]).

than NLO. At NNLO, for example, the background πN interaction corresponding to the crossed Born diagram would begin to contribute to the Δ self-energy in the two-loop diagrams which is the main driving mechanism in generating the Δ -resonance in the Chew-Low theory. Convergence problem aside, EFT in the resonance region does provide a consistent expansion scheme which contains the fundamental features of QCD, namely chiral symmetry, gauge invariance, covariance, and crossing symmetry, as in the case for χ PT for low-energy hadron phenomena.

As in χ PT, dynamical models also start from an effective chiral Lagrangian. However, the calculation of the S -matrix in dynamical models is not based on field theory. Rather, the effective Lagrangian is used to construct a potential used in a Lippmann-Schwinger type of scattering equation. The solution of the scattering equation includes the rescattering effects to all orders and thereby unitarity is ensured while the crossing and the other symmetries are not. In dynamical models applied to pion electromagnetic production, considered in Sect. 3, gauge invariance is problematic. The only hope is that the *ad hoc* schemes which have been proposed provide good approximations. The success of DMT for the $\gamma p \rightarrow \pi^0 p$ at threshold [91] offers a hope in this direction.

Dynamical models [286,190,233,14,287,204] have been able to provide a good description of πN scattering lengths and the phase shifts in S , P , and D waves up to $W \simeq 1.5$ GeV, see for instance Fig. 31. It should be pointed out here that within the dynamical models, the Δ resonance is a coherent contribution of an elementary Δ and Chew-Low graphs as obtained in the cloudy bag model [288]. One advantage of dynamical model calculations over χ EFT is that they provide a unitary framework up to higher energies because they do not rely on a perturbative expansion in small energy scales.

5.2 Pion photoproduction

The majority of the photopion production data comes from measurements of the differential cross section by unpolarized photons on unpolarized nucleons. All other photoproduction experiments involve the use of polarized photon beams, polarized nucleon targets, a combination of both polarization or the measurement of the polarization of the recoil nucleon.

The earliest of the polarization experiments used unpolarized photon beams and unpolarized targets and measured the recoil polarization of the nucleon, $P(\theta)$, by a scattering of this recoiling nucleon on a secondary target. High-energy polarized photon beams have been produced either by laser backscattering or coherent bremsstrahlung in a crystal. They have been used to measure the beam asymmetry, $\Sigma(\theta)$, from an unpolarized target.

The first data on the target asymmetry, $T(\theta)$, was obtained in 1972 for the $\gamma + p \rightarrow \pi^+ + n$ process. Since then an impressive set of measurements of $d\sigma/d\Omega$, $P(\theta)$, $T(\theta)$, and $\Sigma(\theta)$ has been assembled on the final states $\pi^+ n$, $\pi^0 p$, and $\pi^- p$. The data coverage on the first two channels spans the whole resonance region with good angular coverage. The $\pi^- p$ channel data, on the other hand, is more scarce since it involves the neutron (deuterium) target.

Double polarization observables have also been measured. They fall into three categories: beam-target, beam-recoil, and target-recoil. Polarized beam-polarized target experiments yield $G(\theta)$ and $H(\theta)$ and have been measured at Kharkov [298,299] and at MAMI [291,292,300]. Beam-recoil and target-recoil measurements are experimentally more difficult as they involve a

	$A_{1/2}$ (10^{-3} GeV $^{-\frac{1}{2}}$)	$A_{3/2}$ (10^{-3} GeV $^{-\frac{1}{2}}$)	$Q_{p \rightarrow \Delta^+}$ (fm 2)	$\mu_{p \rightarrow \Delta^+}$ (μ_N)	R_{EM} (%)
PDG	-135 \pm 6	-250 \pm 8	-0.0846 \pm 0.0033	3.46 \pm 0.03	-2.5 \pm 0.5
MAMI	-131	-251	-0.082	3.45	-2.5
LEGS	-135.7	-266.9	-0.108	3.642	-3.07
DMT	-134 (-80)	-256 (-136)	-0.081 (0.009)	3.52 (1.922)	-2.4 (0.47)
SL	-121 (-90)	-226 (-155)	-0.056 (0.003)	3.12 (2.188)	-1.85 (0.14)
DUO	-131.5	-255	-0.091	3.49	-2.71
χ EFT	-133	-253	-0.077	3.48	-2.2

Table 4

Comparison of the values for the helicity amplitudes, $Q_{N \rightarrow \Delta}$, $\mu_{N \rightarrow \Delta}$, and R_{EM} extracted from experiment, with their values in dynamical models (DMT [91], SL [14], DUO [182]) and χ EFT calculations [88,89]. The numbers within the parenthesis, in the cases of DMT and SL, correspond to the bare values.

second scattering process to analyze the recoil nucleon polarization. No data have been reported for them. The most precise determination to date of the R_{EM} ratio in the photo-excitation of the $\Delta(1232)$ has come from the simultaneous measurements of $p(\vec{\gamma}, p)\pi^0$ and $p(\vec{\gamma}, n)\pi^+$ with polarized photon beams [22,24].

A comprehensive account of the status of photoproduction experiments can be found in [93] and the full database can be accessed at the SAID website [183].

Let us turn to the results of the theoretical approaches considered above. In the χ EFT [88,89] and in the dynamical model calculations of SL [14], DMT [91], and DUO [182], the $\gamma N \Delta$ coupling constants are all obtained by fitting to the experiments. We present in Table 4 the resulting values for the helicity amplitudes $A_{1/2}$, $A_{3/2}$, transition electric quadrupole moment $Q_{p \rightarrow \Delta^+}$, transition magnetic dipole moment, $\mu_{p \rightarrow \Delta^+}$, and R_{EM} , together with the PDG [15] values and experimental results measured at MAMI [22,23] and LEGS [24,25]. The values for $Q_{p \rightarrow \Delta^+}$ and transition magnetic dipole moment $\mu_{p \rightarrow \Delta^+}$ listed in the same row with the PDG values are the estimates of Eqs. (2.25) and (2.24) respectively.

In the DMT and DUO calculations, the best fit to the multipoles obtained in the recent analyses of the Mainz [166] and VPI groups [203] is shown in Fig. 50. One sees that both models are able to describe the energy dependence of the resonant multipoles very accurately throughout the Δ -resonance region.

Interpreting the results of the dynamical models, one finds that a sizeable part of the $M1$ $\gamma N \Delta$ strength and almost all of the $E2$ strength is generated by the πN rescattering. One sees from Table 4 that the bare values for the helicity amplitudes obtained in both SL and DMT, as given within the parentheses, amount to only about 60% of the corresponding dressed values, and are close to the predictions of the constituent quark model, as was first pointed out in Ref. [14]. The large reduction of the helicity amplitudes from the dressed to the bare ones

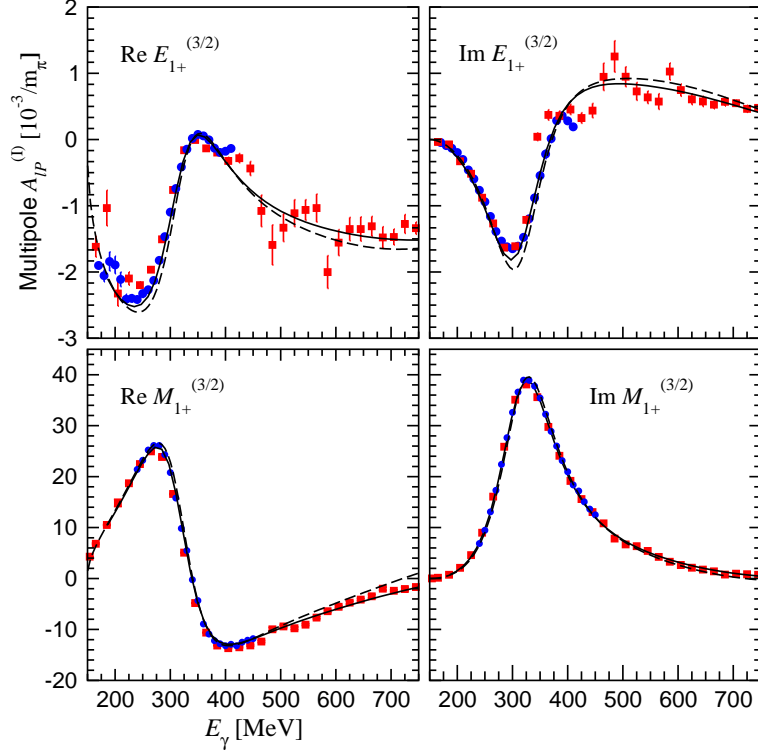


Fig. 50. Real and imaginary parts of the $M_{1+}^{(3/2)}$ and $E_{1+}^{(3/2)}$ multipoles. The solid curves are the full DMT results, whereas the dashed curves are the results of the DUO model. The blue circles are the results from the Mainz dispersion relation analysis [166], whereas the red squares are obtained from the VPI analysis [203].

results from the fact that the principal value integral part of Eq. (3.23), which represents the effects of the off-shell pion rescattering, contributes approximately for half of the $M_{1+}^{(3/2)}$, as seen in Fig. 30 for the DMT model. The large pion rescattering effects obtained in the dynamical models are generally interpreted as an important manifestation of the presence of the pion cloud in the nucleon. In χ EFT, the size of the πN contribution to the $M1$ and $E2$ transitions is quite different from the dynamical models, due to the renormalization of the LECs g_M and g_E at the resonance position for $Q^2 = 0$. The renormalized πN loop contributions then satisfy power counting and as a consequence contribute substantially less than in dynamical models.

The resonant multipoles $M_{1+}^{(3/2)}$ and $E_{1+}^{(3/2)}$ obtained in the χ EFT calculation at NLO are shown in Fig. 40 and Fig. 41, respectively. The imaginary part of these multipoles arise from purely the Δ contributions, see the upper graphs in Fig. 38. The Born graphs (2nd line of Fig. 38) contribute to the real part of the resonant multipoles, as well as to the non-resonant multipoles as shown in Fig. 43. Up to NLO in the δ -expansion, the non-resonant multipoles are thus purely real, whereas the corresponding πN phase shifts are zero, in accordance with the Fermi-Watson.

The predictions of χ EFT and the dynamical model calculations of SL, DMT, and DUO for the total and differential cross sections, single polarizations including beam and target asymmetry and recoil polarization, and double polarizations G and H for both $\gamma p \rightarrow \pi^0 p$ and $\gamma p \rightarrow \pi^+ n$ are shown in Figs. 51-59.

For the $\gamma p \rightarrow \pi^0 p$ and $\gamma p \rightarrow \pi^+ n$ processes, one sees from Figs. 51-59 that below the resonance the dynamical models are in overall agreement with the available data. Above the

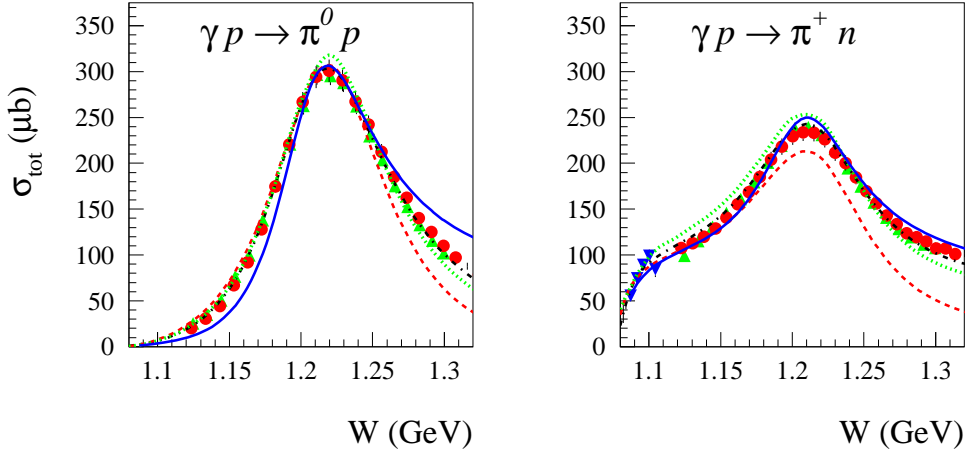


Fig. 51. The total cross sections for $\gamma p \rightarrow \pi^0 p$ (left panel) and $\gamma p \rightarrow \pi^+ n$ (right panel) through the $\Delta(1232)$ resonance region as function of the total *c.m.* energy W . Dashed-dotted (black) curves : DMT01 model. Dashed (red) curves : SL model. Dotted (green) curves : DUO model. Solid (blue) curves : NLO χ EFT calculation. The data points are from Refs. [289] (inverted blue triangles), [290] (green triangles), and [291] (red circles).

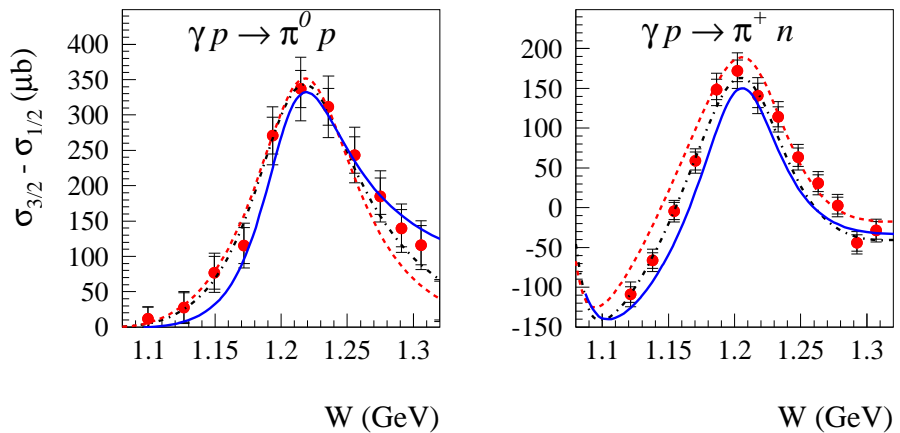


Fig. 52. The helicity difference total cross section $\sigma_{3/2} - \sigma_{1/2}$ for $\gamma p \rightarrow \pi^0 p$ (left panels) and $\gamma p \rightarrow \pi^+ n$ (right panels) through the $\Delta(1232)$ resonance region. Curve conventions as in Fig. 51. The data points are from MAMI [291] (red circles).

resonance, the SL model starts to fall increasingly below the $\pi^0 p$ and in particular the $\pi^+ n$ cross section data, see Figs. 51, 53, and 54. For the DUO model at higher energies, one observes more structure in the $\pi^0 p$ P, T, G , and H observables for forward and backward angles, where however the data base is scarce. The DMT model shows good agreement with all $\pi^0 p$ and $\pi^+ n$ observables throughout the Δ -energy range.

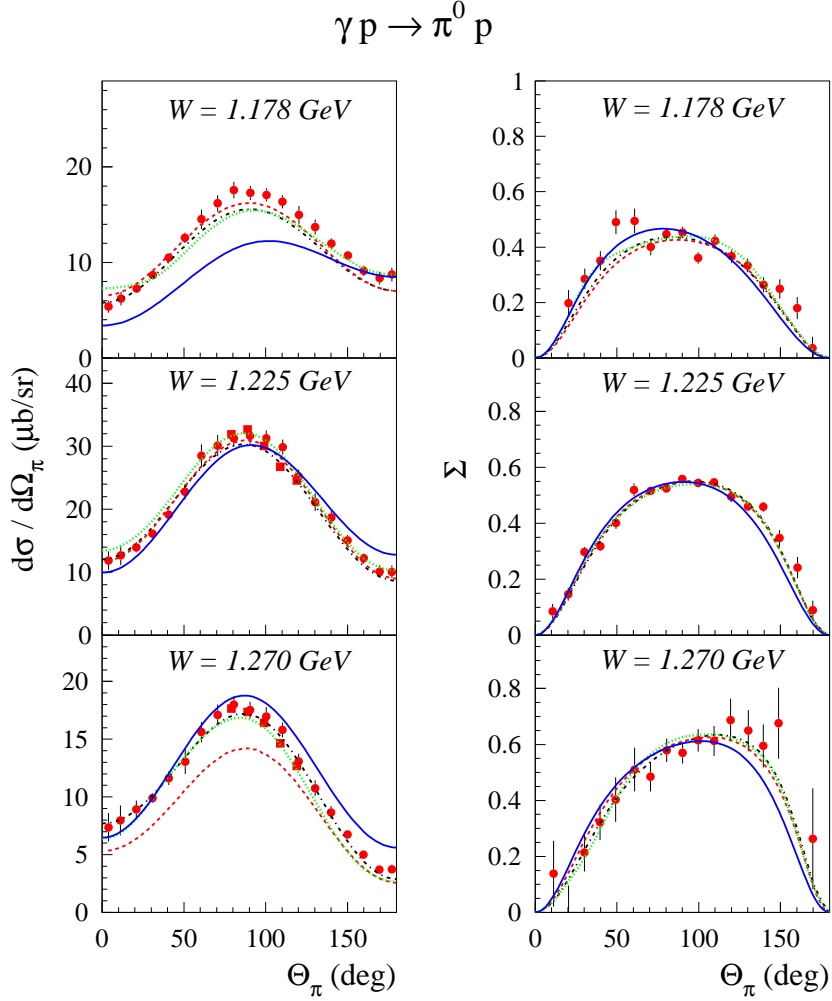


Fig. 53. The differential cross section (left panels) and photon asymmetry (right panels) for $\gamma p \rightarrow \pi^0 p$ through the $\Delta(1232)$ resonance region. Curve conventions as in Fig. 51. The data points are from MAMI : Refs. [23,293] (red circles) and [292] (red squares).

The presented NLO χ EFT calculations (solid blue curves) are done in the scheme designed to work in a small energy domain around the resonance, as discussed in Sect. 4. It is therefore of interest to see how far away from the resonance such calculations actually work. One sees from Figs. 51-59 that the NLO calculation reproduces well the pion angular dependencies of the $\pi^0 p$ and $\pi^+ n$ observables around resonance. Below the resonance, the χ EFT results for the $\pi^0 p$ cross sections, and to lesser extent for the $\pi^+ n$ cross sections, start to fall below the data. It was checked that this is mainly due to the absence of the anomalous magnetic couplings in the Born diagrams and in the πN loop corrections to the $\gamma N \Delta$ vertex. Such effects are coming in at NNLO in the δ -expansion. For energies about 50 MeV or higher above resonance, the NLO begins to overestimate the $\pi^0 p$ cross sections, and to a lesser extent the $\pi^+ n$ cross sections, which also shows up in larger deviations from the data for Σ (for $\pi^+ n$) and T and P (for $\pi^0 p$). Nevertheless, given the simplicity of the NLO calculations in the δ -expansion and its potential for systematic improvement, one can be pleased with the results. Overall, the χ EFT to NLO

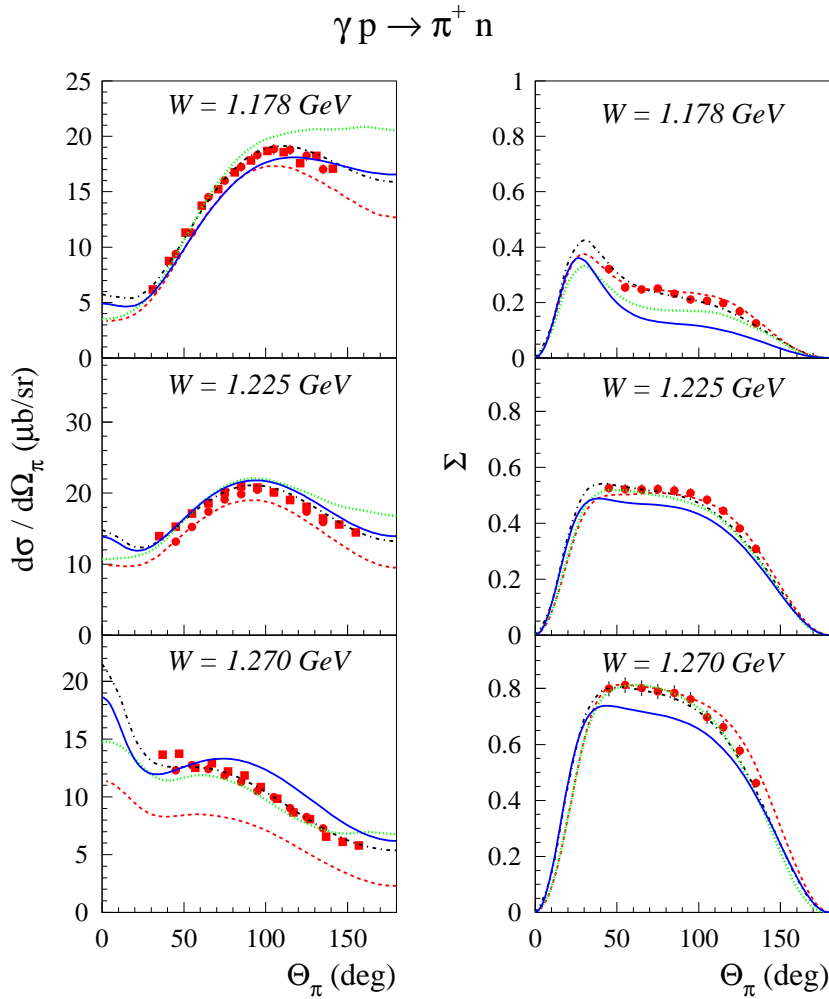


Fig. 54. The differential cross section (left panels) and photon asymmetry (right panels) for $\gamma p \rightarrow \pi^+ n$ through the $\Delta(1232)$ resonance region. Curve conventions as in Fig. 51. The data points are from MAMI : Refs. [23] (red circles) and [292] (red squares).

in the δ -expansion provides a simple and elegant description of pion photoproduction observables in a 100 MeV window around the Δ -resonance. The precision of the available data can be exploited to study the higher order effects in the $\gamma N \Delta$ transition using calculations beyond NLO.

5.3 Pion electroproduction

The pion production by electrons was first observed by Panofsky and his collaborators at Stanford in 1955. Even though it was first attempted at Cornell in 1965, it was not until in the beginning of 1970's that double-arm or coincidence experiments, in which the scattered electron and one of the recoiling hadrons are measured in coincidence, were actively pursued. A summary of the coincidence experimental results on pion electroproduction, up until early

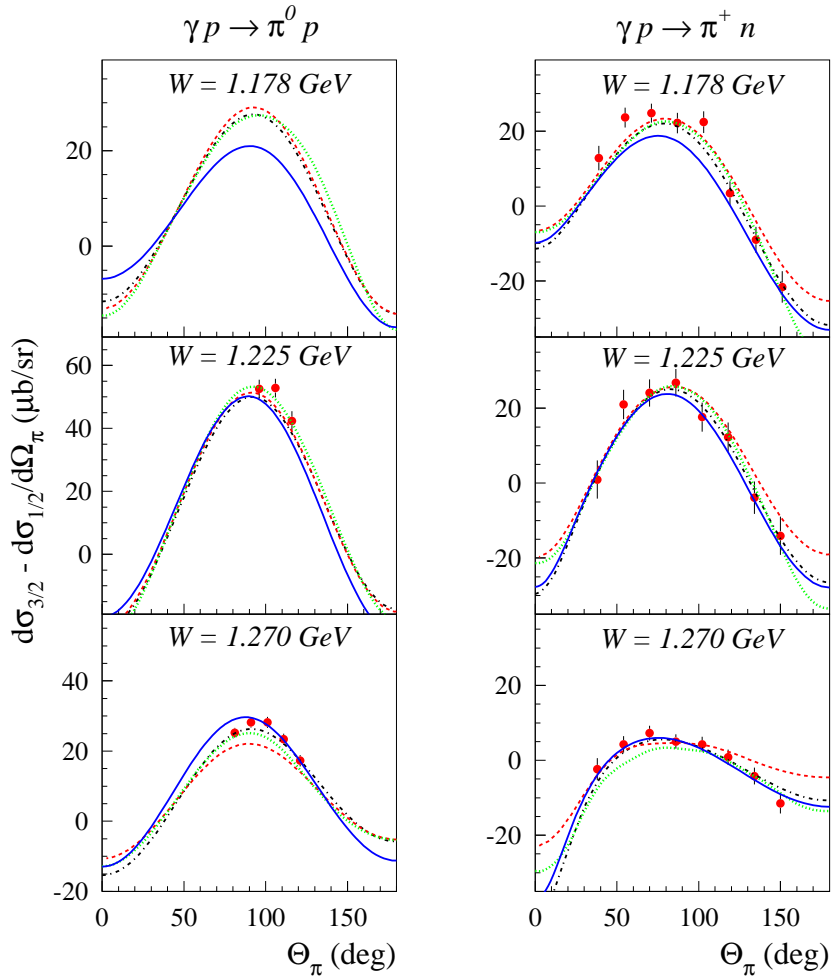


Fig. 55. The helicity difference differential cross section $d\sigma_{3/2} - d\sigma_{1/2}$ for $\gamma p \rightarrow \pi^0 p$ (left panels) and $\gamma p \rightarrow \pi^+ n$ (right panels) through the $\Delta(1232)$ resonance region. Curve conventions as in Fig. 51. The data points are from MAMI [291] (red circles).

1980's can be found in the extensive review of Ref. [303].

Extensive sets of high statistics data of pion electroproduction have been collected at BATES, MAMI, and JLab in the last several years. The majority of them are on the $ep \rightarrow e' p \pi^0$ reaction. They cover a large range of invariant mass W , from threshold up to 2.5 GeV and a wide range in momentum-transfer squared $Q^2 = 0.05 - 6$ GeV 2 , and the full coverage of pion polar and azimuthal angles. Single and double polarization measurements have also been performed. Single polarization experiments are carried out with polarized electron beams to measure the beam helicity asymmetry. Double polarization experiments are performed with a polarized electron beam together with a polarized target or with recoil nucleon polarization measurements. Data on the threshold π^0 production are measured mostly at low Q^2 region in order to test the chiral perturbation theory. They have been obtained prominently at MAMI, see Ref. [304] and references contained therein.

Data on the $\pi^+ n$ channel were much less abundant in the past. Most of them are in the mass

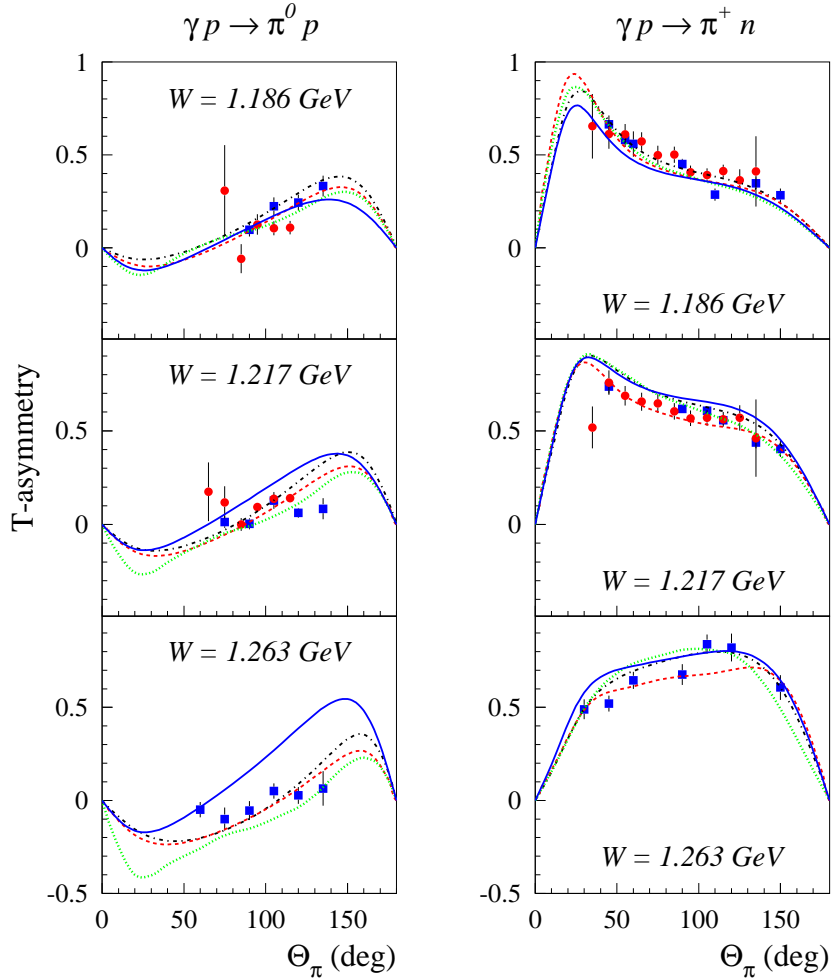


Fig. 56. The target asymmetry T for $\gamma p \rightarrow \pi^0 p$ (left panels) and $\gamma p \rightarrow \pi^+ n$ (right panels) through the $\Delta(1232)$ resonance region. Curve conventions as in Fig. 51. The data points for $\gamma p \rightarrow \pi^0 p$ are from Refs. [294] (blue squares) and [295] (red circles). The data points for $\gamma p \rightarrow \pi^+ n$ are from Refs. [296] (blue squares) and [297] (red circles).

range of the first and second resonances and at forward pion *c.m.* angles, with some at backward angles. As in the case of photoproduction, data on the $\pi^- p$ channel from a neutron (deuterium) target is even more scarce. Currently, CLAS at JLab has an active programs to measure cross sections for the $\pi^+ n$ [305] and $\pi^- p$ [306] channels.

Measurements made before the early 1980's are summarized in Tables 5-7 in Ref. [303]. The new electroproduction data in the resonance region, measured recently at BATES, ELSA, JLab, and MAMI, up until 2003 are given in Table 2 in Ref. [12].

Electroproduction of neutral pions on a proton target has been employed most extensively for the purpose of determining the Q^2 evolution of the R_{EM} and R_{SM} ratios. Many experiments have been performed at BATES, MAMI, and JLab. At BATES, the experiments have been set up for central invariant mass $W = 1.232$ GeV and $Q^2 = 0.127$ GeV 2 . With the use of either unpolarized or polarized electron beams and choice of specific kinematics, quantities like induced

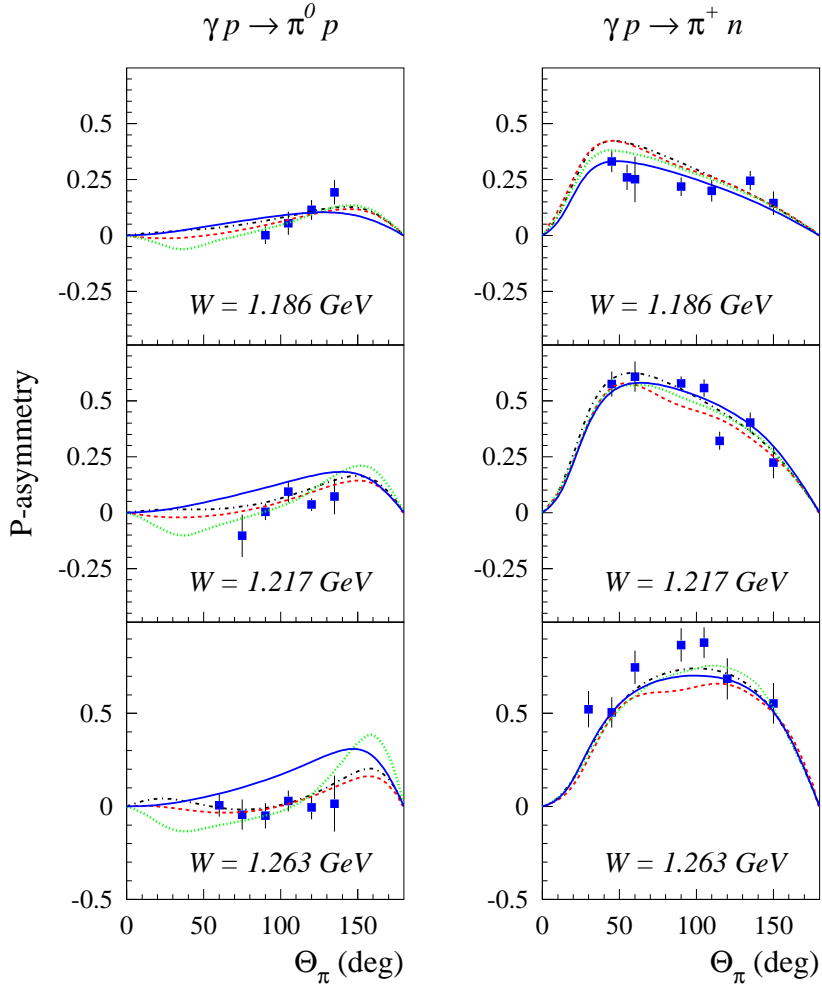


Fig. 57. The recoil asymmetry P for $\gamma p \rightarrow \pi^0 p$ (left panels) and $\gamma p \rightarrow \pi^+ n$ (right panels) through the $\Delta(1232)$ resonance region. Curve conventions as in Fig. 51. The data points for $\gamma p \rightarrow \pi^0 p$ are from Ref. [294]. The data points for $\gamma p \rightarrow \pi^+ n$ are from Ref. [296].

polarization, and σ_0 , σ_{LT} , $\sigma_{TL'}$, and σ_{TT} have been measured [307, 95, 312, 80]. Both unpolarized and polarized experiments are done at MAMI [78, 308, 77, 79] with Q^2 ranges from a low value of 0.06 GeV^2 [79] to 0.2 GeV^2 . In [78], the recoil proton polarization was measured in the double-polarized $p(\vec{e}, e' \vec{p})\pi^0$ reaction and all three proton polarization components were measured simultaneously. All three halls at JLab, Hall A [309, 142], Hall B (CLAS) [81, 310, 131], and Hall C [130], have programs on π^0 electroproduction with either unpolarized or polarized electrons and a large variety of observables have been measured. The experiment of Ref. [131] measured Q^2 values as high as 6.0 GeV^2 . The aim of such large Q^2 measurements is to map out the transition towards the pQCD regime. The large amount of precision data have been used to extract the $N \rightarrow \Delta(1232)$ transition form factors from $Q^2 = 0$ to 6 GeV^2 . They also provide very stringent tests for theoretical models.

In Figs. 60-62, the different virtual photon absorption cross sections around the resonance position are displayed at three different Q^2 values: $Q^2 = 0.06, 0.127, 0.20 \text{ GeV}^2$, where recent

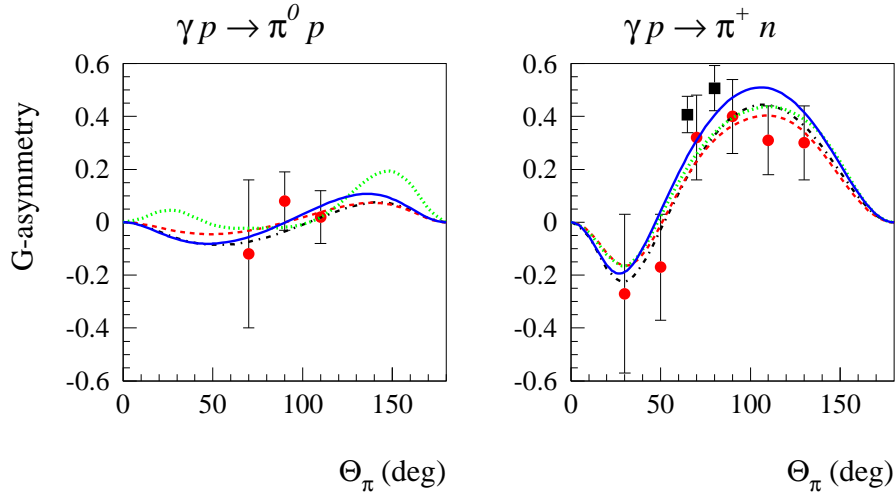


Fig. 58. The double polarization asymmetry G for $\gamma p \rightarrow \pi^0 p$ (left panel) and $\gamma p \rightarrow \pi^+ n$ (right panel) at $W = 1.232$ GeV. Curve conventions as in Fig. 51. The data points are from Kharkov [298] (black squares) and from MAMI [300] (red circles).

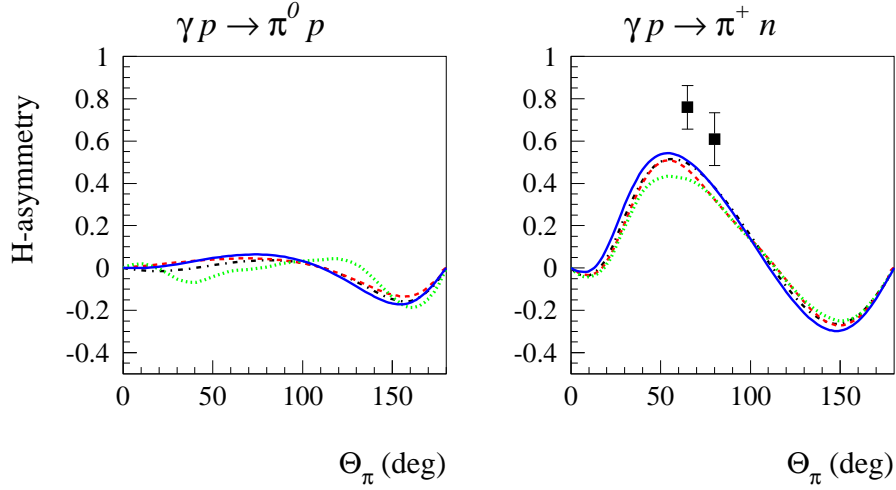


Fig. 59. The double polarization asymmetry H for $\gamma p \rightarrow \pi^0 p$ (left panel) and $\gamma p \rightarrow \pi^+ n$ (right panel) at $W = 1.232$ GeV. Curve conventions as in Fig. 51. The data points are from Kharkov [298] (black squares).

precision data are available. We compare these data with the predictions made within the χ EFT framework [88,89] and using the SL, DMT, and DUO dynamical models.

In the χ EFT calculations, the low-energy constants g_M and g_E , were fixed from the resonant pion photoproduction multipoles. Therefore, the only other low-energy constant from the chiral Lagrangian entering the NLO calculation is g_C . The main sensitivity on g_C enters in σ_{TL} . A best description of the σ_{TL} data at low Q^2 is obtained by choosing $g_C = -2.6$. In Figs. 60-62, we also include as an illustration the theoretical uncertainty of the NLO χ EFT result, estimated

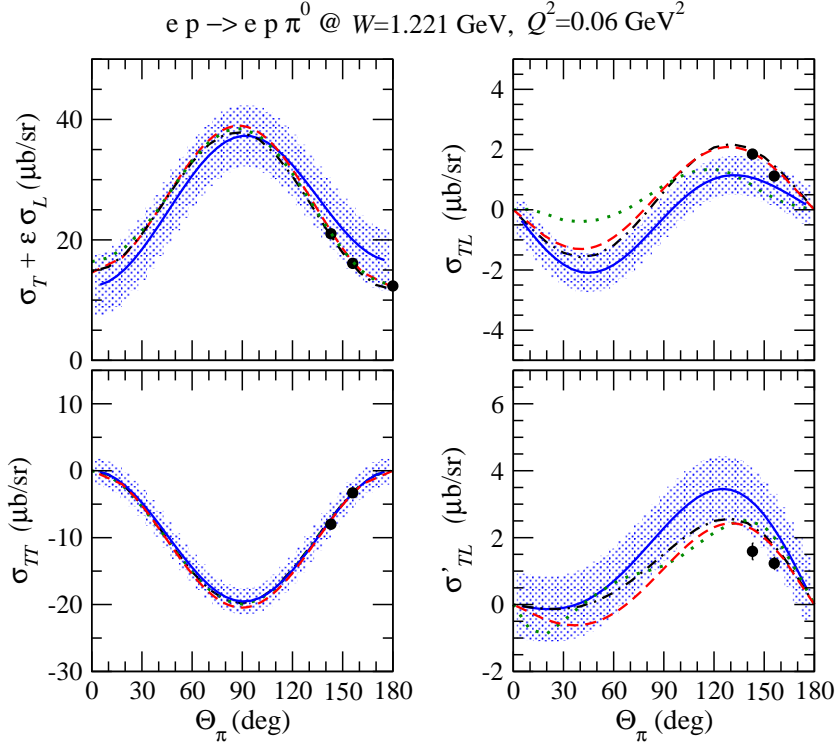


Fig. 60. The pion angular dependence of the $\gamma^* p \rightarrow \pi^0 p$ cross sections at $W = 1.221$ GeV and $Q^2 = 0.06$ GeV 2 . Dashed-dotted (black) curves : DMT01 model. Dashed (red) curves : SL model. Dotted (green) curves : DUO model. Solid (blue) curves : χ EFT results of Refs. [88,89]. The bands provide an estimate of the theoretical error for the χ EFT calculations. Data points are from the MAMI experiment of Ref. [79].

using Eq. (4.78), where the average is taken over the range of Θ_π ²¹. From Figs. 60-62, one sees that the NLO χ EFT calculation, within its accuracy, is consistent with the experimental data for these observables at low Q^2 . Only for $\sigma_{TL'}$, the χ EFT calculation overpredicts the data with increasing Q^2 . This is because this observable is sensitive to the background multipoles E_{0+} and S_{0+} which are not very accurately reproduced in the NLO χ EFT calculation, see Fig. 43.

The dynamical models are in basic agreement with each other and the data for the transverse cross sections. Differences between the models do show up in the σ_{TL} and $\sigma_{TL'}$ cross sections which involve the longitudinal amplitude. In particular for $\sigma_{TL'}$ the differences reflect to large extent how the non-resonant S_{0+} multipole is described in the models.

In Fig. 63, we compare the data for the resonant multipoles up to the largest measured values of Q^2 with the results obtained for the three dynamical models (SL, DMT, DUO) reviewed in this work. One sees that all three models give a very accurate account of the dominant $M_{1+}^{(3/2)}$ multipole. They are also in good agreement with the R_{SM} ratio, which grows to a value of around -25% around $Q^2 \simeq 6$ GeV 2 . Only for the R_{EM} ratio, the three dynamical models show clear differences. While in the DMT and DUO models the R_{EM} ratio shows a zero crossing around $Q^2 \simeq 3$ GeV 2 , the SL result is in good agreement with the data, which give small

²¹ Note that σ_{TL} and $\sigma_{TL'}$ do not receive any LO contributions and therefore the LO= 0 case in Eq. (4.78) must be applied in the estimate.

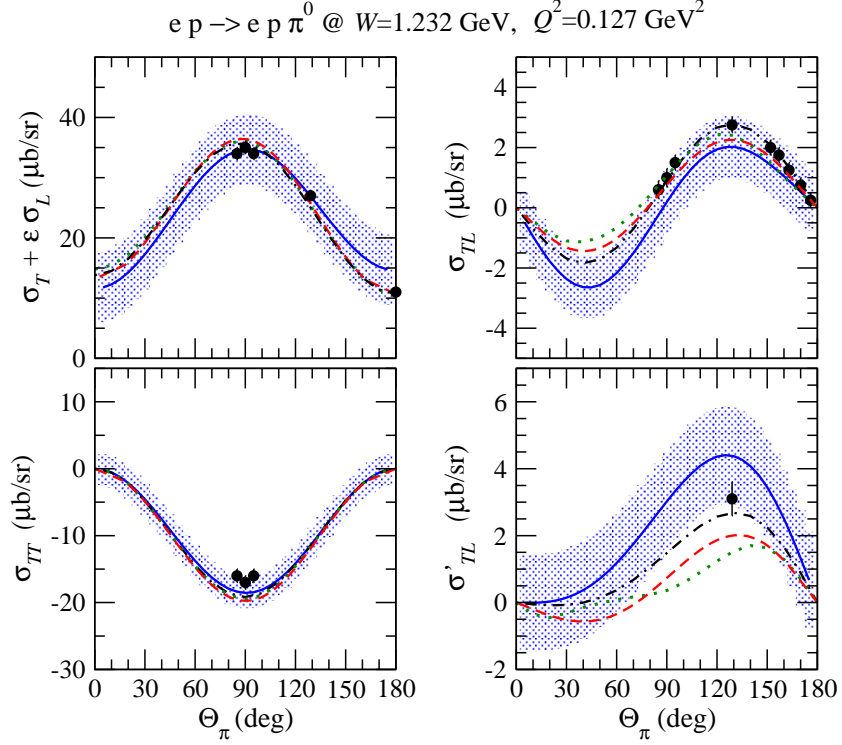


Fig. 61. The pion angular dependence of the $\gamma^* p \rightarrow \pi^0 p$ cross sections at $W = 1.232 \text{ GeV}$ and $Q^2 = 0.127 \text{ GeV}^2$. Curve conventions as in Fig. 60. The bands provide an estimate of the theoretical error for the χ EFT calculations. Data points are from BATES experiments [95,312,80].

negative values for R_{EM} (around -4%) at the largest measured values of $Q^2 \simeq 6 \text{ GeV}^2$. As remarked in Sect. 2.8, the data are very far from the pQCD prediction for R_{EM} which should approach $+100\%$ at asymptotically large values of Q^2 . The DMT calculation [91] finds nearly as large values for the subdominant (according to pQCD) helicity amplitude $A_{3/2}$ as for the pQCD dominant amplitude $A_{1/2}$, at accessible values of Q^2 . In both the calculations and the data, one therefore sees no onset of hadron helicity conservation in the $\gamma N \Delta$ transition up to $Q^2 \simeq 6 \text{ GeV}^2$.

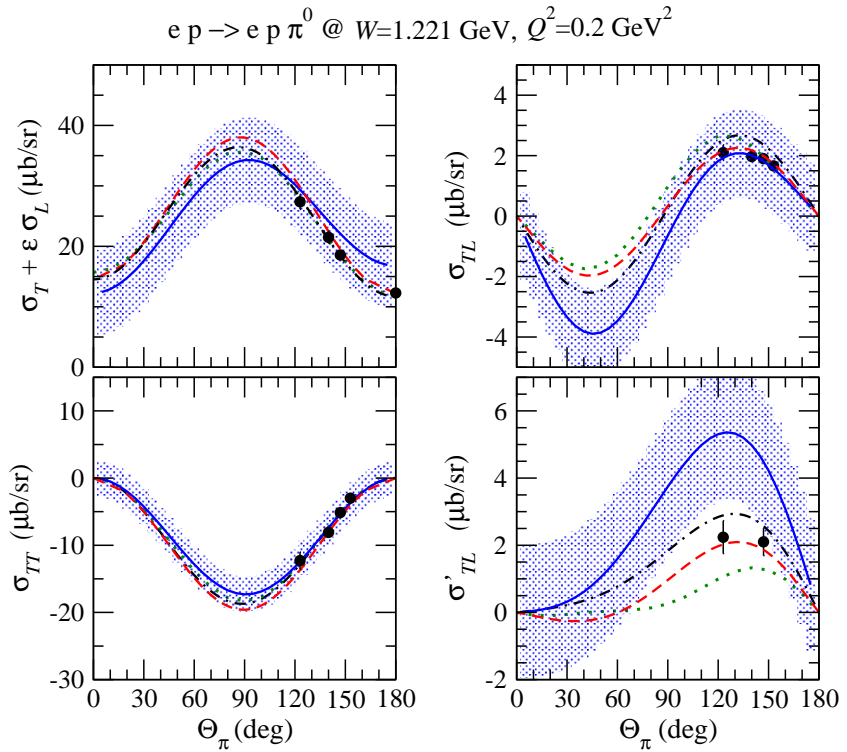


Fig. 62. The pion angular dependence of the $\gamma^* p \rightarrow \pi^0 p$ cross sections at $W = 1.221 \text{ GeV}$ and $Q^2 = 0.20 \text{ GeV}^2$. Curve conventions as in Fig. 60. The bands provide an estimate of the theoretical error for the χ EFT calculations. Data points are from the MAMI experiment of Ref. [141].

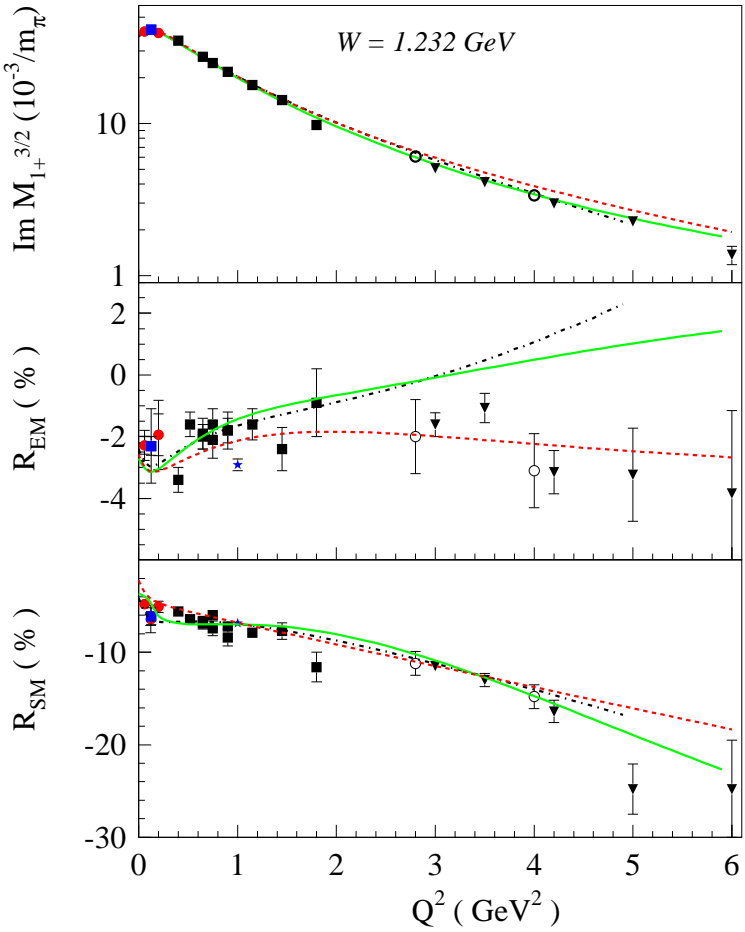


Fig. 63. Q^2 dependence of the resonant multipoles at $W = 1.232$ GeV. Upper panel : imaginary part of $M_{1+}^{(3/2)}$; middle panel : R_{EM} ; lower panel : R_{SM} . The curves are the results obtained in different dynamical models : DMT01 (dashed-dotted black curves); SL (dashed red curves); DUO (solid green curves). The data are from BATES [80] (blue squares), MAMI [23,79,141] (red circles), JLab/Hall C [130] (open circles), JLab/CLAS [81] (black squares) and [131] (inverted triangles), and JLab/Hall A [142] (blue stars).

6 Beyond the one-photon exchange approximation

In all the up-to-date studies of the Δ excitation by electrons ($eN \rightarrow e\Delta$), as discussed in the previous sections, the electromagnetic interaction between the electron and the nucleon is assumed to be mediated by a single photon exchange (1γ). In this Section, we discuss effects beyond this approximation, in particular the effects due to two-photon exchange (2γ). The spectacular discrepancy between the polarization-transfer [152–154] and Rosenbluth-separation measurements [313] of the nucleon elastic form factors is largely due to 2γ -exchange effects [314–316]. Subsequently, the 2γ corrections to the $eN \rightarrow e\Delta$ process were studied in Ref. [317], where these 2γ corrections were evaluated in a parton model. Recently, the 2γ corrections to $eN \rightarrow e\Delta$ were studied in a hadronic model [318]. In what follows, we will review the general formalism for the 2γ corrections to $eN \rightarrow e\Delta$ and discuss their effect within the partonic calculation of Ref. [317].

6.1 General formalism

When describing the $eN \rightarrow e\Delta$ process, the total number of helicity amplitudes is 32, and is reduced to 16 by using parity invariance. Furthermore, in a gauge theory lepton helicity is conserved to all orders in perturbation theory when the lepton mass is zero. Neglecting the lepton mass, reduces the number of helicity amplitudes to 8. Recall that in the 1γ approximation, there are only three independent helicity amplitudes which can be expressed in terms of three form factors of the $\gamma^* N \Delta$ transition as discussed in Sect. 2.1.

The $\gamma^* N \Delta$ transition form factors are usually studied in the $eN \rightarrow e\pi N$ process in the Δ -resonance region. In the 1γ approximation, the $\gamma^* N \rightarrow \pi N$ virtual photon absorption cross section $d\sigma_v/d\Omega_\pi$ was presented in Sect. 3. Beyond the 1γ approximation, one can still formally define a cross section $d\sigma_v/d\Omega_\pi$ from the experimentally measured $eN \rightarrow e\pi N$ five-fold differential cross sections using Eq. (3.7), with momentum transfer q defined as $q \equiv k - k'$. However, beyond the 1γ approximation Γ does not have the physical interpretation any more of a virtual photon flux factor. The expression of the thus defined cross section $d\sigma_v/d\Omega_\pi$ will then also be modified from the 1γ expression of Eq. (3.8). For unpolarized nucleons, the cross section at $W = M_\Delta$ can, in general, be parametrized as (using the notations introduced in Sect. 3) :

$$\begin{aligned} \frac{d\sigma_v}{d\Omega_\pi} = & \sigma_0 + \varepsilon \cos(2\phi_\pi) \sigma_{TT} + h \varepsilon \sin(2\phi_\pi) \sigma'_{TT} \\ & + \sqrt{2\varepsilon} \varepsilon_+ \cos \phi_\pi \sigma_{TL} + h \sqrt{2\varepsilon} \varepsilon_- \sin \phi_\pi \sigma'_{TL}, \end{aligned} \quad (6.1)$$

with $h = \pm 1$ the lepton helicity and $\varepsilon_\pm \equiv \sqrt{1 \pm \varepsilon}$.

It is convenient to multipole expand Eq. (6.1) for the $ep \rightarrow e\Delta^+ \rightarrow e\pi N$ process (*i.e.* keeping only the Δ multipoles) as :

$$\begin{aligned}
\sigma_0 &= A_0 + \frac{1}{2}(3 \cos^2 \theta_\pi - 1) A_2, \\
\sigma_{TT} &= \sin^2 \theta_\pi C_0, \quad \sigma_{TL} = \frac{1}{2} \sin(2\theta_\pi) D_1, \\
\sigma'_{TT} &= \sin^2 \theta_\pi C'_0, \quad \sigma'_{TL} = \frac{1}{2} \sin(2\theta_\pi) D'_1,
\end{aligned} \tag{6.2}$$

where A_0 can be written as:

$$A_0 = \mathcal{I} \frac{e^2}{4\pi} \frac{Q_-^2}{4M_N^2} \frac{(M_\Delta + M_N)}{(M_\Delta - M_N)} \frac{1}{M_\Delta \Gamma_\Delta} (G_M^*)^2 \sigma_R, \tag{6.3}$$

where \mathcal{I} denotes the isospin factor which depends on the final state in the $\Delta^+ \rightarrow \pi N$ decay as : $\mathcal{I}(\pi^0 p) = 2/3$ and $\mathcal{I}(\pi^+ n) = 1/3$, and where σ_R denotes the reduced cross section σ_R , including 2γ corrections.

We are now in position to discuss the corrections to R_{EM} and R_{SM} as extracted from σ_{TT} and σ_{TL} . Experimentally, these ratios have been extracted at $W = M_\Delta$ using :

$$\begin{aligned}
R_{EM}^{exp,I} &= \frac{3A_2 - 2C_0}{12A_0} \stackrel{1\gamma}{=} R_{EM} + \varepsilon \frac{4M_\Delta^2 Q^2}{Q_+^2 Q_-^2} R_{SM}^2 + \dots \\
R_{SM}^{exp} &= \frac{Q_+ Q_-}{Q M_\Delta} \frac{D_1}{6A_0} \stackrel{1\gamma}{=} R_{SM} - R_{SM} R_{EM} + \dots
\end{aligned} \tag{6.4}$$

where the omitted terms involve cubic products of R_{EM} and R_{SM} . These formulas are usually applied [81] by neglecting the smaller quantities R_{SM}^2 and $R_{EM} \cdot R_{SM}$. Ref. [317], however, kept these quadratic terms, and proposed a second method of extracting R_{EM} :

$$R_{EM}^{exp,II} = \frac{-(A_0 - A_2) - 2C_0}{3(A_0 - A_2) - 2C_0} \stackrel{1\gamma}{=} R_{EM}. \tag{6.5}$$

This method apparently avoids corrections at the one-photon level, which may prove to be significant at larger momentum transfer due to an appreciable contribution of the R_{SM}^2 term.

We denote the corrections to R_{EM} and R_{SM} by :

$$R \simeq R^{exp} + \delta R^{1\gamma} + \delta R^{2\gamma}, \tag{6.6}$$

where $\delta R^{1\gamma}$ denotes the corrections due to the quadratic terms in Eqs. (6.4),(6.5), which are :

$$\begin{aligned}
\delta R_{EM}^{1\gamma,I} &= -\varepsilon \frac{4M_\Delta^2 Q^2}{Q_+^2 Q_-^2} R_{SM}^2, \\
\delta R_{EM}^{1\gamma,II} &= 0, \\
\delta R_{SM}^{1\gamma} &= R_{EM} \cdot R_{SM}.
\end{aligned} \tag{6.7}$$

In Fig. 64, we show the effect of the 1γ corrections on R_{EM} and R_{SM} . We see that its effect on

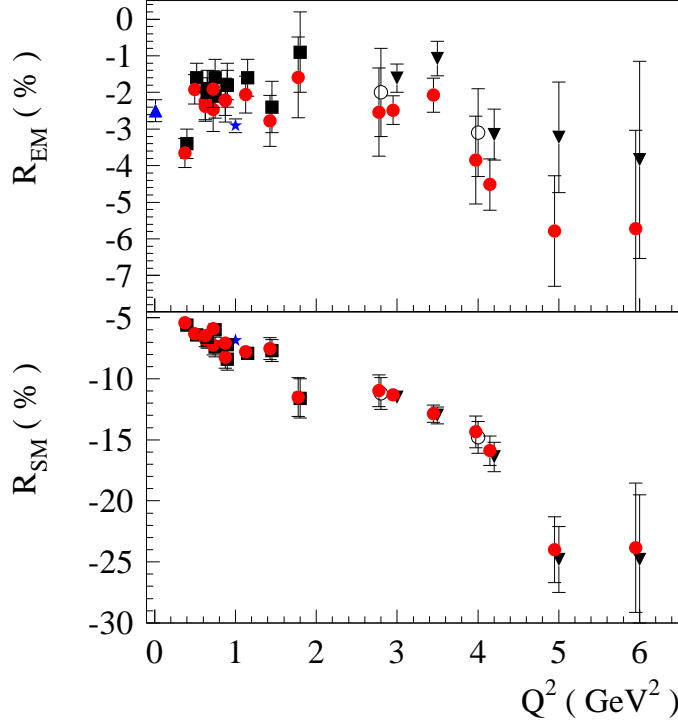


Fig. 64. Q^2 dependence of the 1γ corrections, $\delta R^{1\gamma}$, to R_{EM} (upper panel) and R_{SM} (lower panel) at $W = 1.232$ GeV. The uncorrected data are from JLab/Hall C [130] (open circles), JLab/CLAS [81] (solid squares) and [131] (inverted triangles). The error bars reflect the statistical error only. The red circles include the corrections $\delta R_{EM}^{1\gamma, I}$. The triangle at $Q^2 = 0$ is the real photon point from [23], whereas the star at $Q^2 = 1$ GeV 2 is the extraction from the JLab/Hall A recoil polarization experiment [142], which provides an independent way to extract R_{EM} and R_{SM} .

R_{SM} is negligible, whereas it yields a systematic downward shift of the R_{EM} result. This shift becomes more pronounced at larger ε , and it is found that at the highest Q^2 values it decreases R_{EM} by around 2 %. To avoid such a correction, it calls for extracting R_{EM} according to the procedure *II* as we outlined above. Alternatively, double polarization experiments provide a very useful cross check on the extraction of the R_{EM} and R_{SM} ratios. In Ref. [142], the angular distributions of 14 recoil polarization response functions and two Rosenbluth combinations have been measured for $ep \rightarrow ep\pi^0$ at $Q^2 = 1$ GeV 2 . The analysis of Ref. [142] avoids making a multipole truncation. In particular for R_{EM} , one sees from Fig. 64 that it yields a value which is lower than the one of Ref. [81] based on a multipole truncation, in agreement with the trend observed when applying the correction of Eq. (6.4).

In the following, we briefly describe the partonic estimate of Ref. [317] for the 2γ contribution to the $N \rightarrow \Delta$ electroproduction amplitudes at large Q^2 .

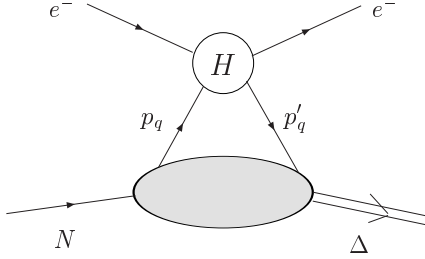


Fig. 65. Handbag approximation for the $eN \rightarrow e\Delta$ process at large momentum transfers. In the partonic scattering process (H), the lepton scatters from quarks with momenta p_q and p'_q . The lower blob represents the $N \rightarrow \Delta$ GPDs.

6.2 Partonic calculation of two-photon exchange effects

In the partonic framework, illustrated in Fig. 65, the 2γ amplitude is related to the $N \rightarrow \Delta$ GPDs, as discussed in Sect. 2.7. This calculation involves a hard scattering subprocess on a quark, which is embedded in the proton by means of the $N \rightarrow \Delta$ GPDs. Besides the dominant vector GPD H_M , corresponding with the magnetic dipole $\gamma N \Delta$ transition considered in Sect. 2.7, it also involves the leading axial-vector GPD, denoted by C_1 , which are the leading GPDs in the large N_c limit [121] contributing to this transition. Analogously to the relation of Eq. (2.57) relating the GPD H_M to the $\gamma^* N \Delta$ magnetic dipole form factor G_M^* , one can relate the GPD C_1 to the $\gamma^* N \Delta$ axial transition form factor C_5^A , introduced by Adler [319].

The $eN \rightarrow e\Delta$ handbag amplitude can then be specified in terms of the following two characteristic integrals [317] :

$$A^* = \int_{-1}^1 \frac{dx}{x} \left[\frac{\hat{s} - \hat{u}}{Q^2} g_M^{hard} + g_A^{(2\gamma)} \right] \sqrt{\frac{2}{3}} \frac{1}{6} H_M, \quad (6.8)$$

$$C^* = \int_{-1}^1 \frac{dx}{x} \left[\frac{\hat{s} - \hat{u}}{Q^2} g_A^{(2\gamma)} + g_M^{hard} \right] \text{sgm}(x) \frac{1}{6} C_1, \quad (6.9)$$

where all hard scattering quantities in the square brackets are given in Ref. [316].

In terms of the above integrals A^* and C^* , the reduced cross section of Eq. (6.3) including 2γ corrections, can be expressed as [317] :

$$\begin{aligned} \sigma_R = 1 + 3 R_{EM}^2 + \varepsilon \frac{16 M_\Delta^2 Q^2}{Q_+^2 Q_-^2} R_{SM}^2 \\ + \frac{1}{G_M^*} \sqrt{\frac{2}{3}} \left[\frac{A^* Q^2 \varepsilon_+ \varepsilon_-}{2 Q_+ Q_-} + 2 C^* \frac{Q^2}{Q_-^2} \varepsilon_-^2 \frac{M_N}{M_N + M_\Delta} \right]. \end{aligned} \quad (6.10)$$

Furthermore, the 2γ exchange corrections to R_{EM} and R_{SM} , are :

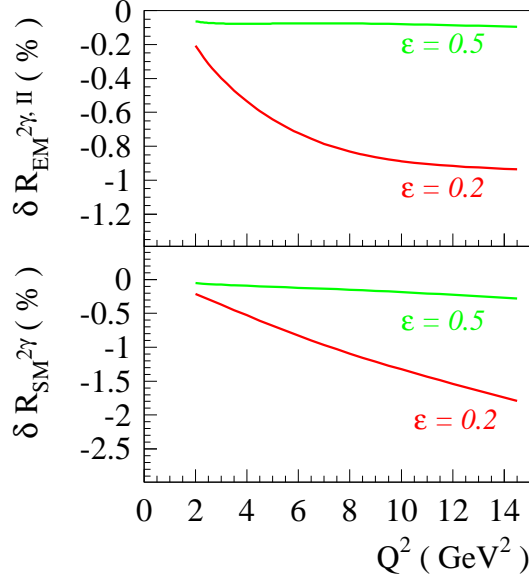


Fig. 66. Q^2 dependence of the 2γ corrections to R_{EM} (upper panel) and R_{SM} (lower panel) at $W = 1.232$ GeV and for different values of ε . Figure from Ref. [317].

$$\begin{aligned}
\delta R_{EM}^{2\gamma,I} &= -\frac{1}{8} \sqrt{\frac{3}{2}} \frac{Q^2}{Q_+ Q_-} \frac{\varepsilon_-^3 \varepsilon_+}{\varepsilon} \frac{1}{G_M^*} A^* + \frac{1}{4} \sqrt{\frac{2}{3}} \frac{Q^2}{Q_-^2} \frac{\varepsilon_-^2 \varepsilon_+^2}{\varepsilon} \frac{M_N}{(M_N + M_\Delta)} \frac{1}{G_M^*} C^*, \\
\delta R_{EM}^{2\gamma,II} &= 2 \delta R_{EM}^{2\gamma,I}, \\
\delta R_{SM}^{2\gamma} &= \sqrt{\frac{2}{3}} \frac{(Q^2 - M_\Delta^2 + M_N^2)}{4 M_\Delta^2} \frac{Q_+}{Q_-} \frac{1}{\sqrt{2\varepsilon}} \frac{\varepsilon_-^2}{\varepsilon_+} \frac{M_N}{(M_N + M_\Delta)} \frac{1}{G_M^*} C^*. \tag{6.11}
\end{aligned}$$

To provide numerical estimates for the 2γ corrections, one needs a model for the $N \rightarrow \Delta$ GPDs which appear in the integrals A^* and C^* . In Ref. [317], the large N_c relations discussed in Sect. 2.7 were used. For the GPD H_M , the model of Sect. 2.7.2 is used, whereas the axial GPD C_1 is expressed through the isovector combination $C_1(x, 0, Q^2) = \sqrt{3}[\tilde{H}^u - \tilde{H}^d](x, 0, Q^2)$ of the nucleon axial GPDs, see Ref. [121].

In Fig. 66 we show the 2γ corrections to R_{EM} and R_{SM} estimated using the modified Regge GPD model. We see that the 2γ effects are mainly pronounced at small ε and larger Q^2 . For R_{EM} they are well below 1 %, whereas they yield a negative correction to R_{SM} by around 1 %, when R_{SM} is extracted from σ_{TL} according to Eq. (6.4).

Another way to obtain R_{SM} is from a Rosenbluth-like analysis of the cross section σ_0 for the $eN \rightarrow e\Delta$ reaction. In Fig. 67, we show the reduced cross section from Eq. (6.10). One sees how a different extraction of R_{SM} can yield a significantly different result. Starting from a value of R_{SM} (e.g., -10 %) extracted from σ_{TL} , adding in the 2γ -exchange corrections gives a sizable change in the slope of the Rosenbluth plot. When fitting the total result by a straight line in an intermediate ε range, one extracts a value of R_{SM} around 3 percentage units lower than its value as extracted from σ_{TL} . This is sizable, as it corresponds with a 30% correction on

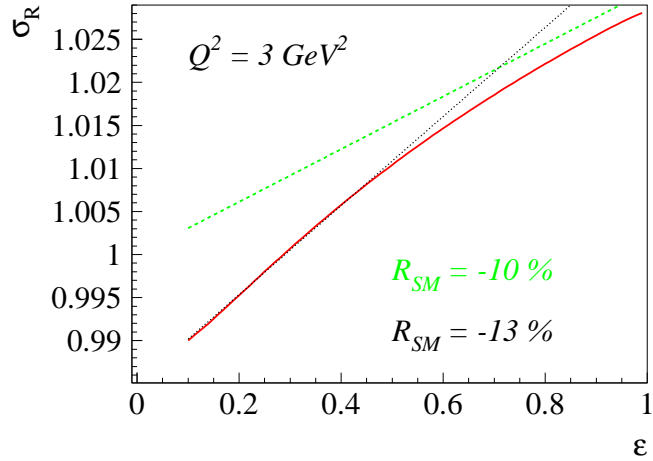


Fig. 67. Rosenbluth plot of the reduced cross section σ_R of Eq. (6.10) for the $eN \rightarrow e\Delta$ reaction at $Q^2 = 3 \text{ GeV}^2$. The dashed curve corresponding with $R_{SM} = -10\%$ is the 1γ result, whereas the solid curve represents the result including 2γ corrections for the same values of R_{SM} . The dotted curve corresponding with $R_{SM} = -13\%$ corresponds with a linear fit to the total result in an intermediate ε range. Figure from Ref. [317].

the absolute value of R_{SM} . This is similar using the Rosenbluth method to extract the proton elastic form factor ratio G_E^p/G_M^p , where the 2γ -corrections were found to be large [314].

Note that obtaining R_{SM} from the D_1/A_0 ratio depends on isolating the $\cos \phi_\pi$ term in the cross section. This term implicitly uses the decay $\Delta \rightarrow N\pi$ to give us some information about the polarization of the Δ . The “ D_1/A_0 ” method is thus the analog of the polarization transfer measurement of G_E/G_M in the elastic case. Like the elastic case, the calculations of Ref. [317] show that there are sizeable corrections to the Rosenbluth-like determination of R_{SM} , and significantly smaller corrections if R_{SM} is obtained from D_1/A_0 . It will therefore be interesting to confront the D_1/A_0 extraction of R_{SM} with the new Rosenbluth separation data in the Δ region up to $Q^2 \simeq 5 \text{ GeV}^2$ which are presently under analysis [320,321].

7 Conclusions and outlook

In this work we have given a review of the recent progress in our understanding of the electromagnetic excitation of the Δ -resonance.

On the experimental side, high-precision data for low- Q^2 pion electroproduction in the Δ -resonance region have become available from BATES, MAMI and JLab. As a result of these measurements, a consistent picture has emerged for the small quadrupole ratios R_{EM} and R_{SM} . The electric quadrupole over magnetic dipole ratio R_{EM} is around -2% . The Coulomb quadrupole over magnetic dipole ratio R_{SM} is around -6% in the Q^2 range up to about 1 GeV^2 , and becomes more negative with increasing values of Q^2 . The measurements at large Q^2 show no trend towards the pQCD predictions. Up to the largest measured Q^2 values around 6 GeV^2 , the dominant magnetic dipole $\gamma^* N \Delta$ form factor decreases faster than the pQCD scaling prediction $\sim 1/Q^4$, and the R_{EM} ratio shows no trend towards a zero crossing to reach the pQCD prediction of $+100\%$.

The small value of the R_{EM} ratio has been understood in the large N_c limit where the R_{EM} ratio is of order $\sim 1/N_c^2$. The large N_c limit leads to the spin-flavor symmetry which is used in many quark models. In such quark models the small non-zero values of R_{EM} and R_{SM} are interpreted as indicators of hadron deformation, because they require d -wave components in the N and/or Δ -wave functions. The constituent quark models yield however too small (absolute) values for the R_{EM} and R_{SM} ratios, and underpredict the $M1\ N \rightarrow \Delta$ transition by about 25% . A natural way to improve on such quark models is to include pion degrees of freedom. A variety of models have shown that pionic effects to the $\gamma N \Delta$ transition are indeed sizeable. In particular the strong tensor interaction due to one-pion exchange between quarks may yield to a simultaneous spin flip of two quarks in the nucleon and yield non-zero $E2$ and $C2$ amplitudes even if the quark wave functions have no d -state admixture.

A systematic framework to account for the pion loop effects in the $N \rightarrow \Delta$ transition has emerged in recent years using a chiral effective field theory. An extension of chiral perturbation theory to the $\Delta(1232)$ -resonance energy region based on the δ -expansion has been developed. In this χ EFT framework the expansion is done in the small parameter δ equal to the excitation energy of the resonance over the chiral symmetry-breaking scale. The other low-energy scale of the theory, the pion mass, counts as δ^2 , which is a crucial point for an adequate counting of the Δ -resonance contributions in both the low-energy and the resonance energy regions. This framework has been applied to the process of pion electroproduction. A complete calculation of this process in the resonance region up to, and including, next-to-leading order in the δ -expansion satisfies *gauge and chiral symmetries* perturbatively, and *Lorentz-covariance, analyticity, unitarity (Watson's theorem)* exactly. The low-energy constants (LECs) entering at this order are the $\gamma N \Delta$ couplings g_M , g_E , g_C characterizing the $M1$, $E2$, $C2$ transitions, respectively. They are extracted from a fit to the pion photoproduction data, and for g_C to the pion electroproduction at low Q^2 . Once these LECs are fitted, both the energy (W) and Q^2 dependencies follow as predictions. The NLO results were found to give a good description of both the energy-dependence around Δ -resonance and the low Q^2 dependence of the pion electroproduction data.

We have also reviewed the tremendous recent progress achieved in the lattice QCD simulations of the $\gamma N \Delta$ transition. They now clearly establish a non-zero negative value for the R_{EM}

and R_{SM} ratios. However the present lattice calculations have been obtained for pion masses well above 300 MeV. A naive linear extrapolation in the quark mass to its physical value, yields a value for R_{SM} which is however in disagreement with experiment. It has been reviewed that the χ EFT framework plays a *dual role* in that it allows for an extraction of resonance parameters from observables *and* predicts their pion-mass dependence. It was seen that the opening of the $\Delta \rightarrow \pi N$ decay channel at $m_\pi = M_\Delta - M_N$ induces a pronounced non-analytic behavior of the R_{EM} and R_{SM} ratios. While the linearly-extrapolated lattice QCD results for R_{SM} are in disagreement with experimental data, the χ EFT prediction of the non-analytic dependencies suggests that these results are in fact consistent with experiment.

We reviewed that the quark structure of the electromagnetic $N \rightarrow \Delta$ transition can be accessed in hard scattering processes such as the deeply virtual Compton scattering processes $\gamma^* N \rightarrow \gamma \Delta$, where the virtual photon γ^* carries a large virtuality. The non-perturbative information in this process can be parametrized in terms of $N \rightarrow \Delta$ generalized quark distributions. The $N \rightarrow \Delta$ transition form factors are obtained as first moments of these GPDs. In the large N_c limit, the dominant magnetic GPD is related to an isovector combination of nucleon GPDs. Using this large N_c relation combined with a Regge parametrization for the nucleon GPDs, fitted to the elastic nucleon form factors, the magnetic dipole GPD was calculated. Its first moment yields a prediction for the Q^2 dependence for the $M1 \gamma^* N \Delta$ form factor. This prediction is very well in agreement with the recent data up to the highest measured Q^2 value of around 6 GeV². This calculation also shows that the $M1 \gamma^* N \Delta$ form factor follows approximately the same fall-off as the nucleon (isovector) Pauli form factor, yielding a faster fall-off at large Q^2 compared with the $1/Q^4$ pQCD prediction. Likewise, we have used a large N_c relation between the low Q^2 R_{EM} ratio and the neutron electric form factor to calculate the electric quadrupole $N \rightarrow \Delta$ GPD.

At large momentum transfer, we discussed the 2γ contribution to the $eN \rightarrow e\Delta(1232) \rightarrow e\pi N$ process. The 2γ amplitude has been related in a partonic model to the $N \rightarrow \Delta$ GPDs. For R_{EM} , the 2γ corrections were found to be small, below the 1 % level. However, the neglect of a quadratic term R_{SM}^2 in a truncated multipole expansion to extract R_{EM} yields corrections at the 1-2 % level. The 2γ corrections to R_{SM} on the other hand are substantially different when extracting this quantity from an interference cross section or from unpolarized cross sections, as has been observed before for the elastic $eN \rightarrow eN$ process. They turn out to be important when extracting R_{SM} at large Q^2 from the unpolarized longitudinal cross section using a Rosenbluth separation.

Before finishing, let us spell out a few open problems and challenges (both theoretical and experimental) in this field :

(1) *Issues in χ EFT:*

- a) To interpret the precise data on pion photo- and electroproduction at low Q^2 with minimal model assumptions, requires χ EFT calculations to go beyond making predictions of $\gamma^* N \Delta$ form factors and directly perform the comparison at the level of the observables. The χ EFT to NLO in the δ -expansion power counting scheme have shown to yield an overall satisfying description of a large number of pion photo- and electroproduction observables.
- b) The χ EFT calculations in the δ -expansion have been obtained at NLO for the $\gamma^* N \rightarrow \pi N$ process. The present theoretical uncertainties of these calculations are larger than the

precision of present data. The next step for the theory is to go beyond a NLO calculation.

- c) The χ EFT calculation also allows to make predictions for Compton and virtual Compton scattering processes in the Δ region. A comparison of the NLO predictions for $\gamma^* N \rightarrow \pi N$, real and virtual Compton scattering may yield a powerful cross-check of the theory.
- d) In the low Q^2 region, it will be very worthwhile to measure the complementary channels in particular virtual Compton scattering in the Δ region.
- e) The M1 excitation of the Δ gives a large (para)magnetic contribution to the magnetic polarizability of the nucleon ($\approx 6 \cdot 10^{-4} \text{ fm}^3$). The challenge is to reconcile this large contribution with the small value observed in experiment.
- f) At present, χ EFT calculations are performed in different power counting schemes. A challenge is to combine the low-energy chiral expansions around threshold with the δ -expansion around Δ -resonance.

(2) *Resonances on the lattice:*

Lattice QCD calculations with dynamical quarks have just started for the electromagnetic $N \rightarrow \Delta$ form factors. They are currently performed for pion masses above 300 MeV where the Δ is stable. The χ EFT shows a strong non-analytic behavior in the quark mass for the $\gamma^* N \Delta$ form factors when the pion mass becomes smaller than the $N - \Delta$ mass difference. It will be a challenge to implement the unstable nature of the Δ on the lattice and to extend these calculations to pion mass values sizeably below 300 MeV.

(3) *Development of dynamical models:*

Building in symmetries in a consistent way is a non-trivial challenge for the dynamical models. Future challenges in this field are finding ways to systematically improve on approximations, identify the limitations, and quantify the theoretical uncertainties.

(4) *The $N \rightarrow \Delta$ GPDs:*

- a) The parametrization of the $N \rightarrow \Delta$ GPD for the C2 transition has not been addressed until now. Model calculations of $N \rightarrow \Delta$ GPDs as well as lattice simulations of its moments will be very useful in order to make a comparison with the quark distributions in a nucleon, as parametrized through the nucleon GPDs.
- b) Of high interest is the measurement of the deeply virtual Compton scattering $\gamma^* N \rightarrow \gamma \Delta$ process to directly access the $N \rightarrow \Delta$ GPDs.

(5) *Large momentum transfer regime:*

- a) At presently accessible momentum transfers ($Q^2 \leq 6 \text{ GeV}^2$), the pQCD prediction ($R_{EM} \rightarrow 1, R_{SM} \rightarrow \text{const}$) seems to be nowhere in sight. A challenge is to map out the transition from χ EFT at low Q^2 to pQCD by measuring the $\gamma^* N \Delta$ form factors to larger Q^2 (e.g. in the near future at the planned JLab 12 GeV facility).
- b) At larger Q^2 , constrain the model dependence in the extraction of multipoles. In this respect, double polarization observables have already been shown to be a very valuable cross-check and should be further investigated.
- c) Check the importance of 2γ exchange corrections by Rosenbluth measurements (via the σ_L cross section) of R_{SM} .

In retrospect, we may say that the impressive level of precision obtained in the measurements of the electromagnetic excitation of the Δ -resonance during the past few years, has challenged the theory to arrive at a QCD based description of the Δ -resonance. Several new theoretical developments are under way and have shown promise and potential. We hope that the present work will stimulate further efforts in this direction and contribute to the very fruitful interplay between theory and experiment in this field.

A General analysis of the electromagnetic pion production on the nucleon

In this Appendix we present the general properties of the pion photo- and electroproduction reactions:

$$\gamma(q) + N(p) \rightarrow N(p') + \pi(k), \quad (\text{A.1})$$

$$e(l_i) + N(p) \rightarrow e'(l_f) + N(p') + \pi(k). \quad (\text{A.2})$$

Namely, we consider the kinematics, various decompositions into invariant amplitudes, the multipole expansion, and the isospin structure.

A.1 Kinematical details

In both cases, the invariant T -matrix can be expressed as

$$T_{fi} = \epsilon_\mu J^\mu, \quad (\text{A.3})$$

where J^μ is the nucleon electromagnetic current matrix element

$$J^\mu = \langle p' k | j^\mu | p \rangle, \quad (\text{A.4})$$

and ϵ_μ is the photon polarization vector for photoproduction and

$$\epsilon_\mu = -\frac{e\bar{u}(q_f)\gamma_\mu u(q_i)}{Q^2}, \quad (\text{A.5})$$

for electroproduction, with $Q^2 = -q^2 = -(l_f - l_i)^2$.

The T-matrix can be expanded in terms of Lorentz-covariant operators as :

$$T_{fi} = \bar{u}(p') \left[\sum_{i=1}^n A_i(s, t, Q^2) M_i \right] u(p), \quad (\text{A.6})$$

where $s = (p + q)^2$, $t = (p' - p)^2$ are the Mandelstam variables, $n = 4(6)$ for photoproduction (electroproduction), and A 's are scalar amplitudes. The expressions for the Lorentz-cavariant operators M_i can be found in Refs. [162,163,202].

A.2 CGLN decomposition

Traditionally the Lorentz structure of the photopion amplitude is expressed in terms of the Pauli matrices and (two-component) spinors [162]:

$$T_{fi}(\gamma^* N \rightarrow \pi N) = \frac{4\pi W}{M_N} \chi_f^\dagger \mathcal{F} \chi_i, \quad (\text{A.7})$$

with \mathcal{F} given by [10,187]:

$$\begin{aligned} \mathcal{F} = & i\tilde{\sigma} \cdot \epsilon F_1 + \sigma \cdot \hat{k} \sigma \cdot (\hat{q} \times \epsilon) F_2 + i\sigma \cdot \hat{q} \tilde{k} \cdot \epsilon F_3 + i\sigma \cdot \hat{k} \tilde{k} \cdot \epsilon F_4 \\ & + i\sigma \cdot \hat{q} \hat{q} \cdot \epsilon F_5 + i\sigma \cdot \hat{k} \hat{q} \cdot \epsilon F_6 - i\sigma \cdot \hat{k} \epsilon_0 F_7 - i\sigma \cdot \hat{q} \epsilon_0 F_8, \end{aligned} \quad (\text{A.8})$$

where σ is spin operator of the nucleon and $\hat{k} = \mathbf{k}/|\mathbf{k}|$, $\hat{q} = \mathbf{q}/|\mathbf{q}|$. Note that with the use of $\tilde{\sigma} = \sigma - (\sigma \cdot \hat{q})\hat{q}$ and $\tilde{k} = \hat{k} - (\hat{k} \cdot \hat{q})\hat{q}$ in the first term of Eq. (A.8), the F_5 and F_6 terms differ from the ones often used in the literature, *e.g.*, [202,164].

Obviously, the first four terms in Eq. (A.8) arise due the transverse polarizations of the photon, while amplitudes F_5 and F_6 come from the longitudinal polarization of the virtual photon. The longitudinal component of the current is related to the scalar component via current conservation and hence:

$$|\mathbf{q}|F_5 = q_0 F_8, \quad |\mathbf{q}|F_6 = q_0 F_7. \quad (\text{A.9})$$

Note also that the scalar amplitudes in Eq. (A.8) (commonly known the ‘CGLN amplitudes’) are complex functions of three independent kinematical variables, *e.g.*, $F_i = F_i(W, \Theta_\pi, Q^2)$, with the total energy W , the pion scattering angle Θ_π , and the photon virtuality Q^2 .

A.3 Helicity amplitudes

Cross sections and polarization observables of pion photo- and electroproduction are also often expressed in terms of the helicity amplitudes (see, *e.g.*, [205]):

$$f_{\mu',\lambda\mu} = <\mu'|\mathcal{F}|\lambda\mu>, \quad (\text{A.10})$$

where μ (μ') denotes the helicity of the initial (final) nucleon and λ the photon helicity.

There are 6 (4) independent helicity amplitudes for the case pion electro- (photo-) production. They are defined Table A.3 provided $\mu' = \frac{1}{2}$ and the phase convention of Jacob and Wick [322] is used.

The six helicity amplitudes H_1, \dots, H_6 can be expressed as the following linear combination of the six independent CGLN amplitudes F_1, \dots, F_6 :

μ	λ	-1	1	0
$\frac{1}{2}$		H_1	H_4	H_5
$-\frac{1}{2}$		H_2	$-H_3$	H_6

Table A.1

Helicity amplitudes $if_{\mu'=\frac{1}{2},\lambda\mu}$

$$\begin{aligned}
H_1 &= -\sqrt{\frac{1}{2}} \sin \theta \cos(\theta/2) (F_3 + F_4), \\
H_2 &= \sqrt{2} \cos(\theta/2) [(F_2 - F_1) + \frac{1}{2}(1 - \cos \theta) (F_3 - F_4)], \\
H_3 &= \sqrt{\frac{1}{2}} \sin \theta \sin(\theta/2) (F_3 - F_4), \\
H_4 &= \sqrt{2} \sin(\theta/2) [(F_1 + F_2) + \frac{1}{2}(1 + \cos \theta) (F_3 + F_4)], \\
H_5 &= \cos(\theta/2) (F_5 + F_6), \\
H_6 &= \sin(\theta/2) (F_6 - F_5).
\end{aligned} \tag{A.11}$$

A.4 Multipole decomposition

Multipole amplitudes are obtained with the use of eigenstates of parity and angular momentum, instead of plane wave states. For electroproduction, there are six types of transitions possible to a πN final state with angular momentum l and parity P , which are classified according to the character of the photon, transverse or scalar (or alternatively, longitudinal) and the total angular momentum $J = l \pm \frac{1}{2}$ of the final state. In addition, the transverse photon states can either be electric, with $P = (-1)^L$, or magnetic, with $P = (-1)^{L+1}$, where L is the total orbital angular momentum of the photon.

The expansion of the CGLN amplitudes in terms of the multipole amplitudes is given as follows [202]:

$$\begin{aligned}
F_1 &= \sum_{l \geq 0} \{ (lM_{l+} + E_{l+})P'_{l+1} + [(l+1)M_{l-} + E_{l-}]P'_{l-1} \}, \\
F_2 &= \sum_{l \geq 1} [(l+1)M_{l+} + lM_{l-}]P'_l, \\
F_3 &= \sum_{l \geq 1} [(E_{l+} - M_{l+})P''_{l+1} + (E_{l-} + M_{l-})P''_{l-1}], \\
F_4 &= \sum_{l \geq 2} (M_{l+} - E_{l+} - M_{l-} - E_{l-})P''_l, \\
F_5 &= \sum_{l \geq 0} [(l+1)L_{l+}P'_{l+1} - lL_{l-}P'_{l-1}], \\
F_6 &= \sum_{l \geq 1} [lL_{l-} - (l+1)L_{l+}]P'_l
\end{aligned} \tag{A.12}$$

where P'_l 's are the derivatives of the Legendre polynomials of argument $x = \cos \theta$. Note that in

in the literature the scalar transitions are sometimes employed and described by $S_{l\pm}$ multipoles, which correspond to the multipole decomposition of the amplitudes F_7 and F_8 . They are connected with the longitudinal ones by $L_{l\pm} = (\omega_{\mathbf{q}}/|\mathbf{q}|)S_{l\pm}$.

A.5 Isospin decomposition

Assuming isospin conservation, there are three independent isospin amplitudes for the single pion production off a nucleon by a photon. These are: $A^{(0)}$ for the isoscalar photon, and $A^{(1/2)}$ and $A^{(3/2)}$ for the isovector photon. The latter two correspond to the πN system with total isospin $I = 1/2$ and $I = 3/2$, respectively. The isospin structure of any photopion amplitude (e.g., the multipoles) can be written as:

$$A = A^{(+)}\delta_{\alpha 3} + A^{(-)}\frac{1}{2}[\tau_{\alpha}, \tau_3] + A^{(0)}\tau_{\alpha}, \quad (\text{A.13})$$

where α is the pion isospin index and τ_{α} the nucleon isospin matrices. The isospin amplitudes $A^{(1/2)}$, and $A^{(3/2)}$ are related to the amplitudes of Eq. (A.13) as :

$$A^{(3/2)} = A^{(+)} - A^{(-)}, \quad A^{(1/2)} = A^{(+)} + 2A^{(-)}. \quad (\text{A.14})$$

It will also be useful to define the proton ${}_p A^{(1/2)}$ and neutron ${}_n A^{(1/2)}$ amplitudes with total isospin 1/2,

$${}_p A^{(1/2)} = A^{(0)} + \frac{1}{3}A^{(1/2)}, \quad {}_n A^{(1/2)} = A^{(0)} - \frac{1}{3}A^{(1/2)}. \quad (\text{A.15})$$

With this convention the physical amplitudes for the four physical pion photo- and electroproduction processes are

$$\begin{aligned} A(\gamma^* p \rightarrow n\pi^+) &= \sqrt{2} \left[{}_p A^{(1/2)} - \frac{1}{3}A^{(3/2)} \right], \\ A(\gamma^* p \rightarrow p\pi^0) &= {}_p A^{(1/2)} + \frac{2}{3}A^{(3/2)}, \\ A(\gamma^* n \rightarrow p\pi^-) &= \sqrt{2} \left[{}_n A^{(1/2)} + \frac{1}{3}A^{(3/2)} \right], \\ A(\gamma^* n \rightarrow n\pi^0) &= - {}_n A^{(1/2)} + \frac{2}{3}A^{(3/2)}. \end{aligned} \quad (\text{A.16})$$

Under the interchange of s and u (crossing), the functions $A_i^{(\pm,0)}$ are either even or odd, i.e., and this crossing symmetry can readily be derived from the assumption of charge conjugation C invariance for photo- and electroproduction. These crossing symmetry properties can be compactly expressed in matrix form with a six-vector \tilde{A} with elements A_1, \dots, A_6 ,

$$\tilde{A}(s, t, u, Q^2) = [\bar{\xi}] \tilde{A}(u, t, s, Q^2), \quad (\text{A.17})$$

where $[\xi]$ is a 6×6 diagonal matrix

$$[\bar{\xi}] = \xi \text{ diag}\{1, 1, -1, 1, -1, -1\}, \quad (\text{A.18})$$

and the parameter ξ is defined by $\xi = 1$ for isospin index $(+, 0)$, and $\xi = -1$ for isospin index $(-, 0)$.

Acknowledgements

The work of V. P and M. V. is supported in part by DOE grant no. DE-FG02-04ER41302 and contract DE-AC05-06OR23177 under which Jefferson Science Associates operates the Jefferson Laboratory. Furthermore, the work of S.N.Y. is supported in part by the National Science Council of ROC under grant No. NSC94-2112-M002-025.

We like to thank C. Alexandrou, I. Aznauryan, A. Bernstein, D. Drechsel, S. Kamalov, C. W. Kao, T.S.H. Lee, D.H. Lu, C. Papanicolas, C. Smith, N. Sparveris, S. Stave, L. Tiator, and R. Young, for useful discussions and correspondence during the course of this work.

We also like to thank A. Bernstein and C. Papanicolas for organizing a very stimulating workshop on “The Shape of Hadrons” (Athens, April 27-29, 2006), where many of the topics reviewed in this work were discussed.

References

- [1] H. L. Anderson, E. Fermi, E. A. Long and D. E. Nagle, Phys. Rev. **85**, 936 (1952).
- [2] G. E. Brown and W. Weise, Phys. Rept. **22**, 279 (1975).
- [3] G. Cattapan and L. S. Ferreira, Phys. Rept. **362**, 303 (2002).
- [4] C. Hanhart, Phys. Rept. **397**, 155 (2004).
- [5] K. Greisen, Phys. Rev. Lett. **16**, 748 (1966); G. T. Zatsepin and V. A. Kuzmin, JETP Lett. **4**, 78 (1966).
- [6] A. Mucke, J. P. Rachen, R. Engel, R. J. Protheroe and T. Stanev, Publ. Astron. Soc. Austral. **16**, 160 (1999).
- [7] S. Weinberg, Physica A **96**, 327 (1979).
- [8] J. Gasser and H. Leutwyler, Annals Phys. **158**, 142 (1984).
- [9] V. Bernard, N. Kaiser, and U. G. Meißner, Int. J. Mod. Phys. E **4**, 193 (1995).
- [10] D. Drechsel and L. Tiator, J. Phys. G: Nucl. Phys. **18**, 449 (1992).
- [11] B. Krusche and S. Schadmand, Prog. Part. Nucl. Phys. **51**, 399 (2003).
- [12] V. D. Burkert and T. S. H. Lee, Int. J. Mod. Phys. E **13**, 1035 (2004).
- [13] H. F. Jones and M. D. Scadron, Ann. Phys. **81**, 1 (1973).
- [14] T. Sato and T.-S.H. Lee, Phys. Rev. C **54**, 2660 (1996); *ibid.* **63**, 055201 (2001).
- [15] W. M. Yao *et al.* [Particle Data Group], J. Phys. G **33**, 1 (2006).
- [16] F. A. Berends and A. Donnachie, Nucl. Phys. B **84**, 342 (1975).
- [17] R. A. Arndt, R. L. Workman, Z. Li and L. D. Roper, Phys. Rev. C **42**, 1864 (1990).
- [18] L. Tiator, D. Drechsel, S. S. Kamalov and S. N. Yang, Eur. Phys. J. A **17**, 357 (2003).
- [19] W. W. Ash *et al.*, Phys. Lett. **24B**, 165 (1967).
- [20] H. J. Weber and H. Arenhovel, Phys. Rept. **36**, 277 (1978).
- [21] S. Nozawa and D.B. Leinweber, Phys. Rev. D **42**, 3567 (1990).
- [22] R. Beck *et al.*, Phys. Rev. Lett. **78**, 606 (1997).
- [23] R. Beck *et al.*, Phys. Rev. C **61**, 035204 (2000).
- [24] G. Blanpied *et al.*, Phys. Rev. Lett. **79**, 4337 (1997).
- [25] G. Blanpied *et al.*, Phys. Rev. C **64**, 025203 (2001).
- [26] L. Tiator, D. Drechsel, O. Hanstein, S. S. Kamalov and S. N. Yang, Nucl. Phys. A **689**, 205 (2001).

[27] N. Isgur and G. Karl, Phys. Rev. D **18**, 4187 (1978); *ibid.* D **19**, 2653 (1979) [Erratum-*ibid.* D **23**, 817 (1981)]; Phys. Rev. D **20**, 1191 (1979);

[28] A. De Rujula, H. Georgi and S. L. Glashow, Phys. Rev. D **12**, 147 (1975).

[29] R. Koniuk and N. Isgur, Phys. Rev. D **21**, 1868 (1980) [Erratum-*ibid.* D **23**, 818 (1981)].

[30] N. Isgur, G. Karl and R. Koniuk, Phys. Rev. D **25**, 2394 (1982).

[31] C. M. Becchi and G. Morpurgo, Phys. Lett. **17**, 352 (1965).

[32] J. F. Donoghue, E. Golowich and B. R. Holstein, Phys. Rev. D **12**, 2875 (1975).

[33] S. L. Glashow, Physica **96A**, 27 (1979).

[34] S. S. Gershtein and G. V. Jikia, Sov. J. Nucl. Phys. **34**, 870 (1981) [Yad. Fiz. **34**, 1566 (1981)].

[35] M. Bourdeau and N. C. Mukhopadhyay, Phys. Rev. Lett. **58**, 976 (1987).

[36] S.A. Gogilidze, Yu.S. Surovtsev, and F.G. Tkembuchava, Sov. J. Nucl. Phys. **45**, 674 (1987) [Yad. Fiz. **45**, 1085 (1987)].

[37] D. Drechsel and M. M. Giannini, Phys. Lett. B **143**, 329 (1984).

[38] M. M. Giannini, Rept. Prog. Phys. **54**, 453 (1990).

[39] S. Capstick and G. Karl, Phys. Rev. D **41**, 2767 (1990).

[40] S. Capstick, in Phys. Rev. D **46**, 2864 (1992).

[41] G. Kaelbermann and J. M. Eisenberg, Phys. Rev. D **28**, 71 (1983).

[42] A. W. Thomas, Adv. Nucl. Phys. **13**, 1 (1984).

[43] K. Bermuth, D. Drechsel, L. Tiator and J. B. Seaborn, Phys. Rev. D **37**, 89 (1988).

[44] D. H. Lu, A. W. Thomas and A. G. Williams, Phys. Rev. C **55**, 3108 (1997).

[45] D. H. Lu, private communication.

[46] M. Fiolhais, B. Golli and S. Sirca, Phys. Lett. B **373**, 229 (1996).

[47] A. Wirzba and W. Weise, Phys. Lett. B **188**, 6 (1987).

[48] A. Abada, H. Weigel and H. Reinhardt, Phys. Lett. B **366**, 26 (1996).

[49] H. Walliser and G. Holzwarth, Z. Phys. A **357**, 317 (1997).

[50] D. I. Diakonov, and V. Petrov, Nucl. Phys. **B272**, 457 (1986).

[51] D. I. Diakonov, V. Petrov, and P. Pobylitsa, Nucl. Phys. **B306**, 809 (1988).

[52] Chr.V. Christov, A. Blotz, H.-C. Kim, P. Pobylitsa, T. Watabe, Th. Meissner, E. Ruiz Arriola, and K. Goeke, Prog. Part. Nucl. Phys. **37**, 91 (1996).

[53] T. Watabe, C. V. Christov and K. Goeke, Phys. Lett. B **349**, 197 (1995).

[54] A. Silva, D. Urbano, T. Watabe, M. Fiolhais and K. Goeke, Nucl. Phys. A **675**, 637 (2000).

[55] A. J. Buchmann, E. Hernandez and A. Faessler, Phys. Rev. C **55**, 448 (1997).

[56] P. Grabmayr and A. J. Buchmann, Phys. Rev. Lett. **86**, 2237 (2001).

[57] A. J. Buchmann, Phys. Rev. Lett. **93**, 212301 (2004).

[58] G. Dillon and G. Morpurgo, Phys. Lett. B **448**, 107 (1999).

[59] A. J. Buchmann and E. M. Henley, Phys. Rev. C **63**, 015202 (2001).

[60] A. J. Buchmann and E. M. Henley, Phys. Rev. D **65**, 073017 (2002).

[61] A. Bohr and B. Mottelson, *Nuclear Structure II*, Benjamin, Reading, MA, 1975.

[62] A. Faessler, T. Gutsche, B. R. Holstein, V. E. Lyubovitskij, D. Nicmorus and K. Pumsa-ard, arXiv:hep-ph/0608015.

[63] G. 't Hooft, Nucl. Phys. B **72**, 461 (1974).

[64] E. Witten, Nucl. Phys. B **160**, 57 (1979).

[65] E. Jenkins, Ann. Rev. Nucl. Part. Sci. **48**, 81 (1998).

[66] R. F. Lebed, Czech. J. Phys. **49**, 1273 (1999).

[67] E. Jenkins and A. V. Manohar, Phys. Lett. B **335**, 452 (1994).

[68] E. Jenkins, X. d. Ji and A. V. Manohar, Phys. Rev. Lett. **89**, 242001 (2002).

[69] A. J. Buchmann, J. A. Hester and R. F. Lebed, Phys. Rev. D **66**, 056002 (2002).

[70] T. D. Cohen, Phys. Lett. B **554**, 28 (2003).

[71] T. D. Cohen and R. F. Lebed, arXiv:hep-ph/0608038.

[72] V. Pascalutsa and D. R. Phillips, Phys. Rev. C **68**, 055205 (2003).

[73] D. B. Leinweber, T. Draper and R. M. Woloshyn, Phys. Rev. D **48**, 2230 (1993).

[74] C. Alexandrou, P. de Forcrand and A. Tsapalis, Phys. Rev. D **66**, 094503 (2002).

[75] C. Alexandrou *et al.*, Phys. Rev. D **69**, 114506 (2004).

[76] T. D. Cohen and D. B. Leinweber, Comments Nucl. Part. Phys. **21**, 137 (1993).

[77] D. Elsner *et al.*, Eur. Phys. J. A **27**, 91 (2006).

[78] T. Pospischil *et al.*, Phys. Rev. Lett. **86**, 2959 (2001).

[79] S. Stave *et al.*, arXiv:nucl-ex/0604013.

[80] N. F. Sparveris *et al.* [OOPS Collaboration], Phys. Rev. Lett. **94**, 022003 (2005).

[81] K. Joo *et al.* [CLAS Collaboration], Phys. Rev. Lett. **88**, 122001 (2002).

[82] C. Alexandrou, P. de Forcrand, H. Neff, J. W. Negele, W. Schroers and A. Tsapalis, Phys. Rev. Lett. **94**, 021601 (2005).

[83] M. N. Butler, M. J. Savage and R. P. Springer, Phys. Lett. B **304**, 353 (1993).

[84] E. Jenkins and A. V. Manohar, Phys. Lett. B **255**, 558 (1991).

[85] G. C. Gellas, T. R. Hemmert, C. N. Ktorides and G. I. Poulis, Phys. Rev. D **60**, 054022 (1999).

[86] T. Hemmert, B. R. Holstein and J. Kambor, Phys. Lett. B **395**, 89 (1997); J. Phys. G **24**, 1831 (1998).

[87] T. A. Gail and T. R. Hemmert, arXiv:nucl-th/0512082.

[88] V. Pascalutsa and M. Vanderhaeghen, Phys. Rev. Lett. **95**, 232001 (2005).

[89] V. Pascalutsa and M. Vanderhaeghen, Phys. Rev. D **73**, 034003 (2006).

[90] V. Pascalutsa and D. R. Phillips, Phys. Rev. C **67**, 055202 (2003).

[91] S.S. Kamalov and S.N. Yang, Phys. Rev. Lett. **83**, 4494 (1999); S.S. Kamalov, S.N. Yang, D. Drechsel, O. Hanstein, and L. Tiator, *ibid.* **64**, 032201(R) (2001); S.S. Kamalov, G.Y. Chen, S.N. Yang, D. Drechsel, and L. Tiator, Phys. Lett. B **522** 27 (2001).

[92] D. Drechsel, O. Hanstein, S. S. Kamalov and L. Tiator, Nucl. Phys. A **645**, 145 (1999).

[93] R. A. Arndt, W. J. Briscoe, I. I. Strakovsky and R. L. Workman, Phys. Rev. C **66**, 055213 (2002).

[94] M. De Sanctis, M. M. Giannini, E. Santopinto and A. Vassallo, Nucl. Phys. A **755**, 294 (2005).

[95] C. Mertz *et al.*, Phys. Rev. Lett. **86**, 2963 (2001).

[96] D. B. Leinweber, A. W. Thomas and R. D. Young, Phys. Rev. Lett. **86**, 5011 (2001); W. Detmold, W. Melnitchouk, J. W. Negele, D. B. Renner and A. W. Thomas, *ibid.* **87**, 172001 (2001).

[97] T. R. Hemmert, M. Procura and W. Weise, Phys. Rev. D **68**, 075009 (2003).

[98] M. K. Banerjee and J. Milana, Phys. Rev. D **52**, 6451 (1995).

[99] D. B. Leinweber, A. W. Thomas, K. Tsushima and S. V. Wright, Phys. Rev. D **61**, 074502 (2000).

[100] R. D. Young, D. B. Leinweber, A. W. Thomas and S. V. Wright, Phys. Rev. D **66**, 094507 (2002); R. D. Young, D. B. Leinweber and A. W. Thomas, Prog. Part. Nucl. Phys. **50**, 399 (2003); D. B. Leinweber, A. W. Thomas and R. D. Young, Phys. Rev. Lett. **92**, 242002 (2004).

[101] V. Bernard, T. R. Hemmert and U. G. Meissner, Phys. Lett. B **565**, 137 (2003).

[102] M. Frink, U. G. Meissner and I. Scheller, Eur. Phys. J. A **24**, 395 (2005).

[103] V. Bernard, T. R. Hemmert and U. G. Meissner, Phys. Lett. B **622**, 141 (2005).

[104] C. Hacker, N. Wies, J. Gegelia and S. Scherer, Phys. Rev. C **72**, 055203 (2005).

[105] V. Pascalutsa and M. Vanderhaeghen, Phys. Lett. B **636**, 31 (2006).

[106] J. N. Labrenz and S. R. Sharpe, Phys. Rev. D **54**, 4595 (1996).

[107] C. W. Bernard *et al.*, Phys. Rev. D **64**, 054506 (2001).

[108] R. D. Young, D. B. Leinweber and A. W. Thomas, Nucl. Phys. Proc. Suppl. **129**, 290 (2004).

[109] V. Pascalutsa and M. Vanderhaeghen, Phys. Rev. Lett. **94**, 102003 (2005).

[110] C. Alexandrou *et al.*, PoS **LAT2005**, 091 (2006) [arXiv:hep-lat/0509140].

[111] X. Ji and J. Osborne, Phys. Rev. D **58**, 094018 (1998).

[112] J.C. Collins and A. Freund, Phys. Rev. D **59**, 074009 (1999).

[113] A.V. Radyushkin, Phys. Rev. D **58**, 114008 (1998).

[114] D. Muller, D. Robaschik, B. Geyer, F. M. Dittes and J. Horejsi, Fortsch. Phys. **42**, 101 (1994).

[115] X. D. Ji, Phys. Rev. Lett. **78**, 610 (1997), Phys. Rev. D **55**, 7114 (1997).

[116] A. V. Radyushkin, Phys. Lett. B **380**, 417 (1996).

[117] X. D. Ji, J. Phys. G **24**, 1181 (1998).

[118] K. Goeke, M. V. Polyakov and M. Vanderhaeghen, Prog. Part. Nucl. Phys. **47**, 401 (2001).

[119] M. Diehl, Phys. Rept. **388**, 41 (2003).

[120] A. V. Belitsky and A. V. Radyushkin, Phys. Rept. **418**, 1 (2005).

[121] L. L. Frankfurt, M. V. Polyakov, M. Strikman and M. Vanderhaeghen, Phys. Rev. Lett. **84**, 2589 (2000).

[122] P. A. M. Guichon, L. Mosse and M. Vanderhaeghen, Phys. Rev. D **68**, 034018 (2003).

[123] M. Guidal, S. Bouchigny, J. P. Didelez, C. Hadjidakis, E. Hourany and M. Vanderhaeghen, Nucl. Phys. A **721**, 327 (2003).

[124] P. Stoler, Phys. Rev. Lett. **91**, 172303 (2003).

[125] M. Burkardt, Phys. Lett. B **595**, 245 (2004).

[126] P. Stoler, Phys. Rev. D **65**, 053013 (2002).

[127] M. Diehl, T. Feldmann, R. Jakob and P. Kroll, Eur. Phys. J. C **39**, 1 (2005).

[128] M. Guidal, M. V. Polyakov, A. V. Radyushkin and M. Vanderhaeghen, Phys. Rev. D **72**, 054013 (2005).

[129] A. D. Martin, R. G. Roberts, W. J. Stirling and R. S. Thorne, Phys. Lett. B **531**, 216 (2002).

[130] V. V. Frolov *et al.*, Phys. Rev. Lett. **82**, 45 (1999).

[131] M. Ungaro, P. Stoler, I. Aznauryan, V. D. Burkert, K. Joo and L. C. Smith [the CLAS Collaboration], arXiv:hep-ex/0606042.

[132] I. G. Aznauryan, Phys. Rev. C **67**, 015209 (2003).

[133] C. Herberg *et al.*, Eur. Phys. J. A **5**, 131 (1999).

[134] M. Ostrick *et al.*, Phys. Rev. Lett. **83**, 276 (1999).

[135] J. Becker *et al.*, Eur. Phys. J. A **6**, 329 (1999).

[136] D. Rohe *et al.*, Phys. Rev. Lett. **83**, 4257 (1999).

[137] I. Passchier *et al.*, Phys. Rev. Lett. **82**, 4988 (1999).

[138] H. Zhu *et al.* [E93026 Collaboration], Phys. Rev. Lett. **87**, 081801 (2001).

[139] G. Warren *et al.* [Jefferson Lab E93-026 Collaboration], Phys. Rev. Lett. **92**, 042301 (2004).

[140] R. Madey *et al.* [E93-038 Collaboration], Phys. Rev. Lett. **91**, 122002 (2003).

[141] N. Sparveris, to appear in Proceedings of the Workshop “Shape of Hadrons”, Athens, 2006. Eds. C.N. Papanicolas and A.M. Bernstein, AIP (2006).

[142] J.J. Kelly *et al.*, Phys. Rev. Lett. **95**, 102001 (2005).

[143] M. Burkardt, Phys. Rev. D **62**, 071503 (2000) [Erratum-ibid. D **66**, 119903 (2002)].

[144] A. V. Belitsky, X. d. Ji and F. Yuan, Phys. Rev. D **69**, 074014 (2004).

[145] M. Burkardt, Int. J. Mod. Phys. A **18**, 173 (2003).

[146] G. P. Lepage and S. J. Brodsky, Phys. Rev. D **22**, 2157 (1980).

[147] V. L. Chernyak and A. R. Zhitnitsky, JETP Lett. **25**, 510 (1977) [Pisma Zh. Eksp. Teor. Fiz. **25**, 544 (1977)].

[148] V. L. Chernyak, A. R. Zhitnitsky and V. G. Serbo, JETP Lett. **26**, 594 (1977) [Pisma Zh. Eksp. Teor. Fiz. **26**, 760 (1977)].

[149] A. V. Efremov and A. V. Radyushkin, Phys. Lett. B **94**, 245 (1980).

[150] C. E. Carlson, Phys. Rev. D **34**, 2704 (1986).

[151] A. F. Sill *et al.*, Phys. Rev. D **48**, 29 (1993).

[152] M. K. Jones *et al.* [Jefferson Lab Hall A Collaboration], Phys. Rev. Lett. **84**, 1398 (2000).

[153] O. Gayou *et al.*, Phys. Rev. C **64**, 038202 (2001).

[154] O. Gayou *et al.* [Jefferson Lab Hall A Collaboration], Phys. Rev. Lett. **88**, 092301 (2002).

[155] A. V. Belitsky, X. d. Ji and F. Yuan, Phys. Rev. Lett. **91**, 092003 (2003).

[156] A. Idilbi, X. d. Ji and J. P. Ma, Phys. Rev. D **69**, 014006 (2004).

[157] V. M. Belyaev and A. V. Radyushkin, Phys. Lett. B **359**, 194 (1995).

[158] V. M. Belyaev and A. V. Radyushkin, Phys. Rev. D **53**, 6509 (1996).

[159] R. P. Feynman, *Photon-Hadron Interactions*, Benjamin, Reading, MA, 1972.

[160] V. M. Braun, A. Lenz, G. Peters and A. V. Radyushkin, Phys. Rev. D **73**, 034020 (2006).

[161] B. L. Ioffe, Nucl. Phys. B **188**, 317 (1981) [Erratum-ibid. B **191**, 591 (1981)].

[162] G.F. Chew, M.L. Goldberger, F.E. Low, and Y. Nambu, Phys. Rev. **106**, 1337 (1956).

[163] S. Fubini, Y. Nambu, and V. Wataghin, Phys. Rev. **111**, 329 (1958).

[164] F.A. Berends, A. Donnachie, and D.L. Weaver, Nucl. Phys. B **4**, 1 (1967); *ibid.* **4**, 54 (1967); *ibid.* **4**, 103 (1967).

[165] D. Schwela, H. Rollnik, R. Weizel, and W. Korth, Z. Phys. **202**, 452 (1967);
D. Schwela and R. Weizel, Z. Phys. **221**, 71 (1969).

[166] O. Hanstein, D. Drechsel and L. Tiator, Nucl. Phys. A **632**, 561 (1998).

[167] I. G. Aznauryan, Phys. Rev. C **67**, 015209 (2003).

[168] S.S. Kamalov *et al.*, Phys. Rev. C **66**, 065206 (2002).

[169] R.D. Peccei, Phys. Rev. **181**, 1902 (1969).

[170] M.G. Olsson and E.T. Osypowski, Nucl. Phys. B **87**, 399 (1975); Phys. Rev. D **17**, 174 (1978).

[171] R.M. Davidson, N.C. Mukhopadhyay, and R.S. Wittman, Phys. Rev. D **43**, 71 (1991).

[172] H. Garcilazo and E. Moya de Guerra, Nucl. Phys. A **562**, 521 (1993);
C. Fernandez-Ramirez, E. Moya de Guerra and J. M. Udias, Annals Phys. **321**, 1408 (2006); Phys. Rev. C **73**, 042201 (2006).

[173] M. Vanderhaeghen, K. Heyde, J. Ryckebusch and M. Waroquier, Nucl. Phys. A **595**, 219 (1995).

[174] V. Pascalutsa and O. Scholten, Nucl. Phys. A **591**, 658 (1995);
O. Scholten, A. Y. Korchin, V. Pascalutsa and D. Van Neck, Phys. Lett. B **384**, 13 (1996);
A. Y. Korchin, O. Scholten and R. G. E. Timmermans, Phys. Lett. B **438**, 1 (1998);
A. Usov and O. Scholten, Phys. Rev. C **72**, 025205 (2005); *ibid.* **74**, 015205 (2006).

[175] T. Feuster and U. Mosel, Phys. Rev. C **59**, 460 (1999);
G. Penner and U. Mosel, Phys. Rev. C **66**, 055211 (2002);
V. Shklyar, G. Penner and U. Mosel, Eur. Phys. J. A **21**, 445 (2004);
V. Shklyar, H. Lenske and U. Mosel, Phys. Rev. C **72**, 015210 (2005).

[176] H. Tanabe and K. Ohta, Phys. Rev. C **31**, 1876 (1985).

[177] S.N. Yang, J. Phys. G **11**, L205 (1985); Phys. Rev. C **40**, 1810 (1989); Chin. J. Phys. **29**, 485 (1991).

[178] S. Nozawa, B. Blankleider, and T.-S.H. Lee, Nucl. Phys. A **513**, 459 (1990).

[179] C. C. Lee, S. N. Yang, and T.-S.H. Lee, J. Phys. G **17**, L131 (1991).

[180] Y. Surya and F. Gross, Phys. Rev. C **53**, 2422 (1996).

[181] G. Y. Chen *et al.*, Nucl. Phys. A **723**, 447 (2003).

[182] V. Pascalutsa and J.A. Tjon, Phys. Rev. C **70**, 035209 (2004);
G. L. Caia, V. Pascalutsa, J.A. Tjon, and L. E. Wright, *ibid.* **70**, 032201(R) (2004);
G. L. Caia, L. E. Wright, and V. Pascalutsa, *ibid.* **72**, 035203 (2005);
G. L. Caia, PhD Thesis (Ohio University, 2004) [<http://www.ohiolink.edu/etd>].

[183] SAID website, <http://gwdac.phys.gwu.edu>.

[184] MAID website, <http://www.kph.uni-mainz.de>.

[185] L.S. Barker, A. Donnachie, and J.K. Storrow, Nucl. Phys. B **95**, 347 (1975).

[186] W.T. Chiang and F. Tabakin, Phys. Rev. C **55**, 2054 (1997).

[187] G. Knoechlein, D. Drechsel, and L. Tiator, Z. Phys. A **352**, 327 (1995).

[188] A.S. Raskin and T.W. Donnelly, Ann. Phys. (N.Y.) **191**, 78 (1989).

[189] C.W. Akerlof *et al.*, Phys. Rev. **163**, 1482 (1967).

[190] C.T. Hung, S.N. Yang, and T.-S.H. Lee, Phys. Rev. C **64**, 034309 (2001).

[191] A. Klein and T.-S.H. Lee, Phys. Rev. D **10**, 4308 (1974).

[192] R. Blankenbecler and R. Sugar, Phys. Rev. **142**, 1051 (1966).

[193] V. G. Kadyshevsky, Nucl. Phys. B **6**, 125 (1968).

[194] R. H. Thompson, Phys. Rev. D **1**, 110 (1970).

[195] M. Cooper and B. Jennings, Nucl. Phys. A **500**, 553 (1989).

[196] C. T. Hung, S. N. Yang and T.-S.H. Lee, J. Phys. **G20**, 1531 (1994).

[197] K. Watson, Phys. Rev. **95**, 228 (1954);
E. Fermi, Suppl. Nuovo Cimento **2**, 58 (1955).

[198] S. N. Yang, in *Progress in Medium-Energy Physics*, Eds. W.-Y.P. Hwang and J. Speth, World Scientific, Singapore, 1988, p. 201-215.

[199] S.S. Kamalov, G.Y. Chen, S.N. Yang, D. Drechsel, and L. Tiator, Phys. Lett. B **522**, 27 (2001).

[200] T. Sato, M. Doi, N. Odagawa, and H. Ohtsubo, Few-Body Syst. Suppl. **5**, 524 (1992); T. Sato, M. Kobayashi, and H. Ohtsubo (unpublished).

[201] S. S. Hsiao *et al.*, Few-Body Systems **25**, 55 (1998).

[202] P. Dennery, Phys. Rev. **124**, 2000 (1961).

[203] R. A. Arndt, I. I. Strakovsky and R. L. Workman, Phys. Rev. C **53**, 430 (1996).

[204] V. Pascalutsa and J. A. Tjon, Phys. Rev. C **61**, 054003 (2000).

[205] A. Donnachie, in *High energy physics*, Vol. V, ed. E.U.S. Burhop (Academic Press, New York, 1972).

[206] G. v. Gehlen, Nucl. Phys. B **9**, 17 (1968).

[207] Ph. Salin, Nuovo Cimento, **32**, 521 (1964).

[208] J. P. Loubaton, Nuovo Cimento, **39**, 591 (1965).

[209] J. D. Walecka, Phys. Rev. **162**, 1462 (1967).

[210] R. L. Crawford and W. T. Morton, Nucl. Phys. B **B211**, 1 (1983);
 Particle Data Group, Phys. Lett. B **239**, 1 (1990);
 R. L. Crawford, in: *Proceedings of NSTAR2001, Mainz, Germany, March 7–10, 2001*, Eds. D. Drechsel and L. Tiator, World Scientific, p. 163.

[211] S. Weinberg, *The quantum theory of fields*, Vol. 2, (Cambridge U. P., Cambridge NY, 1995).

[212] V. Bernard, N. Kaiser and U. G. Meissner, Int. J. Mod. Phys. E **4**, 193 (1995).

[213] D. B. Kaplan, “Five lectures on effective field theory,” arXiv:nucl-th/0510023.

[214] W. Rarita and J. S. Schwinger, Phys. Rev. **60**, 61 (1941).

[215] P.A.M. Dirac, *Lectures on quantum mechanics*, (Yeshiba U. P., New York, 1964).

[216] G. Senjanovic, Phys. Rev. D **16**, 307 (1977).

[217] N. S. Baaklini and M. Tuite, J. Phys. A **11**, L139 (1978).

[218] M. Yamada, The Interacting Spin 3/2 Field,” Nuovo Cim. A **91**, 205 (1986).

[219] V. Pascalutsa, Phys. Rev. D **58**, 096002 (1998).

[220] K. Johnson and E. C. G. Sudarshan, Annals Phys. **13**, 126 (1961).

[221] C. R. Hagen, Phys. Rev. D **4**, 2204 (1971).

[222] G. Velo and D. Zwanziger, Phys. Rev. **186**, 1337 (1969).

[223] L. P. S. Singh, Phys. Rev. D **7**, 1256 (1973).

[224] C. R. Hagen and L. P. S. Singh, Phys. Rev. D **26**, 393 (1982).

[225] H. Haberzettl, arXiv:nucl-th/9812043.

[226] S. Deser, V. Pascalutsa and A. Waldron, Phys. Rev. D **62**, 105031 (2000).

[227] T. Pilling, Mod. Phys. Lett. A **19**, 1781 (2004); Int. J. Mod. Phys. A **20**, 2715 (2005).

[228] N. Wies, J. Gegelia and S. Scherer, Phys. Rev. D **73**, 094012 (2006).

[229] M. Napsuciale, M. Kirchbach and S. Rodriguez, arXiv:hep-ph/0606308.

[230] V. Pascalutsa and R. G. E. Timmermans, Phys. Rev. C **60**, 042201(R) (1999).

[231] H.T. Williams, Phys. Rev. C **29**, 2222 (1985); *ibid.*, **31**, 2297 (1985).

[232] R.A. Adelseck, C. Bennhold, and L.E. Wright, Phys. Rev. C **32**, 1681 (1986).

[233] F. Gross and Y. Surya, Phys. Rev. C **47**, 703 (1993); *ibid.* **53**, 2422 (1996).

[234] V. Pascalutsa, in Proc. of *Nstar 2002: Physics of Excited Baryons*, eds S. A. Dytman and E. S. Swanson (World Scientific, 2003) [arXiv:nucl-th/0303005].

[235] L. M. Nath, B. Etemadi and J. D. Kimel, Phys. Rev. D **3**, 2153 (1971).

[236] V. Pascalutsa, Phys. Lett. B **503**, 85 (2001).

[237] D. Z. Freedman and A. Das, Nucl. Phys. B **120**, 221 (1977).

[238] H.-B. Tang and P. Ellis, Phys. Lett. B **387**, 9 (1996).

[239] N. Fettes and U. G. Meissner, Nucl. Phys. A **679**, 629 (2001).

[240] S. Weinberg in *Lectures on Elementary Particles and Quantum Field Theory*, Volume 1, Brandeis University Summer Institute 1970 (S. Deser, M. Grisaru and H. Pendleton, editors, M.I.T. Press, Cambridge, 1970).

[241] S. Ferrara, M. Porrati and V. L. Telegdi, Phys. Rev. **D46**, 3529 (1992).

[242] B. R. Holstein, arXiv:hep-ph/0607187.

[243] J. Gasser, M. E. Sainio and A. Svarc, Nucl. Phys. B **307**, 779 (1988).

[244] B. Kubis and U. G. Meissner, Nucl. Phys. A **679**, 698 (2001).

[245] V. Pascalutsa, PhD Thesis (University of Utrecht, 1998) [Hadronic J. Suppl. **16**, 1 (2001)].

[246] J. Gegelia and G. Japaridze, Phys. Rev. D **60**, 114038 (1999);
J. Gegelia, G. Japaridze and X. Q. Wang, J. Phys. G **29**, 2303 (2003).

[247] C. Hanhart and N. Kaiser, Phys. Rev. C **66**, 054005 (2002).

[248] A. M. Bincer, Phys. Rev. **118**, 855 (1960);
S. D. Drell and H. R. Pagels, *ibid.* **140**, B397 (1965).

[249] B. R. Holstein, V. Pascalutsa and M. Vanderhaeghen, Phys. Rev. D **72**, 094014 (2005).

[250] S. R. Beane, M. Malheiro, J. A. McGovern, D. R. Phillips and U. van Kolck, Phys. Lett. B **567**, 200 (2003) [Erratum-*ibid.* B **607**, 320 (2005)].

[251] M. Camen *et al.*, Phys. Rev. C **65**, 032202 (2002).

[252] V. Bernard, N. Kaiser, J. Kambor and U. G. Meissner, Nucl. Phys. B **388**, 315 (1992).

[253] V. Bernard, N. Kaiser and U. G. Meissner, Nucl. Phys. B **373**, 346 (1992).

[254] A. I. Lvov, Phys. Lett. B **304**, 29 (1993).

[255] V. Pascalutsa, Prog. Part. Nucl. Phys. **55**, 23 (2005).

[256] J. A. McGovern, Phys. Rev. C **63**, 064608 (2001) [Erratum-*ibid.* C **66**, 039902 (2002)].

[257] S. R. Beane, M. Malheiro, J. A. McGovern, D. R. Phillips and U. van Kolck, Nucl. Phys. A **747**, 311 (2005).

[258] S. Kondratyuk and O. Scholten, Phys. Rev. C **64**, 024005 (2001).

[259] A. I. L'vov, V. A. Petrun'kin and M. Schumacher, Phys. Rev. C **55**, 359 (1997).

[260] D. Drechsel, B. Pasquini and M. Vanderhaeghen, Phys. Rept. **378**, 99 (2003).

[261] R. P. Hildebrandt, H. W. Griesshammer, T. R. Hemmert and B. Pasquini, Eur. Phys. J. A **20**, 293 (2004).

[262] R. P. Hildebrandt, PhD Thesis (University of Munich, 1995), [arXiv:nucl-th/0512064].

[263] C. Hacker, N. Wies, J. Gegelia and S. Scherer, arXiv:hep-ph/0603267.

[264] E. L. Hallin *et al.*, Phys. Rev. C **48**, 1497 (1993).

[265] LEGS Collaboration, Phys. Rev. Lett. **76**, 1023 (1996).

[266] M. Kotulla *et al.*, Phys. Rev. Lett. **89**, 272001 (2002).

[267] A. I. Machavariani, A. Faessler and A. J. Buchmann, Nucl. Phys. A **646**, 231 (1999) [Erratum-*ibid.* A **686**, 601 (2001)].

[268] D. Drechsel, M. Vanderhaeghen, M. M. Giannini and E. Santopinto, Phys. Lett. B **484**, 236 (2000).

[269] D. Drechsel and M. Vanderhaeghen, Phys. Rev. C **64**, 065202 (2001).

[270] W. T. Chiang, M. Vanderhaeghen, S. N. Yang and D. Drechsel, Phys. Rev. C **71**, 015204 (2005).

[271] D. B. Leinweber, T. Draper, and R. M. Woloshyn, Phys. Rev. D **46**, 3067 (1992); I. C. Cloet, D. B. Leinweber and A. W. Thomas, Phys. Lett. B **563**, 157 (2003).

[272] F. X. Lee, R. Kelly, L. Zhou and W. Wilcox, arXiv:hep-lat/0410037.

[273] V. Pascalutsa, B. R. Holstein and M. Vanderhaeghen, Phys. Lett. B **600**, 239 (2004).

[274] M. Kotulla, to appear in Proceedings of the Workshop “Shape of Hadrons”, Athens, 2006. Eds. C.N. Papanicolas and A.M. Bernstein, AIP (2006).

[275] See, e.g., ”Chiral Dynamics: Theory and Experiment”, Eds. A.M. Bernstein, D. Drechsel, and Th. Walcher, Springer-Verlag,

[276] V. Bernard, J. Gasser, N. Kaiser, and Ulf-G. Meißner, Phys. Lett. B **268** (1991) 291.

[277] V. Bernard, N. Kaiser, and Ulf-G. Meißner, Z. Phys. C70 (1996) 483; Nucl. Phys. A **607** (1996) 379, and references therein.

[278] R. Beck *et. al.*, Phys. Lett. Lett. **65**, 1841 (1990).

[279] M. Fuchs *et al.*, Phys. Lett. B **368**, 20 (1996).

[280] J. C. Bergstrom *et al.*, Phys. Rev. C **53**, R1052 (1996); *ibid.* **55**, 2016 (1997).

[281] H. B. van den Brink *et al.*, Phys. Rev. Lett. **74**, 3561 (1995); Nucl. Phys. A **612**, 391 (1997).

[282] M. O. Distler *et al.*, Phys. Rev. Lett. **80**, 2294 (1998).

[283] A. M. Bernstein *et al.*, Phys. Rev. C **55**, 1509 (1997).

[284] A. Schmidt *et al.*, nucl-ex/0105010.

[285] P.U. Sauer, Prog. Part. Nucl. Phys. **16**, 35 (1986).

[286] B. C. Pearce and B. K. Jennings, Nucl. Phys. A **528**, 655 (1991).

[287] A. D. Lahiff and I. R. Afnan, Phys. Rev. C **60**, 024608 (1999).

[288] S. Théberge *et al.*, Phys. Rev. D **22**, 2838 (1980).

[289] D. A. McPherson *et al.*, Phys. Rev. **136**, B1465 (1964).

[290] M. MacCormick *et al.*, Phys. Rev. C **53**, 41 (1996).

[291] J. Ahrens *et al.* [GDH and A2 Collaborations], Phys. Rev. Lett. **84**, 5950 (2000).

[292] J. Ahrens *et al.* [GDH and A2 Collaboration], Eur. Phys. J. A **21**, 323 (2004).

[293] R. Leukel, PhD Thesis, University of Mainz, 2001.

[294] A. A. Belyaev *et al.*, Nucl. Phys. B **213**, 201 (1983).

[295] A. Bock *et al.*, Phys. Rev. Lett. **81**, 534 (1998).

[296] V. A. Getman *et al.*, Nucl. Phys. B **188**, 397 (1981).

[297] H. Dutz *et al.*, Nucl. Phys. A **601**, 319 (1996).

[298] A. A. Belyaev *et al.*, Yad. Fiz. **40**, 133 (1984).

[299] A.A. Belyaev *et al.*, Proc. Int. Sym. High Energy Lepton-Photon Interaction, Kyoto, Japan, August 19-24, 1985.

[300] J. Ahrens *et al.*, Eur. Phys. J. A **26**, 135 (2005).

[301] J. Ahrens *et al.*, Phys. Rev. Lett. **88**, 232002 (2002).

[302] A. Sandorfi, in "NSTAR 2004", Eds. J-P. Bocquet, V. Kuznetsov, and D. Rebreyend, World Scientific, Singapore, 2004, p. 164.

[303] F. Foster and G. Hughes, Rept. Prog. Phys. **46**, 1445 (1983).

[304] H. Merkel *et al.*, Phys. Rev. Lett. **88**, 012301 (2002).

[305] R. De Vita *et al.*, Phys. Rev. Lett. **88**, 082001 (2002).

[306] A.V. Klimenka Phys. Rev. C **73**, 035212 (2002).

[307] G.A. Warren *et al.*, Phys. Rev. C **58**, 3722 (1998).

[308] P. Bartsch *et al.*, Phys. Rev. Lett. **88**, 142001 (2002).

[309] G. Laveissiere *et al.*, Phys. Rev. C **69**, 045203 (2004).

[310] K. Joo *et al.*, Phys. Rev. C **68**, 035202 (2003).

[311] L.D. van Buuren Phys. Rev. Lett. **89**, 012001 (2002).

[312] C. Kunz *et al.*, Phys. Lett. B **564**, 21 (2003).

[313] J. Arrington, Phys. Rev. C **68**, 034325 (2003).

[314] P. A. M. Guichon and M. Vanderhaeghen, Phys. Rev. Lett. **91**, 142303 (2003).

[315] P. G. Blunden, W. Melnitchouk and J. A. Tjon, Phys. Rev. Lett. **91**, 142304 (2003).

[316] Y.C. Chen, A. Afanasev, S.J. Brodsky, C.E. Carlson and M. Vanderhaeghen, Phys. Rev. Lett. **93**, 122301 (2004);
 A. V. Afanasev, S. J. Brodsky, C. E. Carlson, Y. C. Chen and M. Vanderhaeghen, Phys. Rev. D **72**, 013008 (2005).

[317] V. Pascalutsa, C. E. Carlson and M. Vanderhaeghen, Phys. Rev. Lett. **96**, 012301 (2006).

[318] S. Kondratyuk and P. G. Blunden, arXiv:nucl-th/0601063.

[319] S. Adler, Ann. Phys. (N.Y.) **50**, 189 (1968).

[320] V. Tsvaskis, J. Arrington, M. E. Christy, R. Ent, C. E. Keppel, Y. Liang and G. Vittorini, Phys. Rev. C **73**, 025206 (2006).

[321] V. Tsvaskis, talk at the JLab/INT Workshop “Precision Electroweak Physics”, College of William and Mary, August 15-17, 2005.

[322] M. Jacob and G.C. Wick, Ann. Phys. **7**, 404 (1959).